UNIVERSIDAD COMPLUTENSE DE MADRID

FACULTAD DE CIENCIAS FÍSICAS

TESIS DOCTORAL

Parametrizations and forecasts for non-standard cosmological models with galaxy surveys

Parametrizaciones de modelos cosmológicos alternativos y cotas para futuros mapas de galaxias

MEMORIA PARA OPTAR AL GRADO DE DOCTOR

PRESENTADA POR

Miguel Aparicio Resco

DIRECTOR

Antonio López Maroto

Parametrizations and forecasts for non-standard cosmological models with galaxy surveys

---

Parametrizaciones de modelos cosmológicos alternativos y cotas para futuros mapas de galaxias

UNIVERSIDAD
COMPLUTENSE
MADRID

Miguel Aparicio Resco

TESIS DOCTORAL
MADRID 2020

Parametrizations and forecasts for non-standard cosmological models with galaxy surveys

---

Parametrizaciones de modelos cosmológicos alternativos y cotas para futuros mapas de galaxias

por

Miguel Aparicio Resco

bajo la supervisión de

Antonio López Maroto

UNIVERSIDAD
COMPLUTENSE
MADRID

Tesis presentada en la
Universidad Complutense de Madrid
para el grado de Doctor en Física

Departamento de Física Teórica
Facultad de Ciencias Físicas

Diciembre 2020

Contents

Acknowledgements

Estos años de doctorado han sido una etapa realmente importante, tanto a nivel académico como a nivel personal. Valoro especialmente la capacidad de autocrítica y de rigurosidad que la investigación me ha enseñado, así como las herramientas que he aprendido a la hora de enfrentarme a problemas nuevos y desconocidos. A nivel personal, estos años de tesis doctoral me han hecho conocer y visitar personas y lugares maravillosos.

En primer lugar querría agradecer a mi director, Antonio, su dedicación y esfuerzo durante la tesis. Su puerta siempre ha estado abierta para mí. He aprendido de su espíritu crítico y su extraordinaria forma de enfrentarse a los problemas. También querría agradecer a la colaboración J-PAS su acogida y todo lo que he aprendido trabajando con ellos.

En segundo lugar quiero dar las gracias a mis compañeros de despacho: Santiago, Juan Miguel, Laura, Roberto, Pablo, etc. En especial a Juan Miguel, con el cual he compartido muchos momentos y aficiones en común. También quiero dar las gracias a todos los compañeros de departamento: Jose Manuel, Héctor, Clara, Dani, Arkaitz, Merce, Juanjo, Miguel, Rafa, Adolfo, Prado, Valentín, Adrián, etc. En especial a Héctor por su constante ayuda y las valiosas discusiones que hemos tenido en éstos años.

En tercer lugar querría dar las gracias a mis compañeros y amigos de la tuna: Juan, Víctor, Juan Carlos, Fernando, Percy, Gabriel, etc. Por el enorme valor cultural y de amistad de todas nuestras salidas y viajes en común.

En cuarto lugar gracias a mi mejor amiga y compañera de vida Andrea, a la que he conocido durante estos años de doctorado. Tu apoyo y cariño ha sido fundamental en

éstos últimos años. Por último gracias a mi familia, a mis padres por su apoyo y cariño constantes y a mis hermanos Pablo y Moisés. Gracias también en especial a mis abuelos, por vuestra inspiración y afecto. Ésta tesis va dedicada a ellos, a mis abuelos Jesús, Pilar, Teresa y Julio por su humilde esfuerzo y trabajo de toda una vida. Por ellos, a los que la vida no les dio la oportunidad de estudiar, va dedicado este trabajo.

Publications

- Miguel Aparicio Resco, Antonio L. Maroto. "Parametrizing growth in dark energy and modified gravity models". Phys. Rev. D 97, 043518 (2018). DOI: 10.1103/PhysRevD.97.043518. arXiv: 1707.08964.

- Miguel Aparicio Resco, Antonio L. Maroto. "Parametrizing modified gravities with vector degrees of freedom: anisotropic growth and lensing". JCAP, Volume 2018, October 2018. DOI: 10.1088/1475-7516/2018/10/014. arXiv: 1807.04649.

- Miguel Aparicio Resco, Antonio L. Maroto. "Testing for gravitational preferred directions with galaxy and lensing surveys". JCAP, Volume 2020, February 2020. DOI: 10.1088/1475-7516/2020/02/013. arXiv: 1907.12285.

- Miguel Aparicio Resco, Antonio L. Maroto, Jailson S. Alcaniz, L. Raul Abramo, C. Hernández-Monteagudo, et al. "J-PAS: forecasts on dark energy and modified gravity theories". MNRAS 493 (2020) 3616-3631. DOI: 10.1093/mnras/staa367. arXiv: 1910.02694.[1]

- Miguel Aparicio Resco, Antonio L. Maroto. "The Fisher gAlaxy suRvey cOde (FARO)". arXiv: 2007.05360. Accepted for publication in JCAP.

- Miguel Aparicio Resco, Antonio L. Maroto. "Modified gravity or imperfect dark matter: a model-independent discrimination". arXiv: 2010.01368. Accepted for publication in JCAP.

[1]Funding for the J-PAS Project has been provided by the Governments of Spain and Aragón through the Fondo de Inversión de Teruel, European FEDER funding and the Spanish Ministry of Science, Innovation and Universities, and by the Brazilian agencies FINEP, FAPESP, FAPERJ and by the National Observatory of Brazil. Additional funding was also provided by the Tartu Observatory and by the J-PAS Chinese Astronomical Consortium. This paper has gone through internal review by the J-PAS collaboration.

Abstract

The next generation of galaxy surveys will shed new light on our understanding of the Universe on large scales. Thanks to the large number of galaxies and the accuracy of these galaxy maps, the cosmological parameters will be measured at the 1 % level and below. This makes it necessary to develop forecast analysis to explore what are the parameters that galaxy surveys will constrain with better accuracy, and also the best configurations of these surveys to exploit the maximum potential of the observables.

From the theoretical point of view, there are many different models that have been proposed in recent years to describe the yet unknown dark sector of cosmology. Regarding models for the late-time accelerated expansion of the Universe, they can be classified in two types: dark energy models and modified gravity models. The former considers a modification in the matter-energy term, this modification extends the constant dark energy term of ΛCDM model into a dynamical dark energy. Instead, modified gravity models consider a modification in the gravity term that generates accelerated expansion.

In the context of galaxy surveys and cosmological models of the dark sector and modified gravity, this thesis aims at providing model-independent parametrizations of possible modifications of the standard ΛCDM cosmology. We will also perform Fisher forecast analysis in order to estimate the sensitivity of future galaxy surveys for the detection of such deviations.

Regarding modified gravity models, we analyze theories in which a vector degree of freedom is included. We obtain a parametrization of this kind of models in the sub-Hubble regime within the quasi-static approximation. We find that in the case in which dark matter obeys standard conservation equations, eight parameters are needed to fully characterize the theory. In addition, if dark matter vorticity can be neglected, the number of independent parameters is reduced to four. Secondly, we consider models with imperfect

and non-conserved dark matter. We parametrize this kind of models and prove that they can be described with five general functions of time and scale.

Once we have described the parametrizations, we obtain the observable power spectra of galaxy surveys considering these models. In the case of vector field theories with non-vanishing spatial components in the background, we find that a preferred direction is added to the observables. We obtain the expressions for the multipole galaxy power spectrum in redshift space and for the weak-lensing shear, convergence and rotation spectra in the presence of the preferred direction. In the case of non-standard dark matter models, we calculate the observable power spectra of the galaxy distribution, galaxy velocities and weak lensing and find that these observables are only sensitive to three combinations of the initial five functions of the model. Deviations of these three observable functions with respect to ΛCDM give us different characteristic signals which allow us to determine in which cases it is possible to discriminate a modification of gravity from an imperfect or non-conserved dark matter.

Finally, we perform Fisher forecast analysis for each observable parameter of the different models. We start by calculating the Fisher matrices for each observable power spectrum. This is particularly interesting for the case in which a preferred direction is considered. Then we obtain future constraints for preferred direction and non-standard dark matter parametrizations. Finally, we present the results of two additional projects related with Fisher forecast analysis of galaxy surveys. First, we have performed a Fisher forecast analysis of modified gravity models for the J-PAS collaboration; and we have developed the Fisher code FARO for forecast analysis with the linear multitracer 3D galaxy power spectrum, the linear convergence power spectrum for weak lensing, and the linear multitracer power spectrum for the correlation between galaxy distribution and convergence.

Resumen

La próxima generación de mapas de galaxias arrojará luz en nuestra comprensión del Universo a gran escala. Gracias al gran número de galaxias y a la precisión de éstos mapas, se podrán medir los parámetros cosmológicos con precisión del 1 % y menor. Es por ello que es necesario el desarrollo de estimaciones de las futuras medidas para explorar qué parámetros se podrán medir con mayor precisión, así como encontrar las mejores configuraciones de los mapas de galaxias para explotar el máximo potencial de los observables.
Desde el punto de vista teórico, hay una gran cantidad de modelos que se han propuesto recientemente para describir el aún desconocido sector oscuro de la cosmología. En cuanto a los modelos que describen la actual expansión acelerada del Universo, se pueden clasificar principalmente en dos tipos: modelos de energía oscura y modelos de gravedad modificada. El primer tipo considera una modificación en el término de materia y energía, ésta modificación generaliza la constante cosmológica del modelo de ΛCDM en una energía oscura dinámica. Por otro lado, los modelos de gravedad modificada generalizan el término de gravedad de la Relatividad General estándar para poder generar una expansión acelerada. En el contexto de mapas de galaxias y modelos cosmológicos del sector oscuro y gravedad modificada, la presente tesis tiene como objetivo estudiar parametrizaciones independientes del modelo para modelos de gravedad modificada. Además, realizaremos un análisis de Fisher con el fin de estimar la sensibilidad de futuros mapas de galaxias a la hora de detectar tales desviaciones.
En relación a los modelos de gravedad modificada, analizamos teorías con un grado de libertad vectorial. Para su estudio, consideramos el régimen sub-Hubble y la aproximación quasiestática. Encontramos que, en el caso en el cual la materia oscura sigue las ecuaciones estándar de conservación, se necesitan ocho parámetros para describir la teoría. En cambio, si podemos despreciar la vorticidad de la materia oscura, el número de parámetros

independientes se reduce a cuatro. En segundo lugar, se consideran modelos de materia oscura imperfecta y no conservada. Se obtiene una parametrización de éste tipo de modelos y probamos que se pueden describir con únicamente cinco funciones arbitrarias del tiempo y la escala.

Una vez descritas las parametrizaciones, obtenemos los espectros de potencias observables de los mapas de galaxias para los modelos anteriores. En el caso de los modelos con grados de libertad vectoriales y con una componente espacial de fondo no nula, encontramos que aparece una dirección privilegiada en los observables. Obtenemos las expresiones para el espectro de potencias multipolar en espacio de redshift y para los espectros de lente gravitacional débil en presencia de ésta dirección privilegiada. En el caso de los modelos de materia oscura no estándar, calculamos los espectros de distribución de galaxias, distribución de velocidades peculiares y el espectro de lente gravitacional débil; encontramos que éstos observables son sensibles únicamente a tres combinaciones de las cinco funciones del modelo. Las desviaciones de éstos tres parámetros observables respecto de ΛCDM generan diferentes señales características que permiten determinar en qué caso es posible distinguir una modificación de la gravedad de un modelo de materia oscura no estándar.

Finalmente, realizamos un análisis de Fisher para estimar futuros errores para cada modelo anteriormente descrito. Empezamos calculando las matrices de Fisher de cada espectro de potencias observable. Es de particular interés el cálculo de las matrices de Fisher en el caso de una dirección privilegiada. A continuación, obtenemos restricciones a las parametrizaciones de los modelos con dirección privilegiada y de los modelos de materia oscura no estándar. Por último, presentamos los resultados de dos proyectos adicionales relacionados con el análisis de Fisher para mapas de galaxias. Hemos realizado la estimación de futuras cotas a los modelos de gravedad modificada en la colaboración internacional J-PAS; y hemos desarrollado el código FARO para el análisis de Fisher de los espectros de potencias lineales de distribución de galaxias con distintos trazadores, espectro de convergencia de lente gravitacional débil, y el espectro de correlación cruzada entre la distribución de distintos trazadores y el efecto de lente gravitacional débil.

Chapter 1

The standard cosmological model and its standard modifications

General relativity (GR) theory has achieved a lot of success since it was first proposed more than hundred years ago [1–4]. It has explained the anomalous advance of Mercury perihelion, the light deflection by the Sun, the dynamics of binary pulsar systems as an indirect signal of gravitational waves, and finally, the direct measure of gravitational waves [5, 6]. When GR is applied to cosmological scales, it describes very well the evolution of Universe but, unlike small scale astrophysical probes, at a higher cost. On cosmological scales, two new components have to be introduced: dark matter and dark energy [7]. The cold dark matter (CDM) component is a non-relativistic matter fluid that is seemingly not interacting with visible matter, and the dark energy (Λ) component is a negative pressure fluid that would be responsible for the late acceleration of the Universe. With these unexpected ingredients, GR is able to explain the observations, however fundamental theoretical problems and some recent experimental tensions show that the standard cosmological model might be only the first step in our understanding of Universe.

1.1 The standard ΛCDM model

The ΛCDM model is known as the standard cosmological model [8–10]. It is a GR-based theory with the inclusion of the dark matter and dark energy components, and also with the presence of an early epoch of huge acceleration named inflation [11]. Due

to the cosmological principle, i.e. the assumption that at large scales the Universe is homogeneous and isotropic, the geometry can be described by the metric of Friedmann-Lemaître-Robertson-Walker [12],

$$ds^2 = -dt^2 + a^2(t)\left(\frac{dr^2}{1-kr^2} + r^2\left(d\theta^2 + \sin^2\theta d\phi^2\right)\right), \tag{1.1.1}$$

where $a(t)$ is the scale factor, and k is the curvature constant that determines the geometry of the spatial sections. In the context of GR, the field equations that relate the matter content with the geometry are,

$$G_{\mu\nu} = 8\pi G\, T_{\mu\nu}, \tag{1.1.2}$$

where $G_{\mu\nu} \equiv R_{\mu\nu} - \frac{1}{2}g_{\mu\nu}R$ is the Einstein tensor, $R_{\mu\nu}$ the Ricci tensor, R the Ricci scalar and $g_{\mu\nu}$ the metric tensor. The matter and energy content of the Universe is represented by the energy-momentum tensor $T_{\mu\nu}$, that in standard cosmology is described by a perfect fluid,

$$T_{\mu\nu} = (\rho + p)\, u_\mu u_\nu + p g_{\mu\nu}, \tag{1.1.3}$$

here u_μ is the four-velocity, ρ is the matter-energy density and p the isotropic pressure. The matter-energy density and the isotropic pressure are related by the equation of state,

$$p = \omega\rho. \tag{1.1.4}$$

Considering (1.1.1) in the field equations (1.1.2) we can obtain the Friedmann equations,

$$\frac{1}{a^2}\left(\frac{da}{dt}\right)^2 = \frac{8\pi G}{3}\,\rho - \frac{k}{a^2}, \tag{1.1.5}$$

$$\frac{1}{a}\frac{d^2a}{dt^2} = -\frac{4\pi G}{3}\,(\rho + 3p)\,. \tag{1.1.6}$$

ΛCDM considers, in addition to photons, neutrinos and baryonic matter, a dark matter component and a dark energy component in the form of a cosmological constant. This former energy content follows a state equation with $\omega = -1$. The Friedmann equation (1.1.5) can be solved to obtain the Hubble parameter defined as,

$$H(t) \equiv \frac{1}{a}\frac{da}{dt}. \tag{1.1.7}$$

Using the conservation equations of the energy-momentum tensor $\nabla^\nu T_{\mu\nu} = 0$, and defining the density parameters as,

$$\Omega_i(a) = \frac{\rho_i(a)}{\rho_c(a)}, \tag{1.1.8}$$

where $\rho_c = 3H^2/8\pi G$; we obtain the expression for the Hubble parameter (1.1.7) as,

$$H(t) = H_0\sqrt{\Omega_m\, a^{-3} + \Omega_r\, a^{-4} + \Omega_k\, a^{-2} + \Omega_\Lambda}, \tag{1.1.9}$$

with $\Omega_i = \Omega_i(a = 1)$ the density parameters today and $\Omega_k \equiv -k/H_0^2$, m denotes the total pressureless matter, r denotes radiation, k denotes curvature and Λ the dark energy component. The latest data set Planck [13] agree that $\Omega_b h^2 = 0.02222 \pm 0.00023$ for baryonic matter, $\Omega_{CDM} h^2 = 0.1197 \pm 0.0022$ for cold dark matter, $\Omega_k = -0.052^{+0.049}_{-0.055}$ so the curvature compatible with zero and $\Omega_\Lambda = 0.685 \pm 0.013$.

1.2 The new challenges for ΛCDM cosmology

The ΛCDM model shows an excellent agreement with most of the observational data to date, from Cosmic Microwave Background (CMB) [14, 15], the accelerated expansion of Universe via the Supernovae measurements [9,16] or large scale structure (LSS) observables from galaxy maps [17–19]. However, these successes bring a series of controversies: the unsatisfactory explanation of the acceleration of Universe, the coincidence problem, the recent experimental tensions between the CMB and local observables, and some problems related to the standard CDM [20–23].

Although a standard cosmological constant is enough to explain the late-time cosmic acceleration, from a theoretical point of view the cosmological constant Λ could be just an effective constant within the context of a more fundamental theory, either involving modifications of gravity on cosmological scales or extended models with additional degrees of freedom [24,25]. In this line, many models can be proposed to reproduce the acceleration. These models can be mainly classified in two types: dark energy and modified gravity models. The former refers to a new energy component which acts as a source of gravity within the standard GR equations of motion. By modified gravity we understand extensions of GR which include new degrees of freedom that mediate the gravitational interaction. Even though it may seem that these two types of models are radically different, in practice

it is hard to distinguish them with observations because, in most of the situations, a dark energy model can be seen to be equivalent to a modified gravity model at least at the background level. In addition to explain the late-time acceleration, these type of alternative models could alleviate the so called coincidence problem, i.e. why the dark energy density is comparable to matter density precisely today. The coincidence problem is a fine-tuning problem that appears when a cosmological constant is used to explain the Universe acceleration. In this situation, the value of the cosmological constant energy is of the order of the matter component in the present day.

On the other hand, there are some experimental tensions between CMB and local observables. The most important one tension is the known Hubble constant tension. In particular, the latest data from CMB temperature and polarization coming from Planck experiment gives $H_0 = 67.4 \pm 0.5\,\mathrm{km/s/Mpc}$, assuming ΛCDM [10]. While recent local data gives $H_0 = 73.24 \pm 1.74\,\mathrm{km/s/Mpc}$ [26], so there is a tension of order $4\,\sigma$. Another important discrepancy comes from the measurement of σ_8, the amplitude of matter fluctuations, that can be measured by Planck data and by weak lensing surveys such as KiDS450 and CFHTLenS [27, 28]. Considering ΛCDM, Planck and KiDS-450 results have a tension of $2.3\,\sigma$ [27]. Although unresolved systematics can play an important role in explaining these discrepancies, these tensions could be a signal of deviations with respect to the standard cosmology.

Finally, there are some problems related with standard CDM: the problem of missing satellites [20,21], the fact that the Planck collaboration observed less clusters than expected [22] or the cusp-core problem [23]. These problems are related with the form in which dark matter behaves, specially at sub-galactic scales. They could point towards the existence of self-interactions in the dark matter component [29, 30], or a interaction in the dark sector [31, 32].

All these problems motivate the interest on studying modifications with respect to the standard ΛCDM model. Recently, the observation of the binary neutron star merger GW170817 [33] thanks to the joint detection of the gravitational wave emission and the electromagnetic counterpart, has provided a tight bound on the speed of propagation of gravitational waves, $|c_{\mathrm{gw}}/c - 1| \lesssim 10^{-15}$ [34–36]. This detection ruled out all modified gravity theories that predict different propagation speed of gravitational waves. Good news

was only the beginning, future measurements from gravitational waves will be able to give new information about the H_0 tension, and also future large-scale structure experiments will give new powerful constraints of ΛCDM and modified gravity models.

1.3 Beyond the standard ΛCDM model

The theoretical and experimental issues presented before motivate to look for some modifications of the standard ΛCDM cosmology. In this context, we have a large number of different modified gravity and dark energy models, but we are going to review the most important ones. As mentioned before, these alternative models can be roughly classified as dark energy and modified gravity models. Given the Einstein equations (1.1.2), in the dark energy scheme a modification of ΛCDM appears as a non-standard energy content in $T_{\mu\nu}$. On the other hand, a modified gravity model assumes a modification in the gravity part $G_{\mu\nu}$. From a deeper theoretical point of view, this can also be seen in the Einstein-Hilbert action defined as,

$$S = \int \mathrm{d}^4x\,\sqrt{-g}\,\left[\frac{1}{2\kappa}R + \mathcal{L}_{\mathrm{M}}\right], \tag{1.3.1}$$

where $\kappa = 8\pi G$, R is the Ricci scalar and $\mathcal{L}_{\mathrm{M}}$ is the matter content Lagrangian. If we modify the geometric part $R/2\kappa$ we can define it as a modified gravity model, and if we modify the matter-energy part $\mathcal{L}_{\mathrm{M}}$ we can see it as a dark energy model. Then, using the action principle $\delta S = 0$ we can obtain the modified Einstein equations of motion. At the background level, it can be proved that a cosmological evolution given by modified gravity can be mimicked by a dark energy model. However, at the perturbation level it is possible to distinguish between dark energy and modified gravity models [37, 38].

1.3.1 Dark energy models

The first approach to generalize ΛCDM is to consider a dynamical dark energy. The easiest way is to consider a quintessence model. In this situation a scalar field ϕ is introduced in the action with a potential $V(\phi)$ [7, 39],

$$S = \int \mathrm{d}^4x\,\sqrt{-g}\,\left[\frac{1}{2\kappa}R + \mathcal{L}_{\mathrm{M}} - \frac{1}{2}\,g^{\mu\nu}\,\partial_\mu\phi\,\partial_\nu\phi - V(\phi)\right]. \tag{1.3.2}$$

Unlike the cosmological constant case, now we have a time-dependent equation of state that, using a convenient $V(\phi)$, can reproduce the late-time cosmic acceleration. Also, it can be used to generate the inflationary epoch [40] and, due to some attractor-like solutions, this type of models alleviate the coincidence problem [41].

A more general way to consider dynamical dark energy are the K-essence models. Now a scalar field with non-canonical kinetic term is considered [42, 43],

$$S = \int \mathrm{d}^4x\,\sqrt{-g}\,\left[\frac{1}{2\kappa}R + \mathcal{L}_{\mathrm{M}} + P(\phi, X)\right], \tag{1.3.3}$$

being $X = -1/2\, g^{\mu\nu}\,\partial_\mu\phi\,\partial_\nu\phi$. In this situation, the cosmic acceleration can also be carried out by the kinetic energy X. Usually these K-essence models are restricted to the form $P(\phi, X) = f(\phi)\hat{P}(X)$, see for instance [44] for models inspired in string theory.

Finally, a phenomenological way to parametrize deviations with respect to ΛCDM is to take into account an effective equation of state $\omega(a)$ for a perfect fluid, being $a(t)$ the scale factor. In this situation the most typical parametrization is the so called Chevallier-Polarski-Linder (CPL) parametrization [45, 46],

$$\omega(a) = \omega_0 + \omega_a\,(1 - a), \tag{1.3.4}$$

with w_0 and w_a constants and which reduces to the standard ΛCDM model when $\omega_0 = -1$ and $\omega_a = 0$.

1.3.2 Modified gravity models

In this second approach, a generalization of ΛCDM is done in the gravity sector. Now new degrees of freedom that mediate the gravitational interaction are introduced. Then, the cosmic acceleration is no longer generated by dark energy, instead, it is realized by a modified gravity law. Nevertheless, not all modifications are allowed because there are some local constraints that a modified gravitation law has to satisfy [47, 48]. For the sake of concreteness, we will summarize some important modified gravity models: $f(R)$, scalar-tensor theories and finally the Horndeski theory.

We start with the action in $f(R)$ theories [49–52],

$$S = \int \mathrm{d}^4x\,\sqrt{-g}\,\left[\frac{1}{2\kappa}f(R) + \mathcal{L}_{\mathrm{M}}\right], \tag{1.3.5}$$

where $f(R)$ is an arbitrary function of the Ricci scalar R. To obtain the modified Einstein equations, there are two different approaches: the metric and the Palatini formalisms. In the Palatini formalism [53], both $g_{\mu\nu}$ and the affine connection $\Gamma^{\rho}_{\mu\nu}$ are treated as independent variables when the action is varied. As we will see below, a $f(R)$ theory can be written as a scalar-tensor model with an extra scalar degree of freedom. In that context and considering the Palatini formalism, the scalar field degree of freedom does not propagate so the resulting equations of motion are of second order. In addition, a large coupling between the scalar field and ordinary matter is induced [54], this effect generates important growth of perturbations if the model is far from GR.

On the other hand, the metric formalism considers only $g_{\mu\nu}$ as independent variables when the action is varied. In this case, an additional dynamical term is introduced and there is one propagating scalar degree of freedom. As can be seen in (1.3.5), GR is recovered when $f(R) = R$. Some examples of viable $f(R)$ models are the Starobinsky model [55],

$$f(R) = R - \alpha\, R_c \left[1 - \left(1 + \frac{R^2}{R_c^2}\right)^{-n}\right], \tag{1.3.6}$$

with $\alpha > 0$, $n > 0$ and $R_c > 0$, and the Hu-Sawick model [47],

$$f(R) = R - \alpha\, R_c \frac{(R/R_c)^{2n}}{1 + (R/R_c)^{2n}}, \tag{1.3.7}$$

with $\alpha > 0$, $n > 0$ and $R_c > 0$.

As we have seen, scalar fields are a useful tool to modify ΛCDM from the dark energy point of view. But we can also construct a modified gravity model using scalar-tensor fields. This is the situation with the scalar-tensor theories in which the action reads [56, 57],

$$S = \int \mathrm{d}^4x\, \sqrt{-g}\, \left[\frac{1}{2\kappa}\, [f(\varphi, R) - \xi(\varphi)\, g^{\mu\nu}\, \partial_\mu\varphi\, \partial_\nu\varphi] + \mathcal{L}_{\mathrm{M}}\right], \tag{1.3.8}$$

where $f(\varphi, R)$ is a general function of the Ricci scalar R and the scalar field φ, and $\xi(\varphi)$ is a general function of the scalar field φ. As you can see from (1.3.8), $f(R)$ theory is included as a particular case of scalar-tensor theories. As another example of scalar-tensor gravity we have the Brans-Dicke theory in which $f(\varphi, R) = \varphi\, R$ and $\xi(\varphi) = \omega_{BD}/\varphi$ being ω_{BD} the Brans-Dicke parameter [58].

These modifications to the Einstein-Hilbert action can lead to higher derivative order equations of motion. This can be a problem due to the Ostrogradsky theorem that states

that equations of motion of order higher than two typically generate ghost instabilities [59]. This fact led to the construction of the so-called Horndeski theory. The Horndeski theory is the most general scalar-tensor theory in four dimensions that ensures that the equations of motion are of second order [60, 61]. The action reads,

$$S = \int \mathrm{d}^4x\,\sqrt{-g}\,\left[\frac{1}{2\kappa}\sum_{i=2}^{5}\mathcal{L}_i + \mathcal{L}_{\mathrm{M}}\right], \tag{1.3.9}$$

where,

$$\mathcal{L}_2 = G_2(\phi, X), \tag{1.3.10}$$

$$\mathcal{L}_3 = G_3(\phi, X)\,\Box\phi, \tag{1.3.11}$$

$$\mathcal{L}_4 = G_4(\phi, X)\,R + G_{4\,,X}(\phi, X)\,\left[(\Box\phi)^2 - \phi_{;\mu\nu}\,\phi^{;\mu\nu}\right], \tag{1.3.12}$$

$$\mathcal{L}_5 = G_5(\phi, X)\,G_{\mu\nu}\,\phi^{;\mu\nu} - \frac{1}{6}\,G_{5\,,X}(\phi, X)\,\left[(\Box\phi)^3 + 2\,\phi_{;\mu}{}^{\nu}\,\phi_{;\nu}{}^{\alpha}\,\phi_{;\alpha}{}^{\mu} - 3\,\phi_{;\mu\nu}\,\phi^{;\mu\nu}\,\Box\phi\right], \tag{1.3.13}$$

being $X = -1/2\,g^{\mu\nu}\,\partial_\mu\phi\,\partial_\nu\phi$, $\Box\phi = \phi_{;\mu}{}^{\mu}$, $\phi_{;\mu} = \nabla_\mu\phi$ the covariant derivative and $G_{i\,,X} = dG_i/dX$. GR is recovered when $G_2(\phi, X) = G_3(\phi, X) = G_5(\phi, X) = 0$ and $G_4(\phi, X) = 1$. It can be proved that all theories commented before: quintessence, K-essence, $f(R)$ theories and scalar-tensor theories; are enclosed in the Horndeski theory [62].

1.4 Phenomenological scalar modified gravity

As we have seen, the standard ΛCDM cosmology model can be modified in a wide number of manners so it is interesting to look for parametrizations that, considering some approximations, enclose a large number of models in a model-independent way. On the other hand, and we will give more details in next sections, given the importance that large-scale structure observables will have in the future era of precision cosmology, it is also interesting to parametrize our gravity model in the context of these observables. The two main approximations that can be done in this framework are: the quasi-static approximation (QSA), and the sub-Hubble regime. The former sets that time derivatives of gravitational potentials can be neglected compared to spatial derivatives [63, 64]. That approximation can be safely taken for models with large speed of sound of dark energy perturbations. However as shown in [64] it should never be used for the integrated Sachs-Wolfe effect analysis. The second approximation is basically to consider that the scales involved are

much smaller than the Hubble horizon. Taking into account these two approximations, it is possible to parametrize a modified gravity model in a general and model-independent way. In this section we will show how to parametrize a modification of gravity with additional scalar degrees of freedom [65].

To describe the cosmological observables we have mainly two approximation levels: the background and the first order perturbations. For the background we have the Friedmann-Robertson-Walker metric (1.1.1) which describes a homogeneous and isotropic Universe. In the particular case of flat spatial sections this metric reads [39],

$$ds^2 = a^2(\tau)[-d\tau^2 + d\mathbf{x}^2], \tag{1.4.1}$$

where τ is the conformal time, $a(\tau)d\tau = dt$, and $a(\tau)$ is the scale factor. Thus, the background can be described in a model-independent way with only one function of time: the Hubble parameter (1.1.7),

$$H(t) = \frac{1}{a}\frac{da}{dt} = \frac{a'}{a^2} \equiv \frac{\mathcal{H}}{a}, \tag{1.4.2}$$

where primes denote derivatives with respect to τ. In addition to the background, we have that the growth of structures are due to the evolution of inhomogeneities. To describe the evolution we have to perturb, first linearly, the background Friedmann-Robertson-Walker metric. In this section we perturb it in the longitudinal gauge with scalar perturbations $\Psi(\mathbf{x}, t)$ and $\Phi(\mathbf{x}, t)$,

$$ds^2 = a^2[-(1 + 2\Psi)d\tau^2 + (1 - 2\Phi)d\mathbf{x}^2], \tag{1.4.3}$$

as you can see, the scalar gravitational potentials Ψ and Φ are time and space dependent in general. The perturbed Einstein equations in ΛCDM considering only pressureless matter are,

$$\nabla^2\Phi - 3\mathcal{H}\left(\Phi' + \mathcal{H}\Psi\right) = 4\pi G a^2\,\rho\,\delta, \tag{1.4.4}$$

$$\nabla^2\Phi - \nabla^2\Psi = 0. \tag{1.4.5}$$

Considering that gravity is modified with N scalar degrees of freedom ϕ_n, the modified Einstein equations at the perturbation level are,

$$\delta\bar{G}^{\mu}{}_{\nu} = 8\pi G\,\delta T^{\mu}{}_{\nu}, \tag{1.4.6}$$

where the perturbed modified Einstein tensor $\delta\bar{G}^{\mu}{}_{\nu}$ can depend on both the metric potentials Φ, Ψ and the perturbed fields $\delta\phi_n$ to first order. The only matter-energy content relevant at late times is pressureless matter so that,

$$\delta T^{0}{}_{0} = -\rho\,\delta, \tag{1.4.7}$$

$$\delta T^{0}{}_{i} = -\rho\,v_i, \tag{1.4.8}$$

$$\delta T^{i}{}_{j} = 0, \tag{1.4.9}$$

where v_i is the three-velocity of matter, ρ is the density and $\delta \equiv \delta\rho/\rho$ is the density contrast. In components, we have, a priori, the following modified Einstein equations corresponding to $\delta\bar{G}^{0}{}_{0}$, $\delta\bar{G}^{0}{}_{i}$ and $\delta\bar{G}^{j}{}_{i}$, but not all of them are independent because of the Bianchi identities. Thus, imposing $\nabla_{\mu}\bar{G}^{\mu}{}_{\nu} = 0$ at the perturbation level and in the sub-Hubble regime, we find $\partial_i\delta\bar{G}^{i}{}_{\nu} = 0$, so that in the Fourier space we have,

$$\hat{k}^i\delta\bar{G}^{0}{}_{i} = 0, \quad \hat{k}^i\delta\bar{G}^{j}{}_{i} = 0, \tag{1.4.10}$$

being $\hat{k}_i = k_i/k$. Taking these restrictions into account we have only two independent equations which we take as those corresponding to $\delta\bar{G}^{0}{}_{0}$ and $\delta\bar{G}^{i}{}_{i}$. Additionally, we have the equations of motion for the scalar fields ϕ_n so that the system reads,

$$a_{11}\,\Psi + a_{12}\,\Phi + \sum_{n=1}^{N} a_{1n+2}\,\delta\phi_n = -8\pi G\,\rho\,\delta, \tag{1.4.11}$$

$$a_{21}\,\Psi + a_{22}\,\Phi + \sum_{n=1}^{N} a_{2n+2}\,\delta\phi_n = 0, \tag{1.4.12}$$

$$\delta\phi_n = b_{1n}\Psi + b_{2n}\Phi, \tag{1.4.13}$$

where a_{ij} and b_{ij} are general differential operators with time and space derivatives. Now if we apply QSA and the sub-Hubble regime, these operators have only space derivatives so that, in Fourier space, they are just polynomials in the scale k. This approximation is very useful because, in the Fourier space, we are able to convert differential equations into algebraic equations. Thanks to these approximations we can resolve the system and obtain the gravitational potentials as,

$$k^2\,\Phi = -4\pi G\,a^2\,\mu\,\eta\,\rho\,\delta, \tag{1.4.14}$$

$$k^2\,\Psi = -4\pi G\,a^2\,\mu\,\rho\,\delta, \tag{1.4.15}$$

where,

$$\eta = -\frac{a_{21} + \sum_{i=1}^{N} a_{2i+2} b_{1i}}{a_{22} + \sum_{i=1}^{N} a_{2i+2} b_{2i}}, \tag{1.4.16}$$

$$\mu = \frac{2k^2 a^{-2}}{a_{11} + \sum_{i=1}^{N} a_{1i+2} b_{1i} + \gamma\left(a_{12} + \sum_{i=1}^{N} a_{1i+2} b_{2i}\right)}. \tag{1.4.17}$$

If a concrete dependence in k is chosen for a_{ij} and b_{ij} we automatically have the k dependence of μ and η parameters. Notice that this result means that, considering QSA in the sub-Hubble regime, any modified gravity theory with only scalar degrees of freedom can be described with two time and scale functions $\mu(a,k)$ and $\eta(a,k)$. These two functions can be seen as the effective gravitational constant G_{eff} and the gravitational slip,

$$\mu(a,k) = \frac{G_{\text{eff}}}{G}, \tag{1.4.18}$$

$$\eta(a,k) = \frac{\Phi}{\Psi}. \tag{1.4.19}$$

In fact, any deviation of $\mu = \eta = 1$ will be a signal of the breakdown of standard ΛCDM. Although there are two independent functions, different choices can be made. For example, it is also common to choose (μ, Σ) instead of (μ, η) where,

$$\Sigma \equiv \frac{\mu(1+\eta)}{2}, \tag{1.4.20}$$

this is a useful choice for weak lensing because the power spectra for lensing depends on the potential $(\Psi + \Phi)/2$.

Finally, if we want to complete the problem we need the dark matter conservation equations. In the standard case we consider,

$$\nabla_\mu T^\mu_{\ \nu} = 0, \tag{1.4.21}$$

where for presureless matter,

$$T^\mu_{\ \nu} = \rho\,u^\mu u_\nu, \tag{1.4.22}$$

being

$$\rho = \rho_0 + \delta\rho, \tag{1.4.23}$$

and the four-velocity of matter $u^\mu = dx^\mu/ds$ is

$$u^\mu = a^{-1}(1 - \Psi, v^i), \tag{1.4.24}$$

so that

$$u_\mu = a(-1 - \Psi, v_i). \tag{1.4.25}$$

Because we are considering only scalar perturbations, the velocity perturbation is longitudinal so $\hat{v} = \hat{k}$. Then we can obtain from (1.4.21) two scalar equations: $\nabla_\mu T^\mu_0 = 0$ and $k^i \nabla_\mu T^\mu_i = 0$. If we apply the quasi-static approximation we obtain,

$$\delta' = -\theta, \tag{1.4.26}$$

$$\theta' = -\mathcal{H}\theta + k^2\Psi, \tag{1.4.27}$$

where $\theta = ik_i v^i$. If we derive equation (1.4.26) with respect to τ and use equations (1.4.26) and (1.4.27) we can obtain the equation for the evolution of δ,

$$\delta'' + \mathcal{H}\,\delta' + k^2\Psi = 0. \tag{1.4.28}$$

Finally using equation (1.4.15) in (1.4.28) we obtain,

$$\delta'' + \mathcal{H}\,\delta' - \frac{3}{2}\,\mathcal{H}^2\,\Omega_m(a)\,\mu\,\delta = 0, \tag{1.4.29}$$

here we have used $4\pi G\,a^2\,\rho = \frac{3}{2}\,\mathcal{H}^2\,\Omega_m(a)$, being $\Omega_m(a) = \rho_m(a)/\rho_c(a)$, $\rho_c(a) = 3H(a)^2/8\pi G$. Thus we can solve for all the perturbations all physical observable perturbations: gravitational potentials Ψ and Φ, and the matter density contrast δ. In the following sections we will see how these theory observables can be measured using galaxy surveys.

Chapter 2

Galaxy surveys: the new era of precision cosmology

In the next decade new cosmological probes will drive the new era of precision cosmology, these observables are the galaxy surveys. Galaxy maps such as J-PAS [66], DESI [67], Euclid [68], TAIPAN [69], LSST [70], or SKA [71], will be able to measure the distribution of galaxies, their peculiar velocities and their shapes. With this type of information for millions of objects, these surveys will shed new light on the dark sector and on the behaviour of the gravitational interaction on cosmological scales. In the following, we will summarize how these observables are measured and how they can be connected to theory.

2.1 Galaxy surveys and their observables

As we have seen, the recent epoch of cosmic acceleration can be explained by the existence of dark energy or by a modification of the gravitational interaction. From the observational point of view, the most accurate cosmological probe we have to date is the CMB [10, 72, 73]. Unfortunately, CMB observations provide a very precise description of the universe around recombination era, but they are poorly sensitive to the late-time evolution. So the fact that the Universe is accelerating is basically sustained on a combination of CMB observations and late-time observables such as the Hubble diagram measured from SNIa [9, 16]. In this sense, galaxy surveys probing the dark-energy dominated era are an excellent tool to explore the physics of cosmic acceleration. On the other hand, at the background level, there are

strong degeneracies bewteen different dark energy and modified gravity theories which predict the same expansion history of the universe. For this reason, a good determination of the evolution of perturbations is of the outmost importance to discriminate among the different models. The possibility of measuring the growth rate of perturbations or the lensing function with galaxy surveys will thus open a new avenue for model selection.

Galaxy surveys can be classified mainly in three types: spectroscopic surveys, photometric surveys and spectro-photometric surveys. Spectroscopic surveys obtain high-quality spectra from a number of pre-selected extragalactic objects [74–76]. Using the spectra information they are able to extract the spectroscopic redshift of an object with very high precision. However, these type of measurements do not provide any information on the shapes of galaxies and therefore they are not sensitive to the lensing effect. On the other hand, we have the photometric surveys. In this type of surveys a large field of view camera is used to obtain images of the sky. These cameras have a specific number of broadband filters (BB) in which the light intensity at some wavelengths is recorded [77, 78]. Using this information, a reconstruction code is able to obtain photo-spectra of each object and their photo-redshift [79, 80]. Thanks to this technique, a higher number of objects can be detected compared to spectroscopic surveys but with a poorer redshift accuracy. For this reason, these surveys are focused on the determination of 2D power spectra. In addition, from the objects images, it is possible to measure the galaxy shapes and then to perform measurement of the cosmic shear. Finally, the spectro-photometric surveys are also imaging surveys but with a higher number of narrow band filters (NB) than a standard photometric survey [66,81,82]. Thanks to this high number of filters, a photo-redshift with higher accuracy can be reached making the survey competitive with spectroscopic surveys to obtain 3D power spectrum. Also, they can measure galaxy shapes as usual photometric surveys.

The main observable power spectra of the galaxy surveys are: the galaxy distribution power spectrum, the peculiar velocity power spectrum and the weak lensing power spectrum. The galaxy distribution power spectrum can be constructed from two basic measurements, the redshift of a galaxy and its sky position. Thus, the galaxy power spectrum is obtained in the so called *redshift space* and the redshift of an object contains two different contributions, the redshift due to the cosmological expansion and the redshift due

to peculiar velocities. Peculiar velocities imprint a redshift space distortion effect (RSD) in the galaxy power spectrum that is sensitive to the growth of structures [83, 84]. In addition, to compute the galaxy power spectrum in real space, we need to translate redshifts into radial distance assuming a fiducial cosmology. If the fiducial cosmology chosen is not the real one, an additional observable effect is induced in the power spectrum. This is known as the Alcock-Paczynski effect [85]. Finally, we are measuring galaxies as tracers of the total matter perturbation evolution but these galaxies may not be in the center of the gravitational potentials. In fact, in the early Universe, the dark matter density contrast starts to grow earlier than the baryon density contrast due to electromagnetic interactions. Thus, a bias factor should be considered and modeled. In general, this bias factor depends on the galaxy formation and evolution, the selection effects of the galaxy survey and the different galaxy tracers [86–89].

Secondly, galaxy surveys are able to measure the peculiar velocity power spectrum. To construct this power spectrum we need an independent determination of the real distance to an object, in addition to the standard redshift [90]. This independent distance can be obtained with empirical relations like the Tully-Fisher [91] and Fundamental Plane relations [92, 93]; or with standard candles like supernovae [94]. In that situation, we are able to distinguish between the redshift due to the cosmological expansion and the redshift due to peculiar velocities, so that we can obtain the peculiar velocity along the line of sight of the object. Notice that there is no direct observable that can measure the transverse velocity of an extragalactic object. Due to the need of an independent distance measurement, it is hard to have enough statistical significance compared with other galaxy survey observables.

Finally, imaging galaxy surveys can measure the weak lensing power spectrum. This power spectrum is obtained with weak lensing maps in which size and ellipticity of galaxies are obtained [95–97]. When the light of a galaxy travels through the Universe and reaches us, it is weakly deflected by the gravitational potentials of the intervening objects. This subtle effect modifies the size and ellipticity of galaxy images in a particular way. This effect is not observable for an individual galaxy because we do not know its real size and ellipticity. However, if we observe a group of near lensed galaxies, coherent shape and size distortions can be seen and we are able to reconstruct the gravitational potentials

that generate them. Thus, the weak lensing power spectrum has information about the evolution of gravitational perturbations.

When these observables are analyzed at small scales, new non-linear effects appear. These effects are in general harder to model due to baryon and halo interactions. For the galaxy clustering power spectrum, the main non-linear effects in addition to the non-linear matter power spectrum are the non-linear bias and the non-linear RSD. In the linear and Gaussian case, the galaxy bias can be described by a proportionality parameter that relates the dark matter density contrast and the galaxy density contrast. However, at small scales this is no longer possible and more parameters have to be included to take into account non-linear and non-Gaussian effects [98, 99]. These parametrizations are usually based on numerical simulations. On the other hand, the RSD effect has extra terms in non-linear scales. The main effect is known as finger of God effect (FOG) which causes an elongation along the line of sight of overdensities in redshift space compared to those in real space [100]. For the weak lensing power spectrum the non-linear effects are difficult to model. In addition to the non-linear matter power spectrum, non-linear intrinsic alignments are present [101–103].

In the following sections we will construct in detail each observable power spectrum considering only linear effects.

2.2 Clustering power spectrum

One of the main observables is the galaxy distribution power spectrum. This power spectrum basically measures the matter perturbation evolution using the galaxy positions in redshift space. To do that in the linear regime, we have three main effects: the RSD effect [83, 84], the bias effect [104] and the Alcock-Paczynski effect [85]. We start with the RSD effect. This effect is due to the fact that we use redshifts to obtain real distances to objects. When we do not have an independent determination of the real distance, we are not able to disentangle the cosmological redshift from the redshift due to peculiar velocities [90]. In that situation we have to distinguish between the real space $\mathbf{r}$: the real 3D position of a galaxy, and the redshift space $\mathbf{s}$: the 3D position of a galaxy obtained with

the measured redshift,

$$\mathbf{s} = \mathbf{r}\left(1 + \frac{v_\parallel(\mathbf{r})}{\mathcal{H}\, r}\right), \tag{2.2.1}$$

where $v_\parallel$ denotes the line-of-sight (LOS) component of the peculiar velocity. In Fourier space, we are interested in relating the redshift space matter perturbation $\delta^s(\mathbf{k})$ and the real space matter perturbation $\delta^r(\mathbf{k})$. Thus we write,

$$\delta^s(\mathbf{k}) = \int d^3s\, \delta^s(\mathbf{s})\, e^{-i\mathbf{k}\cdot\mathbf{s}}. \tag{2.2.2}$$

Using matter conservation in a given volume we have that,

$$[1 + \delta^s(\mathbf{s})]\, d^3s = [1 + \delta^r(\mathbf{r})]\, d^3r, \tag{2.2.3}$$

and using (2.2.3) in (2.2.2) we obtain,

$$\delta^s(\mathbf{k}) = \int d^3r \left[1 + \delta^r(\mathbf{r}) - \frac{d^3s}{d^3r}\right] e^{-i\mathbf{k}\cdot\mathbf{s}}. \tag{2.2.4}$$

The jacobian $\frac{d^3s}{d^3r}$ is in general of the form,

$$\frac{d^3s}{d^3r} = \frac{s^2 ds}{r^2 dr} = \left(1 + \frac{v_\parallel(\mathbf{r})}{\mathcal{H}\, r}\right)^2 \left(1 + \frac{1}{\mathcal{H}}\frac{\partial v_\parallel(\mathbf{r})}{\partial r}\right), \tag{2.2.5}$$

and using the distant observer approximation in which,

$$\frac{v_\parallel(\mathbf{r})}{r} \ll \frac{\partial v_\parallel(\mathbf{r})}{\partial r}, \tag{2.2.6}$$

we obtain that the Jacobian becomes,

$$\frac{d^3s}{d^3r} \simeq 1 + \frac{1}{\mathcal{H}}\frac{\partial v_\parallel(\mathbf{r})}{\partial r}. \tag{2.2.7}$$

Now we apply the plane-parallel approximation by considering a global LOS in the z direction [83, 105]. Using this approximations on equation (2.2.4) we obtain,

$$\delta^s(\mathbf{k}) = \int d^3r \left[\delta^r(\mathbf{r}) - \frac{1}{\mathcal{H}}\frac{\partial v_z(\mathbf{r})}{\partial z}\right] e^{-i\mathbf{k}\cdot\mathbf{r}[1+v_z/\mathcal{H}r]}, \tag{2.2.8}$$

where we have chosen the LOS to be in z axis. As we only want to keep linear terms in perturbation in (2.2.8) we can approximate,

$$e^{-i\mathbf{k}\cdot\mathbf{r}[1+v_z/\mathcal{H}r]} \simeq e^{-i\mathbf{k}\cdot\mathbf{r}}, \tag{2.2.9}$$

so that we obtain,

$$\delta^s(\mathbf{k}) = \delta^r(\mathbf{k}) - \frac{1}{\mathcal{H}} \int d^3r \, \frac{\partial v_z(\mathbf{r})}{\partial z} \, e^{-i\mathbf{k}\cdot\mathbf{r}}, \tag{2.2.10}$$

which yields,

$$\int d^3r \, \frac{\partial v_z(\mathbf{r})}{\partial z} \, e^{-i\mathbf{k}\cdot\mathbf{r}} = ik_z v_z(\mathbf{k}). \tag{2.2.11}$$

Because we are considering only scalar perturbations, the peculiar velocity perturbation can be written as,

$$v_i(\mathbf{k}) = -i \, \frac{k_i}{k^2} \, \theta(\mathbf{k}), \tag{2.2.12}$$

being $\theta = ik_i v^i$, so that using $v_z = -i\,\theta\,k_z/k^2$ and $\hat{\mu} \equiv \mathbf{k}\cdot\hat{n}/k$ with $\hat{n}$ an unitary vector parallel to the LOS direction, we obtain the final result,

$$\delta^s(\mathbf{k}) = \delta^r(\mathbf{k}) - \hat{\mu}^2 \, \frac{\theta(\mathbf{k})}{\mathcal{H}}. \tag{2.2.13}$$

This is the famous Kaiser equation for the linear RSD effect [83, 84]. It relates the direct density contrast in redshift space δ^s with the density contrast in real space δ^r and the velocity divergence θ.

On the other hand, galaxy surveys cannot directly determine the total matter density contrast since they only detect galactic tracers of the total matter. In the linear regime, the simplest model of a linear bias between galaxies and total matter is [88, 89, 104],

$$\delta_g = b(a)\,\delta, \qquad \theta_g = \theta, \tag{2.2.14}$$

δ_g is the density contrast of galaxies and δ the total matter contrast. On the other hand, it is assumed that there is no bias between the peculiar velocities of galaxies and those of the total matter. However, this assumption might not be correct and, in fact, several studies have attempted to calculate this velocity bias by comparing the velocity divergence power spectrum from simulated halos and the corresponding dark matter field [106–109]. As we commented before, since dark matter perturbations start to grow in the early universe before baryonic perturbations do, there is a bias between galaxy overdensities and total matter overdensities. This bias evolves during galaxy formation so that it depends on the type of the tracer and also on the selection model of each galaxy survey. Nevertheless,

as galaxies tend to follow total matter, the bias is expected to decrease with cosmic time approaching one. For these reason, a simple model for the lineal bias is [110, 111],

$$b(a) = \frac{b_0}{D(a)}, \tag{2.2.15}$$

where $D(a) \equiv \delta(a)/\delta(1)$ is the growth factor.

The bias factor will depend on the specific tracer under considerations. There are several tracers but the main ones for surveys are the Luminous Red Galaxies (LRGs), the Emission Line Galaxies (ELGs) and the quasars (QSO). LRGs are selected on the basis of color and magnitude to yield a sample of luminous, intrinsically red galaxies; typically they are large elliptical galaxies with redshifts from 0 to 1. ELGs are young main sequence galaxies with high stellar formation, they can be detected for higher redshifts than LRGs. QSO are extremely luminous active galactic nucleus of young galaxies generated by supermassive black holes. Taking the bias effect into account, expression (2.2.13) becomes,

$$\delta_g^s = \delta_g^r - \hat{\mu}^2 \frac{\theta_g}{\mathcal{H}}, \tag{2.2.16}$$

so that using equations (2.2.14) and (1.4.26) we obtain,

$$\delta_g^s = (1 + \beta\hat{\mu}^2)\, b\, \delta, \tag{2.2.17}$$

where we have rewritten (1.4.26) as,

$$\theta = -\mathcal{H}\, f\, \delta, \tag{2.2.18}$$

with $f(a)$ the growth function defined as,

$$f(a) = \frac{d\log\delta(a)}{d\log a}, \tag{2.2.19}$$

and where $\beta \equiv f/b$. Now we define the galaxy power spectrum as,

$$\langle \delta_g^s(\mathbf{k})\, \delta_g^{s\,*}(\mathbf{k}')\rangle = (2\pi)^3\, \delta^3(\mathbf{k} - \mathbf{k}')\, P_{gg}(\mathbf{k}), \tag{2.2.20}$$

here $\langle\rangle$ is the ensamble average where $\delta_g(\mathbf{k})$ are Gaussian random variables. Thus, considering the RSD and bias effects with only one tracer, the observable linear power spectrum for galaxy distribution is,

$$P_{gg}(z, \hat{\mu}, k) = \left(1 + \beta(z)\hat{\mu}^2\right)^2\, b(z)^2\, P_m(z, k), \tag{2.2.21}$$

with $P_m(z,k)$ the matter power spectrum at redshift z and scale k. To see how the RSD effect is relevant for the power spectrum, we calculate the multipole expansion of $P_{gg}(z,\hat{\mu},k)$,

$$P_{gg}(z,\hat{\mu},k) = \sum_\ell P_\ell(z,k)\,\mathcal{L}_\ell(\hat{\mu}), \tag{2.2.22}$$

where $\mathcal{L}_\ell$ are the Legendre polynomials so that

$$P_\ell(z,k) = \frac{2\ell+1}{2}\int_{-1}^{1} d\hat{\mu}\, P_{gg}(z,\hat{\mu},k)\,\mathcal{L}_\ell(\hat{\mu}). \tag{2.2.23}$$

The only ℓ that are different from zero are,

$$P_0 = \left(1+\frac{2}{3}\,\beta+\frac{1}{5}\,\beta^2\right) b^2\, P_m(z,k), \tag{2.2.24}$$

$$P_2 = \left(\frac{4}{3}\,\beta+\frac{4}{7}\,\beta^2\right) b^2\, P_m(z,k), \tag{2.2.25}$$

$$P_4 = \frac{8}{35}\,\beta^2\, b^2\, P_m(z,k). \tag{2.2.26}$$

Considering that b may vary between 1 and 2, and f is order 0.8, the RSD correction in the monopole is order $30-60\%$ which is a very relevant correction.

Nevertheless, an additional effect should be taken into account: the Alcock-Paczynski effect. This effect is due to the fact that, to obtain physical distances and volumes using the redshift we have to assume a reference background cosmology. Thus, we want to relate observables obtained in a reference cosmology to observables in any other cosmology. Given a transverse comoving length λ that subtend an angle θ at redshift z we have,

$$D_A = \frac{\lambda}{(1+z)\theta}, \tag{2.2.27}$$

being D_A the angular distance in a given cosmological model. Thus, for the same angle and redshift but in different cosmologies that we denote by 1 and 2, we obtain the relation,

$$\frac{D_{A\,1}}{\lambda_1} = \frac{D_{A\,2}}{\lambda_2}. \tag{2.2.28}$$

In Fourier space this relation implies that a transverse mode $k_\perp$ in a given cosmology corresponds to the $k_{\perp r}$ mode in the fiducial cosmology given by,

$$k_\perp = \frac{D_{A\,r}}{D_A}\,k_{\perp\,r}. \tag{2.2.29}$$

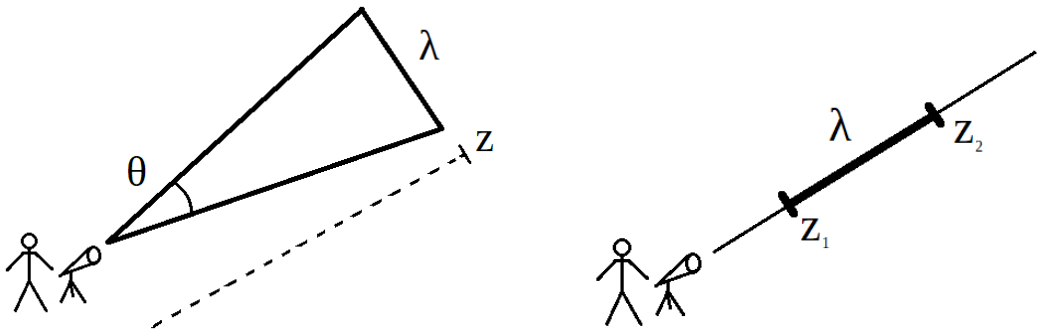

Figure 2.1: Diagrams of transverse and longitudinal distances for the Alcock-Paczynski effect.

On the other hand, for a longitudinal comoving length λ between redshifts z_1 and z_2 ($z_2 > z_1$) we have,

$$\lambda = \frac{z_2 - z_1}{H}. \tag{2.2.30}$$

Accordingly for the same redshifts in different cosmological models,

$$\lambda_1 H_1 = \lambda_2 H_2, \tag{2.2.31}$$

that in Fourier space reads,

$$k_\parallel = \frac{H}{H_r} k_{\parallel r}, \tag{2.2.32}$$

where again the subscript r denotes the fiducial cosmology. As we can see, this effect introduces additional anisotropies because transverse and longitudinal modes to the LOS are modified in different ways.

Using these relationships we can obtain how $(k, \hat{\mu})$ have to be modified,

$$k = Q\, k_r, \tag{2.2.33}$$

$$\hat{\mu} = \frac{H\, \hat{\mu}_r}{H_r\, Q}, \tag{2.2.34}$$

$$Q = \frac{\sqrt{H^2\, D_A^2\, \hat{\mu}_r^2 - H_r^2\, D_{A\,r}^2\, (\hat{\mu}_r^2 - 1)}}{H_r\, D_A}. \tag{2.2.35}$$

Finally, since the power spectrum is proportional to the measured volume, we need also the relation between volumes in different cosmologies,

$$V = \frac{H_r\, D_A^2}{H\, D_{A\,r}^2}\, V_r. \tag{2.2.36}$$

Considering the Alcock-Paczynski effect, the galaxy distribution power spectrum of equation (2.2.21) becomes,

$$P_{gg}(z, \hat{\mu}_r, k_r) = \frac{H_r\, D_A^2}{H\, D_{A\,r}^2}\, \left(1 + \beta(z)\hat{\mu}^2\right)^2\, b(z)^2\, P_m(z, k), \tag{2.2.37}$$

where $k = k(k_r)$ and $\hat{\mu} = \hat{\mu}(\hat{\mu}_r)$ follow equations (2.2.33) and (2.2.34). These are the main effects in the linear galaxy clustering power spectrum. However, since the redshift measurement has an error, the observed power spectrum contains an additional term. To take into account this error, since $dr = dz/H(z)$, a redshift uncertainty can be translated into a distance error $\sigma_r = \sigma_z/H(z)$. Thus, we assume that a radial distance r has a probability distribution function of the form [7],

$$f(r, r_0) = \frac{1}{\sqrt{2\pi}\sigma_r}\, e^{-\frac{(r-r_0)^2}{2\sigma_r^2}}, \tag{2.2.38}$$

where r_0 is the true distance, so that the observed correlation function is convolved with this distribution and after the Fourier transform, the observed power spectrum becomes,

$$P_{gg}(z, \hat{\mu}_r, k_r) = \frac{H_r\, D_A^2}{H\, D_{A\,r}^2}\, \left(1 + \beta(z)\hat{\mu}^2\right)^2\, b(z)^2\, P_m(z, k)\, e^{-k_r^2\, \hat{\mu}_r^2\, \sigma_r^2}. \tag{2.2.39}$$

Typically, redshift uncertainties are parametrized as $\sigma_z = \delta z(1 + z)$. For a spectroscopic survey $\delta z \sim 0.001$ or less, whereas for a photometric survey $\delta z \sim 0.01 - 0.05$.

Finally, when we are considering different types of tracers we can build the auto and cross correlation galaxy density power spectra for each galaxy tracer. In that situation we have,

$$\delta_i^g = (b_i + f\hat{\mu}^2)\, \delta, \tag{2.2.40}$$

where index i denote the different tracers, so the galaxy power spectrum becomes,

$$P_{ij}^{\delta\delta}(z, \hat{\mu}_r, k_r) = \frac{H_r\, D_A^2}{H\, D_{A\,r}^2}\, \left(b_i + f\,\hat{\mu}^2\right)\left(b_j + f\,\hat{\mu}^2\right)\, P_m(z, k)\, e^{\frac{-k_r^2\,\hat{\mu}_r^2\,\sigma_i^2}{2}}\, e^{\frac{-k_r^2\,\hat{\mu}_r^2\,\sigma_j^2}{2}}, \tag{2.2.41}$$

where the radial distance error for tracer i is $\sigma_i = (\delta z_i\,(1 + z))/H(z)$.

2.3 Peculiar-velocity power spectrum

As we have commented before, if there are independent distance measurements like supernovae data, Tully-Fisher [91] or Fundamental Plane relations [92, 93], it is possible to distinguish between the cosmological redshift and the peculiar velocity redshift. In that situation an additional observable is the LOS peculiar velocity defined as [90],

$$u(\mathbf{r}) \equiv \mathbf{v}(\mathbf{r}) \cdot \hat{r}, \tag{2.3.1}$$

where $\hat{r}$ is an unitary vector parallel to $\mathbf{r}$. In Fourier space,

$$u(k, \hat{\mu}) = i\hat{\mu}\, \frac{\theta_g}{k}. \tag{2.3.2}$$

Using equations (2.2.14) and (2.2.18) we obtain,

$$u = -\frac{i\,\mathcal{H} f \hat{\mu}}{k}\, \delta. \tag{2.3.3}$$

With this result we can obtain the LOS peculiar velocity power spectrum defined as $P_{uu} = \langle uu^* \rangle$. In addition, we can obtain the cross-correlation between galaxy distribution $P_{gu} = \langle \delta_g^s u^* \rangle$ where δ_g^s follows equation (2.2.16). Thus, we can write,

$$P_{uu}(z, \hat{\mu}_r, k_r) = \frac{H_r\, D_A^2}{H\, D_{A\,r}^2} \left(\frac{\mathcal{H}\, f\, \hat{\mu}}{k} \right)^2 P_m(z, k), \tag{2.3.4}$$

$$P_{gu}(z, \hat{\mu}_r, k_r) = i\, \frac{H_r\, D_A^2}{H\, D_{A\,r}^2}\, \frac{\mathcal{H}\, f\, \hat{\mu}}{k}\, \left(1 + \beta\, \hat{\mu}^2\right)\, b\, P_m(z, k), \tag{2.3.5}$$

where we have also taken into account the Alcock-Paczynski effect, with $k = k(k_r)$ and $\hat{\mu} = \hat{\mu}(\hat{\mu}_r)$ following equations (2.2.33) and (2.2.34). It can be seen with equations (2.2.37) and (2.3.4) that,

$$\frac{P_{uu}}{P_{gg}} = \frac{f^2 \hat{\mu}^2}{(b + f\hat{\mu}^2)^2} \left(\frac{\mathcal{H}}{k} \right)^2 \propto \left(\frac{\mathcal{H}}{k} \right)^2, \tag{2.3.6}$$

so that in the sub-Hubble regime in which $\mathcal{H}/k \ll 1$ we have that $P_{uu} \ll P_{gg}$. This is one of the reasons why galaxy surveys extract more information from the galaxy distribution than from direct peculiar velocities.

2.4 Weak-lensing power spectrum

Here we will discuss how the weak lensing effect can be measured and how to define the observable power spectrum [96, 97, 112–115]. This effect is due to the distortion effect of the light trajectories due to the perturbed gravitational potentials on large scales. As we will prove, this effect induces extra ellipticities in galaxy shapes that can be statistically measured. First of all, we will describe how light trajectories are modified in a perturbed cosmology, then we will introduce the distortion tensor and finally the observable weak lensing power spectra.

2.4.1 Weak lensing: null geodesics with scalar perturbations

We start with the scalarly perturbed FRW metric in terms of the cosmological time t,

$$ds^2 = -(1+2\Psi)\,dt^2 + a(t)^2\,(1-2\Phi)\,d\mathbf{x}^2. \tag{2.4.1}$$

For this metric, we are interested in deriving the corresponding null geodesics, satisfying

$$\frac{d^2x^i}{d\lambda^2} + \Gamma^i_{\alpha\beta}\,\frac{dx^\alpha}{d\lambda}\,\frac{dx^\beta}{d\lambda} = 0. \tag{2.4.2}$$

We will consider the angular perturbation with respect to the line of sight induced by the metric perturbations. With that purpose, three approximations will be taken into account: the small-angle approximation, the Limber approximation and the flat sky approximation. The small-angle approximation assumes that the deflection angle induced by lensing is small [113]. The Limber approximation is valid for large wavenumber k and simplifies calculations by replacing Bessel with delta functions [116, 117]. Finally, the flat sky approximation assumes that angular effects are negligible in the fields so the geometry of the angular component is assumed to be planar. From the mathematical point of view, this approximation replaces an spherical harmonic expansion by a Fourier expansion [116, 118]. Thus, we define $x^i = \chi\,\theta^i$ where $\chi = \chi(z)$ is the comoving radial distance and $\theta^i = (\theta^1, \theta^2, 1)$, so that θ^i for $i = 1, 2$ are first order in the gravitational perturbations and $x^3 = \chi$. The goal is to obtain the geodesics (2.4.2) for $i = 1, 2$,

$$\frac{d^2x^i}{d\lambda^2} = \frac{d\chi}{d\lambda}\,\frac{d}{d\chi}\left(\frac{d\chi}{d\lambda}\,\frac{d}{d\chi}\,\left(\chi\,\theta^i\right)\right), \tag{2.4.3}$$

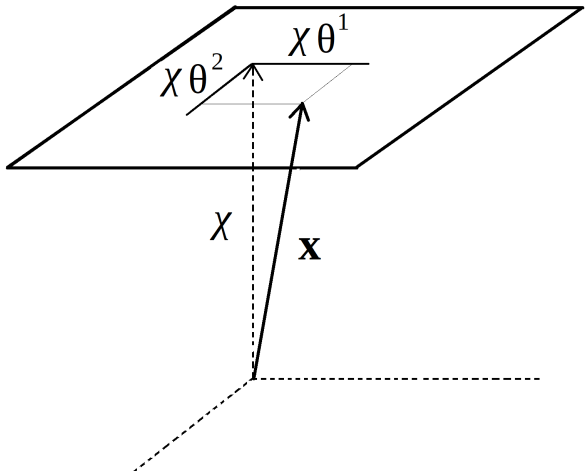

Figure 2.2: Diagram for the perturbed trajectory of a light geodesic. We consider that θ^i for $i = 1, 2$ are first order in the gravitational perturbations.

where,

$$\frac{d\chi}{d\lambda} = \frac{d\chi}{dt}\,\frac{dt}{d\lambda}, \tag{2.4.4}$$

and $\frac{d\chi}{dt} = -\frac{1}{a}$. In order to obtain $\frac{dt}{d\lambda}$ we define $P^\mu = \frac{dx^\mu}{d\lambda}$, where, for null geodesics,

$$g_{\mu\nu} P^\mu P^\nu = 0, \tag{2.4.5}$$

so, at order zero in perturbations, we have,

$$-(P^0)^2 + g_{ij} P^i P^j = 0. \tag{2.4.6}$$

By defining $p^2 \equiv g_{ij} P^i P^j$ we find,

$$\frac{dt}{d\lambda} = p, \tag{2.4.7}$$

so that we obtain $\frac{d\chi}{d\lambda} = -\frac{p}{a}$ and, since for $i = 1, 2$, θ^i is first order in perturbations, we can write

$$\frac{d^2 x^i}{d\lambda^2} = -\frac{p}{a}\,\frac{d}{d\chi}\left(-\frac{p}{a}\,\frac{d}{d\chi}\,(\chi\,\theta^i)\right). \tag{2.4.8}$$

Thus we only need p to zeroth order, which satisfies $p\,a \propto const$ so that,

$$\frac{d^2 x^i}{d\lambda^2} = p^2\,\frac{d}{d\chi}\left(\frac{1}{a^2}\,\frac{d}{d\chi}\,(\chi\,\theta^i)\right). \tag{2.4.9}$$

On the other hand, we have the Christoffel symbol term,

$$\Gamma^i_{\alpha\beta}\,\frac{dx^\alpha}{d\lambda}\,\frac{dx^\beta}{d\lambda}=\left(\frac{d\chi}{d\lambda}\right)^2\,\Gamma^i_{\alpha\beta}\,\frac{dx^\alpha}{d\chi}\,\frac{dx^\beta}{d\chi}. \tag{2.4.10}$$

For the metric (2.4.1), we have,

$$\Gamma^i_{00}=a^{-2}\,\Psi_{,i}, \tag{2.4.11}$$

$$\Gamma^i_{j0}=\delta_{ij}\,\left(H-\Phi_{,0}\right), \tag{2.4.12}$$

$$\Gamma^i_{jk}=\Phi_{,i}\,\delta_{jk}-\Phi_{,k}\,\delta_{ij}-\Phi_{,j}\,\delta_{ki}, \tag{2.4.13}$$

where a comma denotes derivative with respect to the coordinates (t,x^1,x^2,x^3). Let us analyze the different terms of equation (2.4.10):

- $\alpha=\beta=0$: in this case we only have the term $\Gamma^i_{00}\left(\frac{dt}{d\chi}\right)^2$, and $\frac{dt}{d\chi}=-a$ to zeroth order, so that we obtain,

$$\Gamma^i_{00}\left(\frac{dt}{d\chi}\right)^2=\Psi_{,i}. \tag{2.4.14}$$

- $\alpha=j$, $\beta=0$ (and the symmetric case): now we have $\Gamma^i_{j0}\,\frac{dt}{d\chi}\,\frac{dx^j}{d\chi}$. For $j=1,2$ the derivative $\frac{dx^j}{d\chi}$ is first order in perturbations, so that in this case Γ^i_{j0} must be order zero. However, when $j=3$, we have $\frac{dx^3}{d\chi}=1$ then Γ^i_{30} has to be first order in perturbations. Taking all the terms into account we obtain,

$$\Gamma^i_{j0}\,\frac{dt}{d\chi}\,\frac{dx^j}{d\chi}=-a\,H\,\frac{d}{d\chi}(\chi\,\theta^i). \tag{2.4.15}$$

  Notice that since we also have Γ^i_{0j}, the term (2.4.15) contributes twice to the final expression.

- $\alpha=j$, $\beta=k$: finally we have $\Gamma^i_{jk}\,\frac{dx^j}{d\chi}\,\frac{dx^k}{d\chi}$, because x^j is order one when $j\neq 3$ and Γ^i_{jk} is always order one, the only term that contributes corresponds to $j=k=3$ $(i=1,2)$,

$$\Gamma^i_{33}\left(\frac{dx^3}{d\chi}\right)^2=\Phi_{,i}. \tag{2.4.16}$$

As we can see in the previous analysis, $\Gamma^i_{\alpha\beta}\frac{dx^\alpha}{d\chi}\frac{dx^\beta}{d\chi}$ is first order in perturbations, so that the prefactor $\left(\frac{d\chi}{d\lambda}\right)^2$ in (2.4.10) must be of zeroth order. Finally, equation (2.4.10) becomes,

$$\Gamma^i_{\alpha\beta}\frac{dx^\alpha}{d\lambda}\frac{dx^\beta}{d\lambda} = \left(\frac{p}{a}\right)^2\left[(\Phi+\Psi)_{,i} - 2\,a\,H\,\frac{d}{d\chi}(\chi\,\theta^i)\right]. \tag{2.4.17}$$

If we expand (2.4.9), and taking into account that $\frac{d}{d\chi} = -a^2\,H\,\frac{d}{da}$, we find,

$$\frac{d^2x^i}{d\lambda^2} = \left(\frac{p}{a}\right)^2\left[\frac{d^2(\chi\,\theta^i)}{d\chi^2} + 2\,a\,H\,\frac{d}{d\chi}(\chi\,\theta^i)\right]. \tag{2.4.18}$$

Thus, using (2.4.17) and (2.4.18) we can obtain from the geodesic equation (2.4.2),

$$\frac{d^2}{d\chi^2}(\chi\,\theta^i) = -(\Phi+\Psi)_{,i}. \tag{2.4.19}$$

It will be useful to define the source term of equation (2.4.19) as,

$$Y_i \equiv -\left(\Phi+\Psi\right)_{,i}. \tag{2.4.20}$$

Thus, we have found how light propagates through a scalarly perturbed Universe. In the following section we will proceed with the integration of equation (2.4.19) and the definition of the distortion tensor.

2.4.2 The distortion tensor

Once we know how a light ray is weakly deflected due to the perturbed gravitational potentials, we derive the observable effects on galaxy shapes. This weak deflection will induce an ellipticity in the galaxy shape, which can be measured calculating the quadrupole of the galaxy image [7]. The ellipcity can be related with the distortion tensor defined as,

$$\psi_{ij} \equiv \frac{\partial\theta^S_i}{\partial\theta_j} - \delta_{ij}, \tag{2.4.21}$$

with θ^S the angle of the source without perturbations. In absence of inhomogeneities, this angle is equal to the apparent angle θ and then the distortion tensor is zero. Thus, we can obtain the distortion tensor using the results of previous section. By integrating equation (2.4.19) twice we obtain,

$$\theta^S_i = \frac{1}{\chi}\int_0^\chi d\chi''\int_0^{\chi''} d\chi'\,Y_i(\chi'\boldsymbol{\theta}) + \text{const.} \tag{2.4.22}$$

Since the integrand is just a function of χ', we can integrate over χ'' and fix the integration constant as the initial angle θ_i. So that,

$$\theta_i^S = \theta_i + \int_0^\chi d\chi' \, Y_i(\chi' \boldsymbol{\theta}) \left(1 - \frac{\chi'}{\chi}\right). \tag{2.4.23}$$

By using $\frac{\partial}{\partial \theta_j} = \frac{\partial x_k}{\partial \theta_j} \frac{\partial}{\partial x_k} = \chi \frac{\partial}{\partial x_j}$ we obtain,

$$\psi_{ij} = \int_0^\chi d\chi' \, \chi' \, Y_{i,j} \left(1 - \frac{\chi'}{\chi}\right), \tag{2.4.24}$$

where $\psi_{ij} = \psi_{ij}(\chi, \boldsymbol{\theta})$. We want to integrate over χ to project into the two-dimensional (θ_1, θ_2) plane. In general the survey contains a distribution of galaxies $W(\chi)$, which is normalized as $\int_0^{\chi_\infty} d\chi W(\chi) = 1$, where $\chi_\infty = \lim_{z\to\infty} \chi(z)$ so that the projected distortion tensor is,

$$\psi_{ij}(\boldsymbol{\theta}) = \int_0^{\chi_\infty} d\chi \, W(\chi) \int_0^\chi d\chi' \, \chi' \, Y_{i,j} \left(1 - \frac{\chi'}{\chi}\right). \tag{2.4.25}$$

By changing the order of integration, we can obtain,

$$\psi_{ij}(\boldsymbol{\theta}) = \int_0^{\chi_\infty} d\chi \; \chi \, g(\chi) \, Y_{i,j}(\chi, \boldsymbol{\theta}), \tag{2.4.26}$$

where we have defined,

$$g(\chi) \equiv \int_\chi^{\chi_\infty} d\chi' \left(1 - \frac{\chi}{\chi'}\right) W(\chi'). \tag{2.4.27}$$

As we have seen, $i = 1, 2$ so that ψ_{ij} is a 2×2 matrix. Now, we use equation (2.4.20) into (2.4.26) so that

$$\psi_{ij}(\boldsymbol{\theta}) = -\int_0^{\chi_\infty} d\chi \; \chi \, g(\chi) \; (\Phi + \Psi)_{,ij}, \tag{2.4.28}$$

i.e. the distortion tensor with scalar perturbations is symmetric, and in this case the distortion matrix can be written as,

$$\psi_{ij} \equiv \begin{pmatrix} -\kappa - \gamma_1 & -\gamma_2 \\ -\gamma_2 & -\kappa + \gamma_1 \end{pmatrix}$$

Thus, the convergence and shear parameters are,

$$\kappa = -\frac{\psi_{11} + \psi_{22}}{2}, \tag{2.4.29}$$

$$\gamma_1 = -\frac{\psi_{11} - \psi_{22}}{2}, \tag{2.4.30}$$

$$\gamma_2 = -\frac{\psi_{12} + \psi_{21}}{2}. \tag{2.4.31}$$

It can be proved that the observed ellipticities ϵ_1 and ϵ_2 can be related at first order with the shear γ_1 and γ_2 as [7],

$$\epsilon_1 \simeq 2\gamma_1, \qquad \epsilon_2 \simeq 2\gamma_2. \tag{2.4.32}$$

Now, we want to go to the Fourier space of $\boldsymbol{\theta}$ so that we define,

$$\tilde{\psi}_{ij}(\boldsymbol{\ell}) = \int d^2\theta \; \mathrm{e}^{-i\,\boldsymbol{\ell}\cdot\boldsymbol{\theta}}\, \psi_{ij}(\boldsymbol{\theta}). \tag{2.4.33}$$

Taking into account that,

$$\frac{\partial}{\partial x^i} = \frac{1}{\chi}\frac{\partial}{\partial \theta^i}, \tag{2.4.34}$$

the Fourier transform of the distortion matrix is,

$$\tilde{\psi}_{ij}(\boldsymbol{\ell}) = \int_0^{\chi_\infty} d\chi \; \frac{g(\chi)}{\chi}\, \ell_i\, \ell_j \left(\tilde{\Phi} + \tilde{\Psi}\right). \tag{2.4.35}$$

The power spectrum of this distortion matrix is the weak-lensing observable.

2.4.3 Weak-lensing power spectra

We start by defining the power spectrum of the distortion tensor in the following way,

$$P^{\psi}_{ijlm}(\boldsymbol{\ell}) \equiv \frac{1}{(2\pi)^2} \int d^2\ell' \, \langle \tilde{\psi}_{ij}(\boldsymbol{\ell})\, \tilde{\psi}^*_{lm}(\boldsymbol{\ell}')\rangle. \tag{2.4.36}$$

Using expressions (1.4.14) and (1.4.15), we can obtain the power spectrum (2.4.36) as a function of the matter power spectrum,

$$\langle \delta(z,\mathbf{k})\, \delta^*(z,\mathbf{k}')\rangle = (2\pi)^3\, \delta^3(\mathbf{k}-\mathbf{k}')\, P_m(z,\mathbf{k}). \tag{2.4.37}$$

With that purpose it is first necessary to relate the Fourier transforms in $\boldsymbol{\theta}$ and $\mathbf{x}$ variables. Let us thus denote with a bar the Fourier transform in $\mathbf{x}$ at a given time i.e.

$$\bar{f}(\mathbf{k}) \equiv \int d^3x \; \mathrm{e}^{-i\,\mathbf{k}\cdot\mathbf{x}}\, f(\mathbf{x}). \tag{2.4.38}$$

Thus, we can write

$$\bar{f}(k_3,\boldsymbol{\ell}) = \int d\chi \int \chi^2\, d^2\theta\, \mathrm{e}^{-i\,\boldsymbol{\ell}\cdot\boldsymbol{\theta}}\, \mathrm{e}^{-i\,k_3\,\chi}\, f(\mathbf{x}), \tag{2.4.39}$$

where we have used $\ell_i = \chi\, k_i$ for $i = 1, 2$ so that using the definition of the Fourier transform in $\boldsymbol{\theta}$ in (2.4.33) we obtain,

$$\bar{f}(k_3,\boldsymbol{\ell}) = \int d\chi\, \chi^2\, \mathrm{e}^{-i\,k_3\,\chi}\, \tilde{f}(\chi,\boldsymbol{\ell}). \tag{2.4.40}$$

By performing the inverse transform in k_3 we get,

$$\tilde{f}(\chi,\boldsymbol{\ell}) = \frac{1}{2\pi\chi^2} \int dk_3\, \mathrm{e}^{i\,k_3\,\chi}\, \bar{f}(k_3,\boldsymbol{\ell}). \tag{2.4.41}$$

In order to obtain the power spectrum in (2.4.36), we rewrite equation (2.4.35) for $\tilde{\psi}_{ij}(\boldsymbol{\ell})$ in the following compact way,

$$\tilde{\psi}(\boldsymbol{\ell}) = \int_0^{\chi_\infty} d\chi\, \sum_\alpha C_\alpha(\chi,\boldsymbol{\ell})\, \tilde{f}_\alpha(\chi,\boldsymbol{\ell}), \tag{2.4.42}$$

where we have omitted the indices, f_α are the different metric perturbations and C_α the corresponding coefficients. Using this expression we obtain,

$$P^\psi(\boldsymbol{\ell}) = \frac{1}{(2\pi)^2} \int d^2\ell' \int_0^{\chi_\infty} d\chi \int_0^{\chi_\infty} d\chi' \sum_{\alpha,\beta} C_\alpha(\chi,\boldsymbol{\ell})\, C^*_\beta(\chi',\boldsymbol{\ell}')\, \langle \tilde{f}_\alpha(\chi,\boldsymbol{\ell})\, \tilde{f}^*_\beta(\chi',\boldsymbol{\ell}')\rangle, \tag{2.4.43}$$

and using (2.4.41) in $\langle \tilde{f}_\alpha(\chi,\boldsymbol{\ell})\, \tilde{f}^*_\beta(\chi',\boldsymbol{\ell}')\rangle$, we obtain

$$\langle \tilde{f}_\alpha(\chi,\boldsymbol{\ell})\, \tilde{f}^*_\beta(\chi',\boldsymbol{\ell}')\rangle = \frac{1}{2\pi\chi^2}\, \frac{1}{2\pi\chi'^2} \int dk_3\, \mathrm{e}^{ik_3\chi} \int dk'_3\, \mathrm{e}^{-ik'_3\chi'}\, \langle \bar{f}_\alpha(k_3,\boldsymbol{\ell})\, \bar{f}^*_\beta(k'_3,\boldsymbol{\ell}')\rangle. \tag{2.4.44}$$

As we can see from (1.4.14) and (1.4.15), metric perturbations $\bar{f}$ can be related to the density perturbations according to the following generic form,

$$\bar{f}_\alpha(k_3,\boldsymbol{\ell}) = B_\alpha(\mathbf{k})\, \delta(\mathbf{k}), \tag{2.4.45}$$

where $k_i = \ell_i/\chi$ for $i = 1, 2$, so that, formally we obtain,

$$\langle \bar{f}_\alpha(k_3,\boldsymbol{\ell})\, \bar{f}^*_\beta(k'_3,\boldsymbol{\ell}')\rangle = B_\alpha(\mathbf{k}) B^*_\beta(\mathbf{k}')\, \langle \delta(\mathbf{k})\, \delta^*(\mathbf{k}')\rangle. \tag{2.4.46}$$

Using equation (2.4.37) and considering,

$$\delta^3(\mathbf{k}-\mathbf{k}') = \delta^2\left(\frac{\boldsymbol{\ell}}{\chi}-\frac{\boldsymbol{\ell}'}{\chi'}\right)\,\delta(k_3-k_3'), \tag{2.4.47}$$

we obtain,

$$\langle\tilde{f}_\alpha(\chi,\boldsymbol{\ell})\,\tilde{f}^*_\beta(\chi',\boldsymbol{\ell}')\rangle = \frac{2\pi}{\chi^2\,\chi'^2}\,\delta^2\left(\frac{\boldsymbol{\ell}}{\chi}-\frac{\boldsymbol{\ell}'}{\chi'}\right)\int dk_3\,\mathrm{e}^{i\,k_3\,(\chi-\chi')}\,B_\alpha(\mathbf{k})B^*_\beta(\mathbf{k}')\,P_m(z,\mathbf{k}). \tag{2.4.48}$$

For small distortion angles θ, we can consider $k_3 \ll k_1, k_2$ so that, $\mathbf{k} \simeq \boldsymbol{\ell}/\chi$ and accordingly,

$$\langle\tilde{f}_\alpha(\chi,\ell)\,\tilde{f}^*_\beta(\chi',\ell')\rangle = \frac{(2\pi)^2}{\chi^2\,\chi'^2}\,\delta^2\left(\frac{\boldsymbol{\ell}}{\chi}-\frac{\boldsymbol{\ell}'}{\chi'}\right)\,\delta(\chi-\chi')B_\alpha\left(\frac{\boldsymbol{\ell}}{\chi}\right)B^*_\beta\left(\frac{\boldsymbol{\ell}'}{\chi'}\right)\,P_m\left(z,\frac{\boldsymbol{\ell}}{\chi}\right). \tag{2.4.49}$$

Using this expression in (2.4.43) and writing $\delta^2\left(\frac{1}{\chi}(\boldsymbol{\ell}-\boldsymbol{\ell}')\right) = \chi^2\,\delta^2(\boldsymbol{\ell}-\boldsymbol{\ell}')$, we obtain

$$P^\psi(\boldsymbol{\ell}) = \int_0^{\chi_\infty}\,\frac{1}{\chi^2}\,P_m\left(z,\frac{\boldsymbol{\ell}}{\chi}\right)\left[\sum_{\alpha,\beta}\,C_\alpha(\chi,\boldsymbol{\ell})C^*_\beta(\chi,\boldsymbol{\ell})B_\alpha\left(\frac{\boldsymbol{\ell}}{\chi}\right)B^*_\beta\left(\frac{\boldsymbol{\ell}}{\chi}\right)\right]\,d\chi. \tag{2.4.50}$$

Finally changing from χ to the redshift variable $z = 1/(1+a)$ and using $\left[4\pi G a^2\rho\right]^2 = \frac{9H_0^4}{4}\,\Omega_m^2\,(1+z)^2$ we get,

$$P^\psi_{ijlm}(\boldsymbol{\ell}) = \frac{9\,H_0^4\,\Omega_m^2}{4}\,\int_0^\infty dz\,\frac{(1+z)^2}{H(z)}\,g^2(z)\,\frac{\ell_i\,\ell_j\,\ell_l\,\ell_m}{\ell^4}\,\mu^2\,(1+\eta)^2\,\,P_m\left(z,\frac{\boldsymbol{\ell}}{\chi(z)}\right), \tag{2.4.51}$$

where

$$g(z) = \int_z^\infty\left(1-\frac{\chi(z)}{\chi(z')}\right)\,n(z')\,dz', \tag{2.4.52}$$

with $n(z)dz = W(\chi)d\chi$ and $n(z)$ the galaxy density function as a function of redshift. Now we can use expressions (2.4.29)-(2.4.31) to construct the power spectra for convergence and shear,

$$P_\kappa = \frac{1}{4}\,\left(P^\psi_{1111}+P^\psi_{2222}+P^\psi_{1122}+P^\psi_{2211}\right), \tag{2.4.53}$$

$$P_{\gamma_1} = \frac{1}{4}\,\left(P^\psi_{1111}+P^\psi_{2222}-P^\psi_{1122}-P^\psi_{2211}\right), \tag{2.4.54}$$

$$P_{\gamma_2} = \frac{1}{4}\left(P^{\psi}_{1212} + P^{\psi}_{2121} + P^{\psi}_{1221} + P^{\psi}_{2112}\right). \tag{2.4.55}$$

These expressions can be written in a more compact fashion by introducing the following variables. We define $\ell_1 \equiv \ell\,\cos\varphi$ and $\ell_2 \equiv \ell\,\sin\varphi$ where φ is the polar angle of $\boldsymbol{\ell}$ given a reference frame in the plane. So the expressions (2.4.53 - 2.4.55) can be written as,

$$P_{\kappa} = \frac{9\,H_0^4\,\Omega_m^2}{4}\int_0^{\infty} dz\,\frac{(1+z)^2}{H(z)}\,g^2(z)\,\frac{\mu^2\,(1+\eta)^2}{4}\,P_m\left(z,\frac{\ell}{\chi(z)}\right), \tag{2.4.56}$$

$$P_{\gamma_1} = \cos^2(2\varphi)\;P_{\kappa}, \tag{2.4.57}$$

$$P_{\gamma_2} = \sin^2(2\varphi)\;P_{\kappa}, \tag{2.4.58}$$

As we can see from equations (2.4.57) and (2.4.58), we have the following closing relation,

$$P_{\gamma_1} + P_{\gamma_2} = P_{\kappa}. \tag{2.4.59}$$

Finally, if we want to analyze the weak lensing signal at different redshift bins, we define the following window functions,

$$g_a(z) = \int_z^{\infty}\left(1 - \frac{\chi(z)}{\chi(z')}\right)\,n_a(z')\,dz', \tag{2.4.60}$$

where we consider a galaxy density function of the form [119],

$$n(z) = \frac{3}{2\,z_p^3}\,z^2\,e^{-(z/z_p)^{3/2}}, \tag{2.4.61}$$

being $z_p = z_{mean}/\sqrt{2}$ and z_{mean} the survey mean redshift. Then, for each bin we have the following galaxy distribution function, where we have take into account the photometric redshift error σ_a in the corresponding bin,

$$n_a(z) \propto \int_{\bar{z}_{a-1}}^{\bar{z}_a} n(z')\,e^{-\frac{(z'-z)^2}{2\,\sigma_a^2}}\,dz', \tag{2.4.62}$$

being $\sigma_a = \delta z\,(1+z_a)$, $\bar{z}_a$ is the upper limit of the a-bin and $n_a(z)$ is normalized to one. An example can be seen in Fig. 2.3. With these definitions, the convergence power spectrum is,

$$P^{\kappa\kappa}_{ab}(\ell) = \frac{9\,H_0^4\,\Omega_m^2}{4}\int_0^{\infty} dz\,\frac{(1+z)^2}{H(z)}\,g_a(z)\,g_b(z)\,\frac{\mu^2\,(1+\eta)^2}{4}\,P_m\left(z,\frac{\ell}{\chi(z)}\right). \tag{2.4.63}$$

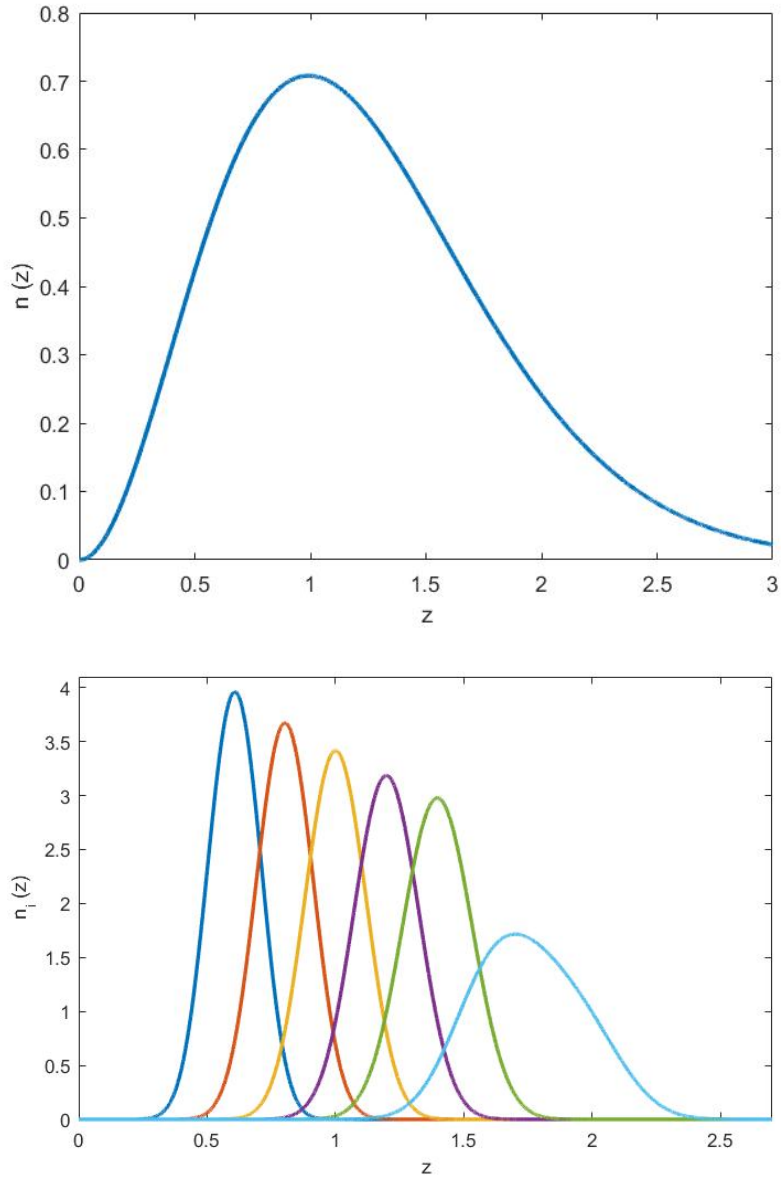

Figure 2.3: Example of galaxy densities (2.4.61) and (2.4.62) for a galaxy survey with $z_{mean} = 0.9$ and $\delta z = 0.05$.

2.5 Cross-correlation power spectra

In this section we will obtain the cross-correlation power spectrum of galaxy distribution and weak lensing [115, 120]. In those galaxy surveys that measure galaxy distribution and also galaxy shapes, it is possible to take into account the cross correlation between them in the 2D plane. To do that, we have to project the 3D matter perturbation into the 2D plane. Notice that, when we perform this projection, we are no longer sensitive to the RSD effect. The 2D matter perturbation for tracer i is defined as [7],

$$\delta_a^i(\boldsymbol{\ell}) = \int_0^{\chi_\infty} d\chi\, n_a(\chi)\, b_i(\chi) \tilde{\delta}\,(\chi, \boldsymbol{\ell})\,, \tag{2.5.1}$$

where $n_a(\chi)$ is the galaxy distribution density for the bin a, and $b_i(\chi)$ is the linear bias for tracer i. In addition, looking at (2.4.29) and (2.4.35), we can write the convergence in the Fourier space as,

$$\kappa_a(\boldsymbol{\ell}) = -\frac{1}{2} \int_0^{\chi_\infty} d\chi\, \frac{g_a(\chi)}{\chi}\, \ell^2 \left(\tilde{\Phi} + \tilde{\Psi}\right), \tag{2.5.2}$$

so that with these two definitions we can calculate the following power spectra,

$$P^{\delta_2\delta_2}_{ab\;ij}(\boldsymbol{\ell}) \equiv \frac{1}{(2\pi)^2} \int d^2\ell'\, \langle \delta_a^i(\boldsymbol{\ell})\, \delta_b^{j\,*}(\boldsymbol{\ell}')\rangle, \tag{2.5.3}$$

and,

$$P^{\kappa\delta_2}_{ab\;i}(\boldsymbol{\ell}) \equiv \frac{1}{(2\pi)^2} \int d^2\ell'\, \langle \kappa_a(\boldsymbol{\ell})\, \delta_b^{i\,*}(\boldsymbol{\ell}')\rangle. \tag{2.5.4}$$

As can be seen in the last section, these types of power spectra follow the derivation of equation (2.4.50). Thus, using that recipe we obtain,

$$P^{\delta_2\delta_2}_{ab\;ij}(\ell) = \int_0^{\chi_\infty} \frac{d\chi}{\chi^2}\, P_m\left(z, \frac{\ell}{\chi}\right)\, n_a(\chi)\, n_b(\chi)\, b_i(\chi)\, b_j(\chi), \tag{2.5.5}$$

and,

$$P^{\kappa\delta_2}_{ab\;i}(\ell) = \int_0^{\chi_\infty} \frac{d\chi}{\chi^2}\, P_m\left(z, \frac{\ell}{\chi}\right)\, \frac{3H_0^2\Omega_m}{2}(1+z)\,\chi\, \frac{\mu(1+\eta)}{2}\, g_a(\chi)\, n_b(\chi)\, b_i(\chi), \tag{2.5.6}$$

where we have used once again that $4\pi G a^2\rho = \frac{3H_0^2}{2}\Omega_m(1+z)$. Now we change from χ to z using that for the galaxy distribution $n_a(\chi) = n_a(z)H(z)$ and $d\chi = dz/H(z)$,

$$P^{\delta_2\delta_2}_{ab\;ij}(\ell) = \int_0^{\infty} dz\, \frac{H(z)}{\chi^2(z)}\, n_a(z)\, n_b(z)\, b_i(z)\, b_j(z)\, P_m\left(z, \frac{\ell}{\chi(z)}\right), \tag{2.5.7}$$

and,

$$P^{\kappa\delta_2}_{ab\,i}(\ell) = \frac{3H_0^2\Omega_m}{2}\int_0^\infty dz\,\frac{(1+z)}{\chi(z)}\,\frac{\mu(1+\eta)}{2}\,g_a(z)\,n_b(z)\,b_i(z)\,P_m\left(z,\frac{\ell}{\chi(z)}\right). \tag{2.5.8}$$

Finally, we can assume for the galaxy distribution with a small redshift error, that galaxies in two redshift bins are not correlated with each other. In this situation integrals in (2.5.7) and (2.5.8) can be simplified as,

$$P^{\delta_2\delta_2}_{ab\,ij}(\ell) = \delta_{ab}\,\frac{H(z_a)}{\chi^2(z_a)}\,b_i(z_a)\,b_j(z_b)\,P_m\left(z_a,\frac{\ell}{\chi(z_a)}\right), \tag{2.5.9}$$

$$P^{\kappa\delta_2}_{ab\,i}(\ell) = \frac{3H_0^2\Omega_m}{2}\,\frac{(1+z_b)}{\chi(z_b)}\,\frac{\mu(1+\eta)}{2}\,g_a(z_b)\,b_i(z_b)\,P_m\left(z_b,\frac{\ell}{\chi(z_b)}\right). \tag{2.5.10}$$

Chapter 3

Fisher matrix analysis for galaxy surveys

The goal of physics is to identify patterns in nature and to determine how they work. To do that, physical models have to be confronted with measurements. Although it seems to be a straightforward procedure, when experiments are designed, technical and theoretical problems may appear. On one hand, experiments are always imperfect and it is necessary to avoid the presence of uncontrolled systematic effects. On the other hand, even if systematic effects are controlled, measurements have always statistical uncertainties which complicate the interpretation of the results of any experiment. This complication is related with the definition of probability, basically in a frequentist or a Bayesian way. In the frequentist approach, a probability is understood as the relative frequency of an event when we repeat an experiment many times. Because of this definition, a probability can only be defined for a repeatable experiment. In this context, for cosmology and ΛCDM, we can not attribute a probability to a parameter like, for example Ω_m, because our Universe being described by a LCDM model with a given value of Om is not a repeatable event. In general, the frequentist approach do not attach probabilities to hypotheses or to any fixed but unknown value. A different probabilistic interpretation has to be used: the Bayesian approach. In this case, a probability is understood in a more general way as a degree of confidence of an event. Now, a probability of 60% that our Universe is modeled by ΛCDM with Ω_m between 0.2 and 0.3 can be interpreted as a degree of confidence with the same level of, for instance, drawing a red ball from a drawer with six red balls and four blue balls. With this

probability definition, we are able to attribute probabilities to hypotheses and unknown physical parameters. Also, we can update our probabilistic knowledge of an hypothesis with independent proves thanks to the Bayes theorem. Given a prior probability ($P(\theta_1)$) of the event θ_1, the conditional and posterior probability ($P(\theta_1|\theta_2)$) of θ_1 given θ_2 is,

$$P(\theta_1|\theta_2) = \frac{P(\theta_2|\theta_1)}{P(\theta_2)}\, P(\theta_1), \tag{3.0.1}$$

where $P(\theta_2|\theta_1)$ is the conditional probability (likelihood) of θ_2 given θ_1 and $P(\theta_2)$ is the probability (evidence) of θ_2. To understand this theorem in a simple way, let us give an example. Assume the event θ_1 is that it will rain this afternoon, so that we have a prior information based on some weather forecast $P(\theta_1)$. Now we will consider three different events θ_2 that update our probabilistic knowledge of θ_1. First, we consider θ_2 is that it was cloudy this morning. In this case the probability of been cloudy in the morning given that it is raining in the afternoon ($P(\theta_2|\theta_1)$) is larger than the generic probability of been cloudy in the morning ($P(\theta_2)$). So our knowledge has been updated and the probability of rain in the afternoon has increased $P(\theta_1|\theta_2) > P(\theta_1)$. Otherwise, if θ_2 is that it is clear in morning, $P(\theta_2|\theta_1) < P(\theta_2)$ and then we have $P(\theta_1|\theta_2) < P(\theta_1)$ i.e. the probability of rain in the afternoon decrease. Finally, if θ_2 is that we saw a woman in the morning with red shoes, because this event is not correlated with the rain in the afternoon $P(\theta_2|\theta_1) = P(\theta_2)$ and then $P(\theta_1|\theta_2) = P(\theta_1)$. As it can be seen, the Bayes theorem is the main tool to update probabilistic information of an event in the Bayes approach.

Now we explain in detail the experimental physics case. In a frequentist approach, we can only obtain the likelihood $f(x_i;\theta_\alpha)$ where x_i are random variables that describe the data and θ_α are the fixed unknown values of the parameters of the model; the likelihood is the conditional probability of having data x_i given the theoretical parameters θ_α. However, in the Bayesian approach, we can calculate the posterior distribution $\mathcal{L}(\theta_\alpha; x_i)$ which is the conditional probability of having the theoretical parameters θ_α given data x_i,

$$\mathcal{L}(\theta_\alpha; x_i) \propto f(x_i;\theta_\alpha)\, p(\theta_\alpha), \tag{3.0.2}$$

where we have used the Bayes theorem. Because we are only interested in the probability density function of the theoretical parameters θ_α, we do not take into account explicitly the evidence in (3.0.2). The prior information of θ_α is $p(\theta_\alpha)$. The most typical prior is the

information of a previous experiment but there are also other kinds of priors, for example the exclusion of a non-physical range for theoretical parameters. Also, the trivial prior $p(\theta_\alpha) = 1$ or the choose of a particular theory are also priors after all. In the cosmology context and using the Bayesian approach, the statistical knowledge of the cosmology is updated with the independent observations like CMB, supernovae data or galaxy maps. Notice that, due to the fact that a posterior from a experiment can be taken as a prior for another experiment, it is common to refer the posterior also as a likelihood. The advantage of adding cosmological information from independent experiments is the reason why Bayesian statistics plays a fundamental role in observational cosmology.

Once we have the normalized posterior distribution $\mathcal{L}(\theta_\alpha)$, the preferred values $\hat{\theta}_\alpha$ given the data and the priors are those maximizing the likelihood, i.e.

$$\frac{\partial \mathcal{L}}{\partial \theta}(\hat{\theta}_\alpha) = 0, \tag{3.0.3}$$

and the confidence regions $R(\gamma)$, which are delimited by a constant value of $\mathcal{L}(\theta_\alpha) < \mathcal{L}(\hat{\theta}_\alpha)$, satisfy,

$$\int_{R(\gamma)} \mathcal{L}(\theta_\alpha)\, d\theta = \gamma, \tag{3.0.4}$$

where $0 < \gamma < 1$. Typically, the values of γ are chosen as $\gamma = 0.683, 0.954, 0.997...$ and are defined as the regions of $1\sigma, 2\sigma, 3\sigma...$ by analogy with the Gaussian case. With these basic tools, we are able to obtain constraints to theories and models. In addition, we can also use these tools to forecast the future capability of experiments to obtain physical information.

Forecast analysis consist on estimating the precision that future experiments will have on their observables and in particular determining the covariance matrix of future data. Then, using a model to describe the data, it is possible to obtain the estimated future constraints on the physical parameters. The two main ways to do that are the numerical simulations and the Fisher matrix approach [121–125]. In the former, a numerical simulation of the experiment is computed using some expected specifications for it. Then we can analyze the mock data as real data and obtain the model constraints. The advantage of this method is that no approximation of the likelihood has to be done. However, the disadvantages are the numerical cost of the mocks and that the data simulation may introduce some biases in the mock covariance matrix. On the other hand we have the Fisher approach, in this approach an approximation of the likelihood is done. Around a fiducial

model, a Gaussian likelihood is considered. Thanks to this approximation, a linear change of variable can be done from the inverse of the data covariance matrix, i.e. the Fisher matrix of data, to the Fisher matrix of the model parameters, so that we can obtain the estimated constraints for theories. Comparing the two approaches, it can be proved that the Fisher matrix case gives the same order of magnitude for the parameter constraints as the numerical approach [126].

3.1 The Fisher matrix approach

Here we explain in detail the Fisher matrix approach [7, 121]. In general, the likelihood of an observable can be written as,

$$\mathcal{L} \propto e^{-\frac{\chi^2}{2}} \equiv \exp\left[-\frac{1}{2}\left(x_i - \tilde{x}_i\right) C_{ij}^{-1}\left(x_j - \tilde{x}_j\right)\right], \tag{3.1.1}$$

where x_i are the observable quantities, $\tilde{x}_i$ is the prediction of a model with parameters θ_k, C_{ij} is the covariance matrix of the data and we are using the Einstein sum convention. Notice that if data are uncorrelated, the covariance matrix is diagonal with elements given by the square of the error of x_i, denoted as σ_i^2. The Fisher matrix is then defined as,

$$F_{ij} \equiv C_{ij}^{-1}. \tag{3.1.2}$$

Although the likelihood defined as (3.1.1) is Gaussian in the observables x_i, the likelihood of the parameters θ_α is not necessarily Gaussian. This is the reason why obtaining the posterior for the parameters θ_α is in general a hard task. Notice that the posterior can have the same expression as (3.1.1) in the case in which we choose a flat prior. In the Fisher approach, an approximation is used that allows to simplify the problem. This approximation consists of expanding the χ^2 of (3.1.1) linearly in the parameters θ_α around the maximum of the likelihood. Then the likelihood for the parameters is now Gaussian and a linear change of variable from the Fisher matrix of the data to the Fisher matrix of the parameters can be done,

$$F_{\alpha\beta}^{\theta} = \left.\frac{\partial x_i}{\partial \theta_\alpha}\right|_{\tilde{\theta}} F_{ij}^{x} \left.\frac{\partial x_j}{\partial \theta_\beta}\right|_{\tilde{\theta}}, \tag{3.1.3}$$

where subscript $\tilde{\theta}$ denotes that the derivative is evaluated in the values of θ_α that maximize the likelihood. Thanks to this definition it is straightforward to see that, once we have the

Fisher matrix for the parameters θ_α, the error for each θ_α is,

$$\sigma_\alpha \equiv \sqrt{F^{-1}_{\alpha\alpha}}. \tag{3.1.4}$$

Then, with a flat prior, the likelihood of the data (3.1.1) can be rewritten as the posterior for the parameters as,

$$\mathcal{L} \propto \exp\left[-\frac{1}{2}\left(\theta_\alpha - \tilde{\theta}_\alpha\right) F^\theta_{\alpha\beta}\left(\theta_\beta - \tilde{\theta}_\beta\right)\right]. \tag{3.1.5}$$

This approach can be used to analyze the data in a simple way. However, the Fisher analysis is more interesting to forecast the capability of future experiments. In that case, we have to estimate the covariance matrix of the experiment and then make a linear change of variable to obtain the Fisher matrix for physical parameters,

$$F^\theta_{\alpha\beta} = \left.\frac{\partial x_i}{\partial\theta_\alpha}\right|_r F^x_{ij} \left.\frac{\partial x_j}{\partial\theta_\beta}\right|_r, \tag{3.1.6}$$

now the derivatives are evaluated in a reference fiducial model denoted by the subscript r. Once we have the Fisher matrix, we have all the information about the parameter constraints. As commented before, by definition, the marginalized errors are obtained with equation (3.1.4). If we want to change from parameters θ to $\hat{\theta}$, the Fisher matrix of the new parameters simply reads,

$$\mathbf{F}^{\hat{\theta}} = \mathbf{P}^t\,\mathbf{F}^\theta\,\mathbf{P}, \tag{3.1.7}$$

where $\mathbf{P} = \mathbf{Q}^{-1}$ and $Q_{\alpha\beta} = \partial\hat{\theta}_\alpha/\partial\theta_\beta$, evaluated on the fiducial model. If instead of marginalizing a parameter we want to fix it to the value that maximizes the likelihood, we just have to remove the corresponding row and column of this parameter from the Fisher matrix. Finally, if we want to add a non trivial prior, looking at the Bayes theorem (3.0.2), we just have to multiply the likelihoods. If the prior (p) on the parameters is also Gaussian, the total Fisher matrix is,

$$F^{tot}_{\alpha\beta} = F^\theta_{\alpha\beta} + F^p_{\alpha\beta}. \tag{3.1.8}$$

Notice that if the prior does not include some subset of parameters we just have to fill a zero matrix of the range of $F^\theta_{\alpha\beta}$ with the sub matrix of the prior $F^p_{\alpha\beta}$. Finally, given a $n \times n$ Fisher matrix we can obtain the 2D contours for two parameters by obtaining the

marginalized 2×2 Fisher matrix of these two parameters $\mathbf{F}_2$. As we are working with Gaussian distributions, the $p-\sigma$ confidence contours are ellipses. They are oriented along the eigenvectors of $\mathbf{F}_2^{-1}$ with lengths $1.51, 2.49, 3.44$ times the respective eigenvalue for contours of $1\sigma, 2\sigma, 3\sigma$ [7]. Once we have introduced in detail the Fisher matrix formalism, we will calculate the Fisher matrices for galaxy surveys observables in next sections.

3.2 Fisher matrices for galaxy-clustering observables

We start with the observables from galaxy distribution [120, 127]. To analyze the most general case, we will consider the multitracer galaxy power spectrum (2.2.41). The strategy is always the same: first we define an estimator for the observable which satisfies that the average of the estimator is the observable power spectrum. Then we compute the covariance matrix using the estimator and taking into account the shot noise effect [7, 128]. Finally by summing in redshifts and scales we obtain the Fisher matrix.

The (differential) Fisher matrix for the multitracer galaxy power spectrum as a function of redshift and scale interval is,

$$dF^{\delta\delta}_{\alpha\beta} = \left.\frac{\partial P^{\delta\delta}_{ij}(z,\hat{\mu}_c,k_c)}{\partial\theta_\alpha}\right|_r C^{-1}_{ijlm}(\hat{\mu}_c,k_c,\hat{\mu}_d,k_d) \left.\frac{\partial P^{\delta\delta}_{lm}(z,\hat{\mu}_d,k_d)}{\partial\theta_\beta}\right|_r . \tag{3.2.1}$$

To define the estimator for $P^{\delta\delta}_{ij}(z,\hat{\mu}_c,k_c)$ we have to take into account the distant observer or plane-parallel approximation. In this approximation the LOS direction for different galaxies can be approximated by an average direction. Therefore to compute the power spectrum we consider a global LOS direction. The estimator for the multitracer galaxy power spectrum is,

$$\hat{P}_{ij}(z,\hat{\mu}_c,k_c) = V_f \int_c \frac{d^3k}{V_s(k_c,\hat{\mu}_c)}\,\delta_i(z,\mathbf{k})\,\delta_j(z,-\mathbf{k}), \tag{3.2.2}$$

where $V_f = (2\pi)^3/V$, being V the volume of the survey and $\int_c d^3\vec{k} = V_s(k_c,\hat{\mu}_c) = 2\pi k_c^2 dk_c d\hat{\mu}_c$ the volume of the $\mathbf{k}_c$ bin. The average of the observed galaxy contrast is,

$$\langle\delta_i(z,\mathbf{k})\delta_j(z,\mathbf{k}')\rangle = \delta_D(\mathbf{k}+\mathbf{k}')\,C_{ij}(z,\hat{\mu},k), \tag{3.2.3}$$

where $\delta_D(x)$ is the Dirac distribution with $\delta_D(0) = 1/V_f$. Here $C_{ij}(z,\hat{\mu},k)$ is the observable power spectrum (2.2.41) with the shot noise effect. The shot noise effect is a white

noise intrinsic of experiments based on counts and it is modeled by a Poisson process. Considering this effect, the observable matter perturbations are,

$$\delta^{obs}(k) = \delta(k) + \epsilon(k), \tag{3.2.4}$$

where $\epsilon(k)$ is a random Gaussian variable with $\langle\epsilon(k)\rangle = 0$ and $\langle\epsilon(k)\epsilon(k')\rangle = \delta_D(k-k')/\bar{n}$ with $\bar{n}$ the average galaxy number density. With these properties the observable power spectrum is $P^{obs}(k) = P(k) + \frac{1}{\bar{n}}$. It is possible to consider a non-Gaussian shot noise $P_s(k)$ and in that case the observable power spectrum is parametrized as $P^{obs}(k) = P(k) + \frac{1}{\bar{n}} + P_s(k)$. Taking into account just the Gaussian shot noise,

$$C_{ij}(z,\hat{\mu},k) = P_{ij}^{\delta\delta}(z,\hat{\mu},k) + \frac{\delta_{ij}}{\bar{n}_i(z)}, \tag{3.2.5}$$

being $\bar{n}_i(z)$ the observed galaxy density of tracer i as a function of redshift and $P_{ij}^{\delta\delta}(z,\hat{\mu},k)$ follows equation (2.2.41). With these definitions, it can be proved that $\langle\hat{P}_{ij}(z,\hat{\mu}_c,k_c)\rangle = C_{ij}(z,\hat{\mu}_c,k_c)$ which is the observed power spectrum. Now we calculate the covariance matrix of (3.2.1),

$$\begin{aligned} C_{ijlm}(\hat{\mu}_c,k_c,\hat{\mu}_d,k_d) =& \langle\hat{P}_{ij}(z,\hat{\mu}_c,k_c)\hat{P}_{lm}(z,\hat{\mu}_d,k_d)\rangle \\ &- \langle\hat{P}_{ij}(z,\hat{\mu}_c,k_c)\rangle\langle\hat{P}_{lm}(z,\hat{\mu}_d,k_d)\rangle. \end{aligned} \tag{3.2.6}$$

Using the estimator (3.2.2) and Gaussian statistics,

$$\begin{aligned} \langle F(s_1)F(s_2)F(s_3)F(s_4)\rangle =& \langle F(s_1)F(s_2)\rangle\langle F(s_3)F(s_4)\rangle \\ &+ \langle F(s_1)F(s_3)\rangle\langle F(s_2)F(s_4)\rangle \\ &+ \langle F(s_1)F(s_4)\rangle\langle F(s_2)F(s_3)\rangle, \end{aligned} \tag{3.2.7}$$

we obtain,

$$\begin{aligned} C_{ijlm}(\hat{\mu}_c,k_c,\hat{\mu}_d,k_d) =& V_f^2 \int_c\int_d \frac{d^3k\,d^3k'}{V_s(k_c,\hat{\mu}_c)V_s(k_d,\hat{\mu}_d)} \left[\langle\delta_i(z,\mathbf{k})\delta_l(z,\mathbf{k}')\rangle\langle\delta_j(z,-\mathbf{k})\delta_m(z,-\mathbf{k}')\rangle\right. \\ &\left.+\langle\delta_i(z,\mathbf{k})\delta_m(z,-\mathbf{k}')\rangle\langle\delta_j(z,-\mathbf{k})\delta_l(z,\mathbf{k}')\rangle\right]. \end{aligned} \tag{3.2.8}$$

Now using equation (3.2.3) and the property $\delta_D^2(x) = \delta_D(0)\delta_D(x)$ we find,

$$\begin{aligned} C_{ijlm}(\hat{\mu}_c,k_c,\hat{\mu}_d,k_d) =& \frac{V_f}{V_s(k_c,\hat{\mu}_c)V_s(k_d,\hat{\mu}_d)} \int_c d^3k \int_d d^3k' \left[\delta_D(\mathbf{k}+\mathbf{k}')\,C_{il}(z,\hat{\mu},k)\,C_{jm}(z,\hat{\mu},k)\right. \\ &\left.+\delta_D(\mathbf{k}-\mathbf{k}')\,C_{im}(z,\hat{\mu},k)\,C_{jl}(z,\hat{\mu},k)\right]. \end{aligned} \tag{3.2.9}$$

Considering that $C_{ij}(z,\hat{\mu},k)$ is constant in the integral of the $\mathbf{k}_c$-bin, we can extract it from the integral as $C_{ij}(z,\hat{\mu}_c,k_c)$. Thus, the integrals in k and k' become,

$$\int_c d^3k \int_d d^3k'\,\delta_D(\mathbf{k}\pm\mathbf{k}') = V_s(k_c,\hat{\mu}_c)\,\delta_{cd}. \tag{3.2.10}$$

Finally, the covariance matrix is,

$$C_{ijlm}(\hat{\mu}_c,k_c,\hat{\mu}_d,k_d) = \frac{4\pi^2\,\delta_{cd}}{V\,k_c^2\,dk_c\,d\hat{\mu}_c}\,\left[C_{il}\,C_{jm}+C_{im}\,C_{jl}\right], \tag{3.2.11}$$

where $C_{ij}=C_{ij}(z,\hat{\mu}_c,k_c)$. We use this result in equation (3.2.1),

$$dF^{\delta\delta}_{\alpha\beta} = \frac{V\,k_c^2\,dk_c\,d\hat{\mu}_c}{4\pi^2}\,\left.\frac{\partial P^{\delta\delta}_{ij}(z,\hat{\mu}_c,k_c)}{\partial\theta_\alpha}\right|_r\,\delta_{cd}\,\left[C_{il}\,C_{jm}+C_{im}\,C_{jl}\right]^{-1}\,\left.\frac{\partial P^{\delta\delta}_{lm}(z,\hat{\mu}_d,k_d)}{\partial\theta_\beta}\right|_r, \tag{3.2.12}$$

due to the fact that C_{ij} is symmetric and that all indices in (3.2.12) are summed, we can simplify the expression as,

$$dF^{\delta\delta}_{\alpha\beta} = \frac{V\,k_c^2\,dk_c\,d\hat{\mu}_c}{8\pi^2}\,\left.\frac{\partial P^{\delta\delta}_{ij}(z,\hat{\mu}_c,k_c)}{\partial\theta_\alpha}\right|_r\,C^{-1}_{jl}\,\left.\frac{\partial P^{\delta\delta}_{lm}(z,\hat{\mu}_c,k_c)}{\partial\theta_\beta}\right|_r\,C^{-1}_{mi}. \tag{3.2.13}$$

This Fisher matrix contains the information of a given scale at redshift z, if we want to sum over a scale range we have to integrate equation (3.2.13) but keeping only linear scales. To do that, there are mainly two approaches. First, we can integrate since a minimum scale k_{min} up to a maximum scale k_{max} defined so that $\sigma(z,\pi/2k_{max}(z))=0.35$ [129], being,

$$\sigma^2(z,R) = \int \frac{k^2\,dk}{2\pi^2}\,P_m(z,k)\,|\hat{W}(R,k)|^2, \tag{3.2.14}$$

where $\hat{W}(R,k)$ is a top-hat filter,

$$\hat{W}(R,k) = \frac{3}{k^3R^3}\,\left[\sin(kR)-kR\cos(kR)\right]. \tag{3.2.15}$$

Then, the Fisher matrix for a given redshift bin is [130, 131],

$$F^{\delta\delta}_{\alpha\beta}(z_a) = \frac{V(z_a)}{8\pi^2}\int_{k_{min}}^{k_{max}} k^2\,dk\int_{-1}^{1}d\hat{\mu}\,\left.\frac{\partial P^{\delta\delta}_{ij}(z_a,\hat{\mu},k)}{\partial\theta_\alpha}\right|_r\,C^{-1}_{jl}\,\left.\frac{\partial P^{\delta\delta}_{lm}(z_a,\hat{\mu},k)}{\partial\theta_\beta}\right|_r\,C^{-1}_{mi}. \tag{3.2.16}$$

The comoving volume $V(z_a)$ of the redshift bin with center z_a is,

$$V(z_a) = \frac{4\pi f_{sky}}{3}\left(\chi(\bar{z}_a)^3-\chi(\bar{z}_{a-1})^3\right), \tag{3.2.17}$$

where f_{sky} is the fraction of the sky of the survey, $\chi(z)$ is the comoving distance and $\bar{z}_a$ is the upper limit of the a-th redshift bin. As an alternative, a cutoff term can be added in the scale integration to remove the contributions from non-linear scales [123]. In that situation,

$$F^{\delta\delta}_{\alpha\beta}(z_a) = \frac{V(z_a)}{8\pi^2} \int_{k_{min}}^{\infty} k^2\, dk \int_{-1}^{1} d\hat{\mu}\, \frac{\partial P^{\delta\delta}_{ij}(z_a,\hat{\mu},k)}{\partial\theta_\alpha}\bigg|_r C^{-1}_{jl}\, \frac{\partial P^{\delta\delta}_{lm}(z_a,\hat{\mu},k)}{\partial\theta_\beta}\bigg|_r C^{-1}_{mi}\, \mathrm{e}^{-k^2\,\Sigma_\perp^2 - k^2\,\hat{\mu}^2\,(\Sigma_\parallel^2-\Sigma_\perp^2)}, \tag{3.2.18}$$

where,

$$\Sigma_\perp(z) = 0.785\, D(z)\, \Sigma_0, \tag{3.2.19}$$

$$\Sigma_\parallel(z) = 0.785\, D(z)\, (1+f(z))\, \Sigma_0, \tag{3.2.20}$$

being $f(z)$ the growth function defined as (2.2.19), $D(z) \equiv \delta(z)/\delta(0)$ the growth factor normalized to one today, and Σ_0 is a parameter that determines the cutoff scale. For the case in which we only have one tracer, equation (3.2.18) is reduced to [129, 132],

$$F^{\delta\delta}_{\alpha\beta}(z_a) = \frac{1}{8\pi^2} \int_{k_{min}}^{\infty} k^2\, dk \int_{-1}^{1} d\hat{\mu}\, V_{eff}\, \frac{\partial \ln P_{gg}(z_a,\hat{\mu},k)}{\partial\theta_\alpha}\bigg|_r \frac{\partial \ln P_{gg}(z_a,\hat{\mu},k)}{\partial\theta_\beta}\bigg|_r \mathrm{e}^{-k^2\,\Sigma_\perp^2 - k^2\,\hat{\mu}^2\,(\Sigma_\parallel^2-\Sigma_\perp^2)}, \tag{3.2.21}$$

where $P_{gg}(z,\hat{\mu},k)$ follows equation (2.2.39) and $V_{eff} = V_{eff}(z_a,\hat{\mu},k)$ is [129, 132],

$$V_{eff}(z,\hat{\mu},k) \equiv V(z) \left(\frac{\bar{n}(z) P_{gg}(z,\hat{\mu},k)}{1+\bar{n}(z) P_{gg}(z,\hat{\mu},k)}\right)^2. \tag{3.2.22}$$

3.2.1 Fisher matrix for the multipole power spectrum

We can also consider that the observable is the multipole power spectrum $P_\ell(z,k_c)$ defined as (2.2.23) instead of considering $P_{gg}(z,\hat{\mu},k)$. In this situation the Fisher matrix can be defined as [133],

$$dF^{\delta_\ell\delta_\ell}_{\alpha\beta} = \frac{\partial P_\ell(z,k_c)}{\partial\theta_\alpha}\bigg|_r C^{-1}_{\ell\ell'}(z,k_c,k_d)\, \frac{\partial P_{\ell'}(z,k_d)}{\partial\theta_\beta}\bigg|_r. \tag{3.2.23}$$

The estimator is constructed using (3.2.2) and (2.2.23) so that,

$$\hat{P}_\ell(z,k_c) = V_f \int_c \frac{d^3k}{V_s(k_c)}\, \frac{2\ell+1}{2} \int_{-1}^{1} d\hat{\mu}\, \delta(z,\hat{\mu},k)^2\, \mathcal{L}_\ell(\hat{\mu}), \tag{3.2.24}$$

where we have considered that, in the standard case, $P_\ell(z,k)$ depends only on the modulus of $\mathbf{k}$ so that $\int_c d^3k = V_s(k_c) = 4\pi k_c^2 dk_c$. Considering one tracer, equation (3.2.3) becomes,

$$\langle \delta(z,\hat{\mu},k)\delta(z,\hat{\mu},k')\rangle = \delta_D(k-k') \left[P_{gg}(z,\hat{\mu},k) + \frac{1}{\bar{n}(z)}\right], \tag{3.2.25}$$

where we have taken into account the shot noise effect. With this estimator we can calculate the covariance matrix,

$$C_{\ell\ell'}(z,k_c,k_d) = \langle \hat{P}_\ell(z,k_c)\hat{P}_{\ell'}(z,k_d)\rangle - P_\ell(z,k_c)P_{\ell'}(z,k_d). \tag{3.2.26}$$

As before, we consider only Gaussian perturbations satisfying (3.2.7), so that

$$C_{\ell\ell'}(z,k_c,k_d) = V_f^2\,\frac{(2\ell+1)(2\ell'+1)}{2}\int_c \frac{d^3k}{V_s(k_c)}\int_d \frac{d^3k'}{V_s(k_d)} \int_{-1}^{1} d\hat{\mu}\int_{-1}^{1} d\hat{\mu}'\mathcal{L}_\ell(\hat{\mu})\,\mathcal{L}_{\ell'}(\hat{\mu}')\,\langle\delta(z,\hat{\mu},k)\delta(z,\hat{\mu}',k')\rangle^2, \tag{3.2.27}$$

now we use the distant observer approximation in which we assume that the integrand of (3.2.27) is non negligible only when $\hat{\mu}' \simeq \hat{\mu}$, then we obtain,

$$C_{\ell\ell'}(z,k_c,k_d) = V_f^2\,(2\ell+1)(2\ell'+1)\int_c \frac{d^3k}{V_s(k_c)}\int_d \frac{d^3k'}{V_s(k_d)} \int_{-1}^{1} d\hat{\mu}\,\mathcal{L}_\ell(\hat{\mu})\,\mathcal{L}_{\ell'}(\hat{\mu})\,\langle\delta(z,\hat{\mu},k)\delta(z,\hat{\mu},k')\rangle^2, \tag{3.2.28}$$

so that using (3.2.25), (3.2.10) and considering that $P_{gg}(z,\hat{\mu},k) \simeq P_{gg}(z,\hat{\mu},k_c)$ in the integral, we obtain,

$$C_{\ell\ell'}(z,k_c,k_d) = \frac{4\pi^2\delta_{cd}}{V\,k_c^2 dk_c}\,\frac{(2\ell+1)(2\ell'+1)}{2}\int_{-1}^{1} d\hat{\mu}\,\mathcal{L}_\ell(\hat{\mu})\,\mathcal{L}_{\ell'}(\hat{\mu})\,\left[P_{gg}(z,\hat{\mu},k_c)+\frac{1}{\bar{n}(z)}\right]^2. \tag{3.2.29}$$

Finally, the Fisher matrix for the multipole power spectrum at redshift bin z_a is [133],

$$F_{\alpha\beta}^{\delta_\ell\delta_\ell}(z_a) = \frac{V(z_a)}{4\pi}\int_{k_{min}}^{k_{max}} k^2\,dk\;\left.\frac{\partial P_\ell(z_a,k)}{\partial\theta_\alpha}\right|_r \hat{C}^{-1}_{\ell\ell'}(z_a,k)\;\left.\frac{\partial P_{\ell'}(z_a,k)}{\partial\theta_\beta}\right|_r \tag{3.2.30}$$

where we have summed over scales with a maximum scale defined as before, and with,

$$\hat{C}_{\ell\ell'}(z,k) = \frac{(2\ell+1)(2\ell'+1)}{2}\int_{-1}^{1} d\hat{\mu}\,\mathcal{L}_\ell(\hat{\mu})\,\mathcal{L}_{\ell'}(\hat{\mu})\,\left[P_{gg}(z,\hat{\mu},k)+\frac{1}{\bar{n}(z)}\right]^2. \tag{3.2.31}$$

Notice that the difference in a factor 1/2 in (3.2.30) with respect to (3.2.16) is due to the fact that, since in this case the integrand does not depend on $\hat{\mu}$, we have integrated $\hat{\mu}$ between -1 and 1. These are the main Fisher matrices for galaxy distribution power spectra. We will analyze the results of the forecast for different galaxy surveys in next sections.

3.3 Fisher matrices for peculiar-velocity observables

In this section we will calculate the Fisher matrix for the peculiar velocity power spectra (2.3.4) and the cross correlation between velocities and galaxy distribution (2.3.5). To do that in a simple way, we will use the same procedure as for the Fisher matrix of the multitracer power spectrum. Following (3.2.2), we define the following estimator,

$$\hat{\Sigma}_{ij}(z,\hat{\mu}_c,k_c) = V_f \int_c \frac{d^3k}{V_s(k_c,\hat{\mu}_c)}\,\sigma_i(z,\mathbf{k})\,\sigma_j(z,-\mathbf{k}), \tag{3.3.1}$$

being $\sigma_1 \equiv \delta$ and $\sigma_2 \equiv u$. Then, considering the shot noise effect, the observable is,

$$\mathbf{\Sigma} = \begin{pmatrix} P_{gg} + \bar{n}_g^{-1} & P_{gu} \\ P_{ug} & P_{uu} + \bar{n}_u^{-1}\,\sigma_u^2 \end{pmatrix}, \tag{3.3.2}$$

where $\bar{n}_g$ is the galaxy density and $\bar{n}_u$ is the galaxy density for the velocity field. In general, the number of galaxies for which the velocity can be obtained is smaller than the total number of galaxies so that $\bar{n}_g > \bar{n}_u$. σ_u is the velocity noise,

$$\sigma_u^2 = \sigma_*^2 + \epsilon\, z, \tag{3.3.3}$$

with $\sigma_* = 10^{-3}$ ($c = 1$) and $\epsilon = 0.2$ the fractional error [134]. Notice that, because the shot noise is a white noise uncorrelated with any other fluctuation, the cross-correlation power spectrum has no shot noise term. This is a general result and one of the advantages of using cross-correlation terms. Considering the estimator (3.3.1) we follow the same procedure as in the previous section and we obtain the following Fisher matrix [134],

$$F^{\sigma\sigma}_{\alpha\beta}(z_a) = \frac{V(z_a)}{8\pi^2}\int_{k_{min}}^{k_{max}} k^2\,dk \int_{-1}^{1} d\hat{\mu}\,\left.\frac{\partial\Sigma_{ij}(z_a,\hat{\mu},k)}{\partial\theta_\alpha}\right|_r \Sigma^{-1}_{jl}\,\left.\frac{\partial\Sigma_{lm}(z_a,\hat{\mu},k)}{\partial\theta_\beta}\right|_r \Sigma^{-1}_{mi}. \tag{3.3.4}$$

Now we can obtain the isolated Fisher matrices for P_{gg}, P_{uu} or P_{gu} using expression (3.3.2),

$$F^{gg}_{\alpha\beta} = \frac{V}{8\pi^2}\int_{k_{\rm min}}^{k_{\rm max}} k^2\,dk \int_{-1}^{1} d\hat{\mu}\,\left.\frac{\partial \ln P_{gg}}{\partial\theta_\alpha}\right|_r \left.\frac{\partial \ln P_{gg}}{\partial\theta_\beta}\right|_r \left[\frac{\bar{n}_g P_{gg}}{1+\bar{n}_g P_{gg}}\right]^2, \tag{3.3.5}$$

$$F^{uu}_{\alpha\beta} = \frac{V}{8\pi^2}\int_{k_{\rm min}}^{k_{\rm max}} k^2\,dk \int_{-1}^{1} d\hat{\mu}\,\left.\frac{\partial \ln P_{uu}}{\partial\theta_\alpha}\right|_r \left.\frac{\partial \ln P_{uu}}{\partial\theta_\beta}\right|_r \left[\frac{\sigma_u^{-2}\bar{n}_u P_{uu}}{1+\sigma_u^{-2}\bar{n}_u P_{uu}}\right]^2, \tag{3.3.6}$$

$$F^{gu}_{\alpha\beta} = \frac{V}{4\pi^2}\int_{k_{\rm min}}^{k_{\rm max}} k^2\,dk \int_{-1}^{1} d\hat{\mu}\,\left.\frac{\partial \ln P_{gu}}{\partial\theta_\alpha}\right|_r \left.\frac{\partial \ln P^*_{gu}}{\partial\theta_\beta}\right|_r \left[\frac{\sigma_u^{-2}\bar{n}_u\bar{n}_g P_{gu}P^*_{gu}}{(1+\bar{n}_g P_{gg})\left(1+\sigma_u^{-2}\bar{n}_u P_{uu}\right)+\sigma_u^{-2}\bar{n}_u\bar{n}_g P_{gu}P^*_{gu}}\right]. \tag{3.3.7}$$

Notice that $P^*_{gu} = P_{ug}$ because P_{gu} is purely imaginary.

3.4 Fisher matrices for weak lensing

In this section we will obtain the Fisher matrix for the convergence power spectrum $P^{\kappa\kappa}_{ab}(\ell)$ that follows (2.4.63). The Fisher matrix for the convergence power spectrum is defined as,

$$dF^{\kappa\kappa}_{\alpha\beta} = \left.\frac{\partial P^{\kappa\kappa}_{ab}(\ell_c)}{\partial\theta_\alpha}\right|_r C^{-1}_{aba'b'}(\ell_c,\ell_d) \left.\frac{\partial P^{\kappa\kappa}_{a'b'}(\ell_d)}{\partial\theta_\beta}\right|_r . \tag{3.4.1}$$

The estimator for the convergence power spectrum is [135, 136],

$$\hat{P}_{ab}(\ell_c) = A_f \int_c \frac{d^2\ell}{A_s(\ell_c)}\,\kappa_a(\boldsymbol{\ell})\kappa_b(-\boldsymbol{\ell}), \tag{3.4.2}$$

where $A_f = (2\pi)^2/\Omega$, being $\Omega = 4\pi f_{sky}$ the total area of the survey and $\int_c d^2\ell = A_s(\ell_c) = 2\pi\ell_c d\ell_c$ the area of the ℓ_c bin. Then we have,

$$\langle\kappa_a(\boldsymbol{\ell}_1)\kappa_b(\boldsymbol{\ell}_2)\rangle = \delta_D(\boldsymbol{\ell}_1+\boldsymbol{\ell}_2)\,C_{ab}(\ell_1), \tag{3.4.3}$$

where $C_{ab}(\ell)$ is the observable convergence power spectrum considering the shot noise effect,

$$C_{ab}(\ell) = P^{\kappa\kappa}_{ab}(\ell) + \frac{\gamma^2_{int}\,\delta_{ab}}{\hat{n}_a}, \tag{3.4.4}$$

being γ_{int} is the intrinsic ellipticity due to the alignment of the galactic plane with respect to our LOS direction. The typical value is $\gamma_{int} = 0.22$ [137] and $\hat{n}_a$ are the number of galaxies per steradian in the a-th bin,

$$\hat{n}_a = n_\theta \frac{\int_{\bar{z}_{a-1}}^{\bar{z}_a} n(z)\,dz}{\int_0^\infty n(z)\,dz}, \tag{3.4.5}$$

where n_θ is the areal galaxy density and $n(z)$ follows (2.4.61). Using this estimator, we build the covariance matrix,

$$C_{aba'b'}(\ell_c,\ell_d) = \langle\hat{P}_{ab}(\ell_c)\hat{P}_{a'b'}(\ell_d)\rangle - C_{ab}(\ell_c)C_{a'b'}(\ell_d). \tag{3.4.6}$$

As before, we take into account (3.2.7) for Gaussian perturbations so that,

$$C_{aba'b'}(\ell_c,\ell_d) = \frac{A_f^2\,\delta_D(0)}{A_s(\ell_c)A_s(\ell_d)} \int_c d^2\ell \int_d d^2\ell'[\delta_D(\boldsymbol{\ell}+\boldsymbol{\ell'})C_{aa'}(\ell)C_{bb'}(\ell) + \delta_D(\boldsymbol{\ell}-\boldsymbol{\ell'})C_{ab'}(\ell)C_{ba'}(\ell)]. \tag{3.4.7}$$

where $\delta_D(0) = 1/A_f$. By assuming that $C_{ab}(\ell)$ is constant within the ℓ_c bin, we can extract it from the integral as $C_{ab}(\ell_c)$. Then, the integrals in ℓ and ℓ' become,

$$\int_c d^2\ell \int_d d^2\ell' \; \delta_D(\boldsymbol{\ell} \pm \boldsymbol{\ell'}) = A_s(\ell_d)\, \delta_{cd}. \tag{3.4.8}$$

Using this result, the covariance matrix is,

$$C_{aba'b'}(\ell_c, \ell_d) = \frac{A_f\, \delta_{cd}}{A_s(\ell_c)} \left[C_{aa'}(\ell_c) C_{bb'}(\ell_c) + C_{ab'}(\ell_c) C_{ba'}(\ell_c)\right]. \tag{3.4.9}$$

If we use the expressions for A_f and $A_s(\ell_c)$ and consider $\ell \simeq (2\ell + 1)/2$ for large ℓ, we obtain the known result [120],

$$C_{aba'b'}(\ell_c, \ell_d) = \frac{\delta_{cd}}{(2\ell_c + 1) f_{sky}\, d\ell_c} \left[C_{aa'}(\ell_c) C_{bb'}(\ell_c) + C_{ab'}(\ell_c) C_{ba'}(\ell_c)\right], \tag{3.4.10}$$

finally using equation (3.4.1) and summing in ℓ, we obtain the Fisher matrix for the convergence power spectrum [138],

$$F^{\kappa\kappa}_{\alpha\beta} = f_{sky} \sum_\ell \Delta \ln \ell \, \frac{(2\ell + 1)\ell}{2} \left.\frac{\partial P^{\kappa\kappa}_{ab}(\ell)}{\partial \theta_\alpha}\right|_r C^{-1}_{ba'} \left.\frac{\partial P^{\kappa\kappa}_{a'b'}(\ell)}{\partial \theta_\beta}\right|_r C^{-1}_{b'a}, \tag{3.4.11}$$

where we sum in ℓ up to a ℓ_{max}. The value of ℓ_{max} depends on the model and the survey. In this situation it is not straightforward to remove the non-linear scales considering a cutoff term in the sum of ℓ because, as can be seen in equation (2.4.63), the matter power spectrum is evaluated at the scale $k = \ell/\chi(z)$.

3.4.1 Cross-correlation power spectrum Fisher matrix

Finally, we will obtain the Fisher matrix for the cross-correlation power spectrum $P^{\kappa\delta_2}_{ab\,i}(\ell)$ that follows equation (2.5.10). The Fisher matrix is defined as,

$$dF^{\kappa\delta_2}_{\alpha\beta} = \left.\frac{\partial P^{\kappa\delta_2}_{ab\,i}(\ell_c)}{\partial \theta_\alpha}\right|_r \left[C^{ij}_{aba'b'}(\ell_c, \ell_d)\right]^{-1} \left.\frac{\partial P^{\kappa\delta_2}_{a'b'\,j}(\ell_d)}{\partial \theta_\beta}\right|_r . \tag{3.4.12}$$

We define the estimator for the cross-correlation power spectrum as,

$$\hat{P}_{ab\,i}(\ell_c) = A_f \int_c \frac{d^2\ell}{A_s(\ell_c)}\, \kappa_a(\boldsymbol{\ell}) \delta^i_b(-\boldsymbol{\ell}), \tag{3.4.13}$$

where δ_b^i is the 2D galaxy distribution of redshift bin b and tracer i. These perturbations satisfy equation (3.4.3),

$$\langle \delta_a^i(\boldsymbol{\ell}_1)\delta_b^j(\boldsymbol{\ell}_2)\rangle = \delta_D(\boldsymbol{\ell}_1+\boldsymbol{\ell}_2)\, C_{ab}^{ij}(\ell_1), \tag{3.4.14}$$

and

$$\langle \kappa_a(\boldsymbol{\ell}_1)\delta_b^i(\boldsymbol{\ell}_2)\rangle = \delta_D(\boldsymbol{\ell}_1+\boldsymbol{\ell}_2)\, P_{ab\ i}^{\kappa\delta_2}(\ell_1), \tag{3.4.15}$$

where, considering the shot noise effect,

$$C_{ab}^{ij}(\ell) = P_{ab\ ij}^{\delta_2\delta_2}(\ell) + \frac{\delta_{ab}\,\delta_{ij}}{\hat{n}_a^i}, \tag{3.4.16}$$

where $P_{ab\ ij}^{\delta_2\delta_2}(\ell)$ follows equation (2.5.9), and $\hat{n}_a^i$ is the number of galaxies per steradian in the a-th bin for the tracer i. We calculate this number of galaxies using the galaxy density $\bar{n}_i(z_a)$,

$$\hat{n}_a^i = \frac{1}{3}\left(\chi(\bar{z}_i)^3 - \chi(\bar{z}_{i-1})^3\right)\,\bar{n}_i(z_a). \tag{3.4.17}$$

The covariance matrix is then,

$$C_{aba'b'}^{ij}(\ell_c,\ell_d) = \langle \hat{P}_{ab\ i}(\ell_c)\hat{P}_{a'b'\ j}(\ell_d)\rangle - P_{ab\ i}^{\kappa\delta_2}(\ell_c)P_{a'b'\ j}^{\kappa\delta_2}(\ell_d). \tag{3.4.18}$$

Considering also Gaussian statistics (3.2.7),

$$C_{aba'b'}^{ij}(\ell_c,\ell_d) = A_f^2\int_c \frac{d^2\ell}{A_s(\ell_c)}\int_d \frac{d^2\ell'}{A_s(\ell_d)}\left[\langle\kappa_a(\boldsymbol{\ell})\kappa_{a'}(\boldsymbol{\ell}')\rangle\langle\delta_b^i(\boldsymbol{\ell})\delta_{b'}^j(\boldsymbol{\ell}')\rangle + \langle\kappa_a(\boldsymbol{\ell})\delta_{b'}^j(\boldsymbol{\ell}')\rangle\langle\kappa_{a'}(\boldsymbol{\ell}')\delta_b^i(\boldsymbol{\ell})\rangle\right]. \tag{3.4.19}$$

Using (3.4.3), (3.4.14) and (3.4.15); considering that the power spectra are constant within the ℓ_c bin, and taking into account (3.4.8) we obtain the covariance matrix,

$$C_{aba'b'}^{ij}(\ell_c,\ell_d) = \frac{A_f\,\delta_{cd}}{A_s(\ell_c)}\left[C_{aa'}(\ell_c)\,C_{bb'}^{ij}(\ell_c) + P_{a'b\ i}^{\kappa\delta_2}(\ell_c)\,P_{ab'\ j}^{\kappa\delta_2}(\ell_c)\right], \tag{3.4.20}$$

where $C_{aa'}(\ell_c)$ follows equation (3.4.4) and $C_{bb'}^{ij}(\ell_c)$ equation (3.4.16). Using this expression in the Fisher matrix (3.4.12) and summing in ℓ, we obtain the Fisher matrix for the cross correlation power spectrum [120],

$$F_{\alpha\beta}^{\kappa\delta_2} = f_{sky}\sum_\ell \Delta\ln\ell\,\frac{(2\ell+1)\ell}{2}\left.\frac{\partial P_{ab\,i}^{\kappa\delta_2}(\ell)}{\partial\theta_\alpha}\right|_r\left[\hat{C}_{aba'b'}^{ij}\right]^{-1}\left.\frac{\partial P_{a'b'\,j}^{\kappa\delta_2}(\ell)}{\partial\theta_\beta}\right|_r, \tag{3.4.21}$$

where

$$\hat{C}_{aba'b'}^{ij} \equiv C_{aa'}(\ell)\,C_{bb'}^{ij}(\ell) + P_{a'b\ i}^{\kappa\delta_2}(\ell)\,P_{ab'\ j}^{\kappa\delta_2}(\ell). \tag{3.4.22}$$

Chapter 4

Parametrizing non-standard cosmology

In Chapter 1, we have shown how non-standard cosmological models based on modified gravity theories with additional scalar degrees of freedom can be described phenomenologically with two additional parameters μ and η. In this Chapter we will extend this analysis to more general models in which not only additional scalar degrees of freedom, but also vectors, can be present . Moreover, we will also consider the possibility that the dark matter sector is modified including imperfect and non-conserved fluids. We will find the new set of effective parameters that describe these extensions in the quasi-static approximation and in the sub-Hubble regime. The results of this chapter correspond to [139–141].

4.1 Vector modified gravity models

As a natural extension of modified gravity with scalar degrees of freedom, modified gravity with vector degrees of freedom has been proposed to model late-time cosmic acceleration and inflation [142–146]. However, this type of theories has a main challenge: to deal with the cosmological principle. This principle ensures that at large scales, the Universe is isotropic and homogeneous. From a theoretical point of view, this is related with the fact that the gravitational interaction respects Lorentz invariance in standard GR [39,147,148]. On the other hand, Lorentz invariance is supported by current observations [149]. In this situation, a vector modified gravity model seems to be quite restricted. Nevertheless, certain anomalies could suggest the existence of Lorentz symmetry breaking on cosmological scales. For example, anomalies have been detected in the low multipoles of the

CMB [149, 150], including the alignment of quadrupole, octupole and ecliptic plane, a dipole anomaly in the power spectrum that breaks statistical isotropy and the hemispherical anomaly whose maximum asymmetry is observed in the ecliptic frame. On the other hand, large scale bulk flows have also been detected with an amplitude which has been claimed to exceed the predictions of standard ΛCDM [151–153]. These observations motivates cosmological descriptions with a vector degree of freedom and thus a small Lorentz symmetry breaking.

One of the simplest frameworks to explore the consequences of Lorentz symmetry breaking is the presence of tensor fields acquiring non-vanishing vacuum expectation values (VEV). This is indeed the case of the so called Standard Model Extension (SME) [154]. In particular, in the case in which such VEV is acquired by a vector field, the first models were proposed by Nambu already in the sixties [155]. Depending on the particular type of vector, this mechanism can induce two kinds of gravitational effects. On one hand, if the vector field is timelike, preferred frame effects would be present. On the other hand, a space-like VEV for the vector field will generate preferred directions effects.

Preferred frame effects have been explored in local gravitational experiments through the so called parametrized post-Newtonian (PPN) formalism [147, 156]. In particular, two PPN parameters, α_1 and α_2, have been restricted by Solar System and pulsar observations. Also, modifications in the gravity wave dispersion relations have been studied in [157]. From a theoretical point of view, theories of gravity such as Horava gravity [158] or Einstein-aether [159] have been shown to generate this kind of preferred frame effects. Also on the cosmological framework, different kinds of vector-tensor theories including temporal background vector fields have been analyzed in the context of dark energy [160–166].

Preferred directions effects have been explored in the framework of the anisotropic PPN formalism [167] and bounds from laboratory experiments have been obtained in [168]. The possible cosmological implications have been studied both on the CMB temperature power spectrum [149, 169] and in the matter distribution in [170–173]. In those works, the evolution both of the background and perturbations is assumed to be the standard in ΛCDM and the anisotropy is assumed to be present only in the primordial power spectra. Such anisotropic power spectrum can be generated for instance in models of inflation with vectors [174–176] or higher-spin fields [177]. A different kind of effects would be those

associated to the presence of non-comoving fluids singling out a preferred direction as those considered in [178–180].

In next section, we will focus on the case in which we have a preferred direction which weakly breaks the background isotropy. This preferred direction can be described with a vector degree of freedom in a modified gravity theory. These type of theories with extra vector degrees of freedom have also been widely studied in recent years. Since the first proposal in [142], different models of vector inflation have been studied in the literature [143–146]. Vector models for dark energy based on massive [160, 161] or massless [162–164] vector fields have also been proposed. Vector dark matter based on hidden sector gauge bosons have been analyzed in [181], and the role of vectors in the generation of metric perturbations in the so called curvaton scenario has also been considered in [182]. Oscillating massive vector fields were considered as non-thermal dark matter candidates in [183] and ultra-light vector dark matter models have been explored in [184]. The most general framework considered so far for modifications of gravity induced by vectors is given by the so called beyond generalized Proca models [165, 166] which propagate three degrees of freedom (two transverse and one longitudinal) corresponding to a massive spin 1 field. The aim of our parametrization is to include all these different types of theories in a simple set of parameters considering QSA approximation and sub-Hubble regime.

4.2 Parametrizing vector modified gravity

Most of the work done with modified gravity theories with vector degrees of freedom focus on the case in which the background field is purely temporal. In that situation, it can be proved that within the QSA approximation and the sub-Hubble regime, a general modified gravity theory with a vector degree of freedom can be described with the usual μ and η parameters. Here, we generalize that result for the case in which a small spatial vector field in the background is present. This preferred direction can produce modifications in the evolution of dark matter perturbations thus introducing anisotropies in the cosmological observables. Our aim is to analyze this kind of effects in a model independent way for the context of galaxy survey observables. We will prove that, when a background preferred direction is considered, we need two independent modified gravity parameters in addition

to μ and η (if dark matter vorticity can be neglected as is usually the case) which relate matter density perturbations to vector and tensor metric perturbations. In addition, and apart from the standard time a and scale k dependence, those four effective parameters can have an additional $x = \hat{\mathbf{k}} \cdot \hat{\mathbf{A}}$ dependence on the angle between the wave-vector direction $\hat{\mathbf{k}}$ and the preferred direction fixed by the background vector field $\hat{\mathbf{A}}$.

We start considering an extra vector field A_μ. Very much as in the scalar case, we will decompose A_μ in a homogeneous background and a perturbation as $A_\mu = A_\mu^{(0)}(\tau) + \delta A_\mu$. Notice that unlike previous works [63, 185], we will allow for the background vector $A_\mu^{(0)}$ to have both non-vanishing temporal and spatial components. For simplicity we will limit ourselves to the case of linearly polarized $A_i^{(0)}(\tau)$. In such a case, the background metric is no longer of the Robertson-Walker type but an axisymmetric Bianchi I metric. This metric is characterized by the spatial metric tensor Ξ_{ij} that in general can be written as [186],

$$\Xi_{ij} = e^{2\beta_i(\tau)}\delta_{ij} \tag{4.2.1}$$

with

$$\sum_{i=1}^{3} \beta_i = 0 \tag{4.2.2}$$

This guarantees that $\Xi^{ik}\Xi_{kj} = \delta^i_j$. Using this metric we can now define a unit spatial vector field $\hat{A}_i$ in the direction of the background vector field as

$$\hat{A}_i = \frac{A_i^{(0)}}{A} \tag{4.2.3}$$

with $A = (\Xi^{ij} A_i^{(0)} A_j^{(0)})^{1/2}$. In terms of the unit vector, the spatial metric can be written as

$$\Xi_{ij} = C_1\, \delta_{ij} + C_2\, \hat{A}_i \hat{A}_j, \tag{4.2.4}$$

being C_1 and C_2 functions of time only and satisfying $C_2 = 1 - C_1^3$ by virtue of (4.2.2). This tensor reduces to $\Xi_{ij} = \delta_{ij}$ in the isotropic limit. The perturbed Bianchi metric in the longitudinal gauge, including scalar (Φ, Ψ), vector Q_i and tensor h_{ij} perturbations reads [186],

$$ds^2 = a^2 \left[-(1+2\Psi)\, d\tau^2 + [(1-2\Phi)\, \Xi_{ij} + h_{ij}]\, dx^i dx^j - 2\, Q_i\, d\tau\, dx^i\right]. \tag{4.2.5}$$

Additionally, the perturbed vector field can be decomposed as δA_0, $\delta A_i^{\parallel}$, $\delta A_i^{\perp}$, where the different perturbations satisfy in Fourier space

$$\hat{k}^i \, Q_i = 0, \tag{4.2.6}$$

$$\hat{k}^i \, h_{ij} = 0, \tag{4.2.7}$$

$$h^i{}_i = 0, \tag{4.2.8}$$

$$\hat{k}^i \, \delta A_i^{\perp} = 0, \tag{4.2.9}$$

$$\delta A_i^{\parallel} = \delta A^{\parallel} \, \hat{k}_i, \tag{4.2.10}$$

being $\hat{k}_i$ the unitary direction of the perturbation wavevector $\mathbf{k}$ with respect to the spatial metric Ξ_{ij}. Notice that indices in spatial vectors are raised and lowered with the metric Ξ_{ij}. As in the scalar field case (1.4.6), we have the perturbed equations,

$$\delta \bar{G}^{\mu}{}_{\nu} = 8\pi G \, \delta T^{\mu}{}_{\nu}, \tag{4.2.11}$$

$$\delta L_{\mu} = 0, \tag{4.2.12}$$

being $\bar{G}^{\mu}{}_{\nu}$ the modified Einstein tensor and δL_{μ} the perturbed vector field equations. The only matter-energy content we consider is presureless matter as in the scalar field case so that

$$T^{\mu}{}_{\nu} = \rho \, u^{\mu} u_{\nu} \tag{4.2.13}$$

where

$$\rho = \rho_0 + \delta\rho \tag{4.2.14}$$

and the four-velocity of matter $u^{\mu} = dx^{\mu}/ds$ is

$$u^{\mu} = a^{-1}(1 - \Psi, v^i) \tag{4.2.15}$$

so that

$$u_{\mu} = a(-1 - \Psi, v_i) \tag{4.2.16}$$

where as mentioned before $v_i = \Xi_{ij} v^j$. The velocity perturbation can also be decomposed in a longitudinal and transverse (vorticity) components as

$$v_i = v_i^{\parallel} + v_i^{\perp} \tag{4.2.17}$$

such that in Fourier space

$$\hat{k}^i \, v_i^{\perp} = 0, \tag{4.2.18}$$

$$v_i^{\parallel} = v^{\parallel} \, \hat{k}_i. \tag{4.2.19}$$

Additionally, Bianchi identities imply the conditions (1.4.10). Taking such conditions into account, and contracting the spatial components with $\hat{k}^i$ or $\hat{A}^i$ we obtain the following set of independent scalar equations: $\delta \bar{G}^0{}_0$, $\hat{A}^i \delta \bar{G}^0{}_i$, $\hat{A}^i \hat{A}_j \delta \bar{G}^j{}_i$ and $\delta \bar{G}^i{}_i$. From the vector field equations we have: δL_0, $\hat{k}^i \delta L_i$ and $\hat{A}^i \delta L_i$. Thus we obtain the following seven independent equations,

$$\delta \bar{G}^0{}_0 = -8\pi G \, \rho \, \delta, \tag{4.2.20}$$

$$\hat{A}^i \delta \bar{G}^0{}_i = -8\pi G \, \rho \, \hat{A}^i v_i, \tag{4.2.21}$$

$$\hat{A}_j \hat{A}^i \delta \bar{G}^j{}_i = 0, \tag{4.2.22}$$

$$\delta \bar{G}^i{}_i = 0, \tag{4.2.23}$$

$$\delta L_0 = 0, \tag{4.2.24}$$

$$\hat{k}^i \delta L_i = 0, \tag{4.2.25}$$

$$\hat{A}^i \delta L_i = 0, \tag{4.2.26}$$

for seven variables: Φ, Ψ, δA_0, $\delta A^{\parallel}$, $\bar{Q} \equiv \hat{A}^i Q_i$, $\delta \bar{A}^{\perp} \equiv \hat{A}^i \delta A_i^{\perp}$ and $\bar{h} \equiv \hat{A}^i \hat{A}^j h_{ij}$. If we apply the QSA, the system (4.2.20)-(4.2.26) transforms into an algebraic system for the above variables in terms of the matter variables δ and $\hat{A}^i v_i^{\perp}$ (notice that very much as in the scalar case, the scalar velocity perturbation $v^{\parallel}$ does not contribute to the equations in the QSA),

$$A_{11} \, \Psi + A_{12} \, \Phi + A_{13} \, \bar{Q} + A_{14} \, \bar{h} + A_{15} \, \delta A_0 + A_{16} \, \delta \hat{A}^{\perp} + A_{17} \, \delta A^{\parallel} = -4\pi G \, a^2 \rho \delta, \tag{4.2.27}$$

$$A_{21} \, \Psi + A_{22} \, \Phi + A_{23} \, \bar{Q} + A_{24} \, \bar{h} + A_{25} \, \delta A_0 + A_{26} \, \delta \hat{A}^{\perp} + A_{27} \, \delta A^{\parallel} = 16\pi G \, a^2 \rho \hat{A}^i v_i^{\perp}, \tag{4.2.28}$$

$$A_{m1}\,\Psi + A_{m2}\,\Phi + A_{m3}\,\bar{Q} + A_{m4}\,\bar{h} + A_{m5}\,\delta A_0 + A_{m6}\,\delta\hat{A}^{\perp} + A_{m7}\,\delta A^{\parallel} = 0, \quad m = 3,4,5,6,7 \tag{4.2.29}$$

here we have introduced a $-4\pi G\,a^2$ factor in (4.2.27) and $16\pi G\,a^2$ factor in (4.2.28) for convenience. Here A_{mn} with $m,n = 1\ldots 7$ are assumed to be arbitrary independent functions of background quantities and k where $k^2 = k_i k_j \Xi^{ij}$. Had we made additional assumptions, such as diffeomorphisms invariance of the starting action, a simplification of the system of equations would be possible. However the approach we will follow in this work is to keep the most general expressions for the equations. Solving for δA_0, $\delta A^{\parallel}$ and $\delta\bar{A}^{\perp}$ from (4.2.29) with $m = 5,6,7$ and substituting in the rest of equations we can obtain each perturbation as a general linear function of δ and $\hat{A}^i v_i^{\perp}$. Restoring indices, we have the following effective equations for the metric perturbations,

$$k^2\,\Phi = -4\pi G\,a^2\,\rho\,(\mu_\Phi\,\delta + \eta_\Phi\,\hat{A}^i v_i^{\perp}), \tag{4.2.30}$$

$$k^2\,\Psi = -4\pi G\,a^2\,\rho\,(\mu_\Psi\,\delta + \eta_\Psi\,\hat{A}^i v_i^{\perp}), \tag{4.2.31}$$

$$k^2\,Q_i = 16\pi G\,a^2\,\rho\,(\mu_Q\,\mathcal{A}_i\,\delta + \eta_Q\,v_i^{\perp}), \tag{4.2.32}$$

$$k^2\,h_{ij} = -4\pi G\,a^2\,\rho\,(\mu_h\,\Sigma_{ij}\,\delta + \eta_h\,\Lambda_{ij}), \tag{4.2.33}$$

so that, defining $x \equiv \hat{A}^i\hat{k}_i$, we have

$$\mathcal{A}_i = \hat{A}_i - x\,\hat{k}_i, \tag{4.2.34}$$

$$\Sigma_{ij} = 2\,\mathcal{A}_i\,\mathcal{A}_j - (1-x^2)(\delta_{ij} - \hat{k}_i\,\hat{k}_j), \tag{4.2.35}$$

$$\Lambda_{ij} = 2\,v^{\perp}_{(i}\,\mathcal{A}_{j)} - \frac{(\delta_{ij} - \hat{k}_i\,\hat{k}_j)\,\hat{A}^k v_k^{\perp}}{1-x^2}. \tag{4.2.36}$$

These quantities satisfy the following properties,

$$\hat{k}^i\mathcal{A}_i = 0, \tag{4.2.37}$$

$$\Sigma_{ij} = \Sigma_{ji}, \;\; \hat{k}^i \Sigma_{ij} = 0, \;\; \Sigma^i{}_i = 0, \tag{4.2.38}$$

$$\begin{aligned} &\Lambda_{ij} = \Lambda_{ji}, \;\; \hat{k}^i \Lambda_{ij} = 0, \\ &\Lambda^i{}_i = 0, \;\; \hat{A}^i \hat{A}^j \Lambda_{ij} = \hat{A}^k v^\perp_k. \end{aligned} \tag{4.2.39}$$

With these definitions we see that eight dimensionless parameters ($\mu_\Phi, \eta_\Phi, \mu_\Psi, \eta_\Psi, \mu_Q, \eta_Q, \mu_h, \eta_h$) are needed to parametrize the theory. In General Relativity they take the values $(1,0,1,0,0,1,0,0)$. Notice that if we consider only a temporal component for the background vector field, so that $A_i^{(0)} = 0$ then the number of parameters is reduced to three $(\mu_\Phi, \mu_\Psi, \eta_Q)$, in agreement with previous works [63,185]. In the general case, if dark matter vorticity can be neglected, the number of parameters can be reduced from eight to four and, in this case, we can define the standard (μ, η) parameters as $\mu = \mu_\Psi$ and $\eta = \mu_\Phi/\mu_\Psi$.

In the following we are going to obtain explicit expressions of the complete set of parameters as a function of k and x. With that purpose, we will firstly derive the dependence in k and x of each A_{ij} coefficient of equations (4.2.27), (4.2.28) and (4.2.29). Notice that on general grounds, Einstein and field equations can be classified in three categories: scalar equations $\delta S = \{\delta \bar{G}^0{}_0, \delta L_0\}$, vector equations $\delta V_i = \{\delta \bar{G}^0{}_i, \delta L_i\}$ and tensor equations $\delta \bar{G}^i{}_j$. These equations have the following general structure taking into account the different linear perturbations. For the left hand side of scalar equations we have

$$\begin{aligned} \delta S =& E^\Phi \, \Phi + E^\Psi \, \Psi + E^0 \, \delta A_0 + E^{Q\,i} \, Q_i \\ &+ E^{\perp\, i} \, \delta A_i^\perp + E^{\parallel\, i} \, \delta A_i^\parallel + E^{ij} \, h_{ij} \, . \end{aligned} \tag{4.2.40}$$

For the vector ones

$$\begin{aligned} \delta V_i =& E^\Phi_i \, \Phi + E^\Psi_i \, \Psi + E^0{}_i \, \delta A_0 \\ &+ E^Q \, Q_i + E^\perp \, \delta A_i^\perp + E^\parallel \, \delta A_i^\parallel \\ &+ E^{Q\,j}_i \, Q_j + E^{\perp\, j}_i \, \delta A_j^\perp + E^{\parallel\, j}_i \, \delta A^\parallel{}_j \\ &+ E^{jk}{}_i \, h_{jk} + E^j \, h_{ji} \, , \end{aligned} \tag{4.2.41}$$

and for the tensor one

$$\begin{aligned}\delta\bar{G}^{i}{}_{j} =& E^{\Phi\,i}_{j}\,\Phi + E^{\Psi\,i}_{j}\,\Psi + E^{0\,i}_{j}\,\delta A_0 \\ &+ E^{Q\,i}\,Q_j + E^{\perp\,i}\,\delta A^{\perp}_{j} + E^{\parallel\,i}\,\delta A^{\parallel}_{j} \\ &+ E^{Q}_{j}\,Q^i + E^{\perp}_{j}\,\delta A^{\perp\,i} + E^{\parallel}_{j}\,\delta A^{\parallel\,i} \\ &+ E^{Q\,ik}_{j}\,Q_k + E^{\perp\,ik}_{j}\,\delta A^{\perp}_{k} + E^{\parallel\,ik}_{j}\,\delta A^{\parallel}_{k} \\ &+ E^{T\,ilm}_{j}\,h_{lm} + E^{T\,il}\,h_{lj} + E^{T\,l}_{j}\,h_{l}{}^{i} + E^{T}\,h^{i}{}_{j}\,, \end{aligned} \tag{4.2.42}$$

where taking into account the QSA, the E operators are second order differential operators involving only spatial derivatives. Notice also that for the scalar and vector equations we have different E operators for each equation, but all of them will have the same structure. Thus in Fourier space the most general form of the operators are:

$$E = A_1 + A^{i}_{2}\,k_i + A_3\,k^2 + A_{4\,lm}\,k^l k^m, \tag{4.2.43}$$

$$\begin{aligned} E_i =& B_{1\,i} + B_{2\,i}^{\ j}\,k_j + B_3\,k_i \\ &+ B_{4\,i}\,k^2 + B_{5\,l}\,k^l k_i + B_{6\,i}^{\ jk}\,k_j k_k, \end{aligned} \tag{4.2.44}$$

$$\begin{aligned} E^{i}_{j} =& C_{1\,j}^{\ i} + C_{2\,j}\,k^i + C_{3}^{\ i}\,k_j \\ &+ C_{4\,jl}^{\ i}\,k^l + C_{5\,j}^{\ i}\,k^2 + C_{6\,jlm}^{\ i}\,k^l k^m \\ &+ C_7\,k^i k_j + C^{i}_{8\,l}\,k^l k_j + C^{l}_{9\,j}\,k^i k_l, \end{aligned} \tag{4.2.45}$$

$$\begin{aligned} E^{ik}_{j} =& D_{1\,j}^{\ ik} + D_{2\,j}^{\ k}\,k^i + D^{i}_{3\,j}\,k^k + D_{4}^{\ ik}\,k_j \\ &+ D_{5\,jl}^{\ ik}\,k^l + D_{6\,j}^{\ ik}\,k^2 + D_{7\,jlm}^{\ ik}\,k^l k^m \\ &+ D_{8\,j}\,k^i k^k + D_{9}^{\ i}\,k_j k^k + D_{10}^{\ k}\,k^i k_j \\ &+ D^{k}_{11\,jl}\,k^l k^i + D^{i}_{12\,jl}\,k^l k^k + D^{ik}_{13\,l}\,k^l k_j. \end{aligned} \tag{4.2.46}$$

$$\begin{aligned} E^{ilm}_{\ \ j} =& F_{1\ \ j}^{\ ilm} + F_{2\ \ j}^{\ ilmn}\,k_n + F_{3\ \ j}^{\ il\ \ m} \\ &+ F_{4\ \ j}^{\ im\ \ l}\,k^l + F_{5\ \ j}^{\ lm\ \ i}\,k^i + F_{6}^{\ ilm}\,k_j \\ &+ F_{7\ \ j}^{\ ilmkn}\,k_k k_n + F_{8\ \ j}^{\ iln\ \ m}\,k_n k^m + F_{9\ \ j}^{\ imn\ \ l}\,k_n k^l \\ &+ F_{10\ \ j}^{\ lmn\ \ i}\,k_n k^i + F_{11}^{\ ilmn}\,k_n k_j + F_{12\ \ j}^{\ m\ \ il}\,k^i k^l \\ &+ F_{13\ \ j}^{\ l\ \ im}\,k^i k^m + F_{14}^{\ lm}\,k^i k_j + F_{15\ \ j}^{\ i\ \ lm}\,k^l k^m \\ &+ F_{16}^{\ im}\,k^l k_j + F_{17}^{\ il}\,k^m k_j + F_{18\ \ j}^{\ ilm}\,k^2\,, \end{aligned} \tag{4.2.47}$$

where A, B, C, D and F coefficients are in general functions of background quantities (depending only on time) and their indices only come from the vector field $A_i^{(0)}$ and the $\delta^i{}_j$ tensor in all possible combinations. Once we have the form of the l.h.s of (4.2.20)-(4.2.26), we can obtain the most general form of the A_{ij} coefficients from the scalar equations and from the equations obtained by contracting the vector type equations as $\hat{A}^i\delta V_i$ and the tensor one as $\hat{A}^i\hat{A}_j\delta\bar{G}^j{}_i$. We summarize in Table 4.1 the general structure of each coefficient.

We can now solve the system of equations (4.2.27), (4.2.28) and (4.2.29), and obtain the coefficients for $\{\Phi, \Psi, \bar{Q}, \bar{h}\}$ in terms of δ and $\hat{A}^i v_i^{\perp}$ which leads to equations (4.2.30)-(4.2.33). We have to notice that apart from k, the other dimensional (comoving) scales appearing in the E operators are the Hubble rate $\mathcal{H}$ and the mass scale of the vector field. Unlike the usual assumptions in modified gravities with scalar degrees of freedom [65, 187], there is no general argument with which we can determine the dependence of each parameter $A \ldots F$ on $\mathcal{H}$ or on the vector mass. Moreover, the comoving mass scale could be of order $\mathcal{H}$ due to the background equations. For these reasons, we cannot a priori neglect any of the A_{ij} terms and we will consider two generic cases: a) we consider the general case in which we keep all the terms in the E operators and b) we assume that all the dimensional parameters of the E coefficients are of order $\mathcal{H}$ or $\mathcal{H}^2$ so that the corresponding terms can be neglected compared to the k^2 terms in the sub-Hubble limit.

A_{ij} for i, j = 1, ... 6	$b_1 + b_2\, x\, k + (b_3 + b_4\, x^2)\, k^2$
A_{7i}, A_{i7} for i = 1, ... 6	$b_1\, x + (b_2 + b_3\, x^2)\, k + (b_4 + b_5\, x^2)\, x\, k^2$
A_{77}	$b_1 + b_2\, x^2 + (b_3 + b_4\, x^2)\, x\, k + (b_5 + b_6\, x^2 + b_7\, x^4)\, k^2$

Table 4.1: Generic structure of the A_{ij} coefficients of the system of equations (4.2.20). Notice that for every A_{ij} coefficient the corresponding $b_\alpha(a)$ are different functions of time only.

a) General case:

We find the following form for the parameters

$$\begin{aligned} M(a,k,x) &= \frac{[P_M^{14}(a,k,x) + P_M^{12}(a,k,x)\, xk]\; k^2}{P_D^{16}(a,k,x) + P_D^{14}(a,k,x)\, xk} \\ \text{with } M &= \mu_\Phi, \mu_\Psi, \eta_\Phi, \eta_\Psi, \eta_Q, \eta_h \end{aligned} \tag{4.2.48}$$

whereas for μ_Q and μ_h we obtain,

$$\mu_Q(a,k,x) = \frac{\left[P^{14}_{\mu_Q}(a,k,x) + P^{12}_{\mu_Q}(a,k,x)\,xk\right]\,k^2}{[P^{16}_D(a,k,x) + P^{14}_D(a,k,x)\,xk]\,(1-x^2)}, \tag{4.2.49}$$

$$\mu_h(a,k,x) = \frac{\left[P^{14}_{\mu_h}(a,k,x) + P^{12}_{\mu_h}(a,k,x)\,xk\right]\,k^2}{[P^{16}_D(a,k,x) + P^{14}_D(a,k,x)\,xk]\,(1-x^2)^2}, \tag{4.2.50}$$

where we have defined the following function,

$$P^n_A(a,k,x) = \sum_{i=1}^{n/2}\sum_{j=0}^{i} p^{(A)}_{ij}(a)\,x^{2j}\,k^{2i}, \tag{4.2.51}$$

being $p^{(A)}_{ij}(a)$ functions of background quantities and we define $P^n_A(a,x) \equiv P^n_A(a,1,x)$ which are polynomials of order n with only even powers of x. Notice also that the polynomials in the numerators are in general different for the different parameters, whereas those in the denominators $P^{14}_D(a,k,x)$ and $P^{16}_D(a,k,x)$ are the same for all of them as they come from the inverse of the determinant corresponding to the system of linear equations [65].

Notice that if we take $x = 0$ i.e. we neglect the anisotropic contributions coming from the spatial components of the background vector field in equation (4.2.48) we get

$$M(a,x,k) = \frac{k^2\,P^{12}_M(a,k)}{P^{14}_D(a,k)}, \tag{4.2.52}$$

i.e. the ratio of two degree-fourteen polynomials in k. We could have anticipated that in this case the result should agree with that corresponding to two scalar degrees of freedom (which can be identified with δA_0 and $\delta A^{\parallel}$). But we see that this is not the case because, unlike the scalar case, we did not neglect k-independent terms in the E expressions. Only if we neglect k-independent terms in all equations, except for those of the vector field perturbations in the vector field equations, we recover the scalar field case:

$$M(a,x,k) = \frac{P^4_M(a,k)}{P^4_D(a,k)}. \tag{4.2.53}$$

b) Coefficients of order $\mathcal{H}$:

If we consider the dimensional coefficients of the E operators to be of order $\mathcal{H}$ and take the sub-Hubble limit, so that only k^2 terms survive, we obtain,

$$\begin{aligned} M(a,x,k) &= \frac{P^{14}_M(a,x)}{P^{16}_D(a,x)}, \\ \text{for} \quad M &= \mu_\Phi, \mu_\Psi, \eta_\Phi, \eta_\Psi, \eta_Q, \eta_h \end{aligned} \tag{4.2.54}$$

and

$$\mu_Q = \frac{P^{14}_{\mu_Q}(a,x)}{(1-x^2)P^{16}_D(a,x)}, \tag{4.2.55}$$

$$\mu_h = \frac{P^{14}_{\mu_h}(a,x)}{(1-x^2)^2P^{16}_D(a,x)}. \tag{4.2.56}$$

As we can see, the expressions are scale independent. If we expand them in multipoles we only have even powers of x, odd powers are suppressed in the sub-Hubble limit. Thus, for small anisotropy, $A \ll A_0^{(0)}$, we can find an expansion for any of the eight parameters (that we denote as β) of the form,

$$\beta(a,x) = \beta_0(a) + \beta_2(a)\,x^2 + \beta_4(a)\,x^4 + O(x^6), \tag{4.2.57}$$

where $\beta_0(a)$ provides the isotropic contribution. In particular we can find this kind of expansion for the standard parameter μ and, without vorticity, also for the parameter η.

As the main result of this section we have found that a general modified gravity theory with a vector degree of freedom, and neglecting dark matter vorticity, can be described with four modified gravity parameters in the QSA approximation and the sub-Hubble regime. In addition, these modified gravity parameters have an extra dependence on $x = \hat{\mathbf{k}} \cdot \hat{\mathbf{A}}$ so the growth evolution is anisotropic in general. In the following sections, we will analyze the effect of this anisotropic growth in the galaxy survey observables.

4.3 Imperfect and non-conserved dark matter models

As we have seen before, ΛCDM model has some observational tensions. Some of those tensions are related with the standard CDM and could indicate an interaction in the dark sector or an imperfect behavior of dark matter. In this sense, in addition to the high variety of dark energy and modified gravity models, there are also several proposals for imperfect and non-conserved dark matter. These models can be classified into three main types: interacting dark sector models [31, 32], models of an imperfect fluid with bulk and shear viscosity [29, 30, 188], and models of an imperfect fluid with heat flux. There are different approaches for interacting models but in most of them, the interaction term is assumed proportional to the dark matter or dark energy densities [189]. These interacting models

have been proved to be compatible with current observations [190, 191]. On the other hand, imperfect fluid models for dark matter have been considered as possible solutions to the small-scale problems of CDM [29]. Regarding models with bulk viscosity, it has been shown that they can generate a negative pressure contribution that can accelerate the universe expansion [192, 193]. Nevertheless, if we consider it as the only contribution to the late-time acceleration, we find problems and it seems necessary to include dark energy [194,195]. Finally, models of dark matter with heat flux are proposed in the context of two interacting fluids [196] and the Generalised Dark Matter (GDM) model [197]. This last approach considers a general energy-momentum tensor for dark matter with bulk and shear viscosities. The main difference with the three previous types of models is that, in the GDM approach, a general equation of state for dark matter is considered [198, 199].

Due to the interest of considering this type of models, we will generalize the standard phenomenological parametrization for the case in which, in addition to modified gravity, we include an imperfect and non-conserved dark matter fluid. As in the vector case, we assume the QSA approximation and the sub-Hubble regime. In general, the energy-momentum tensor for an imperfect presureless non-conserved fluid reads [200],

$$T_{\mu\nu} = T^{pf}_{\mu\nu} + T^{vis}_{\mu\nu} + T^{h}_{\mu\nu}, \tag{4.3.1}$$

with,

$$T^{pf}_{\mu\nu} = \rho\, u_\mu u_\nu, \tag{4.3.2}$$

$$T^{vis}_{\mu\nu} = -\xi\, \Theta\, h_{\mu\nu} - 2\,\tilde{\eta}\, \sigma_{\mu\nu}, \tag{4.3.3}$$

$$T^{h}_{\mu\nu} = q_\mu u_\nu + q_\nu u_\mu, \tag{4.3.4}$$

being,

$$\sigma_{\mu\nu} = \frac{1}{2}\left(h^{\alpha}_{\ \mu}\, \nabla_\alpha u_\nu + h^{\alpha}_{\ \nu}\, \nabla_\alpha u_\mu\right) - \frac{1}{3}\,\Theta\, h_{\mu\nu}, \tag{4.3.5}$$

$$h_{\mu\nu} = g_{\mu\nu} + u_\mu u_\nu, \tag{4.3.6}$$

$$\Theta = \nabla_\alpha u^\alpha. \tag{4.3.7}$$

Here q_μ is a general energy current, ξ is the bulk viscosity parameter and $\tilde{\eta}$ is the shear viscosity parameter. Finally, we will consider that, due to a possible interaction between dark matter and another species (like dark energy), this energy-momentum tensor is not conserved then,

$$\nabla_\mu T^\mu_\nu = Q_\nu. \tag{4.3.8}$$

The interaction term is usually a purely temporal four-vector but we will also consider spatial perturbations. The aim of the following section will be to generalize the conservation equations (1.4.26) and (1.4.27) to take into account a general modification due to an imperfect and non-conserved dark matter fluid. Then we will prove that to describe these type of models in a phenomenological way, we need three new effective parameters in addition to the standard μ and η parameters.

4.4 Parametrizing non-standard dark matter models

Here we will set the most general form of the conservation equations of dark matter in order to describe in a model-independent way an imperfect and non-conserved dark matter fluid. Then, we find that we need five parameters to characterize a general modification of gravity and dark matter conservation equations. Finally we will obtain the general form of these parameters for the three possible type of models: a fluid with bulk and shear viscosities, a fluid with heat flux and a non-conserved fluid.

We start by modifying equations (1.4.26) and (1.4.27) in a general way. We can consider also a general modification of gravity with scalar degrees of freedom which can be encoded in μ and η parameters via equations (1.4.14) and (1.4.15). Because the scalar perturbations are $(\theta, \delta, \Psi, \Phi)$, the most general way we can modify (1.4.26) and (1.4.27) is,

$$\delta' = -c_{11}\,\theta + c_{12}\,\mathcal{H}\delta + c_{13}\,\mathcal{H}\Psi + c_{14}\,\mathcal{H}\Phi, \tag{4.4.1}$$

$$\theta' = -c_{21}\,\mathcal{H}\theta + c_{22}\,\mathcal{H}^2\delta + c_{23}\,k^2\Psi + c_{24}\,k^2\Phi. \tag{4.4.2}$$

Considering this parametrization, c_{ij} are in general dimensionless functions of time and scale, and we recover the standard case when $c_{11} = c_{21} = c_{23} = 1$ and $c_{ij} = 0$ for the rest of i, j. We could have other scalar degrees of freedom with perturbations δq_i but, in this situation, we would also have equations for these degrees of freedom and we could find the relations $\delta q_i = \delta q_i(\theta, \delta, \Psi, \Phi)$. Then we can always find equations of the form of (4.4.1-4.4.2).

Now, we derive equation (4.4.1) with respect to the conformal time. Using (4.4.1) and (4.4.2) and considering the modified gravity equations (1.4.14-1.4.15) we obtain,

$$\delta'' + \mathcal{H}\,\mu_d\,\delta' - \frac{3}{2}\,\mathcal{H}^2\,\Omega_m(a)\,\mu_m\,\delta = 0, \tag{4.4.3}$$

being,

$$\mu_m = c_{11}\,\mu\,\left(c_{23} - \frac{\mathcal{H}^2}{k^2}\,\mathcal{C}_3 + \eta\,\left[c_{24} - \frac{\mathcal{H}^2}{k^2}\,\mathcal{C}_4\right]\right) - \frac{2c_{11}}{3\Omega_m(a)}\,\left(c_{22} - \mathcal{C}_2\right), \tag{4.4.4}$$

$$\mu_d = c_{21} - c_{12} - \frac{c_{11}'}{\mathcal{H}\,c_{11}}, \tag{4.4.5}$$

with,

$$\mathcal{C}_i \equiv \frac{c_{1i}}{c_{11}}\,\left[c_{21} - \frac{c_{11}'}{\mathcal{H}\,c_{11}} + \frac{\mathcal{H}'}{\mathcal{H}^2} + \frac{c_{1i}'}{\mathcal{H}\,c_{1i}}\right]. \tag{4.4.6}$$

As we can see, if we want to parametrize the density contrast evolution, we need only two independent parameters (μ_m, μ_d). On the other hand, in order to obtain the velocity perturbation θ as a function of the matter density contrast δ, we can rewrite equation (2.2.1) in the following form,

$$\theta = -\mu_\theta\,\delta', \tag{4.4.7}$$

where,

$$\mu_\theta = \frac{1}{c_{11}} - \frac{\mathcal{H}\,\delta}{c_{11}\,\delta'}\left[c_{12} - \frac{3}{2}\frac{\mathcal{H}^2}{k^2}\,\Omega_m(a)\,\mu\,(c_{13} + \eta\,c_{14})\right]. \tag{4.4.8}$$

Here δ and δ' are obtained from the solutions of (1.4.29). Thus we see that in order to describe the general modified system of equations for matter and gravity perturbations, we need in total five effective parameters $(\mu, \eta, \mu_m, \mu_d, \mu_\theta)$. Notice that now, the presence of an imperfect dark matter implies that, in general, the effective Newton constant that controls the growth of matter perturbations given by μ_m may be different from the effective constant that light sees, which is given by the combination $\eta(1+\mu)/2$, even when $\eta = 1$.

In the following section we will prove that a very broad class of models can be parametrized with these five parameters.

4.4.1 Dark matter with bulk and shear viscosity

In this first case, we consider only the viscosity term so that $T_{\mu\nu} = T^{pf}_{\mu\nu} + T^{vis}_{\mu\nu}$ and assume it is conserved. We consider a general perturbation in the bulk and shear viscosities,

$$\xi(\tau, \mathbf{x}) = \xi_{\mathbf{0}}(\tau) + \delta\xi(\tau, \mathbf{x}), \tag{4.4.9}$$

$$\tilde{\eta}(\tau, \mathbf{x}) = \tilde{\eta}_{\mathbf{0}}(\tau) + \delta\tilde{\eta}(\tau, \mathbf{x}). \tag{4.4.10}$$

These perturbations can be related with the matter density contrast by the following definition,

$$\delta\xi \equiv \frac{a\rho}{\mathcal{H}}\,\xi_p\,\delta, \tag{4.4.11}$$

$$\delta\tilde{\eta} \equiv \frac{a\rho}{\mathcal{H}}\,\eta_p\,\delta, \tag{4.4.12}$$

where ξ_p and η_p are arbitrary dimensionless functions of time and scale, and the prefactors $a\rho/\mathcal{H}$ are introduced for convenience. Then the conservation equations take the form of

(4.4.1-4.4.2) with,

$$\begin{aligned} c_{11} &= 1-6\bar{\xi}, \quad c_{12} = 9(\xi_p - \bar{\xi}), \quad c_{13} = 9\bar{\xi}, \\ c_{21} &= \frac{1}{1-3\bar{\xi}}\left[1 - 27\bar{\xi}^2 + 6\bar{\xi} - 3\,\frac{\bar{\xi}'}{\mathcal{H}} + \left(\frac{4}{3}\bar{\eta} + \bar{\xi}\right)\,\frac{k^2}{\mathcal{H}^2}\right], \\ c_{22} &= -\frac{3\xi_p}{1-3\bar{\xi}}\,\frac{k^2}{\mathcal{H}^2}, \quad c_{23} = \frac{1}{1-3\bar{\xi}}, \quad c_{14} = c_{24} = 0, \end{aligned} \tag{4.4.13}$$

being,

$$\bar{\xi} = \frac{\mathcal{H}\xi_0}{a\rho}, \quad \bar{\eta} = \frac{\mathcal{H}\tilde{\eta}_0}{a\rho}. \tag{4.4.14}$$

Notice that in order to avoid large modifications, in the sub-Hubble regime, $\bar{\xi}, \xi_p, \bar{\eta} \ll 1$. In this situation,

$$\begin{aligned} c_{21} &= 1 + \left(\frac{4}{3}\bar{\eta} + \bar{\xi}\right)\,\frac{k^2}{\mathcal{H}^2}, \quad c_{22} = -3\xi_p\,\frac{k^2}{\mathcal{H}^2}, \\ c_{11} &= c_{23} = 1, \quad c_{12} = c_{13} = c_{14} = c_{24} = 0, \end{aligned} \tag{4.4.15}$$

using these expressions and relations (4.4.4-4.4.7) we obtain,

$$\mu_m = \mu + \frac{2\xi_p}{\Omega_m(a)}\,\frac{k^2}{\mathcal{H}^2}, \tag{4.4.16}$$

$$\mu_d = 1 + \left(\frac{4}{3}\bar{\eta} + \bar{\xi}\right)\,\frac{k^2}{\mathcal{H}^2}, \tag{4.4.17}$$

$$\mu_\theta = 1. \tag{4.4.18}$$

Notice that, using (4.4.16) in (1.4.29), an effective sound speed $c_s^2 = 3\xi_p$ appears for dark matter.

4.4.2 Dark matter with heat flux

Now we consider only the heat flux contribution so that $T_{\mu\nu} = T^{pf}_{\mu\nu} + T^{h}_{\mu\nu}$ and assume it is conserved. As we are considering an isotropic background, the perturbed heat flux is in general,

$$q_\mu = \left[q_0(\tau) + \delta q_0(\tau, \mathbf{x}), \delta q_i(\tau, \mathbf{x})\right]. \tag{4.4.19}$$

Again we can always relate these perturbations to the dark matter perturbations in the following way,

$$\delta q_0 \equiv q_d \, a\rho \, \delta, \tag{4.4.20}$$

$$\delta q_i \equiv q_v \, a\rho \, v_i, \tag{4.4.21}$$

where q_d and q_v are arbitrary dimensionless functions of time and scale. The conservation equations take also the form of (2.2.1-2.2.2) with,

$$\begin{aligned}
c_{11} &= \frac{1}{1-2q_d}\left[1+q_v-\bar{q}_0\right], \\
c_{12} &= \frac{2}{1-2q_d}\left[\frac{q_d'}{\mathcal{H}}+\left(2+\frac{(a\rho)'}{\mathcal{H}a\rho}\right)q_d\right. \\
&\left.-\frac{\bar{q}_0'}{\mathcal{H}}-\left(2+\frac{(a\rho)'}{\mathcal{H}a\rho}\right)\bar{q}_0\right], \\
c_{13} &= -\frac{2}{1-2q_d}\left[\frac{\bar{q}_0'}{\mathcal{H}}+\left(2+\frac{(a\rho)'}{\mathcal{H}a\rho}\right)\bar{q}_0\right], \\
c_{21} &= \frac{1}{1+q_v-q_0}\left[1+\frac{q_v'}{\mathcal{H}}+\left(3+\frac{(a\rho)'}{\mathcal{H}a\rho}\right)q_v\right. \\
&\left.+\frac{\bar{q}_0'}{\mathcal{H}}+\left(1+\frac{(a\rho)'}{\mathcal{H}a\rho}\right)\bar{q}_0\right], \\
c_{23} &= \frac{1}{1+q_v-q_0}\left[1-2\bar{q}_0\right], \\
c_{14} &= c_{22} = c_{24} = 0,
\end{aligned} \tag{4.4.22}$$

being $\bar{q}_0 = q_0/a\rho$. Then we can use equations (4.4.4-4.4.7) and obtain μ_m, μ_d and μ_θ that are in general different from one. They are lengthy expressions which we do not show explicitly.

4.4.3 Non-conserved dark matter

Finally, we consider that the energy-momentum tensor is not conserved in general. This may be due to an interaction between dark matter and dark energy. We perturb the Q_μ four-vector considering an isotropic background,

$$Q_\mu = \left[Q_0(\tau) + \delta Q_0(\tau, \mathbf{x}), \delta Q_i(\tau, \mathbf{x})\right]. \tag{4.4.23}$$

We relate these perturbations with the dark matter perturbations in the following way,

$$\delta Q_0 \equiv \nu_0 \, \rho \mathcal{H} \, \delta, \tag{4.4.24}$$

$$\delta Q_i \equiv \nu_v \, \rho \mathcal{H} \, v_i, \tag{4.4.25}$$

where ν_0 and ν_v arbitrary dimensionless functions of time and scale. The c_{ij} coefficients of equations (4.4.1-4.4.2) are,

$$\begin{aligned} &c_{12} = x - \nu_0, \quad c_{21} = 1 - x - \nu_v, \\ &c_{11} = c_{23} = 1, \;\; c_{13} = c_{14} = c_{22} = c_{24} = 0, \end{aligned} \tag{4.4.26}$$

with $x = Q_0/\mathcal{H}\rho$. If we use equations (4.4.4-4.4.7) we obtain,

$$\begin{aligned} \mu_m = \mu + \frac{2}{3\,\Omega_m(a)} \, \Big[&\nu_0 \, \nu_v - x \, \nu_v - (1-x) \, (\nu_0 - x) \\ &+ \frac{(\mathcal{H}x)'}{\mathcal{H}^2} - \frac{(\mathcal{H}\nu_0)'}{\mathcal{H}^2} \Big], \end{aligned} \tag{4.4.27}$$

$$\mu_d = 1 + \nu_0 - \nu_v - 2\,x, \tag{4.4.28}$$

$$\mu_\theta = 1 - \frac{\mathcal{H}\,\delta}{\delta'} \, (x - \nu_0). \tag{4.4.29}$$

To summarize what we have shown in the last subsections, a general model for an imperfect non-conserved fluid in a modified gravity scenario can be described with parameters $(\mu, \gamma, \mu_m, \mu_d, \mu_\theta)$. The corresponding modified gravity and modified dark matter equations are,

$$k^2 \, \Phi = -\frac{3}{2} \, \mathcal{H}^2 \, \Omega_m(a) \mu \, \eta \, \delta, \tag{4.4.30}$$

$$k^2\,\Psi = -\frac{3}{2}\,\mathcal{H}^2\,\Omega_m(a)\mu\,\delta, \tag{4.4.31}$$

$$\delta'' + \mathcal{H}\,\mu_d\,\delta' - \frac{3}{2}\,\mathcal{H}^2\,\Omega_m(a)\,\mu_m\,\delta = 0, \tag{4.4.32}$$

$$\theta = -\mu_\theta\,\delta'. \tag{4.4.33}$$

4.5 Growth function analytical parametrizations

Once we have described how to parametrize modifications of gravity and dark matter in different cases, we have to resolve the evolution equations of matter perturbations (1.4.29) and (4.4.32). Although it is always possible to resolve them numerically, it is interesting to find analytical approximations to use in data analysis. Instead of obtaining analytical solutions for δ, it is easier to change from δ to the growth function $f(a)$ defined in (2.2.19). Notice that, with this change, we have to analyze a first order differential equation. In the case of ΛCDM, a good approximation for the growth function is given by,

$$f_\Lambda(a) = \Omega_m^\gamma(a), \tag{4.5.1}$$

where γ is known as the growth index which has a value in ΛCDM of $\gamma_* \simeq 0.55$ [201, 202]. This expression provides accuracies below 0.25% which allows it to be used in the data analysis of present and future surveys such as J-PAS [66], DESI [67] or Euclid [68] which will be able to measure $f(z)$ with precision around $1-3\%$ depending on the survey and the redshift bin.

In the modified gravity case, (4.4.33) does not necessarily provide a good fit of the growth function and different alternatives have been considered in the literature, mainly focused on the modification of the growth index. Such alternative expressions have been obtained on a case by case basis and to the best of our knowledge no model-independent analysis has been performed so far. Here, the purpose is to determine accurate fitting functions for the modified growth function in terms of the phenomenological parameters discussed before. We will start with the simplest case in which dark matter is a perfect

and conserved fluid, so the conservation equation follows (1.4.29). Finally, we will look at the most general case for a imperfect and non-conserved dark matter fluid so that the conservation equation follows (4.4.32).

4.5.1 Time-independent case $\mu = \mu(k)$

We start by studying the simplest case in which $\mu\,(a,\,k) = \mu(k)$ does not depend on the scale factor. Although in general for modified gravities with extra scalar or vector degrees of freedom we expect both time and scale dependence of the μ factor, the time-independent case can be used for phenomenological parametrizations of the effective Newton constant at different length scales. This is also the case in scalar-tensor models as [203] in which G_{eff} rapidly tends to a constant at high redshift. In this simple case, we can develop an analytical study. Making the change of variable from δ to f in equation (1.4.29) we have,

$$\dot{f} + f^2 + \left(2 + \frac{\dot{H}}{H}\right) f - \frac{3}{2}\,\mu\,(k)\,\Omega_m(a) = 0, \tag{4.5.2}$$

where dots denote derivatives with respect to $N \equiv \ln a$. Let us first assume for simplicity a ΛCDM background. Later on we will consider a more general case with time-dependent effective equation of state for the dark energy or modified gravity extra components. The Hubble parameter in ΛCDM reads,

$$H(a) = H_0\,\sqrt{\Omega_m\,a^{-3} + \Omega_\Lambda}, \tag{4.5.3}$$

with this expression and taking into account the definition of $\Omega_m(a)$ as a function of H (1.1.8), we can obtain,

$$\frac{\dot{H}}{H} = -\frac{3}{2}\,\Omega_m(a), \tag{4.5.4}$$

and

$$\dot{\Omega}_m(a) = -3\,\Omega_m(a)\,(1 - \Omega_m(a)). \tag{4.5.5}$$

Inspecting the numerical solutions of (4.5.2), we can see that a parametrization that provides a good fit is of the form,

$$f(a, k) = \beta(k)\,\Omega_m^{\gamma(k)}(a), \tag{4.5.6}$$

where for each Fourier mode, $\beta(k)$ and $\gamma(k)$ are in general the constants to adjust. This parametrization type was considered in [204] for the particular case of a scalar-tensor theories. Using equations (4.5.4) and (4.5.5) together with (4.5.6) in equation (4.5.2) we have,

$$(2-3\gamma)\,\Omega_m^{\gamma-1}(a)+\left(3\gamma-\frac{3}{2}\right)\,\Omega_m^{\gamma}(a)+\beta\,\Omega_m^{2\gamma-1}(a)-\frac{3}{2}\,\frac{\mu}{\beta}=0. \tag{4.5.7}$$

Although this expression can be satisfied exactly only in the case in which $\Omega_m(a)=\Omega_m$ is a constant, as commented before, it is possible to obtain approximate solutions in the general case. Thus, for example, substituting $\mu=\beta=1$, we recover the case of ΛCDM so that for $\gamma=\gamma_*$ equation (4.5.7) is satisfied so that,

$$(2-3\gamma_*)\,\Omega_m^{\gamma_*-1}(a)+(3\gamma_*-3/2)\,\Omega_m^{\gamma_*}(a)+\Omega_m^{2\gamma_*-1}(a)-\frac{3}{2}\simeq 0, \tag{4.5.8}$$

Thus, if we take $\gamma=\gamma_*$ in the case with μ and β different from one, we get from (4.5.7) and (4.5.8)

$$3\left(1-\frac{\mu}{\beta}\right)+2(\beta-1)\,\Omega_m^{2\gamma_*-1}(a)\simeq 0. \tag{4.5.9}$$

We consider a final approximation. Since $\gamma_*\simeq 1/2$, we assume that $\Omega_m^{2\gamma_*-1}(a)\simeq 1$. Thus we are able to find a relationship between μ and β,

$$\beta=\frac{1}{4}\,\left[\sqrt{1+24\,\mu}-1\right]. \tag{4.5.10}$$

Therefore, we have an analytic expression which is an approximate solution of equation (4.5.2) for redshift-independent $\mu(k)$

$$f(a,k)=\frac{1}{4}\,\left[\sqrt{1+24\,\mu(k)}-1\right]\,\Omega_m^{\gamma_*}(a). \tag{4.5.11}$$

The error of this approximation generally depends on the scale factor and reaches a maximum at $a=1$ as discussed below. In Fig. 4.1, we plot the maximum error as a function of μ for $\Omega_m=0.271$. We have taken this particular value in order to compare with previous works although we have checked that the results remain unchanged in the range $\Omega_m=0.27-0.31$ which includes the latest Planck value [13]. The error corresponds to the difference between the fitting function and the numerical solution of (4.5.2) divided by

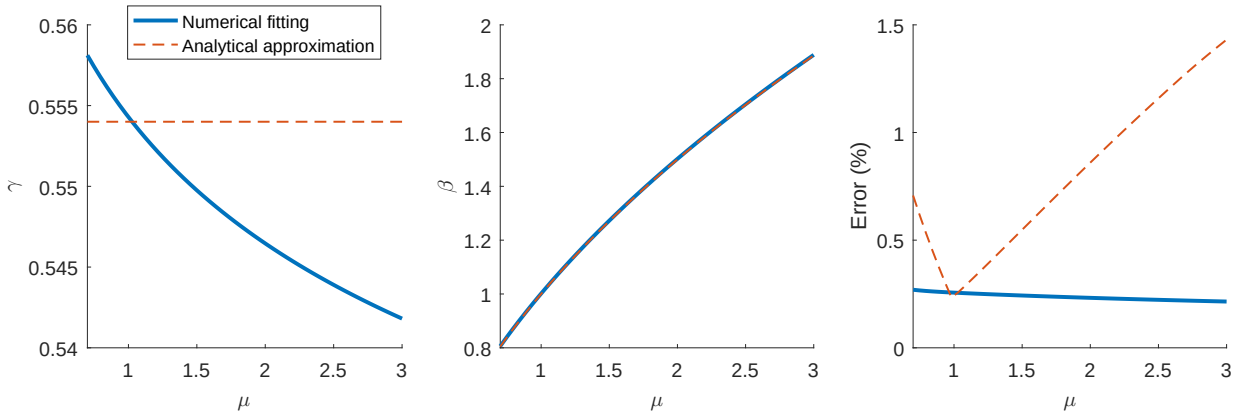

Figure 4.1: From left to right: γ, β and relative error in the growth function as a function of μ. The dashed red line corresponds to analytical approximation in (4.5.11) with $\gamma = \gamma_*$ and β in (4.5.10). The continuous blue line, corresponds to the numerical fitting of β and γ to expression (4.5.13).

their average value. We can see that the error is always below 2%. Notice that we have considered a wide range of μ values, although relatively small deviations from $\mu = 1$ could generate a large integrated Sachs-Wolfe effect.

It is however possible to improve the fit if we allow also the growth index γ to depend on μ. In this case, it is possible to find a good agreement with

$$\gamma\left(\mu\right) = \frac{1}{2} + \frac{0.161}{1.967 + \beta\left(\mu\right)}, \tag{4.5.12}$$

with $\beta(\mu)$ given in (4.5.10). In Fig. 4.1 we plot this relation together with the error corresponding to the improved growth function

$$f(a,k) = \frac{1}{4}\left[\sqrt{1+24\,\mu(k)} - 1\right]\,\Omega_m^{\gamma(\mu(k))}(a). \tag{4.5.13}$$

We can see that in this case, the maximum error can be below 0.25%. Also, we see that for GR ($\mu = 1$), we obtain $\gamma_* = 0.554$ as the value for the best fit, which is slightly different from that quoted in [201] ($\gamma_* = 0.550$). In order to understand the difference, we analyze the error in three different functions, $f(z)$, $\delta(z)$ and $f(z)\delta(z)$ (see also [205]). As we can see in Fig. 4.2, the error in $f(z)$ is larger for low redshift than the error in $\delta(z)$, but in general the errors for the three functions are of the same order. Notice that the value $\gamma_* = 0.554$ minimizes the error in $f(z)$, however, the error in $\delta(z)$ is minimized by $\gamma_* = 0.550$ [201].

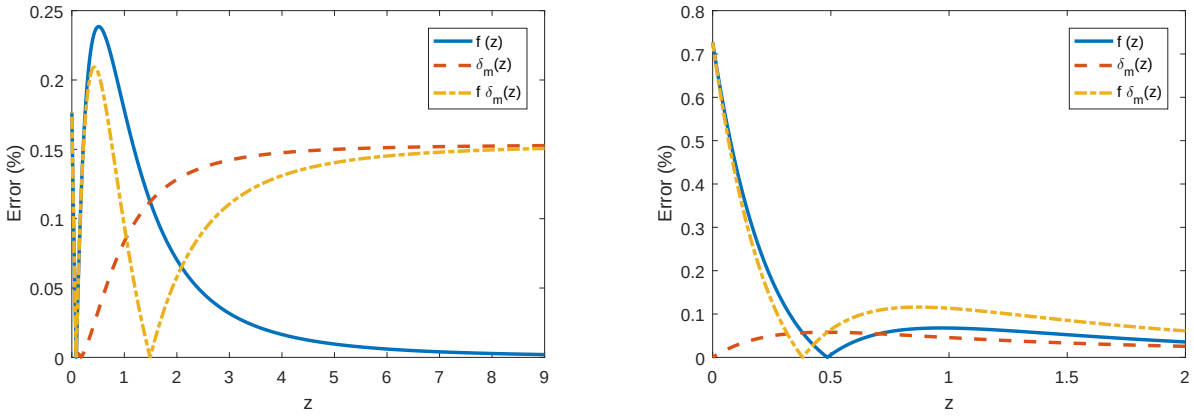

Figure 4.2: Errors for $f(z)$, $\delta(z)$ and $f(z)\delta(z)$ in ΛCDM using $\gamma_* = 0.554$ (left) and $\gamma_* = 0.550$ (right). We see that for $\gamma_* = 0.554$ the error in $f(z)$ is below 0.25% but that in $\delta(z)$ reaches 0.15%, whereas for $\gamma_* = 0.550$, the error in $\delta(z)$ can be reduced below 0.05%, however the corresponding error for $f(z)$ grows to 0.7%.

This value also minimizes the error both in $f(z)$ and $f(z)\delta(z)$ for $z > 0.4$ Since the error in the observable $f(z)\sigma_8(z)$ is dominated by the error in $f(z)$ we have taken $\gamma_* = 0.554$ as our reference value in this thesis. On the other hand, at early times, in the matter dominated era, $\Omega_m(a) \simeq 1$ and equation (4.5.2) can be solved exactly

$$f(a,k) = \frac{1}{4}\left[\sqrt{1+24\,\mu(k)} - 1\right], \tag{4.5.14}$$

therefore $f(a,k)$ is just constant in time. The fitting function (4.5.11) exactly agrees with this result for $\Omega_m(a) = 1$ and this is the reason why the error increases as we move away from the matter era. Thus for matter domination the density contrast grows as

$$\delta(a,k) \propto a^{\frac{1}{4}\left[\sqrt{1+24\,\mu(k)}-1\right]}, \tag{4.5.15}$$

in agreement with [203,206]. This implies that if we want to preserve the growth of density contrast proportional to the scale factor in the matter era, μ should depend on the scale factor and tend to unity at early times.

Beyond the ΛCDM background

We now consider modifications of the background expansion. In order to keep the approach model-independent, we will parametrize them with an extra component $\Omega_{DE}(a)$

with arbitrary equation of state $\omega_{DE}(a)$. This extra component could correspond directly to dark energy or to the effective fluid description of the modified gravity. At late times, i.e. neglecting the radiation contribution, we can write

$$H(a) = H_0 \sqrt{\Omega_m \, a^{-3} + \Omega_{DE}(a)}, \tag{4.5.16}$$

with

$$\Omega_{DE}(a) = \Omega_{DE} \, \exp\left(\int_0^a \frac{3(1+\omega_{DE}(\hat{a}))}{\hat{a}} d\hat{a} \right). \tag{4.5.17}$$

Using (4.5.16) to obtain $\Omega_m(a)$, we get the expressions that replace (4.5.4) and (4.5.5),

$$\frac{\dot{H}}{H} = -\frac{3}{2}\,\Omega_m(a) + \frac{\Omega_m(a)}{2\,\Omega_m}\, a^3\, \dot{\Omega}_{DE}(a), \tag{4.5.18}$$

and

$$\dot{\Omega}_m(a) = -3\,\Omega_m(a)\,(1-\Omega_m(a)) - \frac{\Omega_m^2(a)}{\Omega_m}\, a^3\, \dot{\Omega}_{DE}(a). \tag{4.5.19}$$

Following the same procedure as above, we obtain the analogous equation to (4.5.7) with an extra term,

$$\begin{aligned} &(2-3\gamma)\,\Omega_m^{\gamma-1}(a) + \left(3\gamma - \frac{3}{2}\right)\,\Omega_m^{\gamma}(a) + \beta\,\Omega_m^{2\gamma-1}(a) \\ &-\frac{3}{2}\,\frac{\mu}{\beta} + \left(\frac{1}{2}-\gamma\right)\frac{\dot{\Omega}_{DE}(a)}{\Omega_m}\, a^3\,\Omega_m^{\gamma}(a) = 0. \end{aligned} \tag{4.5.20}$$

We see that the new term is proportional to $(\frac{1}{2}-\gamma)$, so it is expected that it does not increase the errors in an important manner. Thus, considering the fitting function with $\gamma = \gamma_*$ in (4.5.11), we can see that the errors increase in comparison with those for the ΛCDM background up to 3%. As we did in the ΛCDM case, we can obtain better fits by modifying the expressions for $\beta(k)$ and $\gamma(k)$. Thus, the analysis shows that $\beta(k)$ is not sensitive to $\omega_{DE}(a)$ and therefore (4.5.10) provides a good approximation also in this case. The expression for γ is however modified. For example for the effective equation of state given by [45, 46],

$$\omega_{DE}(a) = \omega_0 + \omega_1\,(1-a), \tag{4.5.21}$$

with ω_0 and ω_1 constants, we find

$$\gamma(\mu, \omega_0, \omega_1) = \frac{1}{2} + \frac{0.161}{\beta(\mu) - 1.967\omega_0 - 0.4789\omega_1}. \tag{4.5.22}$$

Thus, the growth function reads in this case

$$f(a,k) = \frac{1}{4}\left[\sqrt{1+24\,\mu(k)}-1\right]\,\Omega_m^{\gamma(\mu(k),\omega_0,\omega_1)}(a). \tag{4.5.23}$$

In Fig. 4.3 and Fig. 4.4 we can see that the error can be reduced to 0.5% with this parametrization.

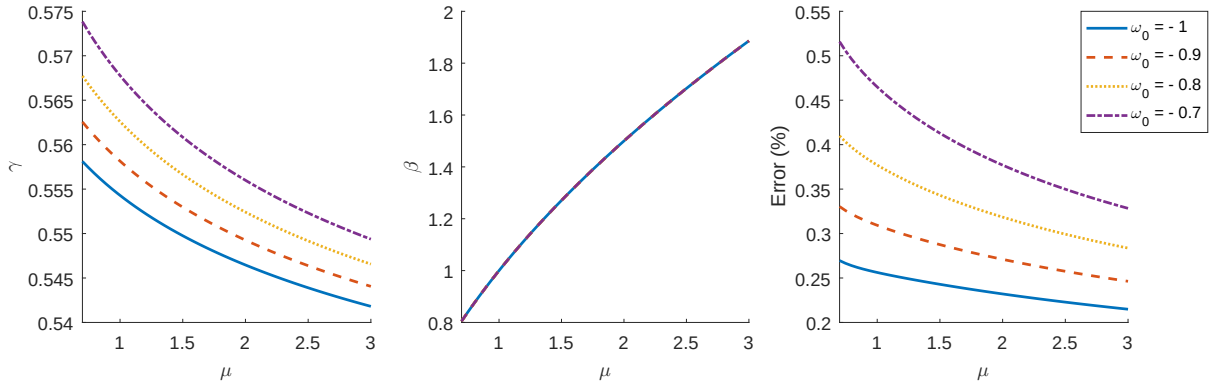

Figure 4.3: From left to right, functions $\gamma\,(\mu)$ (4.5.22), $\beta\,(\mu)$ (4.5.10) and growth function relative error, for time-independent μ for different values of ω_0 with $\omega_1 = 0$. We have assumed that $\Omega_m = 0.271$.

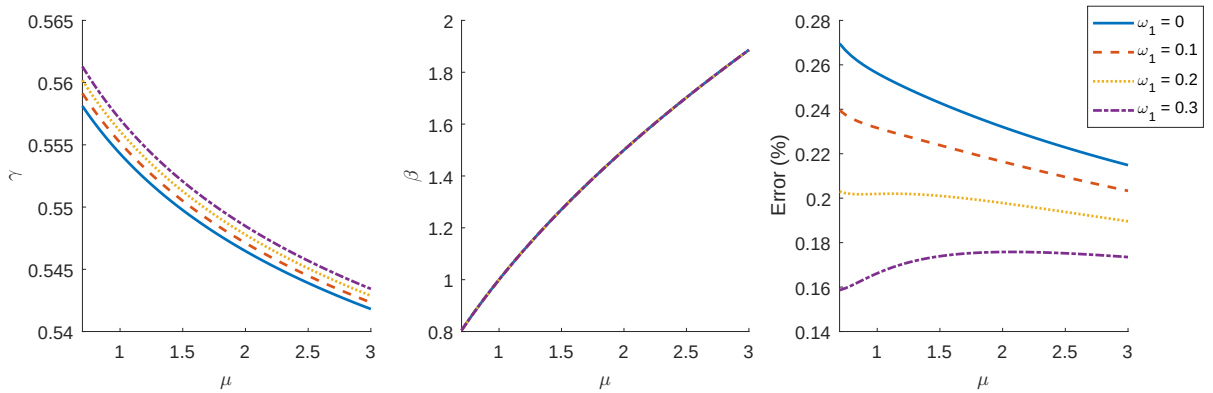

Figure 4.4: From left to right, functions $\gamma\,(\mu)$ (4.5.22), $\beta\,(\mu)$ (4.5.10) and growth function relative error, for time-independent μ for different values of ω_1 with $\omega_0 = -1$. We have assumed that $\Omega_m = 0.271$.

4.5.2 Scale-independent case $\mu = \mu(a)$

We have just seen that in the time-independent μ case, an ansatz of the form,

$$f(a) = \beta\, \Omega_m^{\gamma}(a), \tag{4.5.24}$$

provides a good fit to the numerical solutions. Let us now consider the case in which $\mu = \mu\,(a; p_1, ..., p_n)$ where $[p_1, ..., p_n]$ are the set of n cosmological parameters that μ depends on, i.e. μ can depend on redshift(time) but not on the scale k. We will explore a similar ansatz for the growth function,

$$f(a) = \beta\,(a; p_1^*, ..., p_n^*)\, \Omega_m^{\gamma}(a), \tag{4.5.25}$$

where, in general, $p_i^* = p_i^*(p_1, ..., p_n)$, $\gamma = \gamma(p_1, ..., p_n)$ and let us assume that the β function has the same a-dependence as the μ function (see [207, 208] for similar proposals in particular models). Thus, let us consider a simple example. For instance if $\mu\,(a) = 1 + b\,a$ being b dimensionless constant, then we consider $\beta = 1 + b^* a$, with $b^* = b^*(b)$. In Fig. 4.5 we show the fit error for different values of b. In Fig. 4.6 we can see the growth functions for the corresponding values of b. A ΛCDM background with $\Omega_m = 0.271$ has been assumed. It can be seen how it grows with redshift reaching values larger than one and then decreases tending to one when matter starts dominating. We can see that in this simple example, the parametrization (4.5.25) provides fitting errors below 0.5% in the whole redshift range, but they are even below 0.2% for $z > 0.1$.

After we have studied this simple model, and checked the usefulness of parametrization (4.5.25), we will apply it to more realistic models of modified gravity, such as DGP and certain phenomenological parametrizations of $\mu\,(a)$.

DGP Model

In the DGP model [209], the background evolution differs from ΛCDM so that

$$\Omega_m\,(a) = \frac{\Omega_0\, a^{-3}}{[(1-\Omega_0)/2 + \sqrt{\Omega_0\, a^{-3} + (1-\Omega_0)^2/4}]^2}, \tag{4.5.26}$$

and

$$\frac{\dot{H}}{H} = -\frac{3\,\Omega_m(a)}{1 + \Omega_m(a)}. \tag{4.5.27}$$

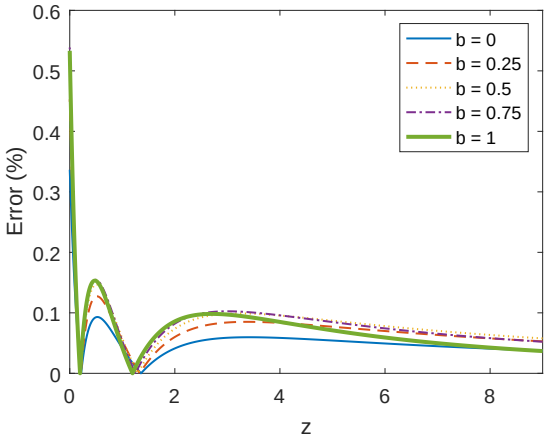

Figure 4.5: Relative difference between the numerical solution and the fitting function (4.5.25) for the model $\mu\,(a) = 1 + b\,a$. As we see, the maximum error is reached at $z = 0$.

being $\Omega_0 = \Omega_m(a = 1)$ the only free parameter at the background level. The modified gravity parameters in this case read [210]

$$\mu\,(a) = \frac{2(1 + 2\,\Omega_m^2\,(a))}{3(1 + \Omega_m^2\,(a))} \tag{4.5.28}$$

and

$$\eta\,(a) = \frac{2 + \Omega_m^2(a)}{1 + 2\,\Omega_m^2(a)}. \tag{4.5.29}$$

which are both k-independent, so that we try the parametrization in (4.5.25). Thus, using (4.5.26), (4.5.27) and (4.5.28) in equation (1.4.29), solving numerically and fitting to (4.5.25), we get

$$f(a) = \frac{2(1 + 2\,\Omega_m^2\,(a;\,\Omega_0^*))}{3(1 + \Omega_m^2\,(a;\,\Omega_0^*))}\,\Omega_m^{\gamma(\Omega_0)}(a), \tag{4.5.30}$$

where $\Omega_m\,(a;\,\Omega_0^*)$ follows equation (4.5.26) replacing Ω_0 by Ω_0^*. So we have two parameters to fit $\Omega_0^*\,(\Omega_0)$ and $\gamma\,(\Omega_0)$, which are given by the following expressions

$$\Omega_0^*(\Omega_0) = 0.8\,\Omega_0^{0.536} \tag{4.5.31}$$

and

$$\gamma(\Omega_0) = 0.52 - 0.47\,\Omega_0 + \Omega_0^2 - 1.2\,\Omega_0^3 \tag{4.5.32}$$

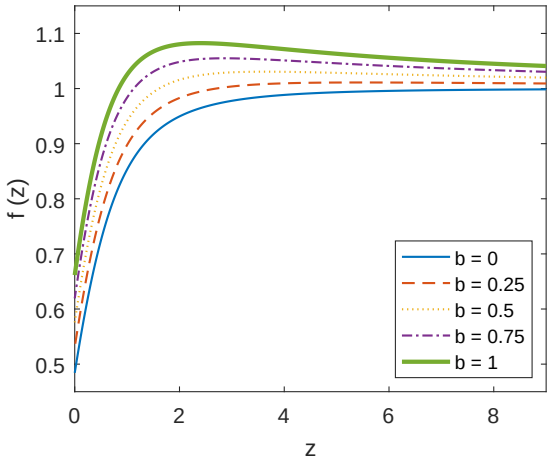

Figure 4.6: Numerical solutions in the model $\mu(a) = 1 + b\,a$ for different values of b. The fit according to the equation (4.5.25) is not represented because it differs in less than 0.6 % with respect to the numerical solution.

In Fig. 4.7 we plot the maximum error for $f(z)$ which is always reached at $z = 0$ as a function of Ω_0. We see that for typical values of $\Omega_0 \simeq 0.3$, the maximum error is below 0.5 %.

Other procedure used to parametrize growth in DGP is to assume that the growth index depends on redshift. Thus, for example, from equation (4.5.2), $\gamma(z)$ has been obtained to first order in $(1 - \Omega_m(a))$ in [211]. Another possibility is to use a parametrization like,

$$\gamma(z) = \gamma_0 + \gamma_1 \frac{z}{1+z}. \tag{4.5.33}$$

Adding more terms, and therefore more fixing constants, a reduced error was obtained in [212]. See also [213], for a different parametrization. In the best cases, these methods reach errors similar to those obtained in the present work.

Phenomenological parametrizations

As a second example, we will study the parametrization for $\mu(a)$ introduced in [214] and also considered in [15],

$$\mu(a) = 1 + (\mu_0 - 1)\frac{1 - \Omega_m(a)}{1 - \Omega_m}. \tag{4.5.34}$$

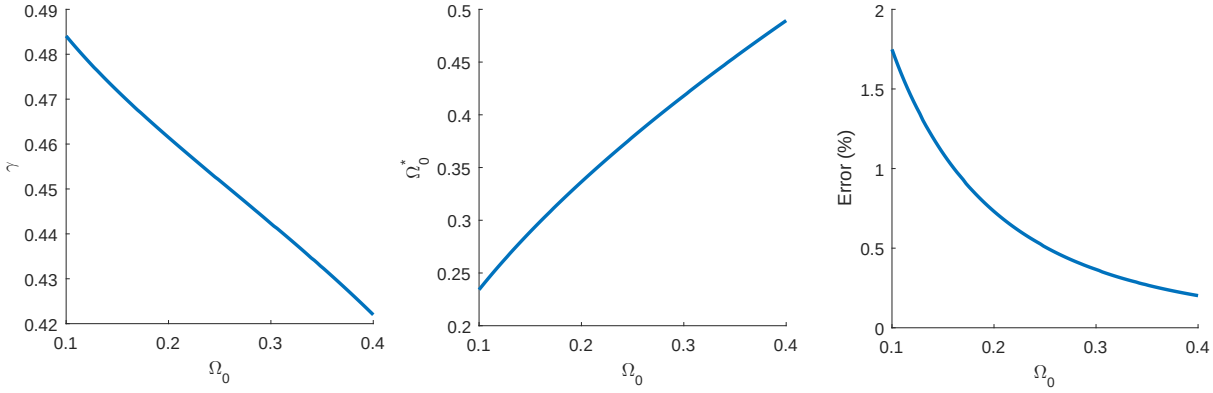

Figure 4.7: From left to right, the functions $\gamma\,(\Omega_0)$, $\Omega_0^*\,(\Omega_0)$ and the relative error of the growth function for the DGP model. The error decreases as we increase the value of Ω_0. The maximum error is less than 0.5 % for typical values of Ω_0.

Let us consider once more the effective equation of state (4.5.21), thus,

$$\Omega_m\,(a) = \frac{\Omega_m}{\Omega_m + (1-\Omega_m)\,a^{-3\,(\omega_0+\omega_1)}\,e^{-3\,\omega_1\,(1-a)}}, \tag{4.5.35}$$

where we have fixed $\Omega_m = 0.271$. Thus following (4.5.25), the growth function becomes,

$$f(a) = \left(1 + (\mu_0^* - 1)\,\frac{1-\Omega_m\,(a)}{1-\Omega_m}\right)\,\Omega_m^{\gamma}\,(a), \tag{4.5.36}$$

In this case, we only need to fit the parameters $\gamma = \gamma\,(\mu_0)$ and $\mu_0^* = \mu_0^*\,(\mu_0)$. We plot in Fig. 4.8 functions $\mu_0^*\,(\mu_0)$, $\gamma\,(\mu_0)$ along with errors in $f(a)$, for different values of ω_0, setting $\omega_1 = 0$. In Fig. 4.9 the same functions are shown, in this case varying ω_1 with $\omega_0 = -1$. In the $\omega_0 = -1$ and $\omega_1 = 0$ case, i.e. ΛCDM background, the fitting functions read

$$\mu_0^* = 0.961 - 0.132\,\mu_0 + 0.245\,\mu_0^2 - 0.066\,\mu_0^3 + 0.0065\,\mu_0^4 \tag{4.5.37}$$

and

$$\gamma = 0.456 + 0.012\,\mu_0 + 0.403\,e^{-1.37\,\mu_0}\,. \tag{4.5.38}$$

We can see that the error is less than 0.25 % even changing the effective equation of state. In this case, a fit of the form (4.5.33) does not reproduce well the numerical results.

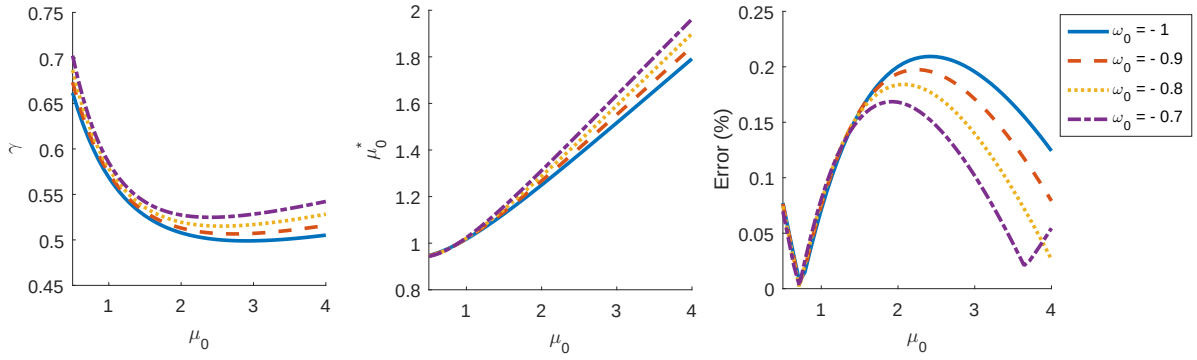

Figure 4.8: From left to right, the functions $\gamma(\mu_0)$, $\mu_0^*(\mu_0)$ and relative error of the growth function for the phenomenological model (4.5.34) for different values of ω_0, setting $\omega_1 = 0$. The case with $\omega_0 = -1$ is parametrized in (4.5.37) and (4.5.38).

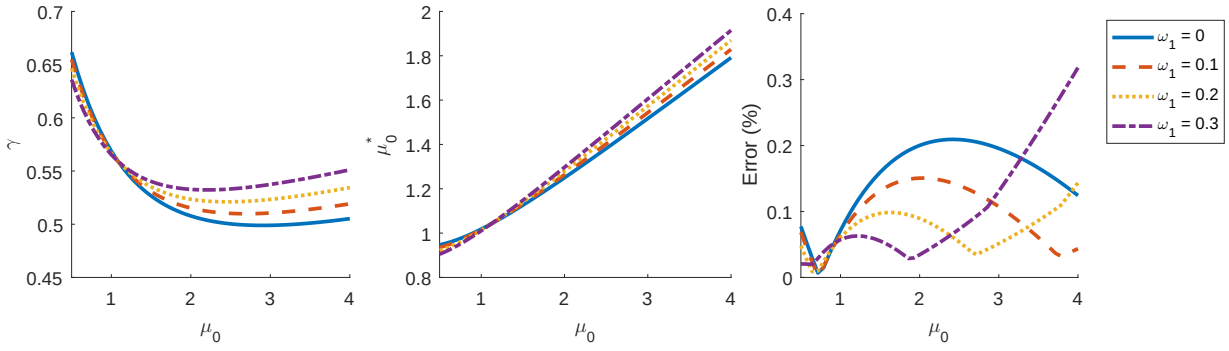

Figure 4.9: From left to right, the functions $\gamma(\mu_0)$, $\mu_0^*(\mu_0)$ and relative error of the growth function for the phenomenological model (4.5.34) for different values of ω_1, setting $\omega_0 = -1$. The case with $\omega_1 = 0$ is parametrized in (4.5.37) and (4.5.38).

4.5.3 General case: perturbative analysis

Let us consider the general case in which $\mu = \mu(a,\, k)$. In order to get closed expressions for the growth function, we will restrict ourselves to small perturbations around the GR case $\mu = 1$. Thus, we start with equation (4.5.2) and write

$$\mu(a,\, k) = 1 + \alpha(a,\, k) \tag{4.5.39}$$

being $|\alpha| \ll 1$. Let us now write the perturbed growth function in the following form,

$$f(a, k) = [1 + \epsilon\,(a,\, k)]\, f_0(a), \tag{4.5.40}$$

with $|\epsilon| \ll 1$ and $f_0(a) = \Omega_m^{\gamma_*}(a)$ the growth function in ΛCDM. We insert (4.5.40) into (4.5.2) and using that f_0 satisfies equation (4.5.2) with $\mu = 1$, we obtain,

$$\dot{\epsilon} + \left[\frac{3}{2}\Omega_m^{1-\gamma_*} + \Omega_m^{\gamma_*}\right]\, \epsilon = \frac{3}{2}\,\Omega_m^{1-\gamma_*}\,\alpha. \tag{4.5.41}$$

We can solve this equation analytically for a given initial condition at $a = a_i$ well inside the matter era where $\alpha(a_i, k) \simeq 0$ and $\epsilon(a_i, k) \simeq 0$, so that

$$\epsilon\,(a,\, k) = \frac{3}{2}\; e^{-g(a)} \int_{a_i}^{a} \Omega_m^{1-\gamma_*}(a')\,\alpha(a',\, k)\; e^{\,g(a')}\,\frac{da'}{a'}, \tag{4.5.42}$$

being,

$$g(a) = \int_{a_i}^{a} \left[\frac{3}{2}\,\Omega_m^{1-\gamma_*}(a') + \Omega_m^{\gamma_*}(a')\right]\, \frac{da'}{a'}. \tag{4.5.43}$$

The result does not depend on the particular value chosen (for concreteness, we took $a_i = 10^{-2}$). If we consider as a hard approximation that $\Omega_m \simeq 1$ then we can simplify equation (4.5.42) as,

$$\epsilon\,(a,\, k) = \frac{3}{2}\; a^{-\frac{5}{2}} \int_{a_i}^{a} \alpha(a',\, k)\; a'^{\frac{3}{2}}\, da', \tag{4.5.44}$$

and we can integrate by parts obtaining,

$$\epsilon\,(a,\, k) = \frac{3}{5}\sum_{n=0}^{\infty} \left(-\frac{2}{5}\right)^n\; \alpha^{(n)}(a,\, k), \tag{4.5.45}$$

where $\alpha^{(n)}$ is the n-th derivative with respect to $\ln a$. Then, if we take α as a constant in a, $\epsilon\,(a,\, k) = \frac{3}{5}\alpha(k)$ and we recover the time-independent case that we analyzed above in (4.5.14). In the following, we apply these results to different examples of modified gravity theories.

f(R) Model

Let us consider $f(R)$ gravities [47,215–218]. The growth function in this kind of models has been studied in several works [219–222]. In particular, we will consider here the Hu-Sawicki model [47] written in the simple form,

$$f(R) = R - \frac{2\Lambda}{1 + \frac{b\Lambda}{R}}, \tag{4.5.46}$$

which, for $b = 0$, reduces to the standard ΛCDM model with a cosmological constant Λ. The corresponding μ function reads [218]

$$\mu\,(a,k) = \frac{1}{f_{,R}} \frac{1 + 4(f_{,RR}(R_0)/f_{,R}(R_0))(k/a)^2}{1 + 3(f_{,RR}(R_0)/f_{,R}(R_0))(k/a)^2}, \tag{4.5.47}$$

where $f_{,R}$ and $f_{,RR}$ denote the first and second derivatives with respect to R and R_0 is the scalar curvature assuming that the background agrees with that of ΛCDM

$$R_0(a) = 3\,H_0^2\,[\Omega_m\,a^{-3} + 4\,(1 - \Omega_m)]. \tag{4.5.48}$$

For small enough b, we can approximate,

$$\frac{f_{,RR}(R_0)}{f_{,R}(R_0)} \left(\frac{k}{a}\right)^2 \simeq \frac{4\,b}{3} \frac{(1-\Omega_m)^2}{a^2 r^2(a)} \frac{k^2}{H_0^2}, \tag{4.5.49}$$

where $r(a) = R_0(a)/3H_0^2$. Also, using that for small x,

$$\frac{1 + 4\,x}{1 + 3\,x} \simeq 1 + 0.44\,x^{0.77}, \tag{4.5.50}$$

we can finally approximate (4.5.47) by

$$\mu(a,k) \simeq 1 + 0.44 \left[\frac{4\,b}{3} \frac{(1-\Omega_m)^2}{a^2 r^2(a)} \frac{k^2}{H_0^2}\right]^{0.77}, \tag{4.5.51}$$

which allows to extract the explicit b and k/H_0 dependence from the integral in equation (4.5.42). We compare in the left panel of Fig. 4.10 this approximation with the exact expression. We see that it provides an excellent fit for $b(k/H_0)^2 < 10$. Then, using (4.5.42) we get

$$\epsilon(a,k) = \left[b \left(\frac{k}{H_0}\right)^2\right]^{0.77} F(a), \tag{4.5.52}$$

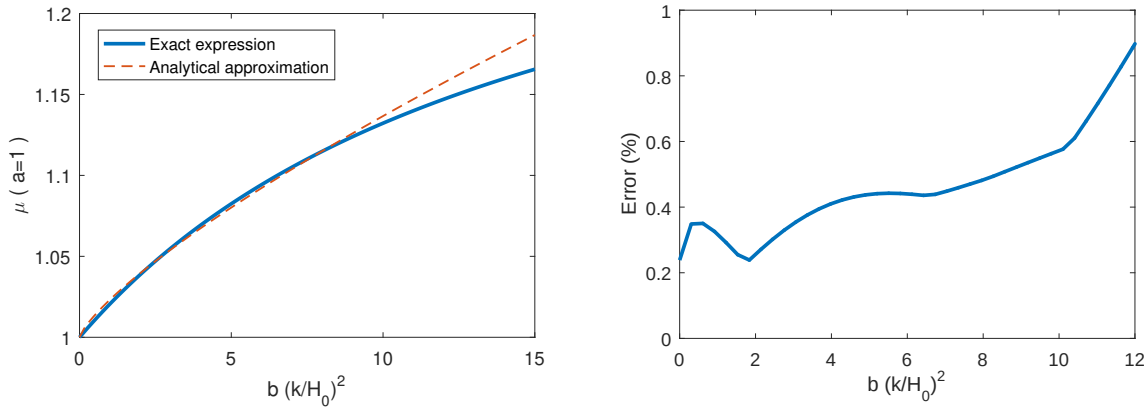

Figure 4.10: Left panel: $\mu(a,k)$ with $a=1$ as a function of $b\,(k/H_0)^2$ for the $f(R)$ theory in (4.5.46). We compare the exact expression in (4.5.47) with the approximation in equation (4.5.51). Right panel: the growth function relative error for the approximation (4.5.51) for the ΛCDM background.

being,

$$F(a) = 0.8236\,(1-\Omega_m)^{1.54}\,e^{-g(a)}\int_{a_i}^{a}\frac{\Omega_m^{1-\gamma^*}(a')}{r^{2.31}(a')a'^{2.54}}\,e^{\,g(a')}\,da'. \tag{4.5.53}$$

The fitting functions for $F(a)$ in terms of $\Omega_m(a)$ can be easily obtained and reads

$$F(a) = 0.140\,\Omega_m(a) - 0.545\,\Omega_m^2(a) + 0.994\,\Omega_m^3(a) - 0.905\,\Omega_m^4(a) + 0.315\,\Omega_m^5(a). \tag{4.5.54}$$

On the right panel of Fig. 4.10, we plot the growth function errors as a function of $b\,(k/H_0)^2$ using the expressions above. We see that the agreement with the numerical solution is better than 1% when $|\mu-1|<0.12$. Since these fits have been obtained for a ΛCDM background, using the above expressions with different backgrounds would increase the errors up to 2%.

Phenomenological parametrization

Let us consider the limit $|\mu_0-1|\ll 1$ in the parametrization given in (4.5.34). Using equation (4.5.42) we find that,

$$\epsilon(a) = \frac{3}{2}\,(\mu_0-1)\;e^{-g(a)}\int_{a_i}^{a}\Omega_m^{1-\gamma^*}(a')\,\frac{1-\Omega_m(a')}{1-\Omega_m}\;e^{\,g(a')}\,\frac{da'}{a'}, \tag{4.5.55}$$

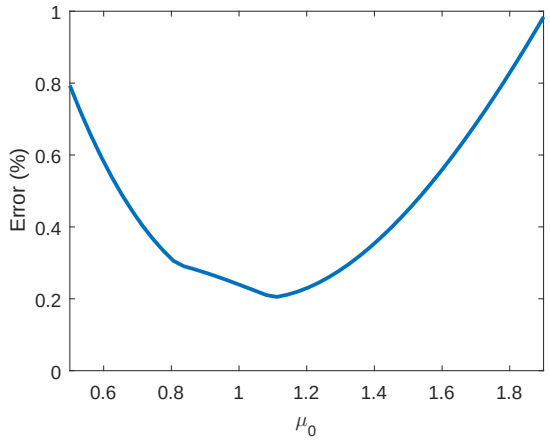

Figure 4.11: Errors in $f(z)$ for the phenomenological parametrization (4.5.54) for the ΛCDM background.

and we can fit this expression as follows,

$$\epsilon(a) \;=\; (\mu_0 - 1)\,(0.505 - 0.646\,\Omega_m(a) + 0.141\,\Omega_m(a)^2). \tag{4.5.56}$$

In this case, as we can see in Fig. 4.11, the error in the growth function is below 1% for $|\mu_0 - 1| < 1$. Since, as in the $f(R)$ case, these fits have been obtained for a ΛCDM background, using the above expressions with different backgrounds would increase the errors up to 2%.

4.5.4 Growth fuction parametrization for μ_m and μ_d

Finally, we will consider the case in which dark matter is an imperfect and non-conserved fluid. In this situation the growth equation follows (4.4.32). Thus we will calculate useful analytical approximations of the growth function in terms of μ_m and μ_d parameters. We will take into account two cases: first of all the simplest case in which μ_m and μ_d are constants, and then the case in which $|1 - \mu_m(a,k)| \ll 1$ and $|1 - \mu_d(a,k)| \ll 1$. We start with the growth equation (4.4.32) and we do the following variable change,

$$\delta' = \mathcal{H}\,\delta\,f, \tag{4.5.57}$$

$$\delta'' = \mathcal{H}^2\,\delta\,\left[\dot{f} + f^2 + \frac{\dot{\mathcal{H}}}{\mathcal{H}}\,f\right]. \tag{4.5.58}$$

Using (4.5.57-4.5.58) in (4.4.32) and $\mathcal{H} = aH$ we obtain,

$$\dot{f} + f^2 + \left[1 + \mu_d + \frac{\dot{H}}{H}\right]\,f = \frac{3}{2}\,\Omega_m(a)\,\mu_m. \tag{4.5.59}$$

Let us assume a solution of the form,

$$f(a) = \zeta(\mu_m, \mu_d)\,\Omega_m^{\gamma}(a), \tag{4.5.60}$$

we also consider a ΛCDM background as before so we use (4.5.4) and (4.5.5). Using (4.5.60) in (4.5.59) and considering the approximation $\Omega_m(a) \simeq 1$ we obtain,

$$\zeta^2 - \left[\frac{1}{2} - \mu_d\right]\,\zeta - \frac{3}{2}\,\mu_m = 0. \tag{4.5.61}$$

Thus we can obtain $\zeta(\mu_m, \mu_d)$ and extend the result in (4.5.23),

$$f(a) = \frac{1}{4}\left[\sqrt{(1-2\mu_d)^2 + 24\mu_m} + 1 - 2\mu_d\right]\,\Omega_m^{\gamma}(a). \tag{4.5.62}$$

Let us know check the accuracy of this analytic approximation with respect to the numerical solution. As we can see in the left panel of Fig. 4.12, if the modifications of μ_m and μ_d are below the 10 %, the analytic approximation has errors of order 1 %.

Now we analyze the case $|1 - \mu_m(a,k)| \ll 1$ and $|1 - \mu_d(a,k)| \ll 1$. Proceeding as in the previous sections, we assume a solution of the form,

$$f(a,k) = [1 + \epsilon(a,k)]\;\Omega_m^{\gamma}(a), \tag{4.5.63}$$

with $\epsilon \ll 1$. We use (4.5.63) into (4.5.59), keeping linear in $1-\mu_m$, $1-\mu_d$ and ϵ; and considering the approximation $\Omega_m(a) \simeq 1$ we obtain,

$$\dot{\epsilon} + \frac{5}{2}\,\epsilon = (1-\mu_d) - \frac{3}{2}\,(1-\mu_m)\,, \tag{4.5.64}$$

solving this last equation and changing to the variable z, we obtain the correction to the growth function ϵ as,

$$\epsilon(z,k) = (1+z)^{5/2}\,\int_z^{z_{mat}}\,\left[(1-\mu_d(z',k)) - \frac{3}{2}\,(1-\mu_m(z',k))\right]\,(1+z')^{-7/2}\,dz', \tag{4.5.65}$$

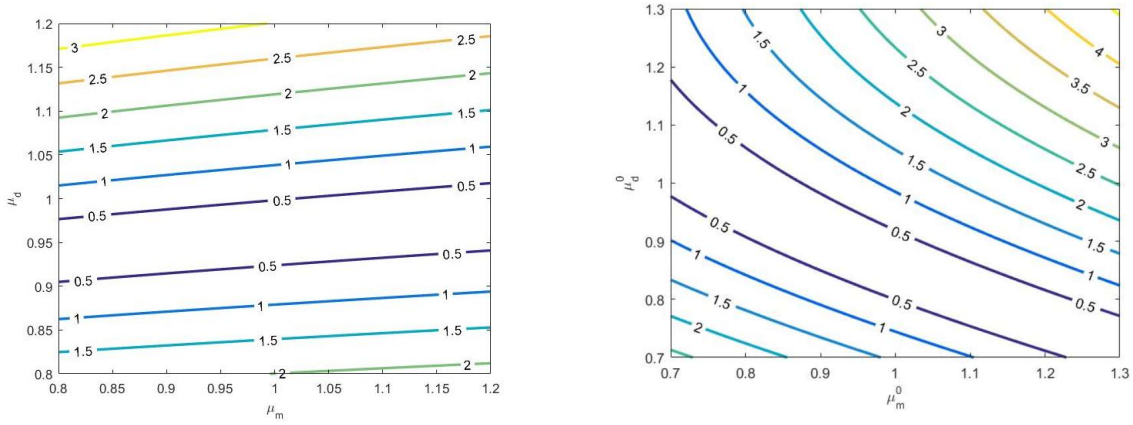

Figure 4.12: Left panel: errors (%) of the analytic expression (4.5.62) with respect to the numerical solution of $f(a)$ for μ_m and μ_d constants. Right panel: errors (%) of the analytic expression (4.5.65) with respect to the numerical solution of $f(z)$ for $\mu_m(z)$ and $\mu_d(z)$ following expressions (4.5.66-4.5.67).

where z_{mat} is the redshift for the matter dominated era ($z_{mat} \simeq 10$), and $\lim_{z\to z_{mat}} \mu_m(z,k) = \lim_{z\to z_{mat}} \mu_d(z,k) = 1$. We test this approximation using the following expressions for $\mu_m(z)$ and $\mu_d(z)$,

$$\mu_m(z) = 1 + (\mu_m^0 - 1)\,\frac{1-\Omega_m(z)}{1-\Omega_m}, \tag{4.5.66}$$

$$\mu_d(z) = 1 + \frac{(\mu_d^0 - 1)}{1+z}. \tag{4.5.67}$$

We plot the errors of this analytic approximation respect to the numerical solution in the right panel of Fig. 4.12. As in the case before, the analytic approximation has errors of order 1 % for modifications of μ_m and μ_d order 10 %, . In addition, we can do an analytical check of expression (4.5.63) for the case in which μ_m and μ_d are constants, using,

$$(1+z)^{5/2}\int_z^{z_{mat}} (1+z')^{-7/2}\,dz' \simeq \frac{2}{5}, \tag{4.5.68}$$

for $z \ll z_{mat}$, we obtain,

$$f(a) = \left[\frac{4}{5} - \frac{2}{5}\mu_d + \frac{3}{5}\mu_m\right]\,\Omega_m^{\gamma}(a). \tag{4.5.69}$$

We also recover this result if we apply the approximation $|1-\mu_m| \ll 1$ and $|1-\mu_d| \ll 1$ in equation (4.5.62).

Chapter 5

Testing modified cosmologies with galaxy surveys

As we have seen in previous chapters in bayesian statistics there are many types of priors when a theory is tested with data. One of these priors is the model choice itself. The effect of this prior is the most challenging to measure as it is difficult to analyze data in a totally model-independent way. The phenomenological parametrizations described before are a first approach to make a model-independent treatment of theory. In this chapter we will use this approach to analyze the potential signals generated in galaxy surveys by modified gravity theories involving additional vector degrees of freedom with explicit preferred directions effects. We will also analyze the possible obervational impact of modified dark matter models. In both cases, the model-independent approach discussed in Chapter 4 will be employed. The results of this chapter correspond to [139, 223].

5.1 Signals of preferred directions in galaxy surveys

The main observables that we will analyze to detect a gravitational preferred direction are the galaxy distribution power spectrum and the weak-lensing power spectrum. We do not take into account the peculiar-velocity power spectrum here because it is not particularly sensitive to the parameters and the additional information provided is negligible compared to that obtained from the galaxy distribution power spectrum.

Our starting point will be the phenomenological description of vector modified gravities

introduced in Section 4.2. For simplicity, we will consider a negligible dark matter vorticity, so that we are left with only four effective parameters $\mu = \mu(a,k,x)$, $\eta = \eta(a,k,x)$, $\mu_Q = \mu_Q(a,k,x)$ and $\mu_h = \mu_h(a,k,x)$, where $\mu = \mu_\Psi$ and $\eta = \mu_\Phi/\mu_\Psi$ are given in (4.2.30) and (4.2.31), and $x = \hat{\mathbf{k}}\cdot\hat{\mathbf{A}}$. In addition, we will also assume that the background vector field is a subdominant contribution with respect to matter so that the background evolution can be correctly described by a Robertson-Walker metric, i.e. $\Xi_{ij} = \delta_{ij}$. The first main effect of parametrization (4.2.30)-(4.2.33) is the modification of the growth evolution,

$$\ddot{\delta} + \left(2 + \frac{\dot{H}}{H}\right)\dot{\delta} - \frac{3}{2}\,\mu(a,k,x)\,\Omega_m(a)\,\delta = 0. \tag{5.1.1}$$

By solving this equation we obtain the growth factor $D(z,k,x) = \delta(z,k,x)/\delta(0,k,x)$, where as usual the redshift is related to the scale factor by $a = 1/(1+z)$, and the growth function $f(z,k,x) = \dot{D}(z,k,x)/D(z,k,x)$ which unlike in the ordinary General Relativity case is anisotropic because of the x dependence. Then the matter power spectrum is in general anisotropic $P_m(z,\mathbf{k}) = P_m(z,k,x)$. Considering the standard contribution of RSD, the galaxy distribution power spectrum (2.2.21) becomes,

$$P_{gg}(z,\hat{\mu},x,k) = \left(1+\beta(z,k,x)\hat{\mu}^2\right)^2\, b(z)^2\, P_m(z,k,x). \tag{5.1.2}$$

As we can see, the redshift-space galaxy power spectrum has two different kinds of anisotropic contributions: on one hand the standard contribution from redshift space distortions (RSD) which introduces a quadrupole and hexadecapole in $\hat{\mu}$, and on the other, an extra contribution coming from the x dependence of the growth function. Thus performing a multipole expansion with respect to the line of sight we find,

$$P_{gg}(z,\hat{\mu},x,k) = \sum_\ell P_\ell(z,k,x)\,\mathcal{L}_\ell(\hat{\mu}), \tag{5.1.3}$$

where $\mathcal{L}_\ell$ are the Legendre polynomials so that

$$P_\ell(z,k,x) = \frac{2\ell+1}{2}\int_{-1}^{1} d\hat{\mu}\, P_{gg}(z,\hat{\mu},x,k)\,\mathcal{L}_\ell(\hat{\mu}). \tag{5.1.4}$$

As in the standard case, $P_\ell(z,k,x)$ are different from zero for $\ell = 0,2,4$ i.e. we recover the well-known monopole, quadrupole and hexadecapole contributions but with the new x dependence. Thus we have,

$$P_0(z,k,x) = \left(1 + \frac{2}{3}\,\beta(z,k,x) + \frac{1}{5}\,\beta^2(z,k,x)\right)\, b^2\, P_m(z,k,x), \tag{5.1.5}$$

$$P_2(z,k,x) = \left(\frac{4}{3}\,\beta(z,k,x) + \frac{4}{7}\,\beta^2(z,k,x)\right)\, b^2\, P_m(z,k,x), \tag{5.1.6}$$

$$P_4(z,k,x) = \frac{8}{35}\,\beta^2(z,k,x)\, b^2\, P_m(z,k,x). \tag{5.1.7}$$

The multipole coefficients P_ℓ, depend in turn on the angular variable x and therefore could be additionally expanded in a different multipole expansion with respect to x. Alternatively, a bi-polar expansion in $(\hat{\mu}, x)$ [172], could have been performed. However for the Fisher analysis that we will perform, we will directly work with the P_ℓ coefficients. So, the main effect of a preferred direction in the galaxy distribution power spectra is the apparition of a new direction that induces an extra angular dependence.

On the other hand we have the weak lensing power spectrum. In this case we will see how the standard derivation of the convergence power spectrum is affected by scalar, vector and tensor perturbations; and the presence of a preferred direction. We start with the Bianchi perturbed metric (4.2.5), where as before we have considered for simplicity $\Xi_{ij} \simeq \delta_{ij}$. We will also work in cosmological time t so that the metric reads

$$ds^2 = -(1+2\Psi)\,dt^2 + a(t)^2\,[(1-2\Phi)\,\delta_{ij} + h_{ij}]\,dx^i dx^j - 2\,Q_i\,a(t)\,dt\,dx^i. \tag{5.1.8}$$

We are interested in the corresponding null geodesics satisfying (2.4.2). For the metric (5.1.8), we have that the Christoffel symbols are,

$$\Gamma^i_{00} = a^{-2}\,\Psi_{,i} - a^{-1}\,\left(H\,Q_i + Q_{i,0}\right), \tag{5.1.9}$$

$$\Gamma^i_{j0} = \delta_{ij}\,\left(H - \Phi_{,0}\right) - a^{-1}\,Q_{[i,j]} + \frac{1}{2}\,h_{ij,0}, \tag{5.1.10}$$

$$\Gamma^i_{jk} = \Phi_{,i}\,\delta_{jk} - \Phi_{,k}\,\delta_{ij} - \Phi_{,j}\,\delta_{ki} + a\,H\,Q_i\,\delta_{jk} + \frac{1}{2}\,(h_{ij,k} + h_{ik,j} - h_{jk,i}), \tag{5.1.11}$$

where a comma denotes derivative with respect to the coordinates (t, x^1, x^2, x^3). Arguing as in the standard case, the remaining contributions at linear level in the Christoffel symbol term (2.4.10) are,

$$\Gamma^i_{00}\,\left(\frac{dt}{d\chi}\right)^2 = \Psi_{,i} - a\,\left[H\,Q_i + Q_{i,0}\right], \tag{5.1.12}$$

$$\Gamma^i_{j0}\,\frac{dt}{d\chi}\,\frac{dx^j}{d\chi} = -a\,H\,\frac{d}{d\chi}(\chi\,\theta^i) + Q_{[i,3]} - \frac{1}{2}\,a\,h_{i3,0}, \tag{5.1.13}$$

and

$$\Gamma^i_{33}\,\left(\frac{dx^3}{d\chi}\right)^2 = \Phi_{,i} + a\,H\,Q_i + h_{i3,3} - \frac{1}{2}\,h_{33,i}. \tag{5.1.14}$$

So considering these contributions at linear regime we obtain that equation (2.4.10) becomes,

$$\Gamma^i_{\alpha\beta}\,\frac{dx^\alpha}{d\lambda}\,\frac{dx^\beta}{d\lambda} = \left(\frac{p}{a}\right)^2\,\left[(\Phi+\Psi)_{,i} - 2\,a\,H\,\frac{d}{d\chi}(\chi\,\theta^i) + 2\,Q_{[i,3]} + h_{i3,3} - \frac{1}{2}\,h_{33,i} - a\,(Q_i + h_{i3})_{,0}\right]. \tag{5.1.15}$$

Thus, as in the standard case, we can obtain from the geodesic equation (2.4.2),

$$\frac{d^2}{d\chi^2}(\chi\,\theta^i) = -(\Phi+\Psi)_{,i} - 2Q_{[i,3]} - h_{i3,3} + \frac{1}{2}\,h_{33,i} + a\,(Q_i + h_{i3})_{,0}. \tag{5.1.16}$$

At this point we apply the quasi-static approximation (QSA) and the sub-Hubble regime in which we can neglect the time derivatives of perturbations with respect to the spatial derivatives,

$$\frac{d^2}{d\chi^2}(\chi\,\theta^i) = -(\Phi+\Psi)_{,i} - 2Q_{[i,3]} - h_{i3,3} + \frac{1}{2}\,h_{33,i}. \tag{5.1.17}$$

It will be useful to define the source term of equation (5.1.17) as,

$$Y_i \equiv -\left(\Phi + \Psi + Q_3 + \frac{1}{2}\,h_{33}\right)_{,i} - (Q_i + h_{i3})_{,3}. \tag{5.1.18}$$

This is how standard equation (2.4.20) is modified when we have vector and tensor perturbations in the QSO approximation and the sub-Hubble regime. Now we will look at the modified distortion tensor defined as (2.4.21),

$$\psi_{ij}(\boldsymbol{\theta}) = \int_0^{\chi_\infty} d\chi\;\chi\,g(\chi)\,Y_{i,j}(\chi,\boldsymbol{\theta}). \tag{5.1.19}$$

Notice that it is no longer symmetric due to the extra terms in (5.1.18). The general distortion tensor can be written as,

$$\psi_{ij} \equiv \begin{pmatrix} -\kappa-\gamma_1 & -\gamma_2-\omega \\ -\gamma_2+\omega & -\kappa+\gamma_1 \end{pmatrix}$$

Although the convergence and shear parameters are defined as in the standard case as (2.4.29)-(2.4.31), an additional parameter responsible for a rotational effect has to be defined,

$$\omega = -\frac{\psi_{12} - \psi_{21}}{2}. \tag{5.1.20}$$

Now, we use equation (5.1.18) into (5.1.19) so that

$$\psi_{ij}(\boldsymbol{\theta}) = -\int_0^{\chi_\infty} d\chi\ \chi\, g(\chi)\ \left(\Phi + \Psi + Q_3 + \frac{1}{2}\, h_{33}\right)_{,ij} - \int_0^{\chi_\infty} d\chi\ \chi\, g(\chi)\ (Q_i + h_{i3})_{,3j}\,. \tag{5.1.21}$$

As we can see from the previous equation, the vector and tensor perturbations generate the rotation effect in the distortion tensor [224]. Since $x^3 = \chi$, we can integrate by parts the second integral to obtain,

$$\begin{aligned}\int_0^{\chi_\infty} d\chi\ \chi\, g(\chi)\ (Q_i + h_{i3})_{,3j} = \cancel{[\chi\, g(\chi)\, (Q_i + h_{i3})_{,j}]|_0^{\chi_\infty}} \\ - \int_0^{\chi_\infty} d\chi\ \left(g + \chi \frac{dg}{d\chi}\right)\ (Q_i + h_{i3})_{,j}\,,\end{aligned} \tag{5.1.22}$$

so that the distortion tensor becomes,

$$\psi_{ij}(\boldsymbol{\theta}) = -\int_0^{\chi_\infty} d\chi\ \chi\, g(\chi)\ \left[\left(\Phi + \Psi + Q_3 + \frac{1}{2}\, h_{33}\right)_{,ij} - \frac{1}{\chi}\ \left(1 + \frac{\chi}{g}\, \frac{dg}{d\chi}\right)\ (Q_i + h_{i3})_{,j}\right]. \tag{5.1.23}$$

Now, we want to go to the Fourier space of $\boldsymbol{\theta}$ so that we define,

$$\tilde{\psi}_{ij}(\boldsymbol{\ell}) = \int\, d^2\theta\ \mathrm{e}^{-i\,\boldsymbol{\ell}\cdot\boldsymbol{\theta}}\, \psi_{ij}(\boldsymbol{\theta}). \tag{5.1.24}$$

Taking into account that,

$$\frac{\partial}{\partial x^i} = \frac{1}{\chi}\, \frac{\partial}{\partial \theta^i}, \tag{5.1.25}$$

the Fourier transform of the distortion matrix is,

$$\tilde{\psi}_{ij}(\boldsymbol{\ell}) = \int_0^{\chi_\infty} d\chi\ \frac{g(\chi)}{\chi}\ \left[\ell_i\, \ell_j\ \left(\tilde{\Phi} + \tilde{\Psi} + \tilde{Q}_3 + \frac{1}{2}\, \tilde{h}_{33}\right) + i\, \ell_j\ \left(1 + \frac{\chi}{g}\, \frac{dg}{d\chi}\right)\ (\tilde{Q}_i + \tilde{h}_{i3})\right]. \tag{5.1.26}$$

Compared to the standard case (2.4.35), we can see in (5.1.26) that there are two modifications: a new non-symmetric term responsible for the rotational effect, and an additional symmetric term that, as we will see, introduces anisotropic terms. To obtain the power spectrum for the distortion tensor we can use the result of (2.4.50). If we change from χ to the redshift variable $z = 1/(1+a)$ and using $[4\pi G a^2 \rho]^2 = \frac{9H_0^4}{4}\,\Omega_m^2\,(1+z)^2$ we get,

$$P^{\psi}_{ijlm}(\boldsymbol{\ell}) = \frac{9\,H_0^4\,\Omega_m^2}{4}\int_0^{\infty} dz\,\frac{(1+z)^2}{H(z)}\,g^2(z)\,\frac{\kappa_i\,\ell_j\,\kappa_l^*\,\ell_m}{\ell^4}\,P_m\left(z,\frac{\boldsymbol{\ell}}{\chi(z)}\right), \tag{5.1.27}$$

where

$$\kappa_i \equiv \ell_i\,\alpha - i\left(1+\frac{1}{g}\frac{dg}{dz}\left(\frac{1}{\chi}\frac{d\chi}{dz}\right)^{-1}\right)\mathrm{v}_i, \tag{5.1.28}$$

$$\alpha \equiv \mu(1+\eta) - 4\mu_Q\mathcal{A}_3 + \frac{1}{2}\,\mu_h\,\Sigma_{33}, \tag{5.1.29}$$

$$\mathrm{v}_i \equiv 4\mu_Q\mathcal{A}_i - \mu_h\Sigma_{i3}, \tag{5.1.30}$$

where

$$g(z) = \int_z^{\infty}\left(1-\frac{\chi(z)}{\chi(z')}\right)\,n(z')\,dz', \tag{5.1.31}$$

with $n(z)dz = W(\chi)d\chi$ and $n(z)$ the galaxy density function as a function of redshift. Now we can use expressions (2.4.29)-(2.4.31) and (5.1.20) to construct the power spectra for convergence, shear and rotation,

$$P_{\kappa} = \frac{1}{4}\left(P^{\psi}_{1111} + P^{\psi}_{2222} + P^{\psi}_{1122} + P^{\psi}_{2211}\right), \tag{5.1.32}$$

$$P_{\gamma_1} = \frac{1}{4}\left(P^{\psi}_{1111} + P^{\psi}_{2222} - P^{\psi}_{1122} - P^{\psi}_{2211}\right), \tag{5.1.33}$$

$$P_{\gamma_2} = \frac{1}{4}\left(P^{\psi}_{1212} + P^{\psi}_{2121} + P^{\psi}_{1221} + P^{\psi}_{2112}\right), \tag{5.1.34}$$

$$P_{\omega} = \frac{1}{4}\left(P^{\psi}_{1212} + P^{\psi}_{2121} - P^{\psi}_{1221} - P^{\psi}_{2112}\right). \tag{5.1.35}$$

These expressions can be written in a more compact fashion by introducing the following variables. We define $\ell_1 \equiv \ell\,\Upsilon$ and $\ell_2 \equiv \ell\,\sqrt{1-\Upsilon^2}$ where,

$$\Upsilon \equiv \frac{\hat{A}^i \ell_i}{\ell\,\sqrt{1-\hat{A}_3^2}}. \tag{5.1.36}$$

Considering the small-angle approximation $k_3 \ll k_1, k_2$, the conditions $\hat{k}^i Q_i = 0$ and $\hat{k}^i h_{ij} = 0$ imply,

$$\ell^i \mathrm{v}_i = 0. \tag{5.1.37}$$

Using this expression we can write v_2 as a function of v_1 and then we relate it with $\mathrm{v}^2 \equiv \mathrm{v}_1^2 + \mathrm{v}_2^2$,

$$\mathrm{v}_1^2 = (1-\Upsilon^2)\,\mathrm{v}^2. \tag{5.1.38}$$

Finally using (5.1.36) and (5.1.37) in the expressions of the power spectra (5.1.32) - (5.1.35) we obtain,

$$P_\kappa = P_\alpha, \tag{5.1.39}$$

$$P_{\gamma_1} = (1-2\,\Upsilon^2)^2\,P_\alpha + 4\,\Upsilon^2\,(1-\Upsilon^2)\,P_\mathrm{v}, \tag{5.1.40}$$

$$P_{\gamma_2} = 4\,\Upsilon^2\,(1-\Upsilon^2)\,P_\alpha + (1-2\,\Upsilon^2)^2\,P_\mathrm{v}, \tag{5.1.41}$$

$$P_\omega = P_\mathrm{v}, \tag{5.1.42}$$

where P_α and P_v are,

$$P_\alpha = \frac{9\,H_0^4\,\Omega_m^2}{4}\int_0^\infty dz\,\frac{(1+z)^2}{H(z)}\,g^2(z)\,\frac{\alpha^2}{4}\,P_m\left(z,\frac{\ell}{\chi(z)}\right), \tag{5.1.43}$$

$$P_\mathrm{v} = \frac{9\,H_0^4\,\Omega_m^2}{4}\int_0^\infty dz\,\frac{(1+z)^2}{H(z)}\,g^2(z)\left(1+\frac{1}{g}\frac{dg}{dz}\left(\frac{1}{\chi}\frac{d\chi}{dz}\right)^{-1}\right)^2\frac{\mathrm{v}^2}{4\,\ell^2}\,P_m\left(z,\frac{\ell}{\chi(z)}\right). \tag{5.1.44}$$

As we can see from equations (5.1.39)-(5.1.42), we have the following closing relation,

$$P_{\gamma_1} + P_{\gamma_2} = P_\kappa + P_\omega, \tag{5.1.45}$$

this is a useful relation since it allows to determine the rotation power spectrum, which is not directly measurable in lensing surveys, from shear and convergence measurements. We can use the expressions of $\mathcal{A}_i$ and Σ_{ij} considering $\hat{k}_3 \ll 1$, and the definition of Υ, to obtain expressions for α and v^2,

$$\alpha = \mu_\Psi\,(1+\gamma) - 4\,\xi\,\mu_Q + (2\,\xi^2 + (1-\xi^2)\Upsilon^2 - 1)\,\frac{\mu_h}{2}, \tag{5.1.46}$$

$$\mathrm{v}^2 = (4\,\mu_Q - 2\,\xi\,\mu_h)^2\,(1-\xi^2)(1-\Upsilon^2), \tag{5.1.47}$$

being $\xi \equiv \hat{A}_3$ with $-1 \leq \xi \leq 1$. Since $\hat{A}_3$ is the projection of $\hat{A}$ along the line of sight, we can perform a multipole expansion of α^2 and v^2 above, using the Legendre polynomials in ξ. Thus for $\alpha^2 = \sum_{r=0}^{4} M_\alpha^r \mathcal{L}_r(\xi)$ we have

$$M_\alpha^0 = \frac{1}{20}\,f_1^2 + \frac{1}{6}\,f_1\,f_2 + \frac{1}{4}\,f_2^2 + \frac{16}{3}\,\mu_Q^2, \tag{5.1.48}$$

$$M_\alpha^1 = -4\,\left(\frac{3}{5}\,f_1 + f_2\right)\,\mu_Q, \tag{5.1.49}$$

$$M_\alpha^2 = \left(\frac{1}{7}\,f_1 + \frac{1}{3}\,f_2\right)\,f_1 + \frac{32}{3}\,\mu_Q^2 \tag{5.1.50}$$

$$M_\alpha^3 = -\frac{8}{5}\,f_1\,\mu_Q, \tag{5.1.51}$$

$$M_\alpha^4 = \frac{2}{35}\,f_1^2 \tag{5.1.52}$$

where $f_1 \equiv (2-\Upsilon^2)\,\mu_h$ and $f_2 \equiv 2\,\mu\,(1+\eta) - (1-\Upsilon^2)\,\mu_h$. On the other hand for $\mathrm{v}^2 = \sum_{r=0}^{4} M_\mathrm{v}^r \mathcal{L}_r(\xi)$

$$M_\mathrm{v}^0 = \frac{8}{15}\,\mu_h^2 + \frac{32}{3}\,\mu_Q^2, \tag{5.1.53}$$

$$M_{\rm v}^1 = -M_{\rm v}^3 = -\frac{32}{5}\,\mu_Q\,\mu_h, \tag{5.1.54}$$

$$M_{\rm v}^2 = \frac{8}{21}\,\mu_h^2 - \frac{32}{3}\,\mu_Q^2, \tag{5.1.55}$$

$$M_{\rm v}^4 = -\frac{32}{35}\,\mu_h^2. \tag{5.1.56}$$

With these definitions we obtain,

$$P_\alpha^r = \frac{9\,H_0^4\,\Omega_m^2}{4}\,\int_0^\infty dz\,\frac{(1+z)^2}{H(z)}\,g(z)^2\,\frac{M_\alpha^r}{4}\,P_m\left(z,\frac{\ell}{\chi(z)}\right), \tag{5.1.57}$$

$$P_{\rm v}^r = \frac{9\,H_0^4\,\Omega_m^2}{4}\,\int_0^\infty dz\,\frac{(1+z)^2}{H(z)}\,g(z)^2\,\left(1+\frac{1}{g}\frac{dg}{dz}\,\left(\frac{1}{\chi}\frac{d\chi}{dz}\right)^{-1}\right)^2\,\frac{(1-\Upsilon^2)\,M_{\rm v}^r}{4\,\ell^2}\,P_m\left(z,\frac{\ell}{\chi(z)}\right), \tag{5.1.58}$$

with $r = 0, 1, 2, 3, 4$. Finally, if we want to analyze the weak lensing signal at different redshift bins, we define the window functions as (2.4.60). With those definitions, the convergence, shear and rotation multipole power spectra are,

$$P_{\kappa\,ab}^r(\ell,\Upsilon) = \frac{9\,H_0^4\,\Omega_m^2}{4}\,\int_0^\infty dz\,\frac{(1+z)^2}{H(z)}\,g_a(z)\,g_b(z)\,\frac{M_\alpha^r}{4}\,P_m\left(z,\frac{\ell}{\chi(z)}\right), \tag{5.1.59}$$

$$P_{\omega\,ab}^r(\ell,\Upsilon) = \frac{9\,H_0^4\,\Omega_m^2}{4}\,\int_0^\infty dz\,\frac{(1+z)^2}{H(z)}\,\tilde{g}_a(z)\,\tilde{g}_b(z)\,\frac{(1-\Upsilon^2)\,M_{\rm v}^r}{4\,\ell^2}\,P_m\left(z,\frac{\ell}{\chi(z)}\right), \tag{5.1.60}$$

$$P_{\gamma_1\,ab}^r(\ell,\Upsilon) = (1-2\,\Upsilon^2)^2\,P_{\kappa\,ab}^r(\ell,\Upsilon) + 4\,\Upsilon^2\,(1-\Upsilon^2)\,P_{\omega\,ab}^r(\ell,\Upsilon), \tag{5.1.61}$$

$$P_{\gamma_2\,ab}^r(\ell,\Upsilon) = 4\,\Upsilon^2\,(1-\Upsilon^2)\,P_{\kappa\,ab}^r(\ell,\Upsilon) + (1-2\,\Upsilon^2)^2\,P_{\omega\,ab}^r(\ell,\Upsilon), \tag{5.1.62}$$

with

$$\tilde{g}_a(z) \equiv g_a(z)\,\left(1+\frac{1}{g_a}\frac{dg_a}{dz}\,\left(\frac{1}{\chi}\frac{d\chi}{dz}\right)^{-1}\right), \tag{5.1.63}$$

where a denote the different redshift bins. As we can see, vector and tensor perturbations induce anisotropies in the convergence power spectrum and an additional rotation effect in the galaxy shapes. This rotation effect can not be directly measured but it could be inferred indirectly from the closing relation (5.1.45). This is the simplest effect of a preferred direction in the weak lensing power spectrum, however, if we consider the full dependence in x of the effective parameters μ, η, μ_Q or μ_h, additional multipoles r could appear in (5.1.57) and (5.1.58).

5.2 Signals of modified dark matter in galaxy surveys

Here we want to analyze how an imperfect and non-conservated dark matter fluid affects the galaxy power spectra. As in this type of theories the conservation equations are modified, LOS velocity field is modified so we will analyze, in addition to the galaxy distribution power spectrum and the weak lensing power spectrum, the velocity field power spectrum. We will follow a model-independent approach in which we will consider each modified gravity parameter to have a different value for each redshift bin. In this approach, we will see that galaxy survey observables are sensitive to a concrete combination of these parameters.

First of all, as we analyzed in the parametrization of the growth function (4.5.62), the growth is affected by a combination $\zeta(\mu_m, \mu_d)$ of the effective parameters so, as a function of the redshift, it is not possible to distinguish μ_m and μ_d in a model independent way. We will be sensitive to a combination $\zeta(\mu_m, \mu_d)$ of them which, in the constant case, follows (4.5.61). However, because the conservation equation (4.4.33) is modified with μ_θ, the velocity divergence is also modified and then the RSD reads,

$$\delta_g^s = \left(1 + \mu_\theta\, \beta\, \hat{\mu}^2\right)\, b\, \delta. \tag{5.2.1}$$

In addition, the LOS peculiar velocity (2.3.3) is modified as,

$$u = -\frac{i\, \mathcal{H}\, \mu_\theta\, f\, \hat{\mu}}{k}\, \delta. \tag{5.2.2}$$

Taking into account these modifications, the power spectra P_{gg}, P_{uu} and P_{gu} now read,

$$P_{gg}(z, \hat{\mu}_r, k_r) = \frac{H_r\, D_A^2}{H\, D_{A\,r}^2}\, \left(1 + \mu_\theta\, \beta \hat{\mu}^2\right)^2\, b^2\, P_m(z, k), \tag{5.2.3}$$

$$P_{uu}(z,\hat{\mu}_r,k_r) = \frac{H_r\,D_A^2}{H\,D_{A\,r}^2}\,\left(\frac{\mathcal{H}\,\mu_\theta\,f\,\hat{\mu}}{k}\right)^2\,P_m(z,k), \tag{5.2.4}$$

$$P_{gu}(z,\hat{\mu}_r,k_r) = i\,\frac{H_r\,D_A^2}{H\,D_{A\,r}^2}\,\frac{\mathcal{H}\,\mu_\theta\,f\,\hat{\mu}}{k}\,\left(1+\mu_\theta\,\beta\,\hat{\mu}^2\right)\,b\,P_m(z,k). \tag{5.2.5}$$

Thus, using galaxy distribution and peculiar velocity power spectra, we are sensitive to (μ_θ,ζ). Notice that with these power spectra we can not distinguish μ from μ_m so we can not distinguish modified gravity from an imperfect dark matter fluid.

On the other hand, for the weak lensing power spectrum, we can see that the modification only enters in the growth evolution thanks to $P_m(z,k)$ or the growth factor $D(z)$. In addition, the convergence power spectrum depends on the combination $\Sigma(z)$ (1.4.20).

Σ	ζ	μ_θ	Underlying theory
1	1	1	ΛCDM
$\neq 1$	1	1	$MG\ \ \eta \neq 1$
1	$\neq 1$	1	BSV
1	1	$\neq 1$	-
1	$\neq 1$	$\neq 1$	$BSV + HNC$
$\neq 1$	1	$\neq 1$	-
$\neq 1$	$\neq 1$	1	$MG + BSV$
$\neq 1$	$\neq 1$	$\neq 1$	$MG + BSV + HNC$

Table 5.1: MG stands for modified gravity, BSV for bulk and shear viscosity, and HNC for heat flux and non-conserved fluid. If the underlying theory is $-$ means that this possible theory has a finetuning of the parameter values.

Thus, as shown in Chapter 4, we need $(\mu,\eta,\mu_m,\mu_d,\mu_\theta)$ to describe, in a model independent way, a general modification of Einstein equations and conservation equations, however, using galaxy power spectra, as we can see in equations (5.2.3-5.2.5) and (2.4.56), we are only sensitive to the following combinations: $D\,b$, $\mu_\theta\,D\,f$, $\Sigma\,D$ and the Hubble parameter H. Assuming that the galaxy bias is fixed by a bias model, the observables are able to constrain the three combinations $(\Sigma,\zeta,\mu_\theta)$ where,

$$\zeta(z,k) \equiv \frac{f(z,k)}{\Omega_m^\gamma(z)}, \tag{5.2.6}$$

$$\mu_\theta(z,k) \equiv -\frac{\theta(z,k)}{\mathcal{H}(z)f(z,k)\delta(z,k)}. \tag{5.2.7}$$

Therefore, parameters (μ, η) and (μ_m, μ_d) are degenerate.

Any deviation from one of any of the three mentioned parameters will imply a modification of General Relativity or a modification of the perfect-fluid description of dark matter. We summarize in Table 5.1 the different combinations of parameters and the compatible underlying theories. Thus, for example, we see that a detection of $\Sigma \neq 1$ with $\zeta = \mu_\theta = 1$ is only compatible with modified gravity. On the other hand, $\zeta \neq 1$ with $\Sigma = \mu_\theta = 1$ can only be produced by modified dark matter. Similarly, $\zeta \neq 1$ and $\mu_\theta \neq 1$ with $\Sigma = 1$ cannot be generated by modified gravity. On the contrary, we see that different from one measurements of the three parameters will not allow to distinguish whether the underlying theory is a modification of gravity or an imperfect dark matter.

Chapter 6

Forecasting non-standard cosmologies with galaxy surveys

In this chapter we will apply the Fisher formalism presented in previous chapters to forecast the precision with which future surveys will be able to measure our phenomenological parameters. Firstly, we will study the possibility of detecting a preferred direction. To do that, we need to generalize the Fisher matrices for galaxy distribution and weak lensing to allow the extra angular dependencies. Then we will analyze the simplest cases in which a preferred direction is considered which, for the galaxy distribution power spectra, correspond to the case with $\mu = \mu(x^2)$. In such a case, we can use the useful analytical approximation for the constant μ case (4.5.11). For the weak lensing power spectrum, we will consider the simplest case in which modified gravity parameters are constants. Notice that in this situation we have already an anisotropic effect due to the μ_Q and μ_h parameters. On the other hand, we will constrain the imperfect and non-conserved dark matter fluid model. In this situation we do not need to modify the standard Fisher matrices. We will consider the simplest case in which the effective parameters parameters are constant, then we will take into account time dependent phenomenological parametrizations. The results of this chapter correspond to [139, 223].

6.1 Forecasts on gravitational preferred directions

As mentioned above our goal is to analyze the impact of preferred directions effects in galaxy and weak lensing surveys. We will analyze the Fisher matrices for galaxy clustering, first considering the multipole power spectrum and then the redshift-space power spectrum. Then we will analyze the Fisher matrix for the weak lensing power spectrum. Finally, we will study the effects of primordial anisotropies.

6.1.1 Fisher analysis for the multipole power spectrum

We will start with the analysis of the multipole power spectrum for galaxy distribution (2.2.23). As we show in Chapter 3, considering a set of cosmological parameters $\{\theta_\alpha\}$ the Fisher matrix for the multipole power spectrum can be written as [133],

$$F_{\alpha\beta}^{\delta_\ell\delta_\ell}(z) = \sum_{c,c'}\sum_{\ell,\ell'} \left.\frac{\partial P_\ell(z,\mathbf{k}_c)}{\partial\theta_\alpha}\right|_r C^{-1}_{\ell\ell'}(\mathbf{k}_c,\mathbf{k}_{c'}) \left.\frac{\partial P_{\ell'}(z,\mathbf{k}_{c'})}{\partial\theta_\beta}\right|_r , \tag{6.1.1}$$

where sub-index r denotes that the corresponding quantity is evaluated on the fiducial model, $\mathbf{k}_c$ are the discrete modes and $C_{\ell\ell'}(\mathbf{k}_c,\mathbf{k}_{c'})$ is the covariance matrix. Now we need to extend the calculation of the covariance matrix done in Chapter 3 to the case in which we have an anisotropic power spectrum depending not only on the full wavevector $\mathbf{k}$, but also on its orientation with respect to the line of sight $\hat{n}$. We consider the estimator for the multipole power spectrum as (3.2.24) but in this situation the sum in modes is $\int_{\mathbf{k}_c} d^3k = V_s(\mathbf{k}_c) = k_c^2\, dk_c\, dx_c\, d\phi_c$, being $x_c = \cos\theta_c$, where the matter perturbation satisfies,

$$\langle\delta(z,\hat{\mu},\mathbf{k})\delta(z,\hat{\mu},\mathbf{k}')\rangle = \delta_D(\mathbf{k}+\mathbf{k}')\left[P_{gg}(z,\hat{\mu},\mathbf{k}) + \frac{1}{\bar{n}(z)}\right]. \tag{6.1.2}$$

With this estimator we can calculate the covariance matrix,

$$C_{\ell\ell'}(\mathbf{k}_c,\mathbf{k}_d) = \langle\hat{P}_\ell(z,\mathbf{k}_c)\hat{P}_{\ell'}(z,\mathbf{k}_d)\rangle - \langle\hat{P}_\ell(z,\mathbf{k}_c)\rangle\langle\hat{P}_{\ell'}(z,\mathbf{k}_d)\rangle. \tag{6.1.3}$$

As in the isotropic case, we consider only Gaussian perturbations satisfying (3.2.7), so that

$$C_{\ell\ell'}(\mathbf{k}_c,\mathbf{k}_d) = V_f^2\,\frac{(2\ell+1)(2\ell'+1)}{4}\int_{\mathbf{k}_c}\frac{d^3k}{V_s(\mathbf{k}_c)}\int_{\mathbf{k}_d}\frac{d^3k'}{V_s(\mathbf{k}_d)} \int_{-1}^{1}d\hat{\mu}\int_{-1}^{1}d\hat{\mu}'\mathcal{L}_\ell(\hat{\mu})\,\mathcal{L}_{\ell'}(\hat{\mu}') [\langle\delta(\hat{\mu},\mathbf{k})\delta(\hat{\mu}',\mathbf{k}')\rangle\,\langle\delta(\hat{\mu},-\mathbf{k})\delta(\hat{\mu}',-\mathbf{k}')\rangle + \langle\delta(\hat{\mu},\mathbf{k})\delta(\hat{\mu}',-\mathbf{k}')\rangle\,\langle\delta(\hat{\mu},-\mathbf{k})\delta(\hat{\mu}',\mathbf{k}')\rangle]\,. \tag{6.1.4}$$

At this stage we use the distant observer approximation in which we assume that the integrand of (6.1.4) is non negligible only when $\hat{\mu}'\simeq\hat{\mu}$, then we obtain,

$$C_{\ell\ell'}(\mathbf{k}_c,\mathbf{k}_d) \simeq V_f^2\,\frac{(2\ell+1)(2\ell'+1)}{2}\int_{\mathbf{k}_c}\frac{d^3k}{V_s(\mathbf{k}_c)}\int_{\mathbf{k}_d}\frac{d^3k'}{V_s(\mathbf{k}_d)} \int_{-1}^{1}d\hat{\mu}\,\mathcal{L}_\ell(\hat{\mu})\,\mathcal{L}_{\ell'}(\hat{\mu}) [\langle\delta(\hat{\mu},\mathbf{k})\delta(\hat{\mu},\mathbf{k}')\rangle\,\langle\delta(\hat{\mu},-\mathbf{k})\delta(\hat{\mu},-\mathbf{k}')\rangle + \langle\delta(\hat{\mu},\mathbf{k})\delta(\hat{\mu},-\mathbf{k}')\rangle\,\langle\delta(\hat{\mu},-\mathbf{k})\delta(\hat{\mu},\mathbf{k}')\rangle]\,. \tag{6.1.5}$$

Using (6.1.2) and taking into account once again that $\delta_D^2(x)=\delta_D(0)\delta_D(x)$ and $\delta_D(0)=1/V_f$, we obtain,

$$C_{\ell\ell'}(\mathbf{k}_c,\mathbf{k}_d) = V_f\,\frac{(2\ell+1)(2\ell'+1)}{2}\int_{\mathbf{k}_c}\frac{d^3k}{V_s(\mathbf{k}_c)}\int_{\mathbf{k}_d}\frac{d^3k'}{V_s(\mathbf{k}_d)} \int_{-1}^{1}d\hat{\mu}\,\mathcal{L}_\ell(\hat{\mu})\,\mathcal{L}_{\ell'}(\hat{\mu})\,[\delta_D(\mathbf{k}+\mathbf{k}')+\delta_D(\mathbf{k}-\mathbf{k}')] \left[P_{gg}(z,\hat{\mu},\mathbf{k})+\frac{1}{\bar{n}(z)}\right]\,\left[P_{gg}(z,\hat{\mu},-\mathbf{k})+\frac{1}{\bar{n}(z)}\right]. \tag{6.1.6}$$

As done before, we consider that $P_{gg}(z,\hat{\mu},\mathbf{k})\simeq P_{gg}(z,\hat{\mu},\mathbf{k}_c)$ in the integral and also that

$$\int_{\mathbf{k}_c}d^3\mathbf{k}\int_{\mathbf{k}_d}d^3\mathbf{k}'\;\delta_D(\mathbf{k}-\mathbf{k}') = V_s(\mathbf{k}_d)\,\delta_{k_c,k_d}\,\delta_{x_c,x_d}\,\delta_{\phi_c,\phi_d}, \tag{6.1.7}$$

and

$$\int_{\mathbf{k}_c}d^3\mathbf{k}\int_{\mathbf{k}_d}d^3\mathbf{k}'\;\delta_D(\mathbf{k}+\mathbf{k}') = V_s(\mathbf{k}_d)\,\delta_{k_c,k_d}\,\delta_{x_c,-x_d}\,\delta_{\phi_c,\phi_d+\pi}. \tag{6.1.8}$$

Using these expressions we obtain,

$$C_{\ell\ell'}(\mathbf{k}_c,\mathbf{k}_d) = \frac{V_f\,\delta_{k_c,k_d}}{V_s(\mathbf{k}_c)}\left[\delta_{x_c,x_d}\,\delta_{\phi_c,\phi_d}+\delta_{x_c,-x_d}\,\delta_{\phi_c,\phi_d+\pi}\right]\frac{(2\ell+1)(2\ell'+1)}{2} \int_{-1}^{1} d\hat{\mu}\,\mathcal{L}_\ell(\hat{\mu})\,\mathcal{L}_{\ell'}(\hat{\mu})\left[P_{gg}(z,\hat{\mu},\mathbf{k}_c)+\frac{1}{\bar{n}(z)}\right]\left[P_{gg}(z,\hat{\mu},-\mathbf{k}_c)+\frac{1}{\bar{n}(z)}\right]. \quad (6.1.9)$$

Now, in our case, we can consider that the fiducial power spectrum is of the form $P_{gg}(z,\hat{\mu},\mathbf{k}_c) = P_{gg}(z,\hat{\mu},k_c)$. The anisotropic contribution of the power spectrum only depends on x^2 due to the effective parameters so, when we sum indices in the Fisher matrix we can replace $\delta_{x_c,-x_d}$ by δ_{x_c,x_d}, and we can integrate in ϕ_c so that $V_s(\mathbf{k}_c) = 2\pi k_c^2\,dk_c\,dx_c$. Considering this approximations the covariance matrix is,

$$C_{\ell\ell'}(\mathbf{k}_c,\mathbf{k}_d) = \delta_{\mathbf{k}_c,\mathbf{k}_d}\,\frac{2\,V_f}{V_s(\mathbf{k}_c)}\,\frac{(2\ell+1)(2\ell'+1)}{2}\int_{-1}^{1} d\hat{\mu}\,\mathcal{L}_\ell(\hat{\mu})\,\mathcal{L}_{\ell'}\,(\hat{\mu})\left[P_{gg}(z,\hat{\mu},k_c)+\frac{1}{\bar{n}(z)}\right]^2. \quad (6.1.10)$$

Summing in the modes, the Fisher matrix (6.1.1) becomes,

$$F^{\delta_\ell\delta_\ell}_{\alpha\beta}(z) = \frac{V(z)}{8\pi^2}\int_{k_{min}}^{k_{max}} dk\int_{-1}^{1} dx\,k^2\,\left.\frac{\partial P_\ell(z,k,x)}{\partial\theta_\alpha}\right|_r C^{-1}_{\ell\ell'}(z,k)\,\left.\frac{\partial P_{\ell'}(z,k,x)}{\partial\theta_\beta}\right|_r, \quad (6.1.11)$$

being,

$$C_{\ell\ell'}(z,k) = \frac{(2\ell+1)(2\ell'+1)}{2}\int_{-1}^{1} d\hat{\mu}\,\mathcal{L}_\ell(\hat{\mu})\,\mathcal{L}_{\ell'}(\hat{\mu})\left[P_{gg}(z,\hat{\mu},k)+\frac{1}{\bar{n}(z)}\right]^2. \quad (6.1.12)$$

Notice that this Fisher matrix is reduced to the standard one (3.2.30) when $P_\ell(z,k,x) = P_\ell(z,k)$ and we integrate in x. Now we will analyze our phenomenological parametrization for a preferred direction (5.1.5)-(5.1.4). For simplicity, we do not considering the Alcock-Paczynski effect for the multipole power spectrum analysis because, as can be see in Chapter 2, it would introduce complicated terms in expressions (2.2.24-2.2.26). We will study the simplest case in which,

$$\mu = \mu_0 + \mu_2\,x^2 + \mu_4\,x^4 + O(x^6). \quad (6.1.13)$$

In this situation the galaxy distribution power spectrum can be written as,

$$P_{gg}(z,\hat{\mu},x,k) = \left[(1+\xi\,\beta_\Lambda\,\hat{\mu}^2)\,b(z)\,D^\xi_\Lambda\right]^2\,P(k,x), \quad (6.1.14)$$

where the $\xi = \xi(\mu(x))$ parameter follows equation (4.5.10) and μ equation (6.1.13). Here we have extracted the growth factor form the matter power spectrum

$$P_m(z,k,x) = D(z,x)\,P(k,x), \tag{6.1.15}$$

being $P(k,x)$ the matter power spectrum today which can be related with the matter power spectrum today in ΛCDM model $P_\Lambda(k)$ as,

$$P(k,x) = \exp\left[2\int_0^{z_{mat}} \frac{f(z',k,x) - f_\Lambda(z')}{1+z'} dz'\right] P_\Lambda(k), \tag{6.1.16}$$

where $f_\Lambda(z)$ is the growth function in ΛCDM and we have assumed that for $z > z_{mat}$, $f(z,k,x) = f_\Lambda(z)$. For the sake of concreteness in the forecast analysis we will assume that $z_{mat} = 10$ although the results are not very sensitive to its precise value. Finally, $\beta_\Lambda \equiv f_\Lambda/b$ and, since we are considering the constant case, $D(z,x) = D_\Lambda(x)^\xi$. In each redshift bin, we will consider as free parameters bD_Λ and the parameters of the model μ_0, μ_2, μ_4. For simplicity, we will not marginalize with respect to $P_\Lambda(k)$. As we will see in detail in next chapter, the galaxy distribution power spectrum depends on three independent parameters in each redshift bin considering the Alcock-Paczynski effect and two without considering it. For the case of a preferred direction, each additional independent anisotropic dependence in x adds an additional freedom. For the fiducial model we assume ΛCDM and we will obtain the constraints for specifications of an Euclid like survey, these specifications can be found in 6.A. We will first consider as independent parameters in each bin $[b\,D_\Lambda, \mu_0, \mu_2]$

z	k_{max}	$\delta\mu_0/\mu_0(\%)$	$\delta\mu_2/\mu_0(\%)$
0.6	0.195	1.77	3.88
0.8	0.225	1.08	1.99
1.0	0.260	0.73	1.06
1.2	0.299	0.66	0.77
1.4	0.343	0.62	0.59
1.8	0.447	0.65	0.57

Table 6.1: Redshift bins, k_{max} values in h/Mpc units and relative errors for μ_0 and μ_2 for an Euclid-like survey. We compare $\delta\mu_2$ with respect to μ_0 because the fiducial value of μ_2 is zero.

and we present the marginalized errors for μ_0 and μ_2 in Table 6.1. In Fig. 6.1 left panel we

plot the 1-sigma and 2-sigma contours summing all the information in the whole redshift range. In such a case we obtain errors for μ_0 and μ_2 of order 1 %. Then, we add the parameter μ_4 in each bin and we present the marginalized errors for μ_0, μ_2 and μ_4 in Table 6.2. In Fig. 6.1 right panel we plot the 1-σ and 2-σ contours for μ_2 and μ_4 summing all the information in the full redshift range. As we can see, if we add a x^4 dependence, the errors for μ_2 increase in a factor $3-4$ but the errors for μ_0 remain the same. Errors for μ_4 are slightly larger than for μ_2.

z	k_{max}	$\delta\mu_0/\mu_0(\%)$	$\delta\mu_2/\mu_0(\%)$	$\delta\mu_4/\mu_0(\%)$
0.6	0.195	2.20	13.6	15.2
0.8	0.225	1.27	6.96	7.78
1.0	0.260	0.81	3.71	4.15
1.2	0.299	0.71	2.69	3.01
1.4	0.343	0.66	2.06	2.30
1.8	0.447	0.67	1.99	2.22

Table 6.2: Redshift bins, k_{max} values in h/Mpc units and relative errors for μ_0 and μ_2 and μ_4 for an Euclid-like survey. We compare $\delta\mu_2$ and $\delta\mu_4$ with respect to μ_0 because the fiducial values of μ_2 and μ_4 are zero.

6.1.2 Fisher analysis for the redshift-space power spectrum

An alternative way to perform the Fisher analysis consists in using the redshift-space power spectrum P_{gg} rather than the multipoles considered in the previous analysis. This, in fact, allows to take into account the Alcock-Paczynski effect [85] so that we can write

$$P_{gg}(z,\hat{\mu}_r,x,k_r) = \frac{H_r\,D_A^2}{H\,D_{A\,r}^2}\,\left[(1+\xi\,\beta_\Lambda\,\hat{\mu}^2)\,b(z)\,D_\Lambda^\xi\right]^2\,P(k,x), \tag{6.1.17}$$

where $k=k(k_r)$ and $\hat{\mu}=\hat{\mu}(\hat{\mu}_r)$ are given by equations (2.2.33)-(2.2.35). Thus, considering a set of cosmological parameters $\{\theta_\alpha\}$, the corresponding Fisher matrix for clustering at a given redshift bin centered at z_a and for a solid angle of the survey centered at the line of sight $\hat{n}$ is,

$$dF_{\alpha\beta}^{\delta\delta} = \frac{1}{2}\int \frac{d^3k}{(2\pi)^3}\,\left.\frac{\partial\log P_{gg}}{\partial\theta_\alpha}\right|_r\,\left.\frac{\partial\log P_{gg}}{\partial\theta_\beta}\right|_r\,\left.\left[\frac{\bar{n}P_{gg}}{1+\bar{n}P_{gg}}\right]\right|_r dV_s, \tag{6.1.18}$$

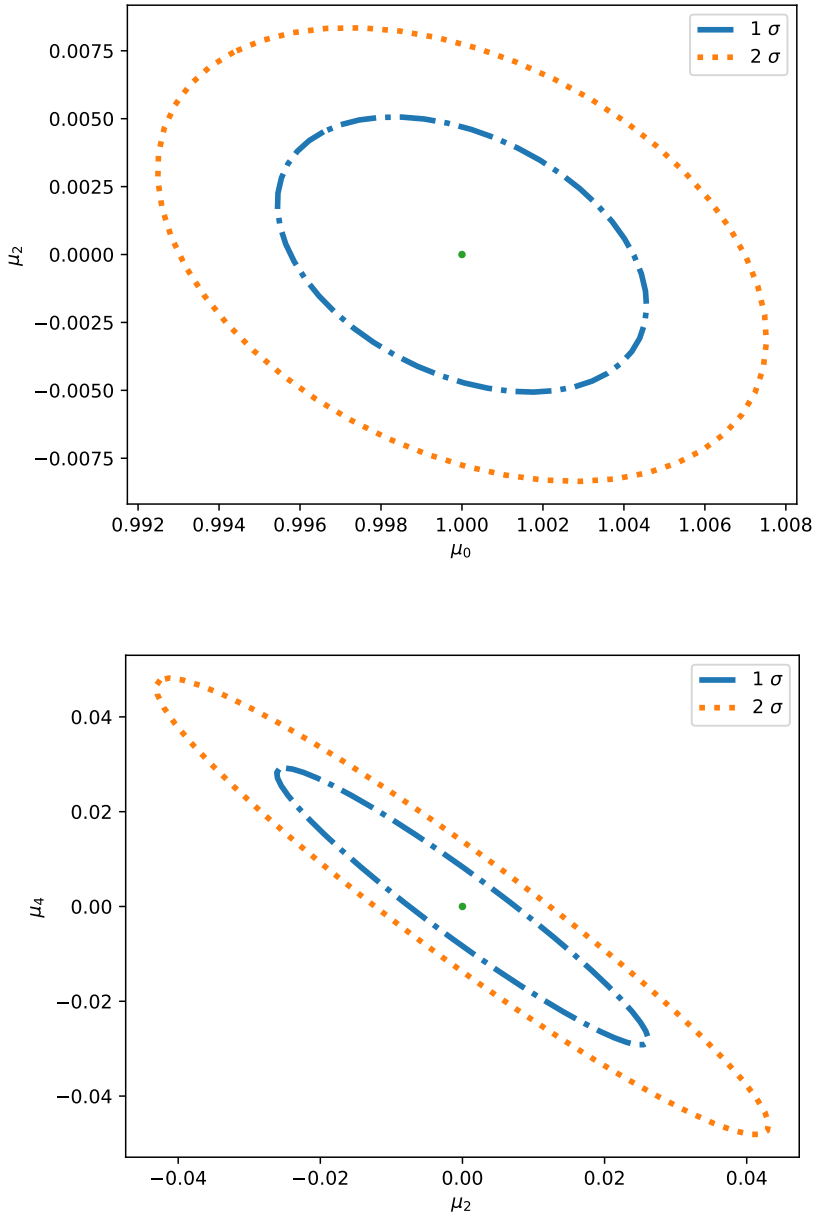

Figure 6.1: Top: marginalized 1σ and 2σ regions for μ_0 and μ_2 for an Euclid-like survey from the multipole power spectrum information. Bottom: marginalized 1σ and 2σ regions for μ_2 and μ_4 for an Euclid-like survey from the multipole power spectrum information.

where,

$$dV_s = V_z \, d\varphi \, d\theta \, \sin\theta, \tag{6.1.19}$$

and

$$V_z = \frac{1}{3} \left[\chi(\bar{z}_a)^3 - \chi(\bar{z}_{a-1})^3 \right], \tag{6.1.20}$$

with $\hat{n}(\theta, \varphi)$ where φ and θ are the azimuthal and polar angles in the axes frame on the left panel of Fig. 6.2.

Since we are interested in summing all the angular information, we have to integrate over the angles φ and θ but taking into account that $\frac{\partial \log P_{gg}}{\partial \theta_\alpha}\Big|_r$ may depend on these angles. Thus, we integrate a spherical cap that encloses a fraction f_{sky} of the sky,

$$F^{\delta\delta}_{\alpha\beta} = \frac{1}{2} \int \frac{d^3k}{(2\pi)^3} \int_0^{2\pi} d\varphi \int_0^{\arccos(1-2f_{sky})} \sin\theta \, d\theta \; \frac{\partial \log P_{gg}}{\partial \theta_\alpha}\bigg|_r \; \frac{\partial \log P_{gg}}{\partial \theta_\beta}\bigg|_r \; \left[\frac{\bar{n} P_{gg}}{1 + \bar{n} P_{gg}} \right]\bigg|_r V_z. \tag{6.1.21}$$

The only angular dependences we have are $\hat{\mu} = \hat{\boldsymbol{k}} \cdot \hat{\boldsymbol{n}}$ and $x = \hat{\boldsymbol{k}} \cdot \hat{\boldsymbol{A}}$. It is useful to keep $\hat{\mu}$ as an integration variable, so that we have to relate x with $\hat{\mu}$. With the choice of axes of Fig. 6.2, we find that,

$$x = \sin\alpha' \sqrt{1 - \hat{\mu}^2} \, \cos\rho + \cos\alpha' \, \hat{\mu}, \tag{6.1.22}$$

and,

$$\cos\alpha' = \sin\alpha \, \sin\theta \, \cos(\varphi - \phi) + \cos\alpha \, \cos\theta, \tag{6.1.23}$$

being $\hat{\boldsymbol{A}}(\alpha, \phi)$ with α and ϕ the polar and azimuthal angles in the axes frame in Fig. 6.2 left, where the Z axis is chosen in the direction of the center of the survey **c**. Thus, $x = x(\alpha, \phi, \hat{\mu}, \rho, \theta, \varphi)$ so that we have the following integration variables $[k, \hat{\mu}, \rho, \theta, \varphi]$. Finally, we have chosen as independent parameters for the Fisher matrix in each bin: $[E, b\, D_\Lambda, \mu_0, \mu_2, \mu_4]$, where $E \equiv H/H_0$. For these parameters the derivatives are,

$$\frac{\partial \log P_{gg}}{\partial E}\bigg|_r = 1 + \frac{2\,\Delta z_a}{E^2 \, H_0 \, \chi(z_a)} + \frac{4\beta_\Lambda \hat{\mu}^2 (1 - \hat{\mu}^2)}{1 + \beta_\Lambda \, \hat{\mu}^2} \left(\frac{1}{E} - \frac{\Delta z_a}{E^2 \, H_0 \, \chi(z_a)} \right), \tag{6.1.24}$$

$$\frac{\partial \log P_{gg}}{\partial \left(b D_\Lambda \right)}\bigg|_r = \frac{2}{b D_\Lambda}, \tag{6.1.25}$$

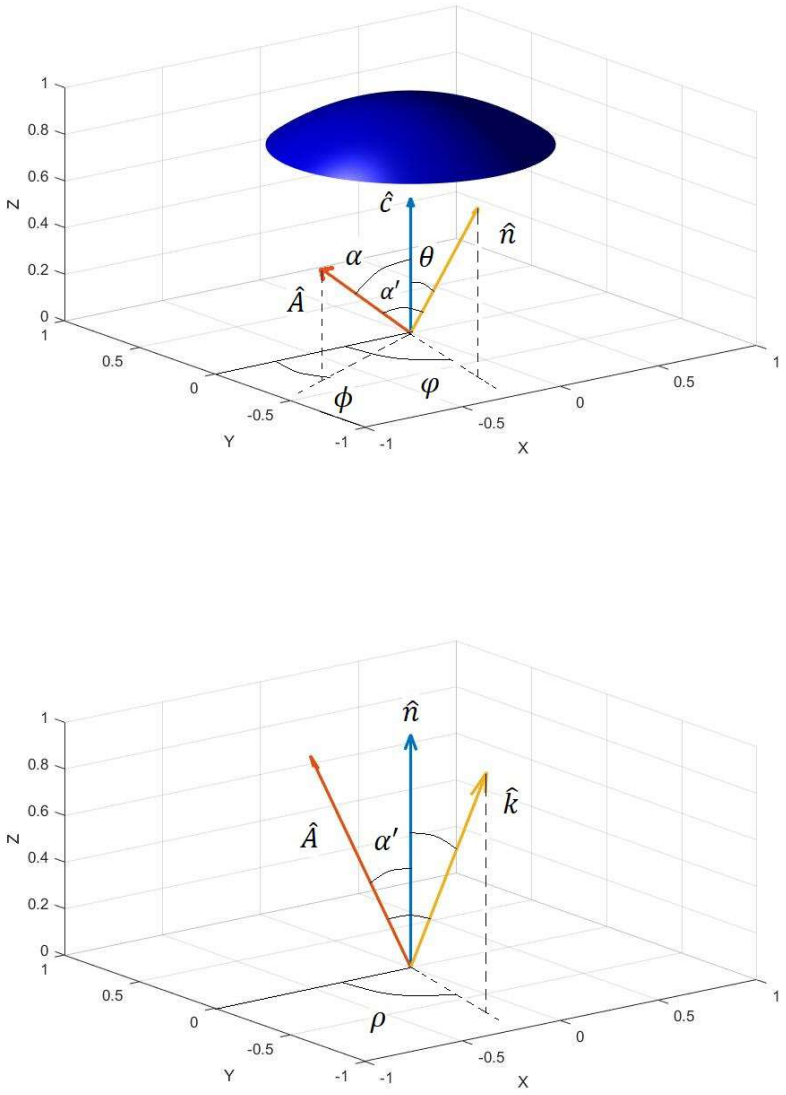

Figure 6.2: From top to bottom, reference frame for the Fisher analysis of the redshift space power spectrum, and auxiliary reference frame to calculate the integral in **k**.

$$\left.\frac{\partial \log P_{gg}}{\partial \mu_0}\right|_r = \frac{6}{5}\left[\log D_\Lambda + \int_{\bar{z}_{i-1}}^{\bar{z}_i} \frac{f_\Lambda(z')}{1+z'}dz' + \frac{\beta_\Lambda\,\hat{\mu}^2}{1+\beta_\Lambda\,\hat{\mu}^2}\right], \tag{6.1.26}$$

$$\left.\frac{\partial \log P_{gg}}{\partial \mu_2}\right|_r = \left.\frac{\partial \log P_{gg}}{\partial \mu_0}\right|_r x^2, \tag{6.1.27}$$

$$\left.\frac{\partial \log P_{gg}}{\partial \mu_4}\right|_r = \left.\frac{\partial \log P_{gg}}{\partial \mu_0}\right|_r x^4. \tag{6.1.28}$$

As we can see, the only angular dependence appears in the derivatives with respect to μ_2 and μ_4 which involve even powers of x. Thus, we can extract this dependence and define the following function,

$$\begin{aligned} f^x_{\alpha\beta}(\hat{\mu},\alpha,\phi) = \int_0^{2\pi} d\varphi \int_0^{\arccos(1-2f_{sky})} \sin\theta\, d\theta \int_0^{2\pi} d\rho \quad & (\delta_{1\alpha}+\delta_{2\alpha}+\delta_{3\alpha}+x^2\,\delta_{4\alpha}+x^4\,\delta_{5\alpha}) \\ \times \quad & (\delta_{1\beta}+\delta_{2\beta}+\delta_{3\beta}+x^2\,\delta_{4\beta}+x^4\,\delta_{5\beta}), \end{aligned} \tag{6.1.29}$$

here $x = x(\alpha,\phi,\hat{\mu},\rho,\theta,\varphi)$ and $\alpha,\beta = E, bD_\Lambda, \mu_0, \mu_2, \mu_4 = 1,2,3,4,5$. Notice that for $\alpha,\beta = 1,2,3$ we have $f^x_{\alpha\beta} = 8\pi^2\, f_{sky}$, and we recover the isotropic case for the Fisher matrix. Finally, the Fisher matrix for the redshift-space power spectrum in the presence of a preferred direction pointing in the (α,ϕ) direction can be written as,

$$F^{\delta\delta}_{\alpha\beta}(z,\alpha,\phi) = \frac{V_z}{16\,\pi^3}\int_{-1}^{1} d\hat{\mu} \int_{k_{min}}^{k_{max}} k^2\, \left.\frac{\partial \log P_{gg}}{\partial \theta_\alpha}\right|_r \left.\frac{\partial \log P_{gg}}{\partial \theta_\beta}\right|_r f^x_{\alpha\beta}(\hat{\mu},\alpha,\phi)\, \left.\left[\frac{\bar{n}P_{gg}}{1+\bar{n}P_{gg}}\right]\right|_r dk, \tag{6.1.30}$$

where in this expression,

$$\left.\frac{\partial \log P_{gg}}{\partial p_4}\right|_r = \left.\frac{\partial \log P_{gg}}{\partial p_5}\right|_r = \left.\frac{\partial \log P_{gg}}{\partial \mu_0}\right|_r. \tag{6.1.31}$$

Notice that the final Fisher matrix (6.1.30) depends on the angles (α,ϕ). We could have considered them as additional cosmological parameters θ_α and obtain and extended Fisher matrix. However, since we are considering an isotropic fiducial model, the corresponding entries would be identically zero. Instead, we will study that dependence of the errors on

the orientation of the vector $\hat{\boldsymbol{A}}$. Thus, we find that errors are maximized for $\alpha = 0$, i.e. when the preferred direction points towards the center of the survey, for any value of ϕ, whereas they are minimized for $\alpha = \pi/2$ for any value of ϕ. Notice that in any case errors vary at most in a 10% of their values. We use the same fiducial cosmology as before for an Euclid-like survey 6.A. Results are summarized in Table 6.3 and in Fig. 6.3 we plot the 1-σ and 2-σ contours for μ_2 and μ_4 summing all the information in each bin.

z	k_{max}	$\delta\mu_0/\mu_0(\%)$	$\delta\mu_2/\mu_0(\%)$	$\delta\mu_4/\mu_0(\%)$
0.6	0.195	2.60	14.8	17.1
0.8	0.225	1.47	7.39	8.68
1.0	0.260	0.99	4.03	4.67
1.2	0.299	0.92	3.03	3.48
1.4	0.343	0.89	2.40	2.74
1.8	0.447	0.87	2.30	2.61

Table 6.3: Redshift bins, k_{max} values in h/Mpc units and relative errors for μ_0, μ_2 and μ_4 for an Euclid-like survey using the redshift space power spectrum with $\alpha = 0$. We compare $\delta\mu_2$ and $\delta\mu_4$ with respect to μ_0 because their fiducial values are zero.

As we can see, with this method we obtain slightly larger errors for μ_0, μ_2 and μ_4 than in the previous analysis. This is because in this situation we are also marginalizing $E(z)$ due to the Alcock-Paczynski effect.

6.1.3 Fisher analysis for the weak lensing power spectrum

Now we will perform the Fisher analysis for the weak lensing power spectrum. Once again, with that purpose we have to extend the Fisher matrix formalism to consider the presence of a preferred direction. Thus, we analyze the multipole power spectrum for the convergence (5.1.57) and sum over all the multipoles r and $\boldsymbol{\ell}$. The Fisher matrix is of the following form,

$$F^{\kappa\kappa}_{\alpha\beta} = \sum_{\boldsymbol{\ell}_c,\boldsymbol{\ell}_d} \sum_{rr'} \left.\frac{\partial P^{r}_{\kappa\, ab}(\boldsymbol{\ell}_c)}{\partial\theta_\alpha}\right|_r \left[\mathrm{Cov}^{rr'}_{ba'b'a}(\boldsymbol{\ell}_c,\boldsymbol{\ell}_d)\right]^{-1} \left.\frac{\partial P^{r'}_{\kappa\, a'b'}(\boldsymbol{\ell}_d)}{\partial\theta_\beta}\right|_r , \tag{6.1.32}$$

where we are summing in indexes a, b, a' and b'. Now we have to obtain the covariance matrix for the case in which the power spectrum depends not only on the full $\boldsymbol{\ell}$ vector but

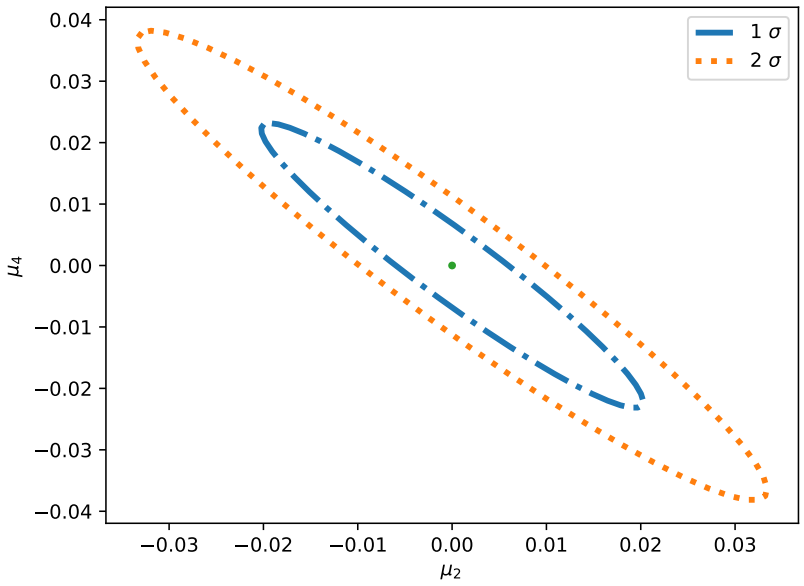

Figure 6.3: Marginalized 1σ and 2σ regions for μ_2 and μ_4 using the information of the redshift space power spectrum and considering $\alpha = 0$ for an Euclid-like survey

also we have a dependence on the observation direction $\hat{\boldsymbol{n}}$, in particular a polar dependence ($\xi = \hat{\boldsymbol{n}} \cdot \hat{\boldsymbol{A}}$) where $\hat{\boldsymbol{A}}$ is the preferred direction. We define the estimator for this multipole power spectrum in the following way,

$$\hat{P}^r_{ab}(\boldsymbol{\ell_c}) = A_f \int_{\boldsymbol{\ell}_c} \frac{d^2\ell}{A_s(\boldsymbol{\ell}_c)} \frac{2r+1}{2} \int_{-1}^{1} d\xi\, \kappa_a(\boldsymbol{\ell}, \xi)\kappa_b(-\boldsymbol{\ell}, \xi)\, \mathcal{L}_r(\xi), \tag{6.1.33}$$

being $\int_{\boldsymbol{\ell}_c} d^2\ell = A_s(\boldsymbol{\ell}_c) = \ell_c d\ell_c d\phi_c$, where $\cos\phi_c = \Upsilon_c$ (5.1.36). Where the perturbation κ_a satisfies,

$$\langle \kappa_a(\boldsymbol{\ell}_1, \xi)\kappa_b(\boldsymbol{\ell}_2, \xi)\rangle = \delta_D(\boldsymbol{\ell}_1 + \boldsymbol{\ell}_2)\, C_{ab}(\boldsymbol{\ell}_1, \xi), \tag{6.1.34}$$

being C_{ab} the observable convergence power spectrum with the shot noise effect (3.4.4). Using this estimator we can calculate the covariance matrix,

$$C^{rr'}_{aba'b'}(\boldsymbol{\ell}_c, \boldsymbol{\ell}_d) = \langle \hat{P}^r_{ab}(\boldsymbol{\ell}_c)\hat{P}^{r'}_{a'b'}(\boldsymbol{\ell}_d)\rangle - P^r_{ab}(\boldsymbol{\ell}_c)P^{r'}_{a'b'}(\boldsymbol{\ell}_d). \tag{6.1.35}$$

As in the previous case, we consider only Gaussian perturbations (3.2.7), so that

$$C^{rr'}_{aba'b'}(\boldsymbol{\ell}_c,\boldsymbol{\ell}_d) = A_f^2\,\frac{(2r+1)(2r'+1)}{4}\int_{\boldsymbol{\ell}_c}\frac{d^2\ell}{A_s(\boldsymbol{\ell}_c)}\int_{\boldsymbol{\ell}_d}\frac{d^2\ell'}{A_s(\boldsymbol{\ell}_d)} \int_{-1}^{1}d\xi\int_{-1}^{1}d\xi'\mathcal{L}_r(\xi)\,\mathcal{L}_{r'}(\xi') [\langle\kappa_a(\boldsymbol{\ell},\xi)\kappa_{a'}(\boldsymbol{\ell}',\xi')\rangle\,\langle\kappa_b(-\boldsymbol{\ell},\xi)\kappa_{b'}(-\boldsymbol{\ell}',\xi')\rangle + \langle\kappa_a(\boldsymbol{\ell},\xi)\kappa_{b'}(-\boldsymbol{\ell}',\xi')\rangle\,\langle\kappa_b(-\boldsymbol{\ell},\xi)\kappa_{a'}(\boldsymbol{\ell}',\xi')\rangle]\,. \tag{6.1.36}$$

At this stage we use once again the distant observer approximation, in which we assume that the integrand of (6.1.36) is non negligible only when $\xi'\simeq\xi$, then we obtain,

$$C^{rr'}_{aba'b'}(\boldsymbol{\ell}_c,\boldsymbol{\ell}_d) \simeq A_f^2\,\frac{(2r+1)(2r'+1)}{2}\int_{\boldsymbol{\ell}_c}\frac{d^2\ell}{A_s(\boldsymbol{\ell}_c)}\int_{\boldsymbol{\ell}_d}\frac{d^2\ell'}{A_s(\boldsymbol{\ell}_d)} \int_{-1}^{1}d\xi\,\mathcal{L}_r(\xi)\,\mathcal{L}_{r'}(\xi) [\langle\kappa_a(\boldsymbol{\ell},\xi)\kappa_{a'}(\boldsymbol{\ell}',\xi)\rangle\,\langle\kappa_b(-\boldsymbol{\ell},\xi)\kappa_{b'}(-\boldsymbol{\ell}',\xi)\rangle + \langle\kappa_a(\boldsymbol{\ell},\xi)\kappa_{b'}(-\boldsymbol{\ell}',\xi)\rangle\,\langle\kappa_b(-\boldsymbol{\ell},\xi)\kappa_{a'}(\boldsymbol{\ell}',\xi)\rangle]\,. \tag{6.1.37}$$

Using (6.1.34) and taking into account once more $\delta_D^2(x)=\delta_D(0)\delta_D(x)$ and $\delta_D(0)=1/A_f$, we obtain,

$$C^{rr'}_{aba'b'}(\boldsymbol{\ell}_c,\boldsymbol{\ell}_d) \approx A_f\,\frac{(2r+1)(2r'+1)}{2}\int_{\boldsymbol{\ell}_c}\frac{d^2\ell}{A_s(\boldsymbol{\ell}_c)}\int_{\boldsymbol{\ell}_d}\frac{d^2\ell'}{A_s(\boldsymbol{\ell}_d)} \int_{-1}^{1}d\xi\,\mathcal{L}_r(\xi)\,\mathcal{L}_{r'}(\xi)\,[\delta_D(\boldsymbol{\ell}+\boldsymbol{\ell}')C_{aa'}(\boldsymbol{\ell},\xi)\,C_{bb'}(-\boldsymbol{\ell},\xi)+\delta_D(\boldsymbol{\ell}-\boldsymbol{\ell}')C_{ab'}(\boldsymbol{\ell},\xi)\,C_{ba'}(-\boldsymbol{\ell},\xi)]\,, \tag{6.1.38}$$

As done before, we consider that $C_{ab}(\boldsymbol{\ell},\xi)\simeq C_{ab}(\boldsymbol{\ell_c},\xi)$ in the integral and also that,

$$\int_{\boldsymbol{\ell}_c}d^2\boldsymbol{\ell}\int_{\boldsymbol{\ell}_d}d^2\boldsymbol{\ell}'\;\delta_D(\boldsymbol{\ell}-\boldsymbol{\ell}') = A_s(\ell_d)\,\delta_{\ell_c\ell_d}\,\delta_{\phi_c\phi_d}, \tag{6.1.39}$$

and

$$\int_{\boldsymbol{\ell}_c}d^2\boldsymbol{\ell}\int_{\boldsymbol{\ell}_d}d^2\boldsymbol{\ell}'\;\delta_D(\boldsymbol{\ell}+\boldsymbol{\ell}') = A_s(\ell_d)\,\delta_{\ell_c\ell_d}\,\delta_{\phi_c\phi_d+\pi}, \tag{6.1.40}$$

so that we finally obtain,

$$C^{rr'}_{aba'b'}(\boldsymbol{\ell}_c,\boldsymbol{\ell}_d) = \frac{A_f\,\delta_{\ell_c\ell_d}}{A_s(\boldsymbol{\ell}_c)}\,\frac{(2r+1)(2r'+1)}{2}\int_{-1}^{1} d\xi\,\mathcal{L}_r(\xi)\,\mathcal{L}_{r'}(\xi) \times\left[\delta_{\phi_c\phi_d+\pi}\,C_{aa'}(\boldsymbol{\ell_c},\xi)\,C_{bb'}(-\boldsymbol{\ell}_c,\xi)+\delta_{\phi_c\phi_d}\,C_{ab'}(\boldsymbol{\ell_c},\xi)\,C_{ba'}(-\boldsymbol{\ell}_c,\xi)\right]. \quad (6.1.41)$$

Notice that if the only dependence in ϕ_c is in the form of Υ_c^2, then $\delta_{\phi_c\phi_d} = \delta_{\phi_c\phi_d+\pi} = \delta_{\Upsilon_c\Upsilon_d}$. If we further consider that the fiducial power spectrum is isotropic, we obtain the final result,

$$C^{rr'}_{aba'b'}(\boldsymbol{\ell}_c,\boldsymbol{\ell}_d) = \frac{2\pi\,(2r+1)\,\delta_{\boldsymbol{\ell}_c\boldsymbol{\ell}_d}\delta_{rr'}}{f_{sky}\,(2\ell_c+1)d\ell_c d\phi_c}\,[C_{aa'}(\ell_c)C_{bb'}(\ell_c)+C_{ab'}(\ell_c)C_{ba'}(\ell_c)], \quad (6.1.42)$$

here $\delta_{\boldsymbol{\ell}_c\boldsymbol{\ell}_d} = \delta_{\ell_c\ell_d}\delta_{\Upsilon_c\Upsilon_d}$ and we have approximated once more $\ell \simeq (2\ell+1)/2$. Notice that, because we are considering that in the fiducial model the convergence power spectrum has no extra anisotropies, different multipoles in r are not mixed in the covariance matrix unlike in the covariance matrix for the multipole power spectrum of galaxy distribution. Considering this covariance matrix, the Fisher matrix (6.1.32) becomes,

$$F^{\kappa\kappa}_{\alpha\beta} = f_{sky}\int_{-1}^{1}\frac{d\Upsilon}{\pi\sqrt{1-\Upsilon^2}}\sum_r\sum_\ell \Delta\ln\ell\,\frac{(2\ell+1)\,\ell}{2\,(2r+1)}\left.\frac{\partial P^r_{\kappa\,ab}}{\partial\theta_\alpha}\right|_r C^{-1}_{ba'}\left.\frac{\partial P^r_{\kappa\,a'b'}}{\partial\theta_\beta}\right|_r C^{-1}_{b'a}, \quad (6.1.43)$$

where C_{ab} follows equation (3.4.4). We sum in ℓ with $\Delta\ln\ell = 0.1$ from $\ell_{min} = 5$ to ℓ_{max}, where ℓ_{max} values are obtained in order to consider linear scales [225] and can be found in Table 6.4. For the multipole power spectrum we use the following expression,

$$P^r_{\kappa\,ab}(\ell,\Upsilon) = \frac{1}{4}\sum_{a'} P_{ab}(z_{a'},\ell)\;M^r_\alpha(\Upsilon). \quad (6.1.44)$$

where

$$P_{ab}(z_{a'},\ell) = \frac{9\,H_0^3\,\Omega_m^2}{4}\,\frac{(1+z_{a'})^2}{E_{a'}}\Delta z_{a'}\,g_a(z_{a'})\,g_b(z_{a'})\,D^2_{a'}\,P\left(\frac{\ell}{\chi(z_{a'})}\right). \quad (6.1.45)$$

Regarding the parameters θ_α, it can be proved that in each bin, the power spectrum depends on four independent parameters, which are chosen as (E_a, η_a, $\mu_{Q\,a}$, $\mu_{h\,a}$) where the sub-index a denotes different redshift bins, so that we have a total Fisher matrix of size $4n\times 4n$, being n the total number of z bins. For the sake of simplicity, we will consider

z	ℓ_{max}	$\delta\eta/\eta(\%)$	$\delta\mu_Q/\mu(\%)$	$\delta\mu_h/\mu(\%)$
0.6	311	6.75	0.64	1.48
0.8	385	5.43	1.45	3.04
1.0	515	9.27	2.71	4.73
1.2	609	20.6	6.70	9.18
1.4	760	70.5	23.0	24.9
1.8	959	816	250	324

Table 6.4: Redshift bins, ℓ_{max} values calculated following Section 3.4 and relative errors for η, μ_Q and μ_h for the Euclid forecast. We compare μ_Q and μ_h with μ because the fiducial values of μ_Q and μ_h are zero.

that the modified gravity parameters are isotropic and scale invariant, i.e. $\eta_a = \eta(z_a)$, $\mu_{Q\,a} = \mu_Q(z_a)$ and $\mu_{h\,a} = \mu_h(z_a)$. The (non-vanishing) derivatives, which are evaluated in ΛCDM as fiducial model, are,

$$\left.\frac{\partial P^0_{\kappa\ ab}}{\partial \eta_{a'}}\right|_r = P_{ab}(z_{a'}), \tag{6.1.46}$$

$$\left.\frac{\partial P^1_{\kappa\ ab}}{\partial \mu_{Q\ a'}}\right|_r = -4\,P_{ab}(z_{a'}), \tag{6.1.47}$$

$$\left.\frac{\partial P^0_{\kappa\ ab}}{\partial \mu_{h\ a'}}\right|_r = \frac{2}{3}\,(2-\Upsilon^2)\,P_{ab}(z_{a'}), \tag{6.1.48}$$

$$\left.\frac{\partial P^2_{\kappa\ ab}}{\partial \mu_{h\ a'}}\right|_r = \frac{4}{3}\,(2-\Upsilon^2)\,P_{ab}(z_{a'}), \tag{6.1.49}$$

$$\begin{aligned}\left.\frac{\partial P^0_{\kappa\ ab}}{\partial E_{a'}}\right|_r = &-\frac{P_{ab}(z_{a'})}{E_{a'}} + \sum_{b'}\,\frac{1}{g_a(z_{b'})}\frac{\partial g_a(z_{b'})}{\partial E_{a'}}\,P_{ab}(z_{b'}) \\ &+ \sum_{b'}\,\frac{1}{g_b(z_{b'})}\frac{\partial g_b(z_{b'})}{\partial E_{a'}}\,P_{ab}(z_{b'}),\end{aligned} \tag{6.1.50}$$

with,

$$\frac{\partial g_a(z_{b'})}{\partial E_{a'}} = \frac{\Delta z_{a'}}{H_0\, E_{a'}^2}\left[-\hat{\theta}(z_{a'}-z_{b'})\,\chi(z_{b'})\int_{z_{a'}}^{\infty}\frac{n_a(z')}{\chi(z')^2}\,dz' + \theta(z_{b'}-z_{a'})\int_{z_{b'}}^{\infty}\left(1-\frac{\chi(z_{b'})}{\chi(z')}\right)\frac{n_a(z')}{\chi(z')}\,dz'\right], \tag{6.1.51}$$

where we have discretized the integration of $E(z)^{-1}$ in $\chi(z)$ for the different bins, and the step functions $\theta(z)$ and $\hat{\theta}(x)$ are defined so that $\hat{\theta}(0) = 0$ and $\theta(0) = 1$. We consider an Euclid like survey, the specifications are detailed in (6.A). We summarize the results in Table 6.4 and in Fig. 6.4 left panel. Finally, if we further assume that η, μ_Q and μ_h are just constants, we can sum the information in all redshift bins. We plot the corresponding 1-σ and 2-σ contours for μ_Q and μ_h in Fig. 6.4 right panel.

We can see that lensing convergence measurements are very sensitive to the dipole term $P^1_{\kappa ij}$, so that errors in μ_Q are much smaller than for η and μ_h. Notice also that multipoles $r = 3, 4$ do not appear in the derivatives (6.1.46)-(6.1.50) since those terms are quadratic in μ_Q and μ_h so that on the fiducial ΛCDM cosmology the corresponding derivatives vanish. For the same reason, the Fisher matrix for the rotation power spectrum also vanishes.

6.1.4 Forecasting primordial anisotropies

So far we have studied the effects of preferred directions in the evolution of density and metric perturbations, but anisotropies could also be present in the primordial curvature power spectrum [169,170]. In this case, and assuming parity symmetry, the leading effects can be described by a modification of the primordial power spectrum from $P(k)$ to $P'(\mathbf{k})$ such that,

$$P'(\mathbf{k}) = \left(1 + g_*\, x^2\right)\, P(k). \tag{6.1.52}$$

Assuming a scale-independent modification, g_* is just a dimensionless constant. We can use the Fisher formalism described before to forecast the sensitivity with which future surveys could measure the g_* parameter. With that purpose, we consider both, the multipole power spectrum for the matter distribution and the multipole power spectrum for lensing

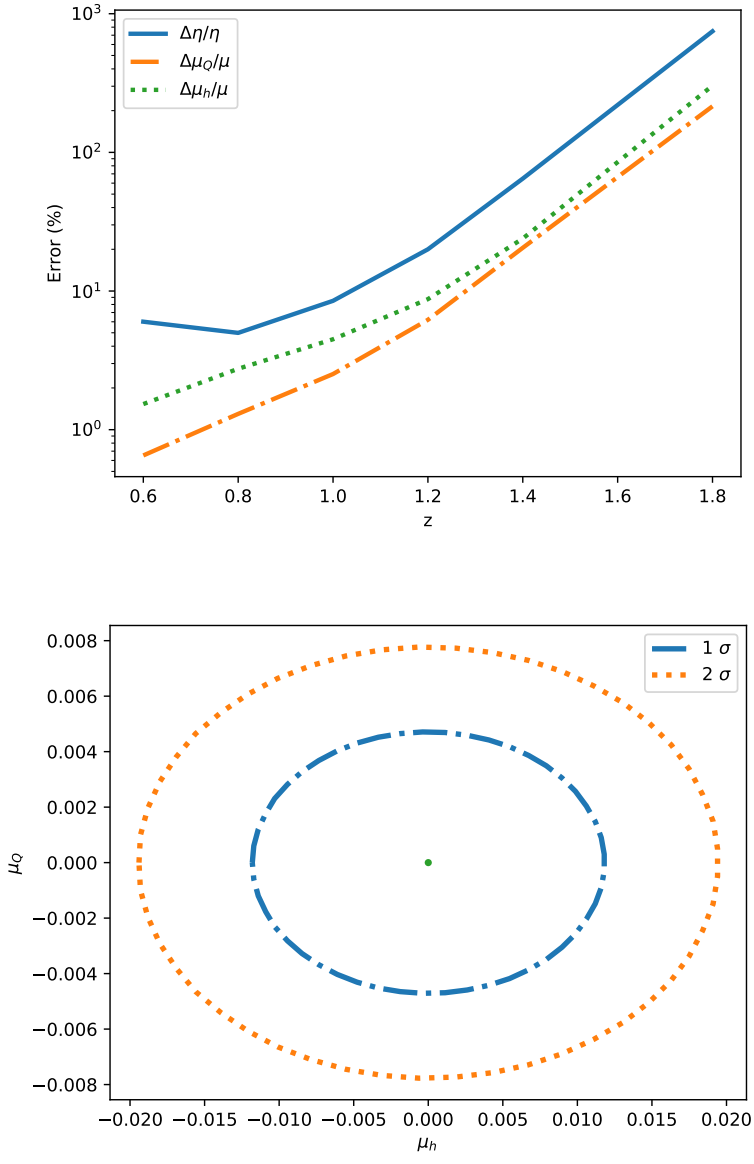

Figure 6.4: Top: Relative errors for η, μ_Q and μ_h using weak lensing information for an Euclid-like survey. Bottom: Marginalized 1σ and 2σ regions for for μ_Q and μ_h summing the information of the whole redshift range for an Euclid-like survey.

convergence. For clustering we consider the following independent parameters in the Fisher analysis (β_a, $b\,D_a$, $g_{*\,a}$), whereas for lensing we take (E_a, L_a, $g_{*\,a}$) where the sub-index a denotes the different redshift bins and $L_a \equiv \Omega_m^2 D_a^2 \sigma_8^2$. We summarize the results in Table 6.5 for an Euclid-like survey as in previous sections.

z	k_{max}	ℓ_{max}	$100 \times \delta g_*^C$	$100 \times \delta g_*^L$
0.6	0.195	311	0.61	4.23
0.8	0.225	385	0.43	7.36
1.0	0.260	515	0.32	9.65
1.2	0.299	609	0.30	16.1
1.4	0.343	760	0.29	38.4
1.8	0.447	959	0.29	591

Table 6.5: Redshift bins, k_{max} values in h/Mpc units, ℓ_{max} values calculated following Section 3.4 and forecasted absolute errors for g_* from clustering (C) and lensing (L) for an Euclid-like survey.

As we can see, we have better precision with the multipole power spectrum of galaxy distribution. If we sum the information of clustering and lensing and in each bin, we obtain and absolute error $\delta g_* = 1.4 \times 10^{-3}$.

6.2 Forecasts for non-standard dark matter

Now we will analyze the phenomenological parametrization for an imperfect and non-conserved dark matter fluid. As shown in the last chapter, the galaxy survey observables are sensitive to the combination $(\mu_\theta, \zeta, \Sigma)$ where Σ is defined in (1.4.20), μ_θ is defined in (4.4.33) and ζ is defined as,

$$f(z,k) = \zeta(z,k)\, f_\Lambda(z), \tag{6.2.1}$$

where $f_\Lambda(z)$ follows (4.5.1). In the case in which μ_m and μ_d defined in (4.4.32) are time independent, ζ follows equation (4.5.62). We will consider two different galaxy surveys, an Euclid-like survey with clustering and weak lensing information; and the WALLABY survey with clustering and peculiar velocity information. The Fisher matrices are the

standard ones,

$$F^{\sigma\sigma}_{\alpha\beta}(z_a) = \frac{V(z_a)}{8\pi^2}\int_{k_{min}}^{k_{max}} k^2\,dk\int_{-1}^{1} d\hat{\mu}\,\frac{\partial\Sigma_{ij}(z_a,\hat{\mu},k)}{\partial\theta_\alpha}\bigg|_r\,\Sigma^{-1}_{jl}\,\frac{\partial\Sigma_{lm}(z_a,\hat{\mu},k)}{\partial\theta_\beta}\bigg|_r\,\Sigma^{-1}_{mi}. \quad (6.2.2)$$

$$F^{\delta\delta}_{\alpha\beta}(z_a) = \frac{1}{8\pi^2}\int_{k_{min}}^{k_{max}} k^2\,dk\int_{-1}^{1} d\hat{\mu}\;V_{eff}\;\frac{\partial\ln P_{gg}(z_a,\hat{\mu},k)}{\partial\theta_\alpha}\bigg|_r\,\frac{\partial\ln P_{gg}(z_a,\hat{\mu},k)}{\partial\theta_\beta}\bigg|_r, \quad (6.2.3)$$

$$F^{\kappa\kappa}_{\alpha\beta} = f_{sky}\sum_{\ell}\Delta\ln\ell\,\frac{(2\ell+1)\ell}{2}\;\frac{\partial P^{\kappa\kappa}_{ab}(\ell)}{\partial\theta_\alpha}\bigg|_r\,C^{-1}_{ba'}\;\frac{\partial P^{\kappa\kappa}_{a'b'}(\ell)}{\partial\theta_\alpha}\bigg|_r\,C^{-1}_{b'a}, \quad (6.2.4)$$

where we have used the convention of summing up to a k_{max} scale defined as $\sigma(z,\pi/2k_{max}(z)) = 0.35$ using (3.2.14). For the weak lensing power spectrum we sum in ℓ with $\Delta\ln\ell = 0.1$ from $\ell_{min} = 5$ to $\ell_{max}(z_{\alpha'}) = \chi(z_{\alpha'})\,k_{\rm max}(z_{\alpha'})$ being $\alpha' = \min(\alpha,\beta)$. The fiducial cosmology we consider is given in the subsection 6.A. For this cosmology $E(z) \equiv H(z)/H_0$,

$$E(z) = \sqrt{\Omega_m\,(1+z)^3 + (1-\Omega_m)}. \quad (6.2.5)$$

For the fiducial cosmology we obtain the present matter power spectrum $P(k)$ from CLASS [226]. Finally, because we use ΛCDM for the fiducial model, $[\Sigma,\zeta,\mu_\theta]|_r = [1,1,1]$.

6.2.1 Euclid survey

In this subsection we would obtain future errors for our parametrization using an Euclid like survey, the survey specifications can be found in 6.A. This survey will measure P_{gg} and P_κ power spectra. First, we will obtain errors for each parameter in each redshift bin using the constant case for ζ and then we will consider a time-dependent phenomenological parametrization. In the former case, we consider (μ_θ,ζ,E) for clustering and (E,Σ) for lensing. Then we combine clustering and lensing information in $(\mu_\theta,\zeta,\Sigma,E)$. We summarize these errors in Table 6.6 and Fig. 6.5. Finally, we sum all the information in each bin and we find $\delta\mu_\theta/\mu_\theta = 0.43\%$, $\delta\zeta/\zeta = 0.31\%$ and $\delta\Sigma/\Sigma = 0.44\%$.

As a second example, we obtain errors for a particular phenomenological time-dependent parametrization. Following [214] we consider $(\mu_\theta(a),\zeta(a),\Sigma(a))$ described by

$$\mu_\theta(a) = 1 + \left(\mu^0_\theta - 1\right)\,\frac{1-\Omega_m(a)}{1-\Omega_m}, \quad (6.2.6)$$

z	$k_{\max}$	$\ell_{\max}$	$\Delta\mu_\theta^C/\mu_\theta(\%)$	$\Delta\zeta^C/\zeta(\%)$	$\Delta\Sigma^L/\Sigma(\%)$	$\Delta\mu_\theta^T/\mu_\theta(\%)$	$\Delta\zeta^T/\zeta(\%)$	$\Delta\Sigma^T/\Sigma(\%)$
0.6	0.195	300	3.03	2.61	2.90	3.00	2.58	0.88
0.8	0.225	437	1.78	1.46	2.08	1.66	1.36	1.58
1.0	0.260	597	1.25	0.97	3.60	1.18	0.92	2.96
1.2	0.299	782	1.00	0.75	8.96	0.97	0.72	7.22
1.4	0.343	994	0.96	0.68	30.0	0.95	0.67	23.7
1.8	0.447	1510	0.84	0.56	340	0.83	0.56	249

Table 6.6: Redshift bins, $k_{\max}$ in h/Mpc, $\ell_{\max}$ values calculated following [225], and relative errors for μ_θ, ζ and Σ for Euclid survey. Super-index C denotes clustering information, L denotes lensing information and T denotes clustering + lensing information.

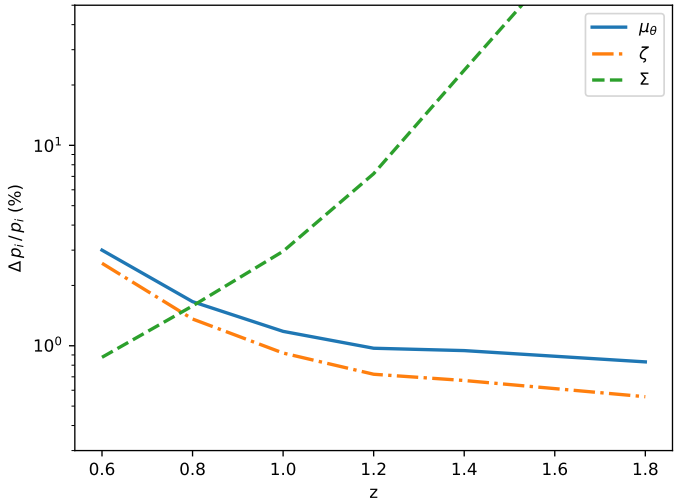

Figure 6.5: Forecasted errors (%) for Σ, ζ and μ_θ using clustering and lensing information for the Euclid survey.

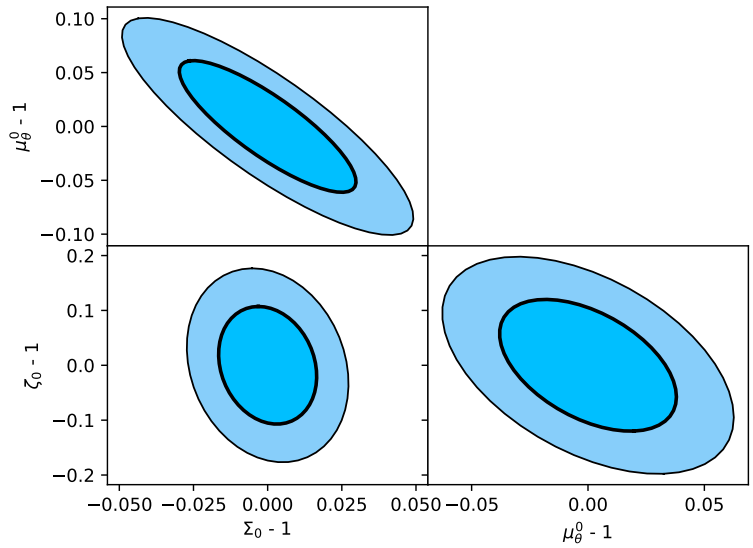

Figure 6.6: Regions for 1 and 2 sigmas for μ_θ^0, ζ_0 and Σ_0 of expressions (6.2.6,6.2.7,6.2.8) using clustering and lensing information for the Euclid survey.

$$\zeta(a) = 1 + (\zeta_0 - 1)\ \frac{1 - \Omega_m(a)}{1 - \Omega_m}, \tag{6.2.7}$$

$$\Sigma(a) = 1 + (\Sigma_0 - 1)\ \frac{1 - \Omega_m(a)}{1 - \Omega_m}, \tag{6.2.8}$$

For a small deviation from ΛCDM we are only sensitive to a combination of these parameters. Using equation (4.2.13) we find,

$$f(z) = \left[1 + (\zeta_0 - 1)\ \frac{5}{2}\ (1+z)^{5/2} \int_z^{z_{mat}} \frac{1 - \Omega_m(z')}{1 - \Omega_m}\ (1+z')^{-7/2}\ dz'\right]\ \Omega_m(z)^\gamma, \tag{6.2.9}$$

and then we obtain the forecast for $(\Sigma_0, \zeta_0, \mu_\theta^0)$. We find $\delta\Sigma_0/\Sigma_0 = 2.21\%$, $\delta\zeta_0/\zeta_0 = 8.90\%$ and $\delta\mu_\theta^0/\mu_\theta^0 = 5.08\%$. We plot the 1 and 2 σ regions for Σ_0, ζ_0 and μ_θ^0 in Fig. 6.6.

6.2.2 The WALLABY survey

WALLABY [227] (Widefield ASKAP L-band Legacy All-sky Blind surveY) is one of the ASKAP Survey Science Projects and is focused on enhancing our understanding of the extragalactic neutral hydrogen (HI) universe. It will be able to map the galaxy distribution and galaxy velocity distribution up to redshift $z = 0.26$. Here we will forecast the size

of errors for our dark matter parametrization using the WALLABY survey which will measure P_{gg}, P_{uu} and P_{gu} power spectra. The fraction of the sky, the bias and the $k_{\rm max}$ are respectively $f_{sky} = 0.75$, $b = 0.7$ and $k_{\rm max} = 0.2$. For $k_{\rm min}$ we take the value $k_{\rm min} = 0.007$ h/Mpc [225]. We summarize the redshift bins and galaxy densities in Table 6.7. As independent parameters we consider (μ_θ, ζ, E) in each bin (considering the constant case for ζ). We summarize the relative errors in Table 6.7.

z	$n_g \times 10^{-3}$	$n_u \times 10^{-3}$	$\Delta\mu_\theta/\mu_\theta(\%)$	$\Delta\zeta/\zeta(\%)$
0.0175	67.4	8.50	2130	2130
0.0350	23.1	1.06	494	492
0.0525	8.59	0.15	870	865
0.0700	3.00	0.031	510	506
0.0875	1.09	0.0026	342	340
0.105	0.45	0.00097	308	307

Table 6.7: Redshift bins, galaxy densities in $(\mathrm{h/Mpc})^3$ and relative errors for μ_θ and ζ for WALLABY forecast.

As we can see, due to the low galaxy densities at low redshift, WALLABY is not competitive measuring modified gravity and imperfect fluid effects. Although peculiar velocity power spectrum could be an interesting observable, current and future surveys will not have enough precision for a competitive measurement of the effective parameters.

6.2.3 Imperfect dark matter with shear viscosity: present constraints and forecasts

Finally as an example, we analyse a particular model for dark matter shear obtaining current constraints using SDSS data and comparing it with the expected precision for Euclid forecast. We consider the particular model of shear viscosity (4.3.3) where we define the dimensionless parameter $\tilde{\eta} \equiv 24\pi G\eta_0/H_0$ [29]. We analyze the case in which this parameter is constant. In that situation we have found a good analytical approximation for the growth function $f(z)$,

k	0.012	0.015	0.018	0.021	0.024	0.028	0.032	0.037	0.043	0.049	0.057	0.065	0.075	0.087
P	124884	118814	134291	58644	105253	77699	57870	56516	50125	45076	39339	39609	31566	24837
ΔP	18775	29400	21638	16647	12736	9666	7264	5466	3991	2956	2214	1679	1284	991

Table 6.8: SDSS luminous red galaxies data [228]: k values in h/Mpc, LRG power spectrum and errors, both in $(\mathrm{Mpc/h})^3$.

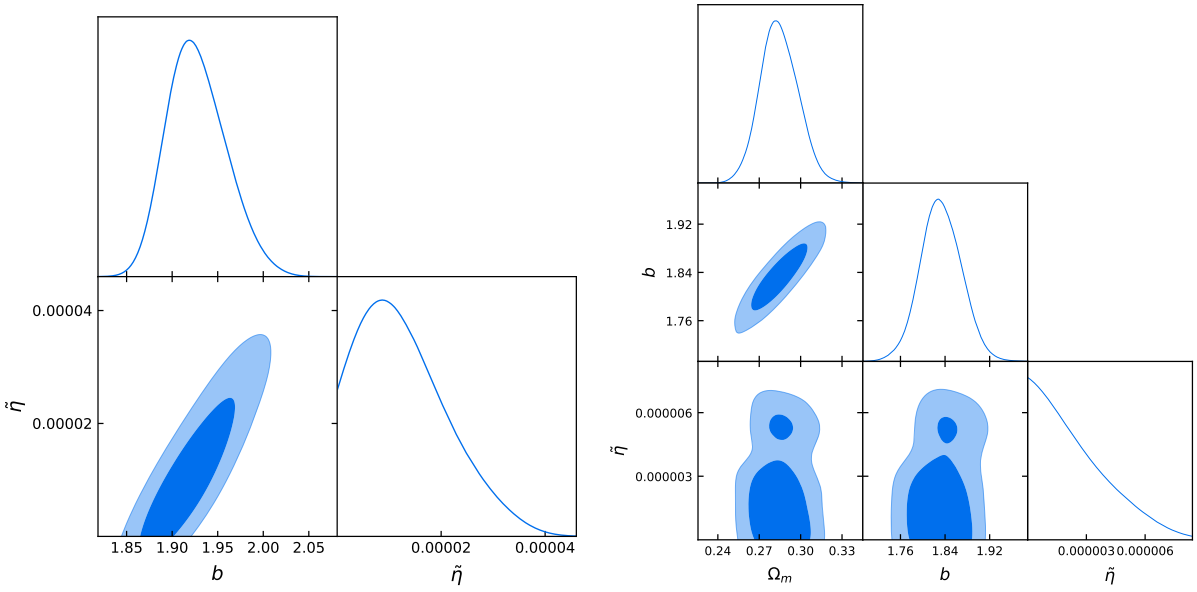

Figure 6.7: Left: likelihood and confidence regions for shear viscosity model using SDSS luminous red galaxies and considering b and $\tilde{\eta}$ as free parameters. Right: likelihood and confidence regions for shear viscosity model using SDSS luminous red galaxies and considering Ω_m, b and $\tilde{\eta}$ as free parameters.

$$f(z) = \left(1 + \frac{a_1}{\left[1 + a_2 z + a_3 z^2\right]^{3/2}}\right) \Omega_m^{\gamma}(z), \tag{6.2.10}$$

$$a_1 = \exp\left[-0.146\ \hat{\eta}^{0.948}\right] - 1, \tag{6.2.11}$$

$$a_2 = 1.447 - 0.106\,\hat{\eta} + 0.003\,\hat{\eta}^2, \tag{6.2.12}$$

$$a_3 = 0.429 - 0.014\,\hat{\eta} + 0.0004\,\hat{\eta}^2, \tag{6.2.13}$$

where $\gamma = 0.545$ and $\hat{\eta} = \tilde{\eta}\,(k/H_0)^2$. We will use SDSS luminous red galaxies data [228] to constrain $\tilde{\eta}$. The observable is the galaxy power spectra today $P^{LRG}(k)$,

$$P^{LRG}(k) = b^2 \left(\frac{\delta(0)}{\delta(z_{mat})}\,\frac{\delta_\Lambda(z_{mat})}{\delta_\Lambda(0)}\right)^2 P_\Lambda(k), \tag{6.2.14}$$

being $\delta_\Lambda(z)$ and $P_\Lambda(k)$ the growth factor and the matter power spectrum in ΛCDM respectively, and,

$$\frac{\delta(0)}{\delta(z_{mat})}\,\frac{\delta_\Lambda(z_{mat})}{\delta_\Lambda(0)} = \exp\left[\int_{N_{mat}}^{0} \left(f(N') - f_\Lambda(N')\right)\, dN'\right], \tag{6.2.15}$$

with $N = -\ln(1+z)$ and $N_{mat} \approx -3$. The observational data of $P^{LRG}(k)$ and errors are in Table 6.8.

We compute the corresponding χ^2 for expression (6.2.14) and obtain the best fit and the confidence regions. First of all we consider parameters $(b, \tilde{\eta})$ in Fig. 6.7 left panel, fixing the rest of parameters to the fiducial ones. The best fit corresponds to the values $b = 1.916^{+0.055}_{-0.051}$ and $\tilde{\eta} = \left(0.953^{+1.579}_{-0.953}\right) \times 10^{-5}$. We see that although the best fit corresponds to a non-vanishing viscosity, it is compatible with zero within one sigma. As a matter of fact, we find $\tilde{\eta} < 3.71 \times 10^{-5}$ at 95% C.L.

We have also considered $(\Omega_m, b, \tilde{\eta})$ as fitting parameters in Fig. 6.7 right panel. In this case, the best fit corresponds to $\Omega_m = 0.280^{+0.027}_{-0.019}$, $b = 1.82^{+0.08}_{-0.05}$, $\tilde{\eta} = \left(0.261^{+6.875}_{-0.261}\right) \times 10^{-6}$, which again is compatible with vanishing viscosity at the one-sigma level. We find $\tilde{\eta} < 7.55 \times 10^{-6}$ at 95% C.L.

Finally, we forecast the precision for the future measurements of $\tilde{\eta}$ with Euclid. We compute clustering and lensing power spectra and we obtain the Fisher matrices (6.2.3) and (6.2.4) using the information of 6.A and considering ΛCDM as the fiducial model. We summarize the results in Table 6.9.

As we can see, Euclid improves $1-2$ orders of magnitude the accuracy of $\tilde{\eta}$ with respect to SDSS luminous red galaxies.

6.A Fiducial cosmology and survey specifications

The fiducial cosmology we consider is given by $\Omega_c\,h^2 = 0.121$, $\Omega_b\,h^2 = 0.0226$, $\Omega_\nu\,h^2 = 0.00064$, $n_s = 0.96$, $h = 0.68$, $H_0^{-1} = 2997.9\,\mathrm{Mpc/h}$, $\Omega_k = 0$ and $\sigma_8 = 0.82$ in the standard

z	$k_{\max}$	$\ell_{\max}$	$\Delta\tilde{\eta}^C \times 10^{-7}$	$\Delta\tilde{\eta}^L \times 10^{-7}$	$\Delta\tilde{\eta}^T \times 10^{-7}$
0.60	0.195	300	2.53	8.18	2.41
0.80	0.225	437	1.55	7.00	1.51
1.00	0.260	597	1.15	8.14	1.14
1.20	0.299	782	1.05	13.1	1.04
1.40	0.343	994	0.97	30.6	0.97
1.80	0.447	1510	0.94	257	0.94

Table 6.9: Redshift bins, $k_{\max}$ in h/Mpc, $\ell_{\max}$ values calculated following [225], and errors for $\tilde{\eta}$ for Euclid forecast. Super-index C denotes clustering information, L denotes lensing information and T denotes clustering + lensing information.

ΛCDM model. For this cosmology,

$$H(z) = H_0 \sqrt{\Omega_m (1+z)^3 + (1-\Omega_m)}. \tag{6.A.1}$$

The growth function f_Λ follows equation (4.4.33) and the growth factor D_Λ is,

$$D_\Lambda(z) = \exp\left[\int_0^{N(z)} f_\Lambda(N')\, dN'\right], \tag{6.A.2}$$

being $N(z) = -\ln(1+z)$. For the fiducial cosmology we obtain the present matter power

z	k_{max}	$n \times 10^{-3}$
0.6	0.195	3.56
0.8	0.225	2.42
1.0	0.260	1.81
1.2	0.299	1.44
1.4	0.343	0.99
1.8	0.447	0.33

Table 6.10: Redshift bins, k_{max} values in h/Mpc units and galaxy densities in $(\mathrm{h/Mpc})^3$ units for an Euclid-like survey.

spectrum $P_\Lambda(k)$ from CLASS [226]. For the survey specifications, we consider an Euclid-like survey. Euclid is a spectroscopy and photometric survey that will be able to cover

15000 deg^2 up to redshift $z = 2$ with a very high number of emission light galaxies. The redshift bins, values of $k_{\max}$ and galaxy densities can be found in Table 6.10. For $k_{\min}$ we take the value $k_{\min} = 0.007\ h/\text{Mpc}$ [225]. For the bias, we use a fiducial value of the form [68],

$$b(z) = \sqrt{1+z}. \tag{6.A.3}$$

The fraction of the sky is $f_{sky} = 0.364$ corresponding to 15000 deg^2, the redshift error for galaxy distribution power spectrum is $\delta z = 0.001$. For the weak lensing power spectrum, the mean redshift is $z_{mean} = 0.9$, the areal galaxy density $n_\theta = 35$ galaxies per square arc minute and the redshift error for weak lensing power spectrum is $\delta z = 0.05$.

Chapter 7

FARO: a new galaxy forecast code

As we have shown in this thesis, Fisher forecast is a useful tool to analyze the impact of future experiments. In addition, in the cosmology context, galaxy surveys will provide useful observables to constrain cosmological parameters. Thus, it is interesting to analyze how these experiments can measure those parameters and the precision they would reach. Also, it is useful to analyze how the different survey configurations and observation strategies affects the precision of cosmological measurements. There are several Fisher matrix codes (`BFF` [229], `CarFisher` [68], `FisherMathica` [230], `fishMath` [231], `SOAPFish` [232], `SpecSAF` [233], ...) for galaxy clustering, cosmic shear and the cross correlation power spectra that have been developed in the last years, although most of them are not public [234]. These codes compute the Fisher matrix for the 3D galaxy power spectrum, the 2D galaxy power spectrum, the convergence power spectrum and the cross correlation. The main approach in these codes is to numerically calculate the derivatives of the power spectra with respect to a given set of cosmological parameters using the outputs of a Boltzmann code. In this chapter we present the Fisher gAlaxy suRvey cOde (FARO) which we have developed in [235]. This is a public code that allows to perform forecasts analysis in a model-independent way, avoiding the numerical evaluation of derivatives, and it is thus particularly useful to test the modified cosmological models discussed in previous chapters in a faster way than existing codes.[1]

[1]The code can be downloaded from `https://www.ucm.es/iparcos/faro`

7.1 Observables and approach of the code

We start by explaining the main features of the code and the parameters that are considered. `FARO` is a Fisher matrix code for galaxy surveys that is totally public and made to be easy to use and modify. The main characteristics of `FARO` can be summarized as:

- **Python code**: The code is written in Python for an easy use and manipulation. It makes extensive use of the powerful function `np.einsum` and it allows to use the Python CLASS [226] functions to obtain the matter power spectrum.

- **Observables**: 3D galaxy power spectrum, convergence power spectrum and cross-correlation power spectrum in the linear regime.

- **Multitracer**: an arbitrary number of different galaxy tracers can be considered. The corresponding multitracer galaxy-lensing cross-correlation is implemented.

- **Redshift and scale binning**: arbitrary number and sizes of redshift and k bins can be chosen in an easy way.

- **Model independent**: A set of model-independent parameters are considered which allows to extract information on the constraining power of a given survey for a wide range of cosmologies. The chosen parameters allow, in addition, to obtain the derivatives involved in the Fisher matrix calculation in an analytical way thus making the code faster.

- **Tomographic errors:** Error information is provided for each redhsift and k bin.

- **Flexible and user friendly**: `FARO` has a simple use mode in which numerical and graphical results can be generated in a simple way. In addition, the code structure is built to be flexible and easy to modify.

The main assumptions of the code are:

- **Flat FRW background**: This approximation simplifies the code and makes the calculations faster.

- **Scale-independent growth factor**: In order to factorize the redshift and scale dependencies of the observables and keep the analysis as model independent as possible, the growth function is assumed to be scale independent.

Once we have described the main characteristics, we summarize here the model-independent parameters that `FARO` considers. Unlike other codes which focus on particular sets of cosmological parameters for specific cosmological models such as ΛCDM, wCDM, modified gravity models described by a generic growth index γ, etc, `FARO` uses a set of model-independent parameters more closely related to the observables [225, 236]. Thus, first of all, we introduce the redshift-dependent functions, given by

$$A_i(z) = \sigma_8(z)\, b_i(z), \tag{7.1.1}$$

$$R(z) = \sigma_8(z)\, f(z), \tag{7.1.2}$$

$$L(z) = \Omega_m\, \sigma_8(z)\, \Sigma(z), \tag{7.1.3}$$

$$E(z) = \frac{H(z)}{H_0}, \tag{7.1.4}$$

where $b_i(z)$ is the bias for tracer i, $H(z)$ is the Hubble parameter, $\sigma_8(z) = \sigma_8\, D(z)$ being $D(z) = \delta_m(z)/\delta_m(0)$ and σ_8 the normalization of the matter power spectrum on scales of $8\,\mathrm{h}^{-1}$Mpc today; and $f(z)$ is the growth function defined as,

$$D(z) = \exp\left[-\int_0^z \frac{f(z')}{1+z'}\, dz'\right]. \tag{7.1.5}$$

Finally, $\Sigma(z)$ is a general function of redshift which takes into account possible modifications of the lensing potential [65, 237] and that in ΛCDM model is $\Sigma(z) = 1$.

Notice that we will not consider an arbitrary non-Gaussian shot noise term $P_s(z)$ as additional parameters in each redshift bin, the reasons are, on one hand, that we are not interested in constraining them, and on the other, that it can be proved that they are poorly correlated with other parameters.

In addition to the redshift-dependent functions, we have the parameters associated to the shape of the matter power spectrum. Thus we define,

$$\hat{P}(k) = \frac{P(k)}{\sigma_8^2}, \tag{7.1.6}$$

$P(k)$ being the matter power spectrum today. Notice that we have to consider $\hat{P}(k)$ as independent function instead of $P(k)$ because σ_8 is already taken into account in the redshift dependent functions (7.1.1-7.1.4).

Thus `FARO` considers the following set of independent parameters:

- *Redshift-dependent parameters*: $[A_i(z_a),\ R(z_a),\ L(z_a),\ E(z_a)]$, where the a index denotes the different redshift bins and the i index the different tracers.

- *Power-spectrum parameters*: a_n corresponding to the amplitude of $\hat{P}(k)$ in the n-th log-spaced k bin.

Notice that this set of parameters exhausts the information that can be extracted from a galaxy and lensing survey at the linear level within the mentioned assumptions[2]. There are two main aspects that differentiate `FARO` from other Fisher codes: on one hand the possibility of performing multitracer analysis, not only at the clustering level, but also with lensing cross-correlations, and on the other, the fact that the parametrization of the matter power-spectrum is fully model-independent. This allows `FARO` to perform forecast analysis of features and other scale-dependent deviations in the standard power-law primordial curvature spectrum or transfer function.

7.1.1 Galaxy surveys observables

Now we summarize the main observables of the galaxy maps that `FARO` computes to obtain the Fisher matrices. These observables are the 3D galaxy power spectrum, the convergence power spectra for weak lensing measurements and the cross-correlation power spectrum for distribution and convergence. So we will rewrite these power spectra, that have been explained in detail before, as a function of the model independent parametrization (7.1.1)-(7.1.4). One of the main observables that the code considers is the multitracer galaxy power spectra. We take into account three effects, the linear Kaiser term for redshift space distortion [105], the convolution redshift error term [7] and the Alcock-Paczynski effect [85].

[2]In principle it would be possible to consider the angular diameter distances $D_A(z_a)$ as independent set of parameters from $E(z_a)$, however in our case, since the background metric is assumed to be flat FRW, this is no longer the case.

Considering these terms the power spectrum for tracers i and j reads reads [125, 238],

$$P_{ij}^{\delta\delta}(z,\hat{\mu}_r,k_r) = \frac{D_{A\,r}^2\,E}{D_A^2\,E_r}\,(A_i + R\,\hat{\mu}^2)\,(A_j + R\,\hat{\mu}^2)\;\hat{P}(k)\;e^{\frac{-k_r^2\,\hat{\mu}_r^2\,\sigma_i^2}{2}}\,e^{\frac{-k_r^2\,\hat{\mu}_r^2\,\sigma_j^2}{2}}, \tag{7.1.7}$$

where we have rewritten the power spectrum (2.2.41) as a function of A_i, E and R. Notice that due to the Alcock-Paczynski effect $k = k(k_r)$ and $\hat{\mu} = \hat{\mu}(\hat{\mu}_r)$ which follow equations (2.2.33) and (2.2.34). For the weak lensing effect, the convergence power spectra reads [116],

$$P_{ab}^{\kappa\kappa}(\ell) = \frac{9H_0^3}{4}\int_0^\infty \frac{(1+z)^2}{E(z)} g_a(z) g_b(z) L(z)^2 \hat{P}\left(\frac{\ell}{\chi(z)}\right) dz, \tag{7.1.8}$$

where the window functions $g_a(z)$ are defined in (2.4.60). The code assumes the standard galaxy distribution used for weak lensing (2.4.61), however it is easy to modify it if necessary. If we have distribution and convergence informations, it is possible to relate the distribution of galaxies in the 2D plane with the convergence of the weak lensing galaxy sample. The 2D galaxy distribution and the cross-correlation power spectra can be written as,

$$P_{ab\;ij}^{\delta_2\delta_2}(\ell) = \delta_{ab} H_0\,\frac{E(z_a)}{\chi^2(z_a)}\,A_i(z_a)\,A_j(z_b)\,\hat{P}\left(\frac{\ell}{\chi(z_a)}\right), \tag{7.1.9}$$

$$P_{ab\;i}^{\kappa\delta_2}(\ell) = \frac{3H_0^2}{2}\,\frac{(1+z_b)}{\chi(z_b)}\,g_a(z_b)\,A_i(z_b)\,L(z_b)\,\hat{P}\left(\frac{\ell}{\chi(z_b)}\right), \tag{7.1.10}$$

where we have assumed for the 2D galaxy distribution that galaxies in two redshift bins are not correlated with each other. Here a, b denote redshift bins and i, æ galaxy tracers. These are the galaxy survey power spectra that `FARO` considers to obtain constraints on the parameters (7.1.1)-(7.1.4) and (7.1.6).

7.1.2 Matter power spectrum parametrization

Here we explain how to parametrize the normalized matter power spectrum today $\hat{P}(k)$ defined in (7.1.6) in a model-independent way. We want the free parameters to be the values of $\hat{P}(k)$ in p logarithmically spaced k bins. However, because of the fixed normalization we will have only $p-1$ degrees of freedom to parametrize $\hat{P}(k)$. Considering that the fiducial model is ΛCDM, a general and model-independent parametrization of $\hat{P}(k)$ with p degrees of freedom can be written as,

$$\hat{P}(k) = g(k)\,\hat{P}_\Lambda(k) \tag{7.1.11}$$

where $\hat{P}_\Lambda(k)$ is the normalized matter power spectrum for the fiducial ΛCDM model, and $g(k)$ is an arbitrary dimensionless function with the form,

$$g(k) = 1 + \sum_{n=0}^{p-1} a_n \, g_n(k). \tag{7.1.12}$$

Notice that, although $g_n(k)$ with $n = 0, ..., p-1$ can be general base functions, we will consider them as window functions for each logarithmic spaced k bins. Due to the σ_8 constraint, these $g_n(k)$ functions cannot be independent so that the following condition is satisfied

$$\int \frac{k'^2 \, dk'}{2\pi^2} \hat{P}(k') |\hat{W}(8, k')|^2 = 1, \tag{7.1.13}$$

where

$$\hat{W}(R, k) = \frac{3}{k^3 R^3} \left[\sin(kR) - kR\cos(kR)\right] \tag{7.1.14}$$

being $R = 8\,\mathrm{Mpc/h}$. Substituting (7.1.12) in (7.1.13) we obtain,

$$\sum_{n=0}^{p-1} a_n \, \alpha_n = 0, \tag{7.1.15}$$

where,

$$\alpha_n \equiv \int \frac{k'^2 \, dk'}{2\pi^2} g_n(k') \, \hat{P}_\Lambda(k') |\hat{W}(8, k')|^2. \tag{7.1.16}$$

Using condition (7.1.15) we can reduce the independent parameters to $p-1$ and, without loss of generality, we can rewrite (7.1.12) as,

$$g(k) = 1 + \sum_{n=1}^{p-1} a_n \left[g_n(k) - \frac{\alpha_n}{\alpha_0} \, g_0(k) \right]. \tag{7.1.17}$$

Once we obtain the Fisher matrix for a_n with $n = 1, ..., p-1$ the corresponding errors for $\hat{P}(k)$ can be calculated by projecting the covariance matrix C_{nm} using the following expression,

$$\frac{\sigma_{\hat{P}(k)}}{\hat{P}(k)} = \sqrt{\left(g_n(k) - \frac{\alpha_n}{\alpha_0} \, g_0(k) \right) C_{nm} \left(g_m(k) - \frac{\alpha_m}{\alpha_0} \, g_0(k) \right)}. \tag{7.1.18}$$

In particular we will consider $g_n(k)$ as a logarithmically-spaced step function of the form,

$$g_n(k) = \tilde{\theta} \left(\log(k) - \left[\log k_n - \frac{\Delta \log k_n}{2} \right] \right) \, \tilde{\theta} \left(\left[\log k_n + \frac{\Delta \log k_n}{2} \right] - \log(k) \right), \tag{7.1.19}$$

where $\log k_n$ are the centers of the $\log(k)$ bins with size $\Delta \log k_n$, and $\tilde{\theta}(x)$ the Heaviside function with $\tilde{\theta}(0) = 1/2$. Using these functions, parameters α_n are,

$$\alpha_n = \int_{\log k_n - \frac{\Delta \log k_n}{2}}^{\log k_n + \frac{\Delta \log k_n}{2}} \frac{k'^3 \, d\log k'}{2\pi^2} \, \hat{P}_\Lambda(k') |\hat{W}(8, k')|^2. \tag{7.1.20}$$

7.1.3 Fisher matrices

Once we have defined the observables, we show the Fisher matrices for each power spectrum. For the clustering multitracer power spectrum the parameters that are considered are: $[a_n, A_a^i, R_a, E_a]$, for the convergence power spectra: $[a_n, E_a, L_a]$; where i denotes different galaxy tracers, a different redshift bins and n the different $p-1$ scale bins. Finally, when we combine clustering and lensing information with the cross-correlation, the parameters are: $[a_n, A_a^i, R_a, L_a, E_a]$. The Fisher matrix for the multitracer power spectrum reads [130, 131],

$$F_{\alpha\beta}^{\delta\delta} = \sum_{a,d,c} \frac{V_a \, \Delta\hat{\mu}_d \, \Delta \log k_c \, k_c^3}{8\pi^2} \left. \frac{\partial P_{ij}^{\delta\delta}(z_a, \hat{\mu}_d, k_c)}{\partial \theta_\alpha} \right|_r C_{jl}^{-1} \left. \frac{\partial P_{lm}^{\delta\delta}(z_a, \hat{\mu}_d, k_c)}{\partial \theta_\beta} \right|_r C_{mi}^{-1} \; \mathrm{e}^{-k_c^2 \Sigma_\perp^2 - k_c^2 \hat{\mu}_d^2 (\Sigma_\parallel^2 - \Sigma_\perp^2)}, \tag{7.1.21}$$

where we have discretized the integrals in $\hat{\mu}$ and k of equation (3.2.18), and also we sum over the redshift bins. The code fixes the value $k_{min} = 0.007$ h/Mpc [225]. Now we show the derivatives with respect to the parameters $[a_n, A_a^i, R_a, E_a]$,

$$\left. \frac{\partial P_{ij}^{\delta\delta}(z_a, \hat{\mu}_d, k_c)}{\partial a_n} \right|_r = \left[g_n(k_c) - \frac{\alpha_n}{\alpha_0} \, g_0(k_c) \right] \, P_{ij}^{\delta\delta}(z_a, \hat{\mu}_d, k_c), \tag{7.1.22}$$

$$\left. \frac{\partial P_{ij}^{\delta\delta}(z_a, \hat{\mu}_d, k_c)}{\partial A_b^l} \right|_r = \left[\frac{\delta_{li}\delta_{ba}}{A_a^i + R_a \, \hat{\mu}_d^2} + \frac{\delta_{lj}\delta_{ba}}{A_a^j + R_a \, \hat{\mu}_d^2} \right] \, P_{ij}^{\delta\delta}(z_a, \hat{\mu}_d, k_c), \tag{7.1.23}$$

$$\left. \frac{\partial P_{ij}^{\delta\delta}(z_a, \hat{\mu}_d, k_c)}{\partial R_b} \right|_r = \left[\frac{\delta_{ba} \, \hat{\mu}_d^2}{A_a^i + R_a \, \hat{\mu}_d^2} + \frac{\delta_{ba} \, \hat{\mu}_d^2}{A_a^j + R_a \, \hat{\mu}_d^2} \right] \, P_{ij}^{\delta\delta}(z_a, \hat{\mu}_d, k_c), \tag{7.1.24}$$

$$\left.\frac{\partial P_{ij}^{\delta\delta}(z_a,\hat{\mu}_d,k_c)}{\partial E_b}\right|_r = \left[\frac{\delta_{ba}}{E_b} - \frac{2}{\chi(z_a)}\frac{\partial\chi(z_a)}{\partial E_b} + \frac{d\log P}{d\log k}(k_c)\,\left(\frac{\hat{\mu}_d^2\delta_{ba}}{E_b} - \frac{(1-\hat{\mu}_d^2)}{\chi(z_a)}\frac{\partial\chi(z_a)}{\partial E_b}\right)\right.$$
$$\left. + \left(\frac{2R_a\hat{\mu}_d^2(1-\hat{\mu}_d^2)}{A_a^i + R_a\,\hat{\mu}_d^2} + \frac{2R_a\hat{\mu}_d^2(1-\hat{\mu}_d^2)}{A_a^j + R_a\,\hat{\mu}_d^2}\right) \times \left(\frac{\delta_{ba}}{E_b} + \frac{1}{\chi(z_a)}\frac{\partial\chi(z_a)}{\partial E_b}\right)\right]\, P_{ij}^{\delta\delta}(z_a,\hat{\mu}_d,k_c), \tag{7.1.25}$$

evaluated on the fiducial model, with,

$$\frac{\partial\chi(z_a)}{\partial E_b} = -\theta(z_a - z_b)\,\frac{\Delta z_b}{H_0\,E_b^2}, \tag{7.1.26}$$

being $\theta(x)$ the Heaviside function with $\theta(0) = 1$. The resulting Fisher matrix has the following form for parameters $[a_n, A_a^i, R_a, E_a]$,

$$\begin{pmatrix}
a_1a_1 & a_1a_2 & ... & a_1A_1^1 & a_1A_1^2 & ... & a_1R_1 & a_1E_1 & ... \\
a_2a_1 & a_2a_2 & ... & a_2A_1^1 & a_2A_1^2 & ... & a_2R_1 & a_2E_1 & ... \\
... & ... & ... & ... & ... & ... & ... & ... & ... \\
A_1^1a_1 & A_1^1a_2 & ... & A_1^1A_1^1 & A_1^1A_1^2 & ... & A_1^1R_1 & A_1^1E_1 & ... \\
A_1^2a_1 & A_1^2a_2 & ... & A_1^2A_1^1 & A_1^2A_1^2 & ... & A_1^2R_1 & A_1^2E_1 & ... \\
... & ... & ... & ... & ... & ... & ... & ... & ... \\
R_1a_1 & R_1a_2 & ... & R_1A_1^1 & R_1A_1^2 & ... & R_1R_1 & R_1E_1 & ... \\
E_1a_1 & E_1a_2 & ... & E_1A_1^1 & E_1A_1^2 & ... & E_1R_1 & E_1E_1 & ... \\
... & ... & ... & ... & ... & ... & ... & ... & ...
\end{pmatrix}.$$

The Fisher matrix for the convergence power spectrum follows (3.4.11) where we sum in ℓ with $\Delta\ln\ell = 0.1$ from $\ell_{\rm min} = 5$ [225] to $\ell_{\rm max}$ with $\ell_{\rm max}(z_{\alpha'}) = \chi(z_{\alpha'})\,k_{\rm max}(z_{\alpha'})$ where $\alpha' = \min(\alpha,\beta)$ and $k_{\rm max}(z_a)$ is defined so that $\sigma(z_a, \pi/2k_{\rm max}(z_a)) = 0.35$. Now we show the derivatives respect to the parameters $[a_n, E_a, L_a]$,

$$\frac{\partial P_{ab}^{\kappa\kappa}(\ell)}{\partial a_n} = \sum_{b'}\left[g_n\left(\frac{\ell}{\chi(z_{b'})}\right) - \frac{\alpha_n}{\alpha_0}\,g_0\left(\frac{\ell}{\chi(z_{b'})}\right)\right]\,P_{ab}^{\kappa\kappa}(z_{b'},\ell), \tag{7.1.27}$$

$$\begin{aligned}
\frac{\partial P_{ab}^{\kappa\kappa}(\ell)}{\partial E_{a'}} &= -\frac{1}{E_{a'}}\,P_{ab}^{\kappa\kappa}(z_{a'},\ell) \\
&+ \sum_{b'}\frac{1}{g_a(z_{b'})}\frac{\partial g_a(z_{b'})}{\partial E_{a'}}\,P_{ab}^{\kappa\kappa}(z_{b'},\ell) \\
&+ \sum_{b'}\frac{1}{g_b(z_{b'})}\frac{\partial g_b(z_{b'})}{\partial E_{a'}}\,P_{ab}^{\kappa\kappa}(z_{b'},\ell) \\
&- \sum_{b'}\frac{1}{\chi(z_{b'})}\frac{\partial\chi(z_{b'})}{\partial E_{a'}}\frac{d\log P}{d\log k}\left(\frac{\ell}{\chi(z_{b'})}\right)\,P_{ab}^{\kappa\kappa}(z_{b'},\ell),
\end{aligned} \tag{7.1.28}$$

$$\frac{\partial P_{ab}^{\kappa\kappa}(\ell)}{\partial L_{a'}} = \frac{2}{L_{a'}}\, P_{ab}^{\kappa\kappa}(z_{a'},\ell), \tag{7.1.29}$$

where,

$$P_{ab}^{\kappa\kappa}(z_{a'},\ell) = \frac{9H_0^3}{4}\frac{(1+z_{a'})^2\Delta z_{a'}}{E_{a'}} g_a(z_{a'}) g_b(z_{a'})\, L_{a'}^2\, \hat{P}\left(\frac{\ell}{\chi(z_{a'})}\right), \tag{7.1.30}$$

$$\frac{\partial g_a(z_b)}{\partial E_{a'}} = \frac{\Delta z_{a'}}{H_0\, E_{a'}^2}\left[-\hat{\theta}(z_{a'}-z_b)\chi(z_b)\int_{z_{a'}}^{\infty}\frac{n_a(z')}{\chi(z')^2}\,dz' + \theta(z_b-z_{a'})\int_{z_b}^{\infty}\left(1-\frac{\chi(z_b)}{\chi(z')}\right)\frac{n_a(z')}{\chi(z')}dz'\right], \tag{7.1.31}$$

with $\hat{\theta}(0)=0$ and $\theta(0)=1$ and Δz_a is the size of the redshift bin z_a. The resulting Fisher matrix has the following form for parameters $[a_n, E_a, L_a]$,

$$\begin{pmatrix}
a_1a_1 & a_1a_2 & ... & a_1E_1 & a_1L_1 & a_1E_2 & a_1L_2 & ... \\
a_2a_1 & a_2a_2 & ... & a_2E_1 & a_2L_1 & a_2E_2 & a_2L_2 & ... \\
... & ... & ... & ... & ... & ... & ... & ... \\
E_1a_1 & E_1a_2 & ... & E_1E_1 & E_1L_1 & E_1E_2 & E_1L_2 & ... \\
L_1a_1 & L_1a_2 & ... & L_1E_1 & L_1L_1 & L_1E_2 & L_1L_2 & ... \\
E_2a_1 & E_2a_2 & ... & E_2E_1 & E_2L_1 & E_2E_2 & E_2L_2 & ... \\
L_2a_1 & L_2a_2 & ... & L_2E_1 & L_2L_1 & L_2E_2 & L_2L_2 & ... \\
... & ... & ... & ... & ... & ... & ... & ...
\end{pmatrix}.$$

The Fisher matrix for cross-correlation power spectrum follows (3.4.21). As we can see in (7.1.10), the cross-correlation power spectrum depends on the product $Q_i(z) \equiv A_i(z)\, L(z)$. It can be proved that the Fisher matrix has only two independent parameters in each redshift bin: $[Q_i(z_a), E(z_a)]$. The degeneracy of $A_i(z)$ and $L(z)$ can be broken when we combine the Fisher matrices for clustering and the convergence power spectrum. Because we are not interested in the information of the cross-correlation power spectrum alone, we project the initial Fisher matrix of $[Q_i(z_a), E(z_a)]$ into a Fisher matrix of $[A_i(z_a), L(z_a), E(z_a)]$ and then we combine it with the Fisher matrices for clustering $[A_i(z_a), R(z_a), E(z_a)]$, and the convergence power spectrum $[E(z_a), L(z_a)]$.

In addition to the redshift-dependent parameters, we also have the scale dependence of $\hat{P}(k)$. Thus, the derivatives of the cross-correlation power spectrum with respect to the parameters $[a_n, A_a^i, L_a, E_a]$ are,

$$\frac{\partial P_{ab\,i}^{\kappa\delta_2}(\ell)}{\partial a_n} = \left[g_n\left(\frac{\ell}{\chi(z_b)}\right) - \frac{\alpha_n}{\alpha_0}\, g_0\left(\frac{\ell}{\chi(z_b)}\right)\right] P_{ab\,i}^{\kappa\delta_2}(\ell), \tag{7.1.32}$$

$$\frac{\partial P^{\kappa\delta_2}_{ab\,i}(\ell)}{\partial A^l_{a'}} = \frac{\delta_{a'b}\,\delta_{il}}{A^l_{a'}}\,P^{\kappa\delta_2}_{ab\,i}(\ell), \tag{7.1.33}$$

$$\frac{\partial P^{\kappa\delta_2}_{ab\,i}(\ell)}{\partial L_{a'}} = \frac{\delta_{a'b}}{L_{a'}}\,P^{\kappa\delta_2}_{ab\,i}(\ell), \tag{7.1.34}$$

$$\begin{aligned}\frac{\partial P^{\kappa\delta_2}_{ab\,i}(\ell)}{\partial E_{a'}} &= \left[\frac{1}{g_a(z_b)}\frac{\partial g_a(z_b)}{\partial E_{a'}} - \frac{1}{\chi(z_b)}\frac{\partial \chi(z_b)}{\partial E_{a'}}\right. \\ &- \left.\frac{1}{\chi(z_b)}\frac{\partial\chi(z_b)}{\partial E_{a'}}\frac{d\log P}{d\log k}\left(\frac{\ell}{\chi(z_b)}\right)\right]\,P^{\kappa\delta_2}_{ab\,i}(\ell).\end{aligned} \tag{7.1.35}$$

The total Fisher matrix for clustering and weak lensing considering the cross-correlation power spectrum has the following form for parameters $[a_n, A^i_a, R_a, L_a, E_a]$,

$$\begin{pmatrix}
a_1a_1 & a_1a_2 & ... & a_1A^1_1 & a_1A^2_1 & ... & a_1R_1 & a_1L_1 & a_1E_1 & ... \\
a_2a_1 & a_2a_2 & ... & a_2A^1_1 & a_2A^2_1 & ... & a_2R_1 & a_2L_1 & a_2E_1 & ... \\
... & ... & ... & ... & ... & ... & ... & ... & ... & ... \\
A^1_1a_1 & A^1_1a_2 & ... & A^1_1A^1_1 & A^1_1A^2_1 & ... & A^1_1R_1 & A^1_1L_1 & A^1_1E_1 & ... \\
A^2_1a_1 & A^2_1a_2 & ... & A^2_1A^1_1 & A^2_1A^2_1 & ... & A^2_1R_1 & A^2_1L_1 & A^2_1E_1 & ... \\
... & ... & ... & ... & ... & ... & ... & ... & ... & ... \\
R_1a_1 & R_1a_2 & ... & R_1A^1_1 & R_1A^2_1 & ... & R_1R_1 & 0 & R_1E_1 & ... \\
L_1a_1 & L_1a_2 & ... & L_1A^1_1 & L_1A^2_1 & ... & 0 & L_1L_1 & L_1E_1 & ... \\
E_1a_1 & E_1a_2 & ... & E_1A^1_1 & E_1A^2_1 & ... & E_1R_1 & E_1L_1 & E_1E_1 & ... \\
... & ... & ... & ... & ... & ... & ... & ... & ... & ...
\end{pmatrix}.$$

7.1.4 Change of variable module

Once we have analyzed how to extract all the tomographic information using clustering and weak lensing observables, we want to obtain constraints on other parameters in each redshift bin. For that purpose, a change of variable module is created. The change of variable module can be used to project from the initial set of parameters to the desired ones. Given an initial Fisher matrix for parameters $\{\theta_\alpha\}$, we can obtain the Fisher matrix for a new set of parameters $\{q_\alpha\}$ as,

$$\mathbf{F}^q = \mathbf{P}^t\,\mathbf{F}^p\,\mathbf{P}, \tag{7.1.36}$$

where $P_{\alpha\beta} = \partial\theta_\alpha/\partial q_\beta$ is evaluated on the fiducial model. The module is built as general as possible to make an arbitrary change of variables. To illustrate how to use it, the code contains an explicit example of a change of variable that we explain below.

Example: breaking degeneracies with σ_8 priors

The redshift-dependent parameters that we are considering $[A_i(z), R(z), L(z), E(z)]$, exhibit degeneracies among different pairs of parameters. In particular, $\sigma_8(z)$ and $b_i(z)$, $\sigma_8(z)$ and $f(z)$ or $\sigma_8(z)$ and $\Sigma(z)$. In flat ΛCDM since the $E(z)$ measurement fixes Ω_M and $\Sigma(z) = 1$, $L(z)$ allows to determine $\sigma_8(z)$. In such a case, it is possible to break the above mentioned degeneracies and determine observationally $[\, b_i(z), f(z), \sigma_8(z), E(z)\,]$. In more general cosmologies with $\Sigma(z) \neq 1$, as is the case of modified gravity models, this is no longer possible and we need additional information to break the mentioned degeneracies. We can consider, for example, the Planck measurement of the matter power spectrum amplitude, σ_8, as a prior [13]. Introducing this prior in the Fisher matrix and using the relation (7.1.5), we can obtain the Fisher matrix for $[\, b_i(z), f(z), \Sigma(z), E(z)\,]$. For that purpose, we need the following non-zero derivatives to perform the change of variable from the initial variables (7.1.1-7.1.4) to the new ones,

$$\frac{\partial A_a^i}{\partial \sigma_8} = \frac{1}{\sigma_8}\, A_a^i, \tag{7.1.37}$$

$$\frac{\partial R_a}{\partial \sigma_8} = \frac{1}{\sigma_8}\, R_a, \tag{7.1.38}$$

$$\frac{\partial L_a}{\partial \sigma_8} = \frac{1}{\sigma_8}\, L_a, \tag{7.1.39}$$

$$\frac{\partial A_a^i}{\partial b_{a'}^j} = \frac{\delta_{aa'}\,\delta_{ij}}{b_{a'}^j}\, A_a^i, \tag{7.1.40}$$

$$\frac{\partial A_a^i}{\partial f_{a'}} = \frac{A_a^i}{D_a}\,\frac{\partial D_a}{\partial f_{a'}}, \tag{7.1.41}$$

$$\frac{\partial R_a}{\partial f_{a'}} = \sigma_8\, D_a\, \delta_{aa'} + \sigma_8\, f_a\, \frac{\partial D_a}{\partial f_{a'}}, \tag{7.1.42}$$

$$\frac{\partial L_a}{\partial f_{a'}} = \frac{L_a}{D_a}\,\frac{\partial D_a}{\partial f_{a'}}, \tag{7.1.43}$$

$$\frac{\partial L_a}{\partial \Sigma_{a'}} = L_a\, \delta_{aa'}, \tag{7.1.44}$$

being,

$$\frac{\partial D_a}{\partial f_{a'}} = \begin{cases} -\frac{D_a \, \Delta z_{a'}}{1+z_{a'}}, & \text{if } a \geq a' \\ 0, & \text{if } a' > a \end{cases} \tag{7.1.45}$$

This explicit change of variable has been implemented explicitly in the code as an example.

7.1.5 Code structure

Here we explain how `FARO` is structured and the content of each folder. The code is designed in such a way that all the basic functions are included in an independent module. We also describe the modules included in each of the four folders that constitute the code. The structure and the relation between different modules are represented in the flux chart in Fig. 7.1.

- `./FARO/`: in this folder we have the modules `Input_file.py` and `FARO.py`. These modules are used to enter the inputs and run the code in a simple way.

- `./FARO/Modules/`: in this folder we have the modules `Plot_table_gen.py` and `Data_Import.py`. The purpose of these modules is to manipulate the results of the Fisher matrices and generate the tables and plots of the outputs.

- `./FARO/Modules/Change_control/`: in this folder we have the modules `Control.py`, `Change.py` and `Change_b_f_Sigma.py`. These modules have two roles, on one hand to run the basic functions to compute the initial Fisher matrices in each case; and on the other, to compute the change of variable from the initial Fisher matrices to the desired ones. An example of change of variable is explained in 7.1.4, but this case could be modified to take into account any other set of variables.

- `./FARO/Modules/Change_control/Basic_prog/`: in this folder we have the modules `Fisher_matrices.py`, `Spec_cov.py`, `DP_param.py`, `Aux_fun.py`, `Win_dens.py` and `Functions.py`. Finally, this folder contains the basic `FARO` functions. The main output of these modules are the initial Fisher matrices for the $A_i(z)$, $R(z)$, $L(z)$ and $E(z)$ parameters in each redshift bin and a_n parameters for the discretization of $\hat{P}(k)$ in each k-bin.

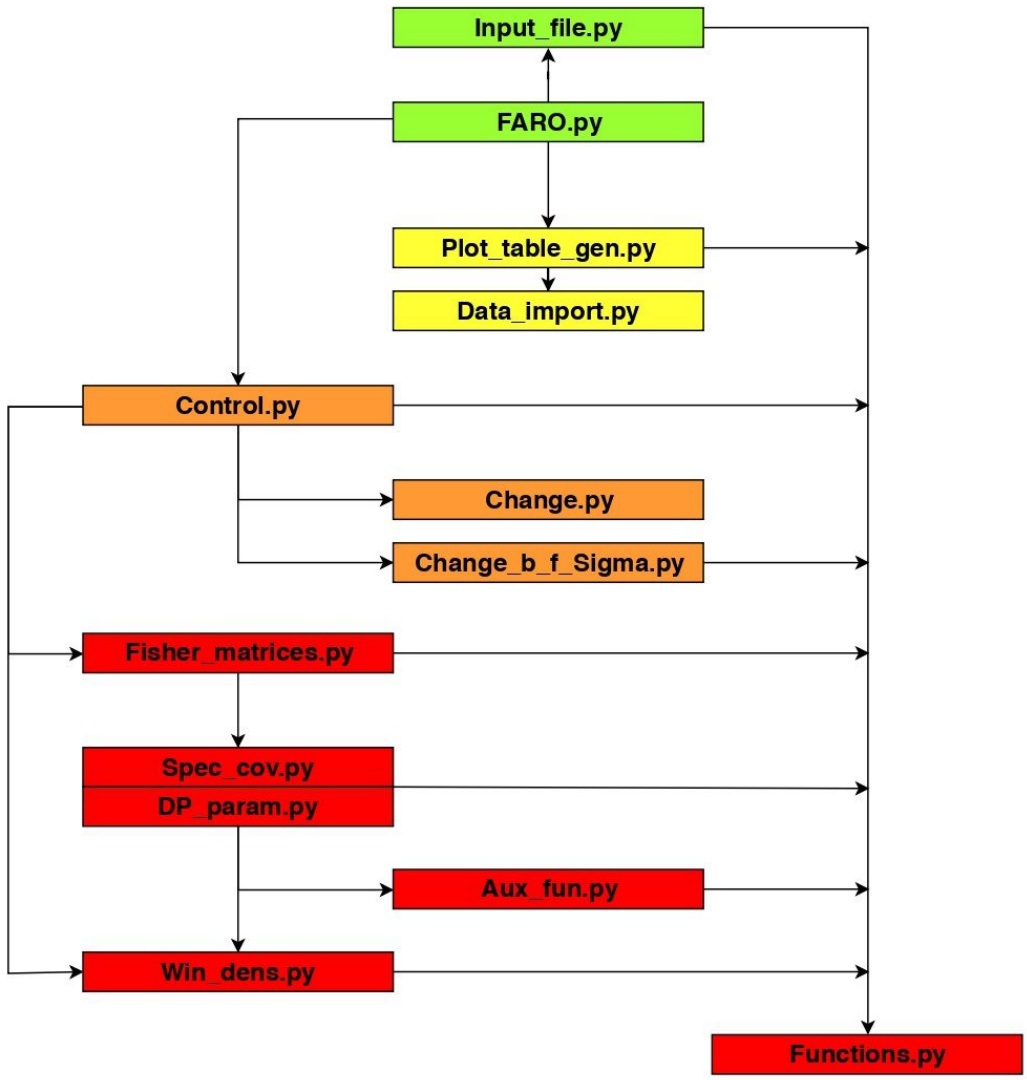

Figure 7.1: Flowchart of the structure of `FARO`. The module color refer the folder in which module is located. In green the modules that are contained in `./FARO/`. In yellow the modules that are contained in `./FARO/Modules/`. In orange the modules that are contained in `./FARO/Modules/Change_control/`. Finally, in red the modules that are contained in `./FARO/Modules/Change_control/Basic_prog/`. Arrows from a module indicate which modules are used in each one. As can be seen, when `FARO.py` is runned all modules are called.

The code is built to define each quantity in the most general way. To do that, each element is defined as a multidimensional matrix and the operations are made with the `numpy` function `np.einsum` which is very useful to calculate products and sums over indices of multidimensional tensors. This is the reason why Fisher matrices are defined with finite sums in (7.1.21), (3.4.11) and (3.4.21), then the observable power spectra are evaluated and summed over discrete bins for k, $\hat{\mu}$, ℓ or z. For example, the derivative $\left.\frac{\partial P_{ij}^{\delta\delta}(z_a,\hat{\mu}_d,k_c)}{\partial\theta_\alpha}\right|_r$ from the Fisher matrix (7.1.21) is defined in the code as a multidimensional matrix with the structure:

$$\left.\frac{\partial P_{ij}^{\delta\delta}(z_a,\hat{\mu}_d,k_c)}{\partial\theta_p}\right|_r \equiv \texttt{DPT[p][a][d][c][i][j]}. \tag{7.1.46}$$

This is very useful because if we want to modify the code in a particular point, we just have to calculate numerically or analytically the concrete multidimensional matrix and substitute it in the code. The structure of each matrix is specified in the code. In addition, this approach is useful to compute the inverse covariance matrices of the power spectra, in particular the covariance matrix for the cross correlation power spectrum (3.4.21).

7.2 Forecasts for future surveys

Finally, we will use `FARO` with the current specifications of several future galaxy and lensing surveys and compare their sensitivity in different redshift and scale ranges. Thus, in particular, we will focus on Euclid [68], DESI [67], J-PAS [66] and LSST [70]. For Euclid we will use the latest specifications from [234] and analyze separately the photometric and spectroscopic surveys. All the surveys specifications can be found in subsection 7.A. Note that in some cases there are redshift bins in which we only have one or two galaxy tracers. In this situation one should make the multitracer galaxy analysis separately. For example, in DESI we have some redshift bins with only BGS, so we should do, on one hand, the BGS forecast and, on the other hand, the LRG+ELG+QSO forecast. Zero values for galaxy densities should never be considered, unless they are in the last redshift bins. For the sake of performing a correct comparison of different galaxy surveys, we have to use redshift bins of the same size. If we used different sizes we would not be comparing the same parameters. In most cases, a larger redshift-bin size implies more information for the parameters in each redshift bin, and smaller errors. However, for the multitracer

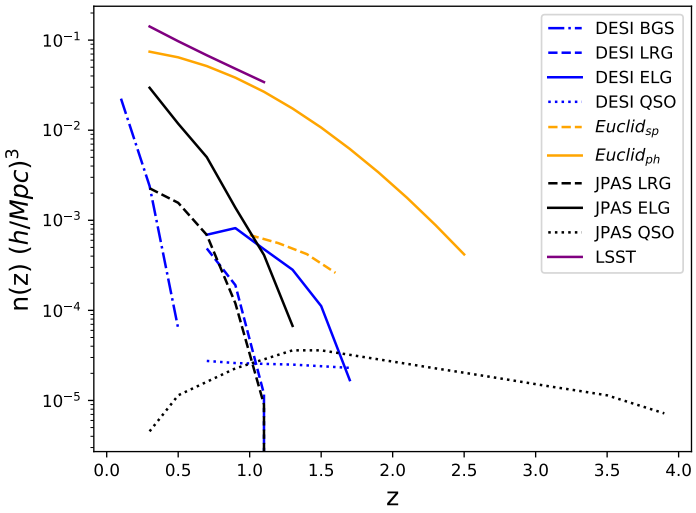

Figure 7.2: Galaxy densities for each galaxy survey and each tracer in units of $(h/\text{Mpc})^3$ [67, 70, 234, 239].

power spectra, there are correlations between different redshift bins due to (7.1.26) that can increase errors if they are important. In order to avoid this effect, $1/\chi(z_a)\,\partial\chi(z_a)/\partial E_b$ should be negligible in (7.1.25) when using (7.1.26). This implies that the redshift bin size should satisfy $\Delta z_a < H_0\,\chi(z_a)\,E^2(z_a)$.

Regarding the k bining, the error in $\hat{P}(k)$ increases with the number of k bins as expected. Correlations between redshift and scale-dependent parameters are negligible for a reasonable number of k bins. However, if we increase the number of k bins, these correlations can be relevant and errors for redshift-dependent parameters would increase. As we have checked for the k range of the example, the number of k-bins should be between 4 and 20 depending on the volume of the survey to have reasonable relative errors below 10% for $\hat{P}(k)$. In the examples of this paper, a number of 10 bins in k is appropriate for all the surveys except for DESI BGS that requires only 5 bins in k due to the reduced z range.

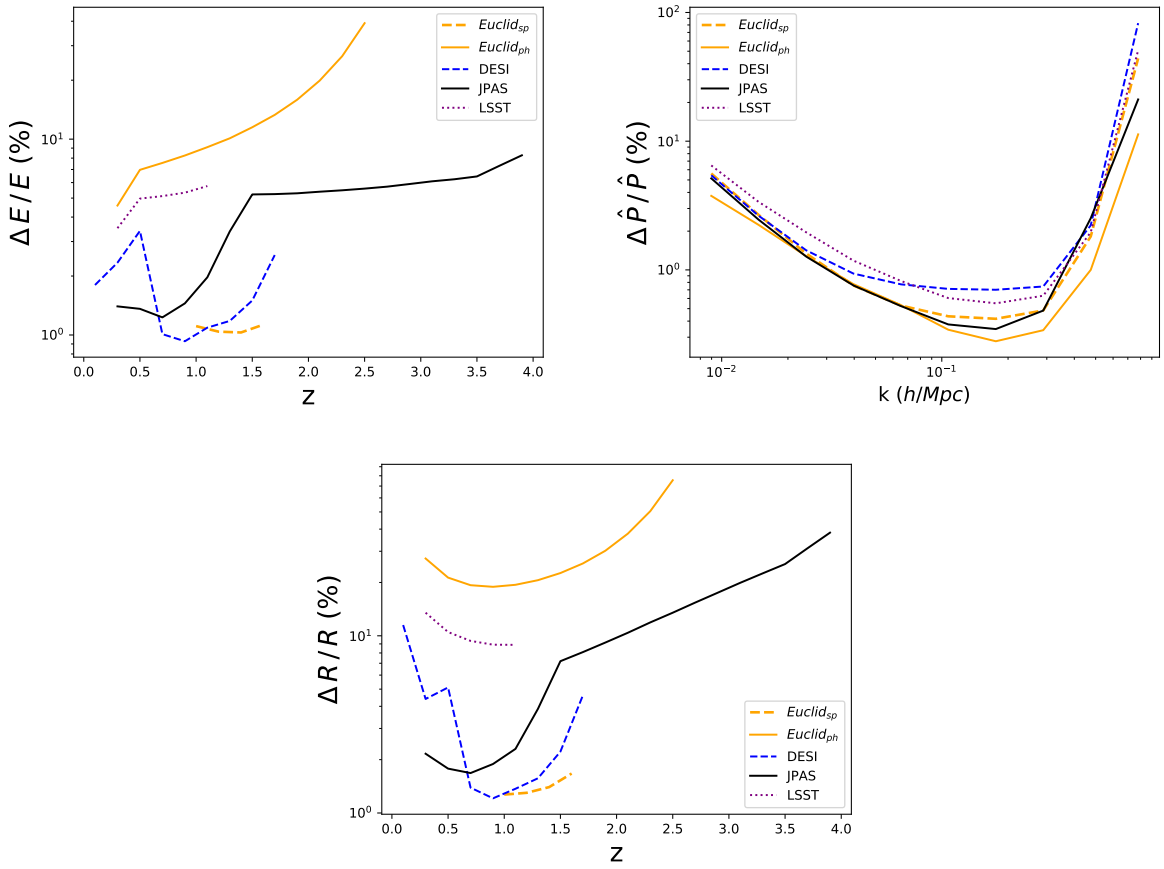

Figure 7.3: Upper left panel: percentage relative errors for $E(z)$ in each redshift bin for different galaxy surveys using clustering information. Upper right panel: percentage relative errors for $\hat{P}(k)$ in each k bin for different galaxy surveys using clustering information. Lower panel: Percentage relative errors for $R(z)$ in each redshift bin for different galaxy surveys using clustering information.

7.2.1 Multitracer 3D galaxy power spectrum information

Here we analyze the results for the multitracer 3D galaxy power spectrum. In Fig. 7.2 we plot the galaxy densities for each survey and each tracer.

First we focus on the initial model-independent parameters. In Fig. 7.3 we plot errors for $E(z)$, $\hat{P}(k)$ and for $R(z)$. As we can see, in order to have good accuracy for $E(z)$ and $R(z)$, it is necessary to have large number densities of galaxies with precise redshifts, $\delta z^C \lesssim 0.01$. So the most appropriate surveys to measure these parameters are spectroscopic and spectro-photometric surveys. On the other hand, for $\hat{P}(k)$, it can be seen that the main characteristic that determines the sensitivity of the survey is the effective volume. In this case, all the surveys analyzed have comparable precision in most of the k range, with more remarkable differences around $k = 2 \times 10^{-1}\ h/\mathrm{Mpc}$. On the other hand, considering the change of variable with the Planck prior for σ_8 mentioned before, we plot errors for the growth function $f(z)$ using clustering information in Fig. 7.4 left panel.

Finally, in order to assess the impact of multitracer measurements, in Fig. 7.5 we compare the precision in $R(z)$ for the J-PAS survey using their different galaxy tracers alone and the total combination. As it can be seen, the total combination improves the sensitivity obtained with the best galaxy tracer only that, in this case, are the ELGs. A recent analysis of the improvement from multiple tracer using Fisher formalism can be found in [240].

7.2.2 Lensing convergence power spectrum information

Now we show the results for the lensing convergence power spectrum, focusing on the model-independent parameters. In Fig. 7.6 we plot errors for $E(z)$, $\hat{P}(k)$ and for $L(z)$. As we can see in the survey specifications, DESI and the spectroscopic Euclid do not collect weak lensing data. In this situation the constraints are essentially dominated by the angular density of galaxies n_θ. Notice that despite the low redshift precision of the pure photometric surveys, still good measurements of $E(z)$ are possible using lensing information alone.

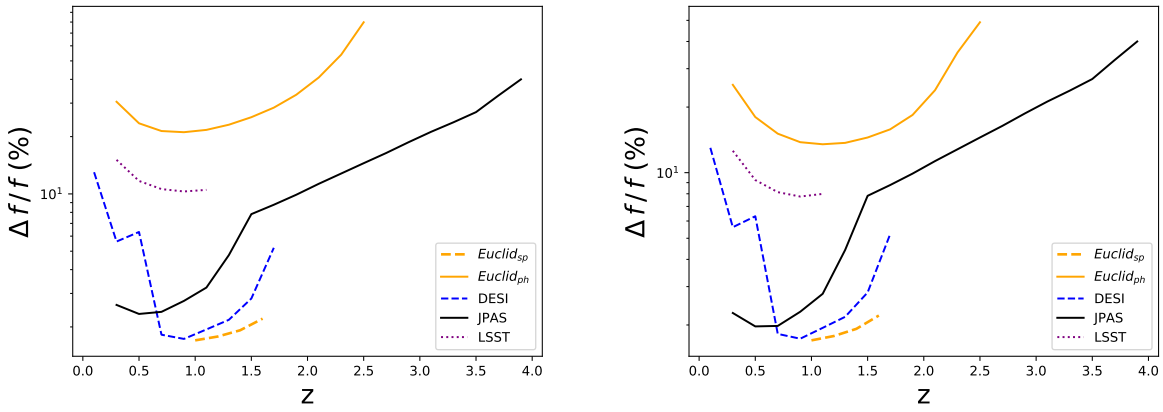

Figure 7.4: Left: percentage relative errors for $f(z)$ in each redshift bin for different galaxy surveys using clustering information. Right: percentage relative errors for $f(z)$ in each redshift bin for different galaxy surveys using clustering, lensing and the cross correlation information. In both plots, the Planck prior on σ_8 has been imposed as shown in Section 7.1.4.

7.2.3 Multitracer, convergence and cross-correlation power spectra information

Finally, we combine information from clustering and lensing. First we will focus on the initial model-independent parameters. In Fig. 7.7 we plot errors for $E(z)$, $\hat{P}(k)$, $R(z)$ and for $L(z)$. The combination of clustering and lensing improves the constraints of both clustering and lensing parameters thanks to the improved constraints on the dimensionless Hubble parameter $E(z)$. The improvement on the Hubble parameter constraints depends on the relative differences of the clustering and lensing sensitivities. In general, if those sensitivities alone are comparable, the combined one improves significantly as is the case of LSST and $\text{Euclid}_{\text{ph}}$.

Also, as expected, if one of the sensitivities is much larger than the other, such sensitivity dominates the combined one. For $\hat{P}(k)$, it can be seen that the combination of clustering and lensing improves the clustering constraints specially at small scales $k \gtrsim 10^{-1}\ h/\text{Mpc}$. Finally, considering the change of variable with the Planck prior for σ_8 mentioned before, we plot in Fig. 7.4 right panel the errors for $f(z)$ and in Fig. 7.8 the errors for $\Sigma(z)$. Notice that one of the main advantages of combining clustering and lensing, and using a prior on σ_8, is that it is possible to measure $\Sigma(z)$ in each redshift bin.

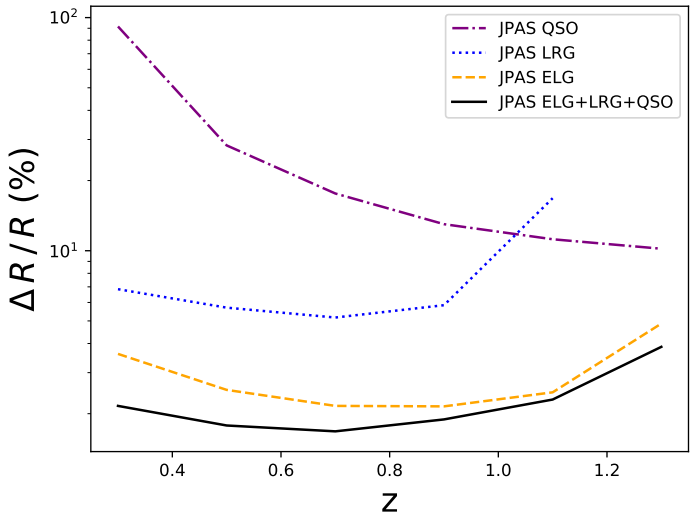

Figure 7.5: Percentage relative errors for $R(z)$ considering different galaxy tracers of J-PAS survey and the combination of all these tracers.

The impact of cross-correlation

In order to estimate the impact of the cross-correlation between clustering and lensing, in Fig. 7.9 we plot the ratio between the precision of the lensing parameter $L(z)$ obtained with and without cross-correlation. As it can be seen the cross-correlation can improve the precision, up to three orders of magnitude depending on redshift. Similarly, the constraints on $\Sigma(z)$ obtained with the σ_8 prior depends strongly on both clustering and lensing information. In particular, as it can be seen in Fig. 7.10, the cross-correlation information between clustering and lensing improves significantly the precision. The relevant role of cross-correlation in the determination of certain parameters has been recently discussed for $\text{Euclid}_{\text{ph}}$ in [241].

This analysis has been done considering the different data of all future surveys separately. Thus, each galaxy survey has its best targets and redshift ranges. A combined analysis of the data collected by different surveys would give more precise cosmological measurements. In particular, the combination of spectroscopic and photometric surveys improves significantly the constraints, as can be seen with a spectro-photometric survey like J-PAS.

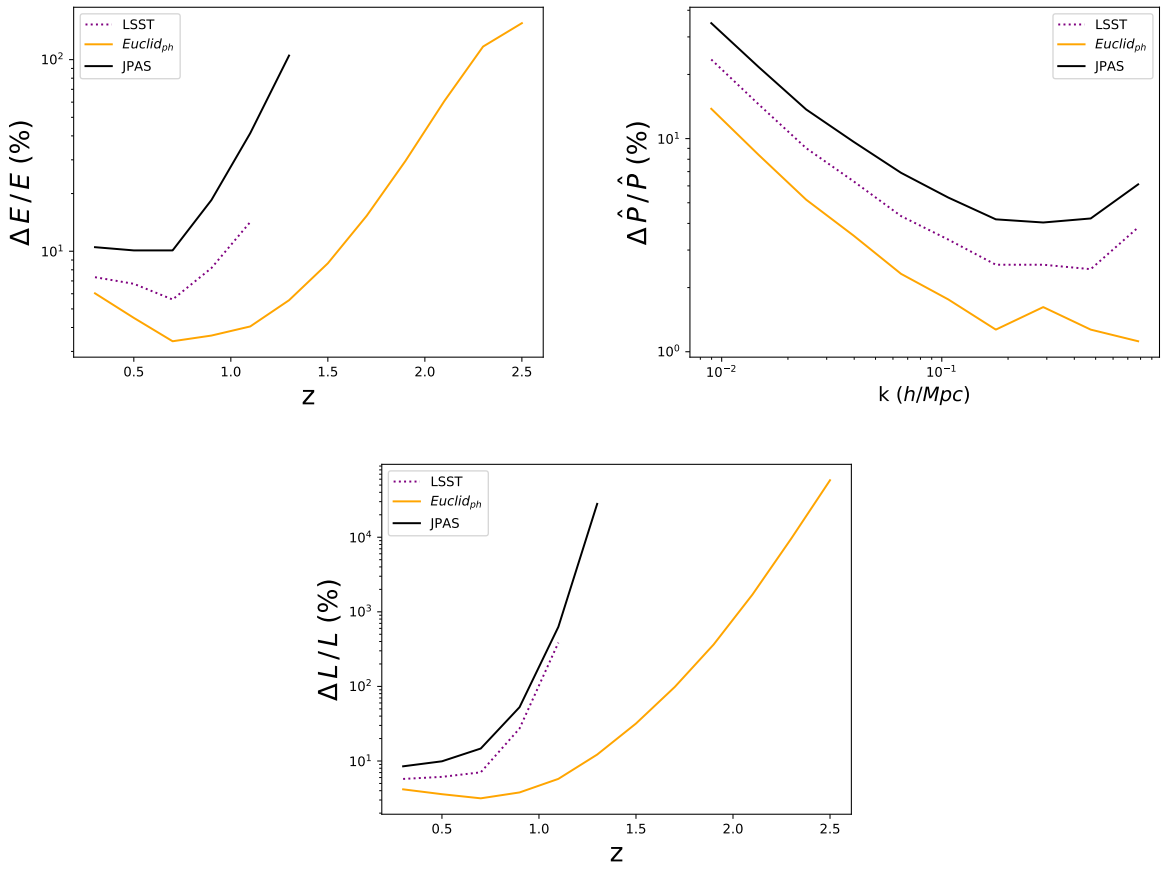

Figure 7.6: Upper left panel: percentage relative errors for $E(z)$ in each redshift bin for different galaxy surveys using lensing information. Upper right panel: percentage relative errors for $\hat{P}(k)$ in each k bin for different galaxy surveys using lensing information. Lower panel: Percentage relative errors for $L(z)$ in each redshift bin for different galaxy surveys using lensing information.

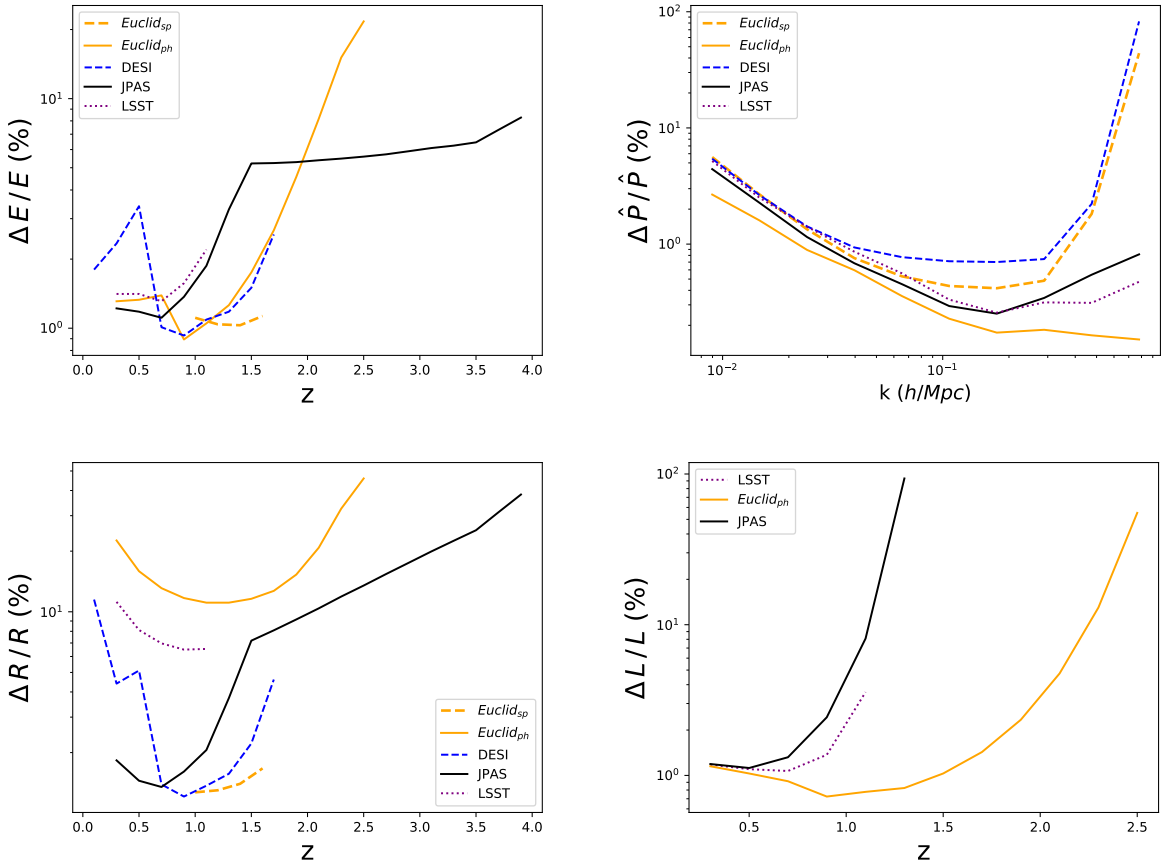

Figure 7.7: Upper left panel: percentage relative errors for $E(z)$ in each redshift bin for different galaxy surveys using clustering, lensing and the cross correlation information. Upper right panel: percentage relative errors for $\hat{P}(k)$ in each k bin for different galaxy surveys using clustering, lensing and the cross correlation information. Lower left panel: percentage relative errors for $R(z)$ in each redshift bin for different galaxy surveys using clustering, lensing and the cross correlation information. Lower right panel: percentage relative errors for $L(z)$ in each redshift bin for different galaxy surveys using clustering, lensing and the cross correlation information.

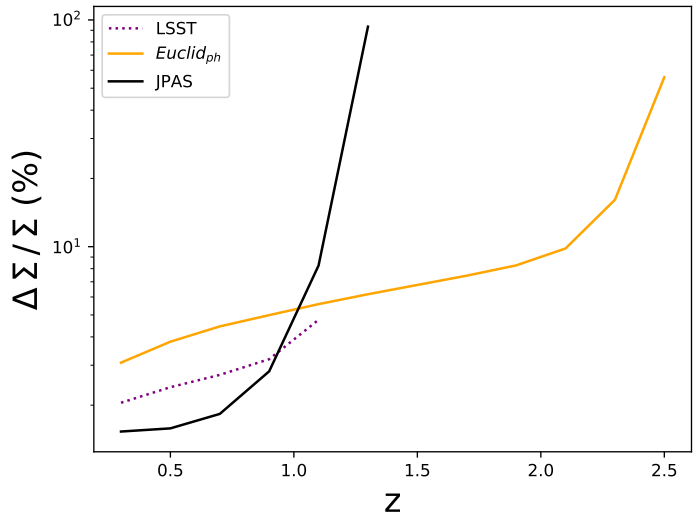

Figure 7.8: Percentage relative errors for $\Sigma(z)$ in each redshift bin for different galaxy surveys using clustering, lensing and the cross correlation information. The Planck prior on σ_8 has been imposed as shown in Section 7.1.4.

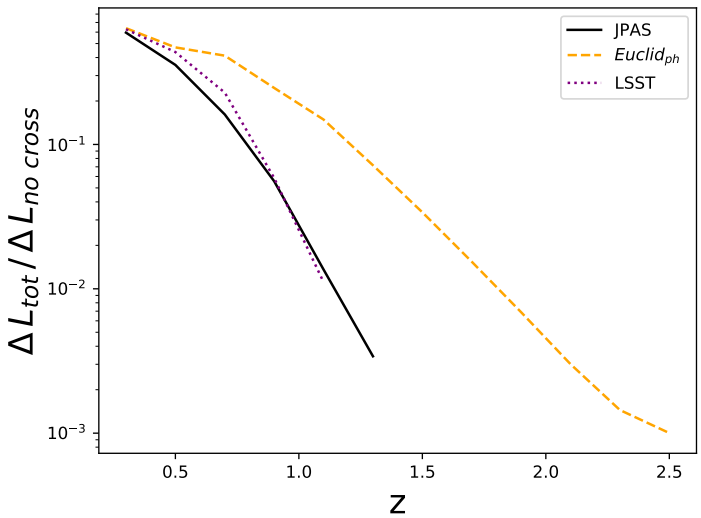

Figure 7.9: Ratio between errors of $L(z)$ considering clustering, lensing and the cross correlation information, and the errors of $L(z)$ considering clustering and lensing informations without cross correlation. The cross correlation information improves $L(z)$ constraints from one to three orders of magnitude depending on redshift.

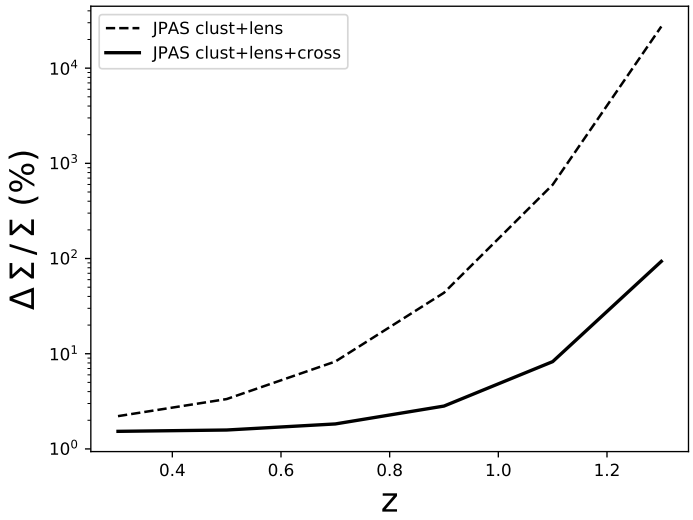

Figure 7.10: Relative errors for $\Sigma(z)$ using J-PAS survey with clustering and lensing information; and with clustering, lensing and the cross correlation information.

7.A Fiducial cosmology and survey specifications

Now we summarize all the specifications of each galaxy survey to compute the Fisher matrices. The fiducial cosmology we use for all the forecast have the following values: $\Omega_m = 0.31$, $\omega_b = 0.0226$, $n_s = 0.96$, $h = 0.68$, $H_0^{-1} = 2997.9\,\mathrm{Mpc/h}$, $\gamma = 0.545$ [202] and $\sigma_8 = 0.82$. In addition, we use the same values for the non linear cut off $\Sigma_0 = 11\,\mathrm{Mpc/h}$ and the intrinsic ellipticity $\gamma_{int} = 0.22$. Redshift bin centers of each survey are shown in Table 7.1. Scale bins are logspaced in 10 bins from $k = 0.007\,\mathrm{h/Mpc}$ to $k = 1\,\mathrm{h/Mpc}$. The sky area of each survey is the following: 8500 deg^2 for J-PAS, 14000 deg^2 for DESI, 14300 deg^2 for LSST and 15000 deg^2 for both Euclid surveys. The redshift error for clustering information is: $\delta z_C = 0.003$ for J-PAS, $\delta z_C = 0.0005$ for DESI, $\delta z_C = 0.03$ for LSST, $\delta z_C = 0.001$ for spectroscopic Euclid and $\delta z_C = 0.05$ for photometric Euclid. For the bias, we consider four different types of galaxies: Luminous Red Galaxies (LRGs), Emission Line Galaxies (ELGs), Bright Galaxies (BGS) and quasars (QSO) [242, 243]. Each type has different fiducial bias given by

$$b(z) = \frac{b(0)}{D(z)}, \tag{7.A.1}$$

being $b_0 = 0.84$ for ELGs, $b_0 = 1.7$ for LRGs and $b_0 = 1.34$ for BGS. For photometric Euclid survey we use a fiducial bias for ELGs of the form $b(z) = \sqrt{1+z}$ [68], for spectroscopic Euclid the fiducial bias are shown in Table 7.1, while the bias for quasars is $b(z) = 0.53 + 0.289\,(1+z)^2$. Finally the bias of LSST galaxies follows equation (7.A.1) with $b_0 = 0.95$ [70]. Finally, for lensing features we have that the redshift errors are: $\delta z_L = 0.03$ for J-PAS and $\delta z_L = 0.05$ for LSST and photometric Euclid. The areal galaxy densities are: $n_\theta = 12.32$ for J-PAS, $n_\theta = 27$ for LSST and $n_\theta = 30$ for Euclid. Values of the mean redshift are $z_{mean} = 0.5$ for J-PAS and $z_{mean} = 0.9$ for Euclid, for LSST the galaxy density distribution is, following [70],

$$n(z) \propto z^2\, e^{-(z/0.11)^{0.68}}, \tag{7.A.2}$$

this galaxy distribution is used instead of (2.4.61) for LSST.

J-PAS			
z	LRG	ELG	QSO
0.3	226.6	2958.6	0.45
0.5	156.3	1181.1	1.14
0.7	68.8	502.1	1.61
0.9	12.0	138.0	2.27
1.1	0.9	41.2	2.86
1.3	0	6.7	3.60
1.5	0	0	3.60
1.7	0	0	3.21
1.9	0	0	2.86
2.1	0	0	2.55
2.3	0	0	2.27
2.5	0	0	2.03
2.7	0	0	1.81
2.9	0	0	1.61
3.1	0	0	1.43
3.3	0	0	1.28
3.5	0	0	1.14
3.7	0	0	0.91
3.9	0	0	0.72

$\text{Euclid}_{\text{ph}}$	
z	ELG
0.3	7440
0.5	6440
0.7	5150
0.9	3830
1.1	2670
1.3	1740
1.5	1070
1.7	620
1.9	341
2.1	178
2.3	88.3
2.5	41.8

DESI				
z	BGS	LRG	ELG	QSO
0.1	2240	0	0	0
0.3	240	0	0	0
0.5	6.3	0	0	0
0.7	0	48.7	69.1	2.75
0.9	0	19.1	81.9	2.60
1.1	0	1.18	47.7	2.55
1.3	0	0	28.2	2.50
1.5	0	0	11.2	2.40
1.7	0	0	1.68	2.30

LSST	
z	n
0.3	14170
0.5	9720
0.7	6790
0.9	4810
1.1	3420

$\text{Euclid}_{\text{sp}}$		
z	ELG	$b(z)$
1.0	68.6	1.46
1.2	55.8	1.61
1.4	42.1	1.75
1.6	26.1	1.90

Table 7.1: From left to right: redshift bins and densities of luminous red galaxies, emission line galaxies and quasars for J-PAS. Redshift bins and densities of emission line galaxies for photometric Euclid survey. Redshift bins and densities of bright galaxies, luminous red galaxies, emission line galaxies and quasars for DESI. Redshift bins and galaxy densities for LSST. Finally, redshift bins, emission line galaxy densities and bias for spectroscopic Euclid survey. Galaxy densities in units of 10^{-5} $\mathrm{h^3\,Mpc^{-3}}$.

Chapter 8

J-PAS: Javalambre Physics of the Accelerating Universe Astrophysical Survey

The Javalambre Physics of the Accelerating Universe Astrophysical Survey (J-PAS) [66] is a spectro-photometric survey to be conducted at the Observatorio Astrofísico de Javalambre (OAJ) in the Javalambre Survey Telescope (JST/T250), a 2.5 m diameter, altazimuthal telescope that will be equipped with the Javalambre Panoramic Camera (JPCam), a 14-CCD mosaic camera using a new large format e2v 9.2 k-by-9.2 k 10 μm pixel detectors, and will incorporate a 54 narrow- and 4 broad-band filter set covering the optical range [244]. Thanks to this large number of filters, J-PAS will be able to measure photo redshifts with a high accuracy in addition to obtain galaxy shapes. In this chapter we will review the characteristics of J-PAS survey in addition with the already finished mini-JPAS survey. Then we will discuss the cosmology forecast of J-PAS survey applied to dark energy and modified gravity theories. The results of this chapter correspond to [239].

8.1 The J-PAS survey

As we have explained before, a spectro-photometric survey is a photometric survey with a high number of narrow band (NB) filters that is able to reach photo-z with an error comparable to that of a spectroscopic measurement. J-PAS being a imaging survey will

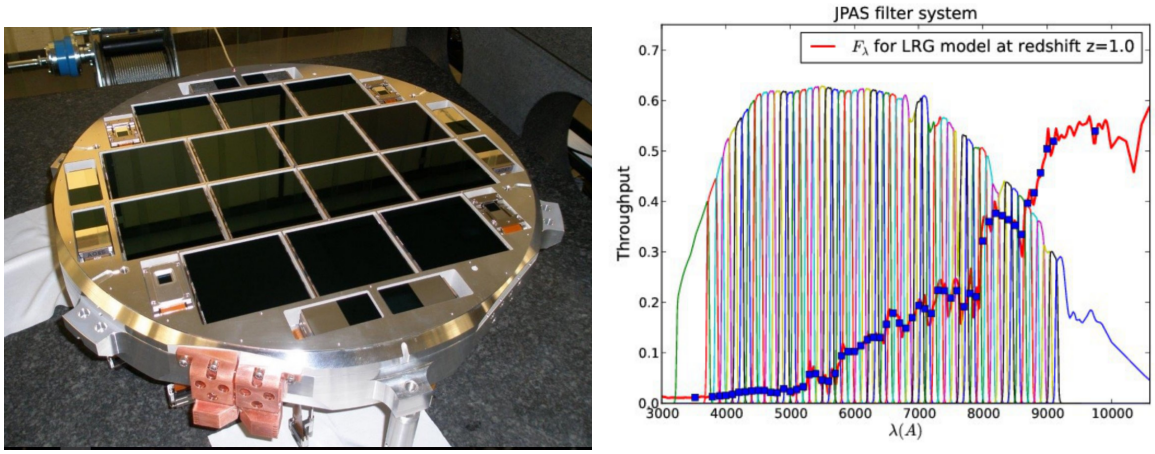

Figure 8.1: Left: JPCam, the 14-CCD mosaic camera, with the new e2v 9k-by-9k 10μm-pixel 16-channel detectors that is already equipped at the OAJ. Right: The J-PAS filter system with a redshifted spectrum of an early type galaxy at $z = 1.0$.

allow to measure galaxy shapes to compute weak lensing power spectra. The J-PAS survey will be the reference spectro-photometric survey in the next decades. As it can be seen in [245], a filter system with contiguous NB filters with order 100Å width is able to measure photometric redshifts with a precision $\sigma_z = 0.003(1 + z)$ for LRGs. This was the original goal of the PAU survey [245, 246] but J-PAS generalizes it to measure also ELGs and QSO at high redshifts and also with a larger sky area. In addition to obtain valuable cosmological information on dark energy and modified gravity, J-PAS will be able to explore galaxy and star formation science. Now we will summarize the main J-PAS characteristics, the camera with which JST will be equipped JPCam, the filter system that will be implemented in the camera and finally the J-PAS sky footprint. The JPCam is a mosaic camera with 14 CCDs that is equipped with the NB filters. In each CCD, four filters can be incorporated. The camera has also three main subsystems, the non-cryogenic subsystem or filter shutter unit (FSU) which comprises the filter exchange mechanism and shutter working at ambient temperature; a cryogenic camera subsystem (Cryo-Cam), and a hexapod actuator system (HAS) which actuates the Cryo-Cam. The filter system of J-PAS is adapted to the JPCam, so there are 56 main filters, 54 of them NB, 1 medium band (MB) and 1 broad band (BB). The NB filters are spaced by 100Å but they have a width of 145Å, so the NB filters overlap. In addition to these filters, three BB filters are added: the filters u, g and r. The r BB is

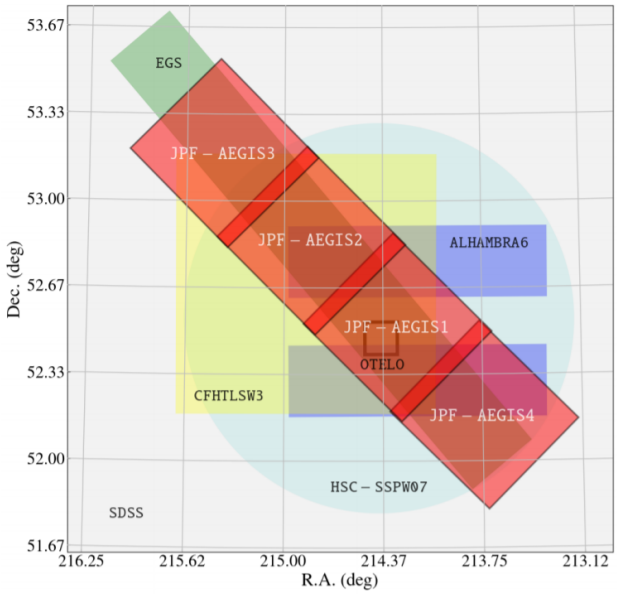

Figure 8.2: Sky footprint of mini-JPAS, with tiles shown as red squares. The footprints of other projects are also shown.

the main filter used for the detection of weak lensing effect. We show the filter system in Fig. 8.1 right panel. The J-PAS survey is planned to measure 9×10^7 LRGs and ELGs up to $z = 1.3$ plus several million QSOs up to $z = 3.9$ over 8500 sq. deg of the northern hemisphere. Considering these specifications and the prior galaxy distribution from [247], mocks are generated to obtain expected galaxy densities for LGRs, ELGs and QSO. The galaxy densities are given in Table 7.1 of Section 7.A [66].

8.2 The mini-JPAS survey

The mini-JPAS survey [248, 249] was conducted before the JPCam was installed at the OAJ. A pathfinder camera (PF) with one 9k × 9k CCD camera, 0.3 deg^2 field-of-view and 0.225 arcsec pixel size, was used to obtain mini-JPAS data as a prove of the potential of the upcoming JPAS survey. Between May and September 2018, a total of approximately one square degree was observed with 60 filters. The 54 NB filters of J-PAS, two BB filters and the u, g, r, i SDSS BB filters. With this measurement, a detailed analysis of the photo-z and the galaxy densities has been done which allow to update the initial prediction in [66].

The one square degree of mini-JPAS is on the famous Extended Gorth Stip (EGS) field, overlaping with other surveys like AEGIS, ALHAMBRA or HSC.

8.3 J-PAS forecasts on modified gravity

In this section, we will obtain future constraints to modified gravity for the J-PAS survey and we will compare with other upcoming surveys like Euclid and DESI. We will constraint μ and η parameters (1.4.18, 1.4.19) using clustering and weak lensing power spectra, then we consider the combined information without the cross correlation power spectrum. Fiducial cosmology and the survey specifications can be found in Section 8.A. We have adopted a model-independent parametrization that considers all the free and independent parameters that are needed to describe such power spectra in the linear regime, and then we project them to μ and η parameters. In this analysis, we have fixed the initial matter power spectrum $\hat{P}(k)$ defined in (7.1.6) to the fiducial model, corresponding to a flat ΛCDM cosmology. As a main difference with respect to Chapter 7, we do not take into account the cross-correlation power spectrum because these results were obtained before the code was able to compute it.

We will consider two different cases for μ and η. First, considering the time-independent case, we have performed both a tomographic redshift bin analysis and an analysis in k-bins. By summing over all the redshift range we have obtained errors for the modified gravity parameters. Second, for a time-dependent case, we have considered the particular parametrization in terms of μ_0 and η_0 (6.2.6-6.2.7) usually employed in the literature.

For clustering power spectrum, we consider the redshift dependent parameters A_i, R and E with i denoting the different tracers, defined in (7.1.1)-(7.1.4). Because we have checked that marginalizing with respect to a non-Poissonian shot noise component has a minimal effect, for simplicity, we do not consider it as a free parameter in this case. Once we have obtained the Fisher matrix for $[\,A_i,\, R,\, E\,]$, we project first into $[\,A_i,\, f,\, E\,]$, and then to $[\,A_i,\, \mu,\, E\,]$ using the relation (4.5.11).

Forecasts for the relative errors in μ and $f(z)$ in the different redshift bins can be seen in Figure 8.3. As we can see, ELGs provide the tightest constraints for J-PAS. Compared to Euclid or DESI, we find that J-PAS provides the best precision in the redshift range

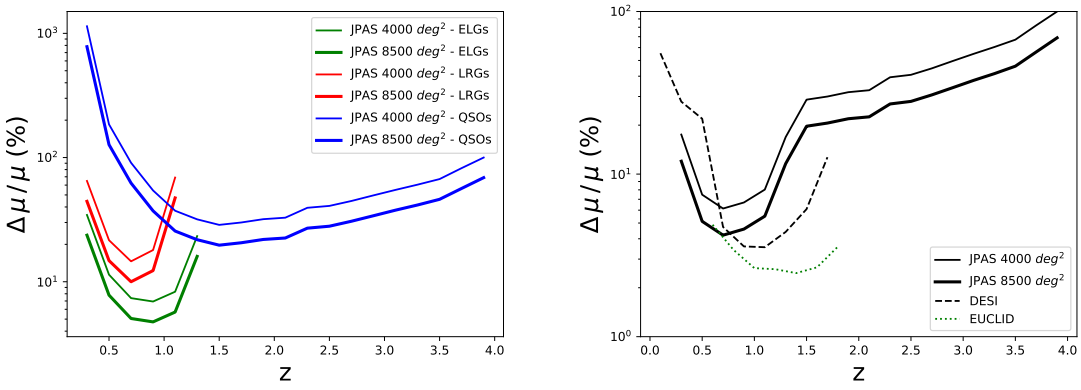

Figure 8.3: Left: tomographic relative errors of μ for J-PAS with ELGs, LRGs and quasars. Right: tomographic relative errors of μ for J-PAS (ELGs+LRGs+QSOs), DESI (BGS+ELGs+LRGs+QSOs) and Euclid (ELGs) using clustering information.

$z = 0.3 - 0.6$. Notice this is also the case in the 4000 sq. deg. configuration. This is mainly thanks to the large number of expected ELG detection in that redshift range which compensates the smaller fraction of sky of J-PAS as compared to other surveys.

In Figure 8.4 we show $f(z)$ and $f\sigma_8(z)$ with the expected error bars. To obtain errors for μ in different k-bins we just calculate the Fisher matrix (3.2.16) considering the k_{min} and k_{max} values the edges of each different k-bin and summing all the information in z. Results can be seen in Figure 8.5 left panel. We find that the best precision is obtained for scales around $k = 0.1$ h/Mpc, which are slightly below Euclid and DESI best scales. Finally, in Figure 8.6 left panel we show errors for the Hubble dimensionless parameter $E(z)$ in the different redshift bins. Once more, J-PAS provides better precision below $z = 0.6$, but also thanks to QSOs observation at higher redshifts, J-PAS will be able to measure the expansion rate in the practically unexplored region up to redshift $z = 3.5$ with precision below 30%.

For weak lensing power spectrum, we will obtain the errors on the η parameter. First, we compute the Fisher matrix for $[E,\, L]$ in each bin. Now it is necessary to change the initial parameters $[E, L]$ to the new ones $[E, \eta]$. Using (7.1.1) we obtain $\frac{\partial \eta}{\partial L} = \frac{2}{L}$ and $\frac{\partial \eta}{\partial E} = 0$. For time-independent parameters, we show in Figure 8.5 middle panel the relative errors in η for the different redshift bins for J-PAS and Euclid. Again, J-PAS provides the

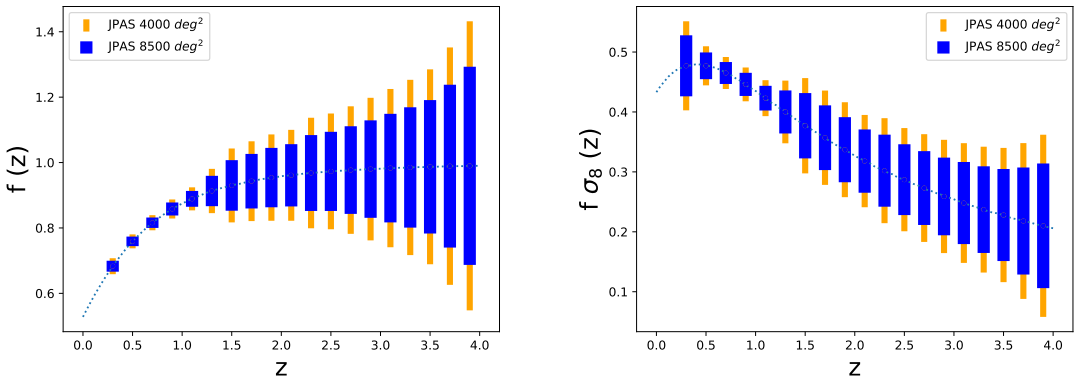

Figure 8.4: Growth function and $f\sigma_8$ function for the fiducial cosmology with error bars for J-PAS 8500 and 4000 square degrees, using ELGs+LRGs+QSOs.

best errors in the range $z = 0.3 - 0.6$. In order to obtain the errors of η in different ℓ-bins we introduce a window function in the Fisher matrix (3.4.11) in order to take into account only the information of a bin ℓ_c of width $\Delta\ell_c$,

$$F^{\kappa\kappa}_{\alpha\beta}(\ell_c) = f_{sky} \sum_{\ell} \Delta\ell \, \frac{(2\ell+1)}{2} \, W_c(\ell) \mathrm{Tr}\left[\frac{\partial \mathbf{P}}{\partial\theta_\alpha}\mathbf{C}^{-1}\frac{\partial \mathbf{P}}{\partial\theta_\beta}\mathbf{C}^{-1}\right], \tag{8.3.1}$$

where $W_c(\ell)$ is defined as

$$W_c(\ell) = \theta\left(\ell - \left[\ell_c - \frac{\Delta\ell_c}{2}\right]\right)\theta\left(\left[\ell_c + \frac{\Delta\ell_c}{2}\right] - \ell\right), \tag{8.3.2}$$

being $\theta(x)$ the Heaviside function. We first change from $[E, L]$ to $[E, \eta]$ in each redshift bin and then sum the information of η for the different redshift bins. The corresponding errors can be seen in Figure 8.5 right panel for Euclid and J-PAS.

Now, we analyze the case in which information from clustering and lensing are combined without cross correlation. We take the Fisher matrix of parameters $[A_i, \mu, E]$ for clustering and $[E, \eta]$ for weak lensing and build the full matrix with parameters $[A_i, \mu, E, \eta]$. By inverting this Fisher matrix, we obtain the errors for μ and η. These results are shown in Figure 8.7 where we compare the sensitivity of Euclid and J-PAS for time-independent μ and η in the different redshift bins. For completeness, we also show the same comparison for the function $E(z)$ in Figure 8.6. As we can see, the combination of clustering and lensing information improves the sensitivity in around a 10% for all the parameters. We

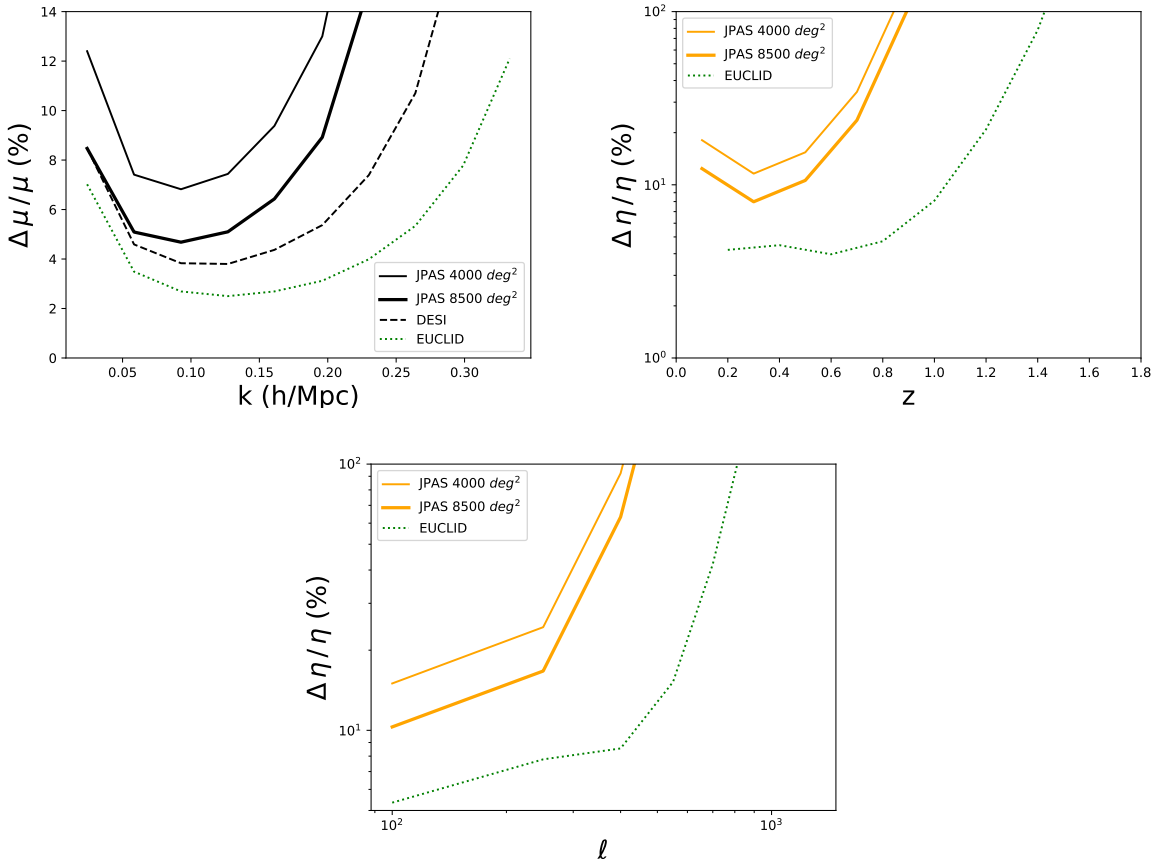

Figure 8.5: Upper left panel: relative errors of $\mu(k)$ for J-PAS (ELGs+LRGs+QSOs), DESI (BGS+ELGs+LRGs+QSOs) and Euclid (ELGs) using clustering information. Upper right panel: tomographic relative errors of η for J-PAS (ELGs+LRGs) and Euclid (ELGs) using lensing information. Lower panel: relative errors of $\eta(\ell)$ for J-PAS (ELGs+LRGs) and Euclid (ELGs) using lensing information.

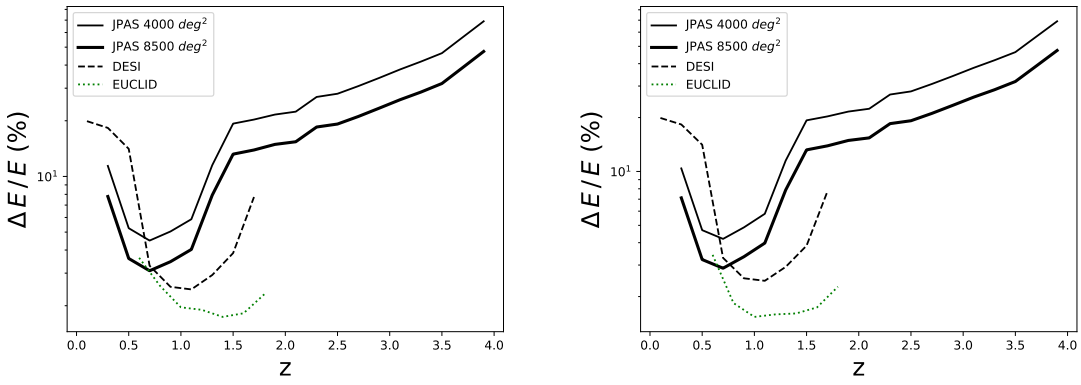

Figure 8.6: Relative errors for $E(z)$ for J-PAS (ELGs+LRGs+QSOs), DESI (BGS+ELGs+LRGs+QSOs) and Euclid (ELGs) using clustering information (left panel), and using clustering and lensing information (right panel). In the case of DESI and J-PAS quasars, only clustering information is taken into account. For lensing in J-PAS the redshift error is $\delta z = 3\%$.

sum all the information in the whole redshift range for μ and η and plot their error ellipses in the right panel of Figure 8.8. These results are summarized in Table 8.1.

Finally, we consider the phenomenological time-dependent parametrization (6.2.6-6.2.7). Using the analytical fitting function for this particular expressions obtained in 4.5.2, we obtain errors for μ_0 and η_0 with fiducial values $\mu_0 = \eta_0 = 1$. We plot on the left panel of Figure 8.8 error ellipses for μ_0 and η_0.

From the tomographic analysis, we find that using the clustering information alone, J-PAS will allow to measure the expansion rate $H(z)$ with precision 3% in the best redshift bin ($z = 0.7$) and the μ parameter with a precision around 5% in the best redshift bin. From lensing alone, J-PAS will be able to measure η with a precision around 8% in the best redshift bin. The combination of clustering and lensing will allow to improve the precision in μ down to 4% in the best bin. Considering the information in the whole redshift range, we have found that J-PAS will be able to measure time-independent μ and η with precision better than 3% for both parameters. For μ_0 and η_0 we have obtained errors of 10% and 5%, respectively.

When compared to future spectroscopic surveys such as DESI or spectroscopic and photometric ones such as Euclid, we have shown that from clustering and lensing infor-

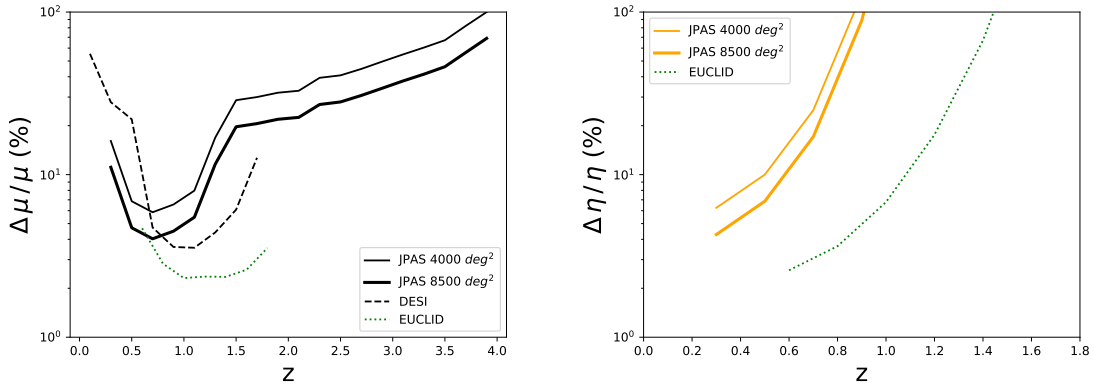

Figure 8.7: From left to right, tomographic relative errors for μ and η for J-PAS (ELGs+LRGs+QSOs), DESI (BGS+ELGs+LRGs+QSOs) and Euclid (ELGs) using clustering and lensing information. In the case of DESI and J-PAS quasars only clustering information is taken into account. For lensing in J-PAS the redshift error is $\delta z = 3\%$.

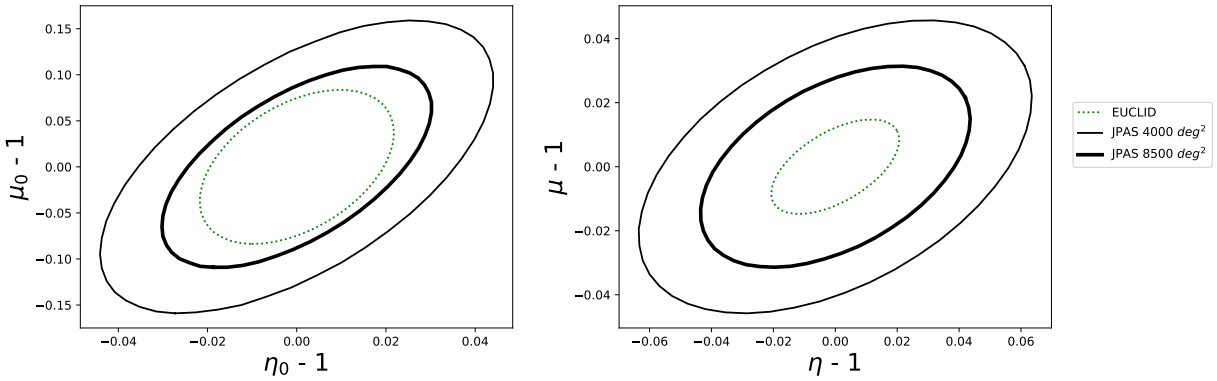

Figure 8.8: 1σ contour error for μ_0 and η_0 (left panel) defined in (6.2.6) and (6.2.7), and (right panel) for constant μ and η. All in J-PAS (ELGs+LRGs+QSOs) and Euclid (ELGs) surveys combining clustering and lensing information, for 8500 deg^2 and 4000 deg^2.

Survey	$\Delta\mu/\mu(\%)$	$\Delta\eta/\eta(\%)$	$\Delta\mu_0/\mu_0(\%)$	$\Delta\eta_0/\eta_0(\%)$
Euclid	0.98	1.37	7.13	3.38
J-PAS 8500	2.08	2.89	9.66	4.58
J-PAS 4000	3.03	4.21	14.1	6.68

Table 8.1: Relative errors for constant μ and η, and μ_0 and η_0 for Euclid and JPAS (with 8500 and 4000 square degrees), considering clustering and lensing information.

mation, J-PAS will have the best errors for redshifts between $z = 0.3 - 0.6$, thanks to the large number of ELGs detectable in that redshift range. Note also that thanks to QSOs observation at higher redshifts, J-PAS will be able to measure the expansion rate and modified gravity parameters in the practically unexplored region up to redshift $z = 3.5$ with precision below 30%.

In the whole redshift range, the J-PAS precision in both μ and η will be a factor 1.5-2 below Euclid in their respective best bins. For the time-dependent (μ_0, η_0) parametrization (6.2.6-6.2.7), we have shown that J-PAS is closer to Euclid than in the constant case. This is due to the fact that low-redshift measurements are more sensitive to μ_0 and η_0 than high-redshift ones, and at low redshift J-PAS precision surpasses that of Euclid.

8.A Fiducial cosmology and survey specifications

The fiducial J-PAS cosmology [250] assumed in our analysis is the flat ΛCDM model with the parameters $\Omega_m = 0.31$, $\Omega_b = 0.049$, $n_s = 0.96$, $h = 0.68$, $H_0^{-1} = 2997.9\,\mathrm{Mpc/h}$, and $\sigma_8 = 0.82$ which are compatible with Planck 2018 [10]. For this cosmology, the $E(z)$ function defined previously is given by

$$E(z) = \sqrt{\Omega_m\,(1+z)^3 + (1-\Omega_m)}\,, \tag{8.A.1}$$

whereas the growth function can be written as

$$f_\Lambda(z) = \left(\Omega_m\,(1+z)^3 \frac{1}{E^2(z)}\right)^\gamma, \tag{8.A.2}$$

with the growth index $\gamma = 0.545$ [202]. For the bias, we consider four different types of galaxies: Luminous Red Galaxies (LRGs), Emission Line Galaxies (ELGs), Bright Galaxies

(BGS) ans quasars (QSO) [242, 243]. Each type has different fiducial bias given by

$$b(z) = \frac{b(0)}{D(z)}, \tag{8.A.3}$$

being $b_0 = 0.84$ for ELGs, $b_0 = 1.7$ for LRGs and $b_0 = 1.34$ for BGS. For Euclid survey we use a fiducial bias for ELGs of the form $b(z) = \sqrt{1+z}$ [68], while the bias for quasars is $b(z) = 0.53 + 0.289\,(1+z)^2$. Finally, we summarize the surveys specifications necessary to compute the different Fisher matrices. For clustering we have considered: redshift bins and galaxy densities for each bin which can be found in the left panel of Table 8.2 for J-PAS, in the center panel of Table 8.2 for DESI and in the right panel of Table 8.2 for Euclid. We consider two configurations of total area for J-PAS, namely 8500 deg^2 and 4000 deg^2 which correspond to fractions of the sky of $f_{sky} = 0.206$ and $f_{sky} = 0.097$ respectively. $f_{sky} = 0.339$ for DESI with 14000 deg^2 and $f_{sky} = 0.364$ for Euclid with 15000 deg^2. The redshift error is $\delta z = 0.003$ for galaxies and QSO in J-PAS, $\delta z = 0.0005$ for galaxies in DESI and $\delta z = 0.001$ for QSO in DESI and galaxies in Euclid.

For the weak lensing analysis we have used: redshift bins and the fraction of the sky f_{sky}, which are the same as in the clustering analysis; mean redshifts for the galaxy density which are $z_{mean} = 0.5$ for J-PAS and $z_{mean} = 0.9$ for Euclid; the angular number density n_θ for J-PAS considering ELGs and LRGs with $\delta z = 0.03$ is $n_\theta = 12.32$. For Euclid, $n_\theta = 35$ galaxies per square arc minute with $\delta z = 0.05$.

Notice that there are some differences with respect to Subsection 7.A, mainly in the Euclid specifications. This is because, in Subsection 7.A, we considered updated specifications for Euclid [234] that were not available when the J-PAS forecast was performed.

J-PAS			
z	LRG	ELG	QSO
0.3	226.6	2958.6	0.45
0.5	156.3	1181.1	1.14
0.7	68.8	502.1	1.61
0.9	12.0	138.0	2.27
1.1	0.9	41.2	2.86
1.3	0	6.7	3.60
1.5	0	0	3.60
1.7	0	0	3.21
1.9	0	0	2.86
2.1	0	0	2.55
2.3	0	0	2.27
2.5	0	0	2.03
2.7	0	0	1.81
2.9	0	0	1.61
3.1	0	0	1.43
3.3	0	0	1.28
3.5	0	0	1.14
3.7	0	0	0.91
3.9	0	0	0.72

DESI				
z	BGS	LRG	ELG	QSO
0.1	2240	0	0	0
0.3	240	0	0	0
0.5	6.3	0	0	0
0.7	0	48.7	69.1	2.75
0.9	0	19.1	81.9	2.60
1.1	0	1.18	47.7	2.55
1.3	0	0	28.2	2.50
1.5	0	0	11.2	2.40
1.7	0	0	1.68	2.30

Euclid	
z	ELG
0.6	356
0.8	242
1.0	181
1.2	144
1.4	99
1.6	66
1.8	33

Table 8.2: Left panel: redshift bins and densities of luminous red galaxies, emission line galaxies and quasars for J-PAS. Center panel: redshift bins and densities of bright galaxies, luminous red galaxies, emission line galaxies and quasars for DESI. Right panel: redshift bins and densities of emission line galaxies for Euclid. Galaxy densities in units of 10^{-5} $\mathrm{h^3\,Mpc^{-3}}$.

Chapter 9

Conclusions

The goal of this thesis has been the model-independent parametrization of modified cosmologies and the forecast of the precision with which future galaxy surveys will be able to detect such modifications. We have analyzed in detail non-standard cosmologies involving vector degrees of freedom and non-standard dark matter behaviour. We have parametrized them in a phenomenological way, considering the QSA approximation in the sub-Hubble regime, by introducing extra effective parameters. Once we obtain these parametrizations, we have performed a forecast analysis considering galaxy survey observables. With that purpose, we have developed the publicly available FARO Fisher code and we have applied this formalism to obtain modified gravity constraints for the J-PAS survey. The main results of this thesis are summarized below:

- We have shown that general modified gravity models with a vector degree of freedom can be described with eight effective parameters, in contrast with the two parameters needed in the standard scalar case. In the case in which dark matter vorticity is negligible, the number of independent parameters is reduced to four. Unlike previous works, we consider a spatial component in the background vector field that introduces a preferred direction. For this reason, the effective parameters have an extra dependence on the direction of the wavevector. We have analyzed the general dependence of the parameters with $x = \hat{\mathbf{k}} \cdot \hat{\mathbf{A}}$ being $\hat{\mathbf{A}}$ the background vector field. In the simplest case, we have shown that the effective parameters depend only on even powers of x.

- We have considered models with modified dark matter, either imperfect or non-conserved. We have shown that five independent effective parameters $(\mu, \gamma, \mu_m, \mu_d, \mu_\theta)$ are needed to describe this type of models. In addition and in order to make forecast codes faster, we have analyzed how to analytically parametrize the growth function in different cases.

- When we apply the vector phenomenological parametrization to galaxy survey observables, we have shown that the existence of a preferred direction modifies the observable power spectra. For the galaxy distribution power spectrum, we find that a new angular dependence on the line of sight appears which is different from the usual effect induced by redshift space distortions. For the weak-lensing power spectrum, a dependence on the line of sight is introduced in the shear and convergence power spectra which is absent in the isotropic case. In addition, images rotation is induced in addition to the standard convergence and shear effects. Finally, we have found a useful relation between the different power spectra, $P_{\gamma_1} + P_{\gamma_2} = P_\kappa + P_\omega$, which shows that even though P_ω cannot be measured directly using weak lensing maps, it can be derived from P_{γ_1}, P_{γ_2} and P_κ.

- Considering the non-standard dark matter parametrization for galaxy survey observables, we have shown that, in the simplest case in which the effective parameters are constant, the observables only depend on a reduced subset of parameters $(\Sigma, \zeta, \mu_\theta)$. This is interesting because a measurement of these parameters can give us some clues about the underlying theory. There are two cases in which we would extract a lot of information. If $\zeta = \mu_\theta = 1$ but $\Sigma \neq 1$ i.e. we measure standard galaxy and peculiar velocity power spectra but a non-standard convergence power spectrum, this can only be generated by a modified gravity with $\mu = 1$ but $\gamma \neq 1$. If $\Sigma = \mu_\theta = 1$ but $\zeta \neq 1$ i.e. we measure standard power spectra but with a non-standard growth function, this can only be generated by a modified dark matter theory with bulk and shear viscosity. More complicated situations produce a degeneration between underlying theories as we can see in Table 5.1.

- In order to analyze the capability of future surveys to measure this type of models, we have performed a Fisher forecast analysis. With that purpose, we have extended

the standard Fisher matrix approach in order to include the presence of preferred directions. We have considered two cases for the galaxy distribution power spectrum. First, we have obtained the Fisher matrix for the multipole power spectrum, and then we have obtained the Fisher matrix for the power spectrum in redshift space, which allows us to include the Alcock-Paczynski effect. In both cases, we obtain that the precision on measurements of the effective Newton constant $\mu = \mu_0 + \mu_2 x^2 + \mu_4 x^4$ for an Euclid-like survey will be around 1% for μ_0 and a few percent for μ_2 and μ_4. On the other hand, the weak-lensing forecast analysis indicates that the γ parameter could be measured with a few percent precision, wheras μ_Q and μ_h parameters could be determined with precision around 1%. The forecast analysis for the non-standard dark matter parametrization shows that an Euclid-like survey could measure $(\Sigma, \zeta, \mu_\theta)$ with accuracy of order 1 %. However, peculiar velocity surveys will not be competitive measuring these parameters.

- One important contribution of this thesis is the development of the new public Python `FARO` code, which has been designed to perform model-independent Fisher forecast analysis for multitracer galaxy and lensing surveys. The main observables used by the code are the multitracer 3D power spectrum, the lensing convergence power spectrum and the power spectrum for the multitracer cross correlation between galaxy distribution and shapes. The code follows a model-independent approach in which we consider as free parameters $A_a(z)$, $R(z)$, $L(z)$ and $E(z)$ in each redshift bin, in addition to a model-independent parametrization of $\hat{P}(k)$ in logarithmically spaced k bins. Using the code, we have analyzed as an example the forecast of future surveys like Euclid, DESI, JPAS or LSST. In particular, we have shown that the combination of clustering, lensing and the cross-correlation information improves significantly the constraints.

- Finally, in this thesis we have analyzed the ability of the J-PAS survey to constrain modified gravity models. We have considered the μ and η phenomenological parameterization of modified gravity models. As can be seen in Section 8.3, comparing J-PAS with other future surveys like DESI and Euclid, J-PAS will have the best precision for redshifts between $z = 0.3 - 0.6$.

Forecasting the capability of future galaxy surveys to constrain alternative cosmologies is an important topic in cosmology. The results of this thesis provide a model-independent approach to test preferred directions and non-standard dark matter models. In addition, the presented results show that future galaxy surveys like J-PAS, Euclid or DESI, will be able to measure the parameters of these models at the one percent level. For future analysis, the results of this thesis can contribute to improve forecast analysis of galaxy surveys. In particular, it will be interesting to perform forecasts for combined galaxy surveys, to explore survey configurations to maximize constraints or to combine large-scale structure information with other observables like the CMB. Thanks to the upcoming galaxy surveys, we will know more about the nature of dark matter and dark energy. In the most optimistic scenario, we will be able to determine if standard GR needs to be modified on cosmological scales.

Bibliography

[1] C. M. Will, "The Confrontation between general relativity and experiment," *Living Rev. Rel.* **9** (2006) 3, arXiv:gr-qc/0510072.

[2] E. Berti *et al.*, "Testing General Relativity with Present and Future Astrophysical Observations," *Class. Quant. Grav.* **32** (2015) 243001, arXiv:1501.07274 [gr-qc].

[3] A. Lyne *et al.*, "A Double - pulsar system - A Rare laboratory for relativistic gravity and plasma physics," *Science* **303** (2004) 1153–1157, arXiv:astro-ph/0401086.

[4] P. Demorest, T. Pennucci, S. Ransom, M. Roberts, and J. Hessels, "Shapiro Delay Measurement of A Two Solar Mass Neutron Star," *Nature* **467** (2010) 1081–1083, arXiv:1010.5788 [astro-ph.HE].

[5] **LIGO Scientific, Virgo** Collaboration, B. P. Abbott *et al.*, "GW151226: Observation of Gravitational Waves from a 22-Solar-Mass Binary Black Hole Coalescence," *Phys. Rev. Lett.* **116** no. 24, (2016) 241103, arXiv:1606.04855 [gr-qc].

[6] **LIGO Scientific, Virgo** Collaboration, B. Abbott *et al.*, "Observation of Gravitational Waves from a Binary Black Hole Merger," *Phys. Rev. Lett.* **116** no. 6, (2016) 061102, arXiv:1602.03837 [gr-qc].

[7] L. Amendola and S. Tsujikawa, *Dark Energy*. Cambridge University Press, 2015. http://www.cambridge.org/academic/subjects/physics/cosmology-relativity-and-gravitation/dark-energy-theory-and-observations?format=PB&isbn=9781107453982.

[8] T. Padmanabhan, "Cosmological constant: The Weight of the vacuum," *Phys. Rept.* **380** (2003) 235–320, arXiv:hep-th/0212290.

[9] **Supernova Search Team** Collaboration, A. G. Riess *et al.*, "Observational evidence from supernovae for an accelerating universe and a cosmological constant," *Astron. J.* **116** (1998) 1009–1038, arXiv:astro-ph/9805201 [astro-ph].

[10] **Planck** Collaboration, N. Aghanim *et al.*, "Planck 2018 results. VI. Cosmological parameters," arXiv:1807.06209 [astro-ph.CO].

[11] A. H. Guth, "The Inflationary Universe: A Possible Solution to the Horizon and Flatness Problems," *Adv. Ser. Astrophys. Cosmol.* **3** (1987) 139–148.

[12] S. Dodelson, *Modern cosmology*. Elsevier, 2003.

[13] **Planck** Collaboration, P. A. R. Ade *et al.*, "Planck 2015 results. XIII. Cosmological parameters," *Astron. Astrophys.* **594** (2016) A13, arXiv:1502.01589 [astro-ph.CO].

[14] **Planck** Collaboration, R. Adam *et al.*, "Planck 2015 results. I. Overview of products and scientific results," *Astron. Astrophys.* **594** (2016) A1, arXiv:1502.01582 [astro-ph.CO].

[15] **Planck** Collaboration, P. A. R. Ade *et al.*, "Planck 2015 results. XIV. Dark energy and modified gravity," *Astron. Astrophys.* **594** (2016) A14, arXiv:1502.01590 [astro-ph.CO].

[16] **Supernova Cosmology Project** Collaboration, S. Perlmutter *et al.*, "Measurements of Ω and Λ from 42 high redshift supernovae," *Astrophys. J.* **517** (1999) 565–586, arXiv:astro-ph/9812133 [astro-ph].

[17] **BOSS** Collaboration, K. S. Dawson *et al.*, "The Baryon Oscillation Spectroscopic Survey of SDSS-III," *Astron. J.* **145** (2013) 10, arXiv:1208.0022 [astro-ph.CO].

[18] **BOSS** Collaboration, L. Anderson *et al.*, "The clustering of galaxies in the SDSS-III Baryon Oscillation Spectroscopic Survey: baryon acoustic oscillations in

the Data Releases 10 and 11 Galaxy samples," *Mon. Not. Roy. Astron. Soc.* **441** no. 1, (2014) 24–62, arXiv:1312.4877 [astro-ph.CO].

[19] **BOSS** Collaboration, S. Alam *et al.*, "The clustering of galaxies in the completed SDSS-III Baryon Oscillation Spectroscopic Survey: cosmological analysis of the DR12 galaxy sample," *Mon. Not. Roy. Astron. Soc.* **470** no. 3, (2017) 2617–2652, arXiv:1607.03155 [astro-ph.CO].

[20] B. Moore, S. Ghigna, F. Governato, G. Lake, T. R. Quinn, J. Stadel, and P. Tozzi, "Dark matter substructure within galactic halos," *Astrophys. J.* **524** (1999) L19–L22, arXiv:astro-ph/9907411 [astro-ph].

[21] A. A. Klypin, A. V. Kravtsov, O. Valenzuela, and F. Prada, "Where are the missing Galactic satellites?," *Astrophys. J.* **522** (1999) 82–92, arXiv:astro-ph/9901240 [astro-ph].

[22] **Planck** Collaboration, P. A. R. Ade *et al.*, "Planck 2015 results. XXIV. Cosmology from Sunyaev-Zeldovich cluster counts," *Astron. Astrophys.* **594** (2016) A24, arXiv:1502.01597 [astro-ph.CO].

[23] W. J. G. de Blok, "The Core-Cusp Problem," *Adv. Astron.* **2010** (2010) 789293, arXiv:0910.3538 [astro-ph.CO].

[24] S. Weinberg, "The Cosmological Constant Problem," *Rev. Mod. Phys.* **61** (1989) 1–23.

[25] P. J. E. Peebles and B. Ratra, "The Cosmological Constant and Dark Energy," *Rev. Mod. Phys.* **75** (2003) 559–606, arXiv:astro-ph/0207347 [astro-ph].

[26] A. G. Riess *et al.*, "A 2.4% Determination of the Local Value of the Hubble Constant," *Astrophys. J.* **826** no. 1, (2016) 56, arXiv:1604.01424 [astro-ph.CO].

[27] H. Hildebrandt *et al.*, "KiDS-450: Cosmological parameter constraints from tomographic weak gravitational lensing," *Mon. Not. Roy. Astron. Soc.* **465** (2017) 1454, arXiv:1606.05338 [astro-ph.CO].

[28] C. Heymans *et al.*, "CFHTLenS: The Canada-France-Hawaii Telescope Lensing Survey," *Mon. Not. Roy. Astron. Soc.* **427** (2012) 146, arXiv:1210.0032 [astro-ph.CO].

[29] C. M. S. Barbosa, H. Velten, J. C. Fabris, and R. O. Ramos, "Assessing the impact of bulk and shear viscosities on large scale structure formation," *Phys. Rev.* **D96** no. 2, (2017) 023527, arXiv:1702.07040 [astro-ph.CO].

[30] H. Velten and D. J. Schwarz, "Constraints on dissipative unified dark matter," *JCAP* **1109** (2011) 016, arXiv:1107.1143 [astro-ph.CO].

[31] B. Wang, E. Abdalla, F. Atrio-Barandela, and D. Pavon, "Dark Matter and Dark Energy Interactions: Theoretical Challenges, Cosmological Implications and Observational Signatures," *Rept. Prog. Phys.* **79** no. 9, (2016) 096901, arXiv:1603.08299 [astro-ph.CO].

[32] N. Tamanini, "Phenomenological models of dark energy interacting with dark matter," *Phys. Rev.* **D92** no. 4, (2015) 043524, arXiv:1504.07397 [gr-qc].

[33] **LIGO Scientific, Virgo** Collaboration, B. P. Abbott *et al.*, "GW170817: Observation of Gravitational Waves from a Binary Neutron Star Inspiral," *Phys. Rev. Lett.* **119** no. 16, (2017) 161101, arXiv:1710.05832 [gr-qc].

[34] J. Sakstein and B. Jain, "Implications of the Neutron Star Merger GW170817 for Cosmological Scalar-Tensor Theories," *Phys. Rev. Lett.* **119** no. 25, (2017) 251303, arXiv:1710.05893 [astro-ph.CO].

[35] J. M. Ezquiaga and M. Zumalacárregui, "Dark Energy After GW170817: Dead Ends and the Road Ahead," *Phys. Rev. Lett.* **119** no. 25, (2017) 251304, arXiv:1710.05901 [astro-ph.CO].

[36] P. Creminelli and F. Vernizzi, "Dark Energy after GW170817 and GRB170817A," *Phys. Rev. Lett.* **119** no. 25, (2017) 251302, arXiv:1710.05877 [astro-ph.CO].

[37] M. Kunz and D. Sapone, "Dark Energy versus Modified Gravity," *Phys. Rev. Lett.* **98** (2007) 121301, arXiv:astro-ph/0612452.

[38] A. Joyce, L. Lombriser, and F. Schmidt, "Dark Energy Versus Modified Gravity," *Ann. Rev. Nucl. Part. Sci.* **66** (2016) 95–122, arXiv:1601.06133 [astro-ph.CO].

[39] S. Weinberg, *Gravitation and Cosmology*. Wiley, 1972.

[40] P. J. E. Peebles and A. Vilenkin, "Quintessential inflation," *Phys. Rev.* **D59** (1999) 063505, arXiv:astro-ph/9810509 [astro-ph].

[41] G. Mangano, G. Miele, and V. Pettorino, "Coupled quintessence and the coincidence problem," *Mod. Phys. Lett.* **A18** (2003) 831–842, arXiv:astro-ph/0212518 [astro-ph].

[42] C. Armendariz-Picon, V. F. Mukhanov, and P. J. Steinhardt, "Essentials of k essence," *Phys. Rev.* **D63** (2001) 103510, arXiv:astro-ph/0006373 [astro-ph].

[43] R. J. Scherrer, "Purely kinetic k-essence as unified dark matter," *Phys. Rev. Lett.* **93** (2004) 011301, arXiv:astro-ph/0402316 [astro-ph].

[44] J. Garriga and V. F. Mukhanov, "Perturbations in k-inflation," *Phys. Lett.* **B458** (1999) 219–225, arXiv:hep-th/9904176 [hep-th].

[45] M. Chevallier and D. Polarski, "Accelerating universes with scaling dark matter," *Int. J. Mod. Phys.* **D10** (2001) 213–224, arXiv:gr-qc/0009008 [gr-qc].

[46] E. V. Linder, "Exploring the expansion history of the universe," *Phys. Rev. Lett.* **90** (2003) 091301, arXiv:astro-ph/0208512 [astro-ph].

[47] W. Hu and I. Sawicki, "Models of f(R) Cosmic Acceleration that Evade Solar-System Tests," *Phys. Rev.* **D76** (2007) 064004, arXiv:0705.1158 [astro-ph].

[48] B. Jain, V. Vikram, and J. Sakstein, "Astrophysical Tests of Modified Gravity: Constraints from Distance Indicators in the Nearby Universe," *Astrophys. J.* **779** (2013) 39, arXiv:1204.6044 [astro-ph.CO].

[49] S. Nojiri and S. D. Odintsov, "Modified f(R) gravity consistent with realistic cosmology: From matter dominated epoch to dark energy universe," *Phys. Rev.* **D74** (2006) 086005, arXiv:hep-th/0608008 [hep-th].

[50] T. P. Sotiriou and V. Faraoni, "f(R) Theories Of Gravity," *Rev. Mod. Phys.* **82** (2010) 451–497, arXiv:0805.1726 [gr-qc].

[51] A. De Felice and S. Tsujikawa, "f(R) theories," *Living Rev. Rel.* **13** (2010) 3, arXiv:1002.4928 [gr-qc].

[52] T. Clifton, P. G. Ferreira, A. Padilla, and C. Skordis, "Modified Gravity and Cosmology," *Phys. Rept.* **513** (2012) 1–189, arXiv:1106.2476 [astro-ph.CO].

[53] G. J. Olmo, "Palatini Approach to Modified Gravity: f(R) Theories and Beyond," *Int. J. Mod. Phys.* **D20** (2011) 413–462, arXiv:1101.3864 [gr-qc].

[54] T. Koivisto and H. Kurki-Suonio, "Cosmological perturbations in the palatini formulation of modified gravity," *Class. Quant. Grav.* **23** (2006) 2355–2369, arXiv:astro-ph/0509422 [astro-ph].

[55] A. A. Starobinsky, "A New Type of Isotropic Cosmological Models Without Singularity," *Phys. Lett.* **91B** (1980) 99–102.

[56] B. Boisseau, G. Esposito-Farese, D. Polarski, and A. A. Starobinsky, "Reconstruction of a scalar tensor theory of gravity in an accelerating universe," *Phys. Rev. Lett.* **85** (2000) 2236, arXiv:gr-qc/0001066 [gr-qc].

[57] S. Nojiri and S. D. Odintsov, "Unified cosmic history in modified gravity: from F(R) theory to Lorentz non-invariant models," *Phys. Rept.* **505** (2011) 59–144, arXiv:1011.0544 [gr-qc].

[58] C. Brans and R. H. Dicke, "Mach's principle and a relativistic theory of gravitation," *Phys. Rev.* **124** (1961) 925–935.

[59] R. P. Woodard, "Avoiding dark energy with 1/r modifications of gravity," *Lect. Notes Phys.* **720** (2007) 403–433, arXiv:astro-ph/0601672 [astro-ph].

[60] G. W. Horndeski, "Second-order scalar-tensor field equations in a four-dimensional space," *Int. J. Theor. Phys.* **10** (1974) 363–384.

[61] T. Kobayashi, M. Yamaguchi, and J. Yokoyama, "Generalized G-inflation: Inflation with the most general second-order field equations," *Prog. Theor. Phys.* **126** (2011) 511–529, arXiv:1105.5723 [hep-th].

[62] J. Gleyzes, D. Langlois, and F. Vernizzi, "A unifying description of dark energy," *Int. J. Mod. Phys.* **D23** no. 13, (2015) 1443010, arXiv:1411.3712 [hep-th].

[63] M. Lagos, E. Bellini, J. Noller, P. G. Ferreira, and T. Baker, "A general theory of linear cosmological perturbations: stability conditions, the quasistatic limit and dynamics," *JCAP* **1803** no. 03, (2018) 021, arXiv:1711.09893 [gr-qc].

[64] I. Sawicki and E. Bellini, "Limits of quasistatic approximation in modified-gravity cosmologies," *Phys. Rev.* **D92** no. 8, (2015) 084061, arXiv:1503.06831 [astro-ph.CO].

[65] A. Silvestri, L. Pogosian, and R. V. Buniy, "Practical approach to cosmological perturbations in modified gravity," *Phys. Rev.* **D87** no. 10, (2013) 104015, arXiv:1302.1193 [astro-ph.CO].

[66] **J-PAS** Collaboration, N. Benitez *et al.*, "J-PAS: The Javalambre-Physics of the Accelerated Universe Astrophysical Survey," arXiv:1403.5237 [astro-ph.CO].

[67] **DESI** Collaboration, A. Aghamousa *et al.*, "The DESI Experiment Part I: Science,Targeting, and Survey Design," arXiv:1611.00036 [astro-ph.IM].

[68] **EUCLID** Collaboration, R. Laureijs *et al.*, "Euclid Definition Study Report," arXiv:1110.3193 [astro-ph.CO].

[69] E. da Cunha *et al.*, "The Taipan Galaxy Survey: Scientific Goals and Observing Strategy," *Publ. Astron. Soc. Austral.* **34** (2017) 47, arXiv:1706.01246 [astro-ph.GA].

[70] **LSST Dark Energy Science** Collaboration, D. Alonso *et al.*, "The LSST Dark Energy Science Collaboration (DESC) Science Requirements Document," arXiv:1809.01669 [astro-ph.CO].

[71] C. Howlett, L. Staveley-Smith, and C. Blake, "Cosmological Forecasts for Combined and Next Generation Peculiar Velocity Surveys," *Mon. Not. Roy. Astron. Soc.* **464** no. 3, (2017) 2517–2544, arXiv:1609.08247 [astro-ph.CO].

[72] A. Lewis and S. Bridle, "Cosmological parameters from CMB and other data: A Monte Carlo approach," *Phys. Rev.* **D66** (2002) 103511, arXiv:astro-ph/0205436 [astro-ph].

[73] **WMAP** Collaboration, D. N. Spergel *et al.*, "Wilkinson Microwave Anisotropy Probe (WMAP) three year results: implications for cosmology," *Astrophys. J. Suppl.* **170** (2007) 377, arXiv:astro-ph/0603449 [astro-ph].

[74] **SDSS** Collaboration, D. G. York *et al.*, "The Sloan Digital Sky Survey: Technical Summary," *Astron. J.* **120** (2000) 1579–1587, arXiv:astro-ph/0006396 [astro-ph].

[75] **SDSS** Collaboration, D. J. Eisenstein *et al.*, "Spectroscopic target selection for the Sloan Digital Sky Survey: The Luminous red galaxy sample," *Astron. J.* **122** (2001) 2267, arXiv:astro-ph/0108153 [astro-ph].

[76] **SDSS** Collaboration, M. A. Strauss *et al.*, "Spectroscopic Target Selection in the Sloan Digital Sky Survey: The Main Galaxy Sample," *Astron. J.* **124** (2002) 1810, arXiv:astro-ph/0206225 [astro-ph].

[77] M. Bolzonella, J.-M. Miralles, and R. Pello', "Photometric redshifts based on standard SED fitting procedures," *Astron. Astrophys.* **363** (2000) 476–492, arXiv:astro-ph/0003380 [astro-ph].

[78] F. B. Abdalla, A. Amara, P. Capak, E. S. Cypriano, O. Lahav, and J. Rhodes, "Photo-z for weak lensing tomography from space: the role of optical and near-IR photometry," *Mon. Not. Roy. Astron. Soc.* **387** (2008) 969–986, arXiv:0705.1437 [astro-ph].

[79] S. Arnouts, S. Cristiani, L. Moscardini, S. Matarrese, F. Lucchin, A. Fontana, and E. Giallongo, "Measuring and modeling the redshift evolution of clustering: The

Hubble Deep Field North," *Mon. Not. Roy. Astron. Soc.* **310** (1999) 540–556, arXiv:astro-ph/9902290 [astro-ph].

[80] N. Benitez, "Bayesian photometric redshift estimation," *Astrophys. J.* **536** (2000) 571–583, arXiv:astro-ph/9811189 [astro-ph].

[81] S. Jouvel *et al.*, "Designing Future Dark Energy Space Mission: I. Building Realistic Galaxy Spectro-Photometric Catalogs and their first applications," *Astron. Astrophys.* **504** (2009) 359, arXiv:0902.0625 [astro-ph.CO].

[82] P. G. Perez-Gonzalez *et al.*, "SHARDS: an optical spectro-photometric survey of distant galaxies," *Astrophys. J.* **762** (2013) 46, arXiv:1207.6639 [astro-ph.CO].

[83] A. J. S. Hamilton, "Linear redshift distortions: A Review," in *Ringberg Workshop on Large Scale Structure Ringberg, Germany, September 23-28, 1996*. 1997. arXiv:astro-ph/9708102 [astro-ph].

[84] L. Samushia, W. J. Percival, and A. Raccanelli, "Interpreting large-scale redshift-space distortion measurements," *Mon. Not. Roy. Astron. Soc.* **420** (2012) 2102–2119, arXiv:1102.1014 [astro-ph.CO].

[85] C. Alcock and B. Paczynski, "An evolution free test for non-zero cosmological constant," *Nature* **281** (1979) 358–359.

[86] M. Davis, M. J. Geller, and J. Huchra, "The local mean mass density of the universe: new methods for studying galaxy clustering.," *The Astrophysical Journal* **221** (Apr., 1978) 1–18.

[87] N. Kaiser, "On the spatial correlations of Abell clusters.," *The Astrophysical Journal* **284** (Sept., 1984) L9–L12.

[88] J. A. Peacock and S. J. Dodds, "Reconstructing the linear power spectrum of cosmological mass fluctuations," *Mon. Not. Roy. Astron. Soc.* **267** (1994) 1020–1034, arXiv:astro-ph/9311057 [astro-ph].

[89] **DES** Collaboration, A. I. Salvador *et al.*, "Measuring Linear and Non-linear Galaxy Bias Using Counts-in-Cells in the Dark Energy Survey Science Verification Data," *Mon. Not. Roy. Astron. Soc.* **482** no. 2, (2019) 1435–1451, arXiv:1807.10331 [astro-ph.CO].

[90] P. Zhang, J. Pan, and Y. Zheng, "Peculiar velocity decomposition, redshift space distortion, and velocity reconstruction in redshift surveys: The methodology," *Phys. Rev.* **D87** no. 6, (2013) 063526, arXiv:1207.2722 [astro-ph.CO].

[91] R. B. Tully and J. R. Fisher, "A New method of determining distances to galaxies," *Astron. Astrophys.* **54** (1977) 661–673.

[92] S. Djorgovski and M. Davis, "Fundamental properties of elliptical galaxies," *Astrophys. J.* **313** (1987) 59.

[93] A. Dressler, D. Lynden-Bell, D. Burstein, R. L. Davies, S. M. Faber, R. Terlevich, and G. Wegner, "Spectroscopy and Photometry of Elliptical Galaxies. I. New Distance Estimator," *The Astrophysical Journal* **313** (Feb., 1987) 42.

[94] M. M. Phillips, "The absolute magnitudes of Type IA supernovae," *Astrophys. J.* **413** (1993) L105–L108.

[95] N. Kaiser and G. Squires, "Mapping the dark matter with weak gravitational lensing," *Astrophys. J.* **404** (1993) 441–450.

[96] A. Refregier, "Weak gravitational lensing by large scale structure," *Ann. Rev. Astron. Astrophys.* **41** (2003) 645–668, arXiv:astro-ph/0307212 [astro-ph].

[97] H. Hoekstra and B. Jain, "Weak Gravitational Lensing and its Cosmological Applications," *Ann. Rev. Nucl. Part. Sci.* **58** (2008) 99–123, arXiv:0805.0139 [astro-ph].

[98] J. N. Fry and E. Gaztanaga, "Biasing and hierarchical statistics in large scale structure," *Astrophys. J.* **413** (1993) 447–452, arXiv:astro-ph/9302009.

[99] L. Verde *et al.*, "The 2dF Galaxy Redshift Survey: The Bias of galaxies and the density of the Universe," *Mon. Not. Roy. Astron. Soc.* **335** (2002) 432, arXiv:astro-ph/0112161.

[100] S. Hatton and S. Cole, "Modeling the redshift-space distortion of galaxy clustering," *Mon. Not. Roy. Astron. Soc.* **296** (1998) 10–20, arXiv:astro-ph/9707186.

[101] C. M. Hirata and U. Seljak, "Intrinsic alignment-lensing interference as a contaminant of cosmic shear," *Phys. Rev. D* **70** (2004) 063526, arXiv:astro-ph/0406275.

[102] S. Bridle and L. King, "Dark energy constraints from cosmic shear power spectra: impact of intrinsic alignments on photometric redshift requirements," *New J. Phys.* **9** (2007) 444, arXiv:0705.0166 [astro-ph].

[103] B. Joachimi, R. Mandelbaum, F. B. Abdalla, and S. L. Bridle, "Constraints on intrinsic alignment contamination of weak lensing surveys using the megaz-lrg sample," *Astron. Astrophys.* **527** (Jan, 2011) A26. http://dx.doi.org/10.1051/0004-6361/201015621.

[104] V. Desjacques, D. Jeong, and F. Schmidt, "Large-Scale Galaxy Bias," *Phys. Rept.* **733** (2018) 1–193, arXiv:1611.09787 [astro-ph.CO].

[105] N. Kaiser, "Clustering in real space and in redshift space," *Mon. Not. Roy. Astron. Soc.* **227** (1987) 1–27.

[106] J. Diemand, B. Moore, and J. Stadel, "Velocity and spatial biases in CDM subhalo distributions," *Mon. Not. Roy. Astron. Soc.* **352** (2004) 535, arXiv:astro-ph/0402160 [astro-ph].

[107] A. Elia, A. D. Ludlow, and C. Porciani, "The spatial and velocity bias of linear density peaks and proto-haloes in the Lambda cold dark matter cosmology," *Mon. Not. Roy. Astron. Soc.* **421** (2012) 3472, arXiv:1111.4211 [astro-ph.CO].

[108] S. de la Torre and L. Guzzo, "Modelling non-linear redshift-space distortions in the galaxy clustering pattern: systematic errors on the growth rate parameter," *Mon. Not. Roy. Astron. Soc.* **427** (2012) 327, arXiv:1202.5559 [astro-ph.CO].

[109] P. Zhang, Y. Zheng, and Y. Jing, "Sampling artifact in volume weighted velocity measurement. I. Theoretical modeling," *Phys. Rev.* **D91** no. 4, (2015) 043522, arXiv:1405.7125 [astro-ph.CO].

[110] J. N. Fry, "The Evolution of Bias," *Astrophys. J.* **461** (1996) L65.

[111] M. Tegmark and P. J. E. Peebles, "The Time evolution of bias," *Astrophys. J.* **500** (1998) L79, arXiv:astro-ph/9804067 [astro-ph].

[112] Y. Mellier, "Probing the universe with weak lensing," *Ann. Rev. Astron. Astrophys.* **37** (1999) 127–189, arXiv:astro-ph/9812172 [astro-ph].

[113] M. Bartelmann and P. Schneider, "Weak gravitational lensing," *Phys. Rept.* **340** (2001) 291–472, arXiv:astro-ph/9912508 [astro-ph].

[114] D. Munshi, P. Valageas, L. Van Waerbeke, and A. Heavens, "Cosmology with Weak Lensing Surveys," *Phys. Rept.* **462** (2008) 67–121, arXiv:astro-ph/0612667 [astro-ph].

[115] M. Kilbinger, "Cosmology with cosmic shear observations: a review," *Rept. Prog. Phys.* **78** (2015) 086901, arXiv:1411.0115 [astro-ph.CO].

[116] P. Lemos, A. Challinor, and G. Efstathiou, "The effect of Limber and flat-sky approximations on galaxy weak lensing," *JCAP* **1705** no. 05, (2017) 014, arXiv:1704.01054 [astro-ph.CO].

[117] M. LoVerde and N. Afshordi, "Extended Limber Approximation," *Phys. Rev. D* **78** (2008) 123506, arXiv:0809.5112 [astro-ph].

[118] T. D. Kitching, J. Alsing, A. F. Heavens, R. Jimenez, J. D. McEwen, and L. Verde, "The Limits of Cosmic Shear," *Mon. Not. Roy. Astron. Soc.* **469** no. 3, (2017) 2737–2749, arXiv:1611.04954 [astro-ph.CO].

[119] Z.-M. Ma, W. Hu, and D. Huterer, "Effect of photometric redshift uncertainties on weak lensing tomography," *Astrophys. J.* **636** (2005) 21–29, arXiv:astro-ph/0506614.

[120] J. Guzik, B. Jain, and M. Takada, "Tests of Gravity from Imaging and Spectroscopic Surveys," *Phys. Rev.* **D81** (2010) 023503, arXiv:0906.2221 [astro-ph.CO].

[121] R. A. Fisher, "The logic of inductive inference," *Journal of the Royal Statistical Society* **98** no. 1, (1935) 39–82. http://www.jstor.org/stable/2342435.

[122] M. Tegmark, A. Taylor, and A. Heavens, "Karhunen-Loeve eigenvalue problems in cosmology: How should we tackle large data sets?," *Astrophys. J.* **480** (1997) 22, arXiv:astro-ph/9603021 [astro-ph].

[123] H.-J. Seo and D. J. Eisenstein, "Improved forecasts for the baryon acoustic oscillations and cosmological distance scale," *Astrophys. J.* **665** (2007) 14–24, arXiv:astro-ph/0701079 [astro-ph].

[124] A. F. Heavens, T. D. Kitching, and L. Verde, "On model selection forecasting, Dark Energy and modified gravity," *Mon. Not. Roy. Astron. Soc.* **380** (2007) 1029–1035, arXiv:astro-ph/0703191 [astro-ph].

[125] M. White, Y.-S. Song, and W. J. Percival, "Forecasting Cosmological Constraints from Redshift Surveys," *Mon. Not. Roy. Astron. Soc.* **397** (2008) 1348–1354, arXiv:0810.1518 [astro-ph].

[126] L. Wolz, M. Kilbinger, J. Weller, and T. Giannantonio, "On the Validity of Cosmological Fisher Matrix Forecasts," *JCAP* **1209** (2012) 009, arXiv:1205.3984 [astro-ph.CO].

[127] K. Yamamoto, M. Nakamichi, A. Kamino, B. A. Bassett, and H. Nishioka, "A Measurement of the quadrupole power spectrum in the clustering of the 2dF QSO Survey," *Publ. Astron. Soc. Jap.* **58** (2006) 93–102, arXiv:astro-ph/0505115 [astro-ph].

[128] U. Seljak, N. Hamaus, and V. Desjacques, "How to suppress the shot noise in galaxy surveys," *Phys. Rev. Lett.* **103** (2009) 091303, arXiv:0904.2963 [astro-ph.CO].

[129] H.-J. Seo and D. J. Eisenstein, "Probing dark energy with baryonic acoustic oscillations from future large galaxy redshift surveys," *Astrophys. J.* **598** (2003) 720–740, arXiv:astro-ph/0307460 [astro-ph].

[130] L. R. Abramo, "The full Fisher matrix for galaxy surveys," *Mon. Not. Roy. Astron. Soc.* **420** (2012) 3, arXiv:1108.5449 [astro-ph.CO].

[131] L. R. Abramo, L. F. Secco, and A. Loureiro, "Fourier analysis of multitracer cosmological surveys," *Mon. Not. Roy. Astron. Soc.* **455** no. 4, (2016) 3871–3889, arXiv:1505.04106 [astro-ph.CO].

[132] M. Tegmark, "Measuring cosmological parameters with galaxy surveys," *Phys. Rev. Lett.* **79** (1997) 3806–3809, arXiv:astro-ph/9706198 [astro-ph].

[133] A. Taruya, S. Saito, and T. Nishimichi, "Forecasting the Cosmological Constraints with Anisotropic Baryon Acoustic Oscillations from Multipole Expansion," *Phys. Rev.* **D83** (2011) 103527, arXiv:1101.4723 [astro-ph.CO].

[134] J. Koda, C. Blake, T. Davis, C. Magoulas, C. M. Springob, M. Scrimgeour, A. Johnson, G. B. Poole, and L. Staveley-Smith, "Are peculiar velocity surveys competitive as a cosmological probe?," *Mon. Not. Roy. Astron. Soc.* **445** no. 4, (2014) 4267–4286, arXiv:1312.1022 [astro-ph.CO].

[135] M. Takada and S. Bridle, "Probing dark energy with cluster counts and cosmic shear power spectra: including the full covariance," *New J. Phys.* **9** (2007) 446, arXiv:0705.0163 [astro-ph].

[136] I. Kayo and M. Takada, "Cosmological parameters from weak lensing power spectrum and bispectrum tomography: including the non-Gaussian errors," arXiv:1306.4684 [astro-ph.CO].

[137] S. Hilbert, D. Xu, P. Schneider, V. Springel, M. Vogelsberger, and L. Hernquist, "Intrinsic Alignments of Galaxies in the Illustris Simulation," *Mon. Not. Roy. Astron. Soc.* **468** no. 1, (2017) 790–823, arXiv:1606.03216 [astro-ph.CO].

[138] D. J. Eisenstein, W. Hu, and M. Tegmark, "Cosmic complementarity: Joint parameter estimation from CMB experiments and redshift surveys," *Astrophys. J.* **518** (1999) 2–23, arXiv:astro-ph/9807130 [astro-ph].

[139] M. A. Resco and A. L. Maroto, "Modified gravity or imperfect dark matter: a model-independent discrimination," arXiv:2010.01368 [astro-ph.CO].

[140] M. A. Resco and A. L. Maroto, "Parametrizing modified gravities with vector degrees of freedom: anisotropic growth and lensing," *JCAP* **10** (2018) 014, arXiv:1807.04649 [gr-qc].

[141] M. A. Resco and A. L. Maroto, "Parametrizing growth in dark energy and modified gravity models," *Phys. Rev. D* **97** no. 4, (2018) 043518, arXiv:1707.08964 [astro-ph.CO].

[142] L. H. Ford, "INFLATION DRIVEN BY A VECTOR FIELD," *Phys. Rev.* **D40** (1989) 967.

[143] A. Golovnev, V. Mukhanov, and V. Vanchurin, "Vector Inflation," *JCAP* **0806** (2008) 009, arXiv:0802.2068 [astro-ph].

[144] T. Koivisto and D. F. Mota, "Vector Field Models of Inflation and Dark Energy," *JCAP* **0808** (2008) 021, arXiv:0805.4229 [astro-ph].

[145] M.-a. Watanabe, S. Kanno, and J. Soda, "Inflationary Universe with Anisotropic Hair," *Phys. Rev. Lett.* **102** (2009) 191302, arXiv:0902.2833 [hep-th].

[146] S. Kanno, J. Soda, and M.-a. Watanabe, "Anisotropic Power-law Inflation," *JCAP* **1012** (2010) 024, arXiv:1010.5307 [hep-th].

[147] C. M. Will, *Theory and Experiment in Gravitational Physics*. Cambridge University Press, 1993. https://doi.org/10.1017/CBO9780511564246.

[148] L. Shao and N. Wex, "Tests of gravitational symmetries with radio pulsars," *Sci. China Phys. Mech. Astron.* **59** no. 9, (2016) 699501, arXiv:1604.03662 [gr-qc].

[149] **Planck** Collaboration, P. A. R. Ade *et al.*, "Planck 2015 results. XVI. Isotropy and statistics of the CMB," *Astron. Astrophys.* **594** (2016) A16, arXiv:1506.07135 [astro-ph.CO].

[150] D. J. Schwarz, C. J. Copi, D. Huterer, and G. D. Starkman, "CMB Anomalies after Planck," *Class. Quant. Grav.* **33** no. 18, (2016) 184001, arXiv:1510.07929 [astro-ph.CO].

[151] **Planck** Collaboration, P. A. R. Ade *et al.*, "Planck intermediate results. XIII. Constraints on peculiar velocities," *Astron. Astrophys.* **561** (2014) A97, arXiv:1303.5090 [astro-ph.CO].

[152] F. Atrio-Barandela, A. Kashlinsky, H. Ebeling, D. J. Fixsen, and D. Kocevski, "Probing the Dark Flow Signal in Wmap 9 -year and Planck Cosmic Microwave Background Maps," *Astrophys. J.* **810** no. 2, (2015) 143, arXiv:1411.4180 [astro-ph.CO].

[153] M. I. Scrimgeour *et al.*, "The 6dF Galaxy Survey: Bulk Flows on $50 - 70h^{-1}$ Mpc scales," *Mon. Not. Roy. Astron. Soc.* **455** no. 1, (2016) 386–401, arXiv:1511.06930 [astro-ph.CO].

[154] D. Colladay and V. A. Kostelecky, "Lorentz violating extension of the standard model," *Phys. Rev.* **D58** (1998) 116002, arXiv:hep-ph/9809521 [hep-ph].

[155] Y. Nambu, "Quantum electrodynamics in nonlinear gauge," *Prog. Theor. Phys. Suppl.* **E68** (1968) 190–195.

[156] Q. G. Bailey and V. A. Kostelecky, "Signals for Lorentz violation in post-Newtonian gravity," *Phys. Rev.* **D74** (2006) 045001, arXiv:gr-qc/0603030 [gr-qc].

[157] D. Blas and E. Lim, "Phenomenology of theories of gravity without Lorentz invariance: the preferred frame case," *Int. J. Mod. Phys.* **D23** (2015) 1443009, arXiv:1412.4828 [gr-qc].

[158] P. Horava, "Quantum Gravity at a Lifshitz Point," *Phys. Rev.* **D79** (2009) 084008, arXiv:0901.3775 [hep-th].

[159] T. Jacobson and D. Mattingly, "Gravity with a dynamical preferred frame," *Phys. Rev.* **D64** (2001) 024028, arXiv:gr-qc/0007031 [gr-qc].

[160] C. Armendariz-Picon, "Could dark energy be vector-like?," *JCAP* **0407** (2004) 007, arXiv:astro-ph/0405267 [astro-ph].

[161] C. G. Boehmer and T. Harko, "Dark energy as a massive vector field," *Eur. Phys. J.* **C50** (2007) 423–429, arXiv:gr-qc/0701029 [gr-qc].

[162] J. Beltran Jimenez and A. L. Maroto, "A cosmic vector for dark energy," *Phys. Rev.* **D78** (2008) 063005, arXiv:0801.1486 [astro-ph].

[163] J. Beltran Jimenez and A. L. Maroto, "Cosmological electromagnetic fields and dark energy," *JCAP* **0903** (2009) 016, arXiv:0811.0566 [astro-ph].

[164] J. Beltran Jimenez and A. L. Maroto, "The electromagnetic dark sector," *Phys. Lett.* **B686** (2010) 175–180, arXiv:0903.4672 [astro-ph.CO].

[165] J. Beltran Jimenez and L. Heisenberg, "Derivative self-interactions for a massive vector field," *Phys. Lett.* **B757** (2016) 405–411, arXiv:1602.03410 [hep-th].

[166] J. Beltran Jimenez and L. Heisenberg, "Generalized multi-Proca fields," *Phys. Lett.* **B770** (2017) 16–26, arXiv:1610.08960 [hep-th].

[167] J. K. Nordtvedt, "Anisotropic parametrized post-Newtonian gravitational metric field," *Phys. Rev.* **D14** (1976) 1511–1517.

[168] H. Muller, S.-w. Chiow, S. Herrmann, S. Chu, and K.-Y. Chung, "Atom Interferometry tests of the isotropy of post-Newtonian gravity," *Phys. Rev. Lett.* **100** (2008) 031101, arXiv:0710.3768 [gr-qc].

[169] L. Ackerman, S. M. Carroll, and M. B. Wise, "Imprints of a Primordial Preferred Direction on the Microwave Background," *Phys. Rev.* **D75** (2007) 083502, arXiv:astro-ph/0701357 [astro-ph].

[170] A. R. Pullen and C. M. Hirata, "Non-detection of a statistically anisotropic power spectrum in large-scale structure," *JCAP* **1005** (2010) 027, arXiv:1003.0673 [astro-ph.CO].

[171] D. Jeong and M. Kamionkowski, "Clustering Fossils from the Early Universe," *Phys. Rev. Lett.* **108** (2012) 251301, arXiv:1203.0302 [astro-ph.CO].

[172] M. Shiraishi, N. S. Sugiyama, and T. Okumura, "Polypolar spherical harmonic decomposition of galaxy correlators in redshift space: Toward testing cosmic rotational symmetry," *Phys. Rev.* **D95** no. 6, (2017) 063508, arXiv:1612.02645 [astro-ph.CO].

[173] V. Tansella, C. Bonvin, G. Cusin, R. Durrer, M. Kunz, and I. Sawicki, "Redshift-space distortions from vector perturbations II: Anisotropic signal," *Phys. Rev.* **D98** no. 10, (2018) 103515, arXiv:1807.00731 [astro-ph.CO].

[174] N. Bartolo, S. Matarrese, M. Peloso, and A. Ricciardone, "Anisotropic power spectrum and bispectrum in the $f(\phi)F^2$ mechanism," *Phys. Rev.* **D87** no. 2, (2013) 023504, arXiv:1210.3257 [astro-ph.CO].

[175] N. Bartolo, S. Matarrese, M. Peloso, and M. Shiraishi, "Parity-violating CMB correlators with non-decaying statistical anisotropy," *JCAP* **1507** no. 07, (2015) 039, arXiv:1505.02193 [astro-ph.CO].

[176] M.-a. Watanabe, S. Kanno, and J. Soda, "The Nature of Primordial Fluctuations from Anisotropic Inflation," *Prog. Theor. Phys.* **123** (2010) 1041–1068, arXiv:1003.0056 [astro-ph.CO].

[177] N. Bartolo, A. Kehagias, M. Liguori, A. Riotto, M. Shiraishi, and V. Tansella, "Detecting higher spin fields through statistical anisotropy in the CMB and galaxy power spectra," *Phys. Rev.* **D97** no. 2, (2018) 023503, arXiv:1709.05695 [astro-ph.CO].

[178] A. L. Maroto, "Moving dark energy and the cmb dipole," *JCAP* **0605** (2006) 015, arXiv:astro-ph/0512464 [astro-ph].

[179] J. Beltran Jimenez and A. L. Maroto, "Cosmology with moving dark energy and the CMB quadrupole," *Phys. Rev.* **D76** (2007) 023003, arXiv:astro-ph/0703483 [astro-ph].

[180] J. A. R. Cembranos, A. L. Maroto, and H. Villarrubia-Rojo, "Non-comoving Cosmology," *JCAP* **1906** no. 06, (2019) 041, arXiv:1903.11009 [astro-ph.CO].

[181] P. Arias, D. Cadamuro, M. Goodsell, J. Jaeckel, J. Redondo, and A. Ringwald, "WISPy Cold Dark Matter," *JCAP* **1206** (2012) 013, arXiv:1201.5902 [hep-ph].

[182] K. Dimopoulos, "Can a vector field be responsible for the curvature perturbation in the Universe?," *Phys. Rev.* **D74** (2006) 083502, arXiv:hep-ph/0607229 [hep-ph].

[183] A. E. Nelson and J. Scholtz, "Dark Light, Dark Matter and the Misalignment Mechanism," *Phys. Rev.* **D84** (2011) 103501, arXiv:1105.2812 [hep-ph].

[184] J. A. R. Cembranos, A. L. Maroto, and S. J. Núñez Jareño, "Perturbations of ultralight vector field dark matter," *JHEP* **02** (2017) 064, arXiv:1611.03793 [astro-ph.CO].

[185] A. De Felice, L. Heisenberg, R. Kase, S. Mukohyama, S. Tsujikawa, and Y.-l. Zhang, "Effective gravitational couplings for cosmological perturbations in generalized Proca theories," *Phys. Rev.* **D94** no. 4, (2016) 044024, arXiv:1605.05066 [gr-qc].

[186] T. S. Pereira, C. Pitrou, and J.-P. Uzan, "Theory of cosmological perturbations in an anisotropic universe," *JCAP* **0709** (2007) 006, arXiv:0707.0736 [astro-ph].

[187] S. Tsujikawa, K. Uddin, S. Mizuno, R. Tavakol, and J. Yokoyama, "Constraints on scalar-tensor models of dark energy from observational and local gravity tests," *Phys. Rev.* **D77** (2008) 103009, arXiv:0803.1106 [astro-ph].

[188] A. Atreya, J. R. Bhatt, and A. Mishra, "Viscous Self Interacting Dark Matter and Cosmic Acceleration," *JCAP* **02** (2018) 024, arXiv:1709.02163 [astro-ph.CO].

[189] J.-L. Cui, L. Yin, L.-F. Wang, Y.-H. Li, and X. Zhang, "A closer look at interacting dark energy with statefinder hierarchy and growth rate of structure," *JCAP* **1509** no. 09, (2015) 024, arXiv:1503.08948 [astro-ph.CO].

[190] J.-H. He, B. Wang, and E. Abdalla, "Stability of the curvature perturbation in dark sectors' mutual interacting models," *Phys. Lett.* **B671** (2009) 139–145, arXiv:0807.3471 [gr-qc].

[191] J.-H. He, B. Wang, and Y. P. Jing, "Effects of dark sectors' mutual interaction on the growth of structures," *JCAP* **0907** (2009) 030, arXiv:0902.0660 [gr-qc].

[192] G. M. Kremer and F. P. Devecchi, "Viscous cosmological models and accelerated universes," *Phys. Rev.* **D67** (2003) 047301, arXiv:gr-qc/0212046 [gr-qc].

[193] J. R. Wilson, G. J. Mathews, and G. M. Fuller, "Bulk Viscosity, Decaying Dark Matter, and the Cosmic Acceleration," *Phys. Rev.* **D75** (2007) 043521, arXiv:astro-ph/0609687 [astro-ph].

[194] O. F. Piattella, J. C. Fabris, and W. Zimdahl, "Bulk viscous cosmology with causal transport theory," *JCAP* **1105** (2011) 029, arXiv:1103.1328 [astro-ph.CO].

[195] M. Giovannini, "Non-linear curvature inhomogeneities and backreaction for relativistic viscous fluids," *Class. Quant. Grav.* **32** (2015) 155004, arXiv:1503.08739 [hep-th].

[196] J. Krisch and E. Glass, "Velocity and Heat Flow in a Composite Two Fluid System," *J. Math. Phys.* **52** (2011) 102503, arXiv:1110.0128 [gr-qc].

[197] M. Kopp, C. Skordis, and D. B. Thomas, "Extensive investigation of the generalized dark matter model," *Phys. Rev. D* **94** no. 4, (2016) 043512, arXiv:1605.00649 [astro-ph.CO].

[198] W. Hu, "Structure formation with generalized dark matter," *Astrophys. J.* **506** (1998) 485–494, arXiv:astro-ph/9801234.

[199] M. Kunz, S. Nesseris, and I. Sawicki, "Constraints on dark-matter properties from large-scale structure," *Phys. Rev. D* **94** no. 2, (2016) 023510, arXiv:1604.05701 [astro-ph.CO].

[200] O. M. Pimentel, G. A. González, and F. D. Lora-Clavijo, "The Energy-Momentum Tensor for a Dissipative Fluid in General Relativity," *Gen. Rel. Grav.* **48** no. 10, (2016) 124, arXiv:1604.01318 [gr-qc].

[201] E. V. Linder, "Cosmic growth history and expansion history," *Phys. Rev.* **D72** (2005) 043529, arXiv:astro-ph/0507263 [astro-ph].

[202] E. V. Linder and R. N. Cahn, "Parameterized Beyond-Einstein Growth," *Astropart. Phys.* **28** (2007) 481–488, arXiv:astro-ph/0701317 [astro-ph].

[203] R. Gannouji and D. Polarski, "The growth of matter perturbations in some scalar-tensor DE models," *JCAP* **0805** (2008) 018, arXiv:0802.4196 [astro-ph].

[204] C. Di Porto and L. Amendola, "Observational constraints on the linear fluctuation growth rate," *Phys. Rev.* **D77** (2008) 083508, arXiv:0707.2686 [astro-ph].

[205] E. V. Linder, "Testing Dark Matter Clustering with Redshift Space Distortions," *JCAP* **1304** (2013) 031, arXiv:1302.4754 [astro-ph.CO].

[206] J. N. Fry, "DYNAMICAL MEASURES OF DENSITY IN EXOTIC COSMOLOGIES," *Phys. Lett.* **158B** (1985) 211–214.

[207] J. B. Dent, S. Dutta, and L. Perivolaropoulos, "New Parametrization for the Scale Dependent Growth Function in General Relativity," *Phys. Rev.* **D80** (2009) 023514, arXiv:0903.5296 [astro-ph.CO].

[208] J. C. Bueno Sanchez, J. B. Dent, S. Dutta, and L. Perivolaropoulos, "Parametrization for the Scale Dependent Growth in Modified Gravity," *JCAP* **1009** (2010) 021, arXiv:1004.4905 [astro-ph.CO].

[209] G. R. Dvali, G. Gabadadze, and M. Porrati, "4-D gravity on a brane in 5-D Minkowski space," *Phys. Lett.* **B485** (2000) 208–214, arXiv:hep-th/0005016 [hep-th].

[210] L. Amendola, M. Kunz, and D. Sapone, "Measuring the dark side (with weak lensing)," *JCAP* **0804** (2008) 013, arXiv:0704.2421 [astro-ph].

[211] M. Ishak and J. Dossett, "Contiguous redshift parameterizations of the growth index," *Phys. Rev.* **D80** (2009) 043004, arXiv:0905.2470 [astro-ph.CO].

[212] S. Chen and J. Jing, "Improved parametrization of the growth index for dark energy and DGP models," *Phys. Lett.* **B685** (2010) 185–189, arXiv:0908.4379 [gr-qc].

[213] Y. Gong, "The growth factor parameterization and modified gravity," *Phys. Rev.* **D78** (2008) 123010, arXiv:0808.1316 [astro-ph].

[214] F. Simpson *et al.*, "CFHTLenS: Testing the Laws of Gravity with Tomographic Weak Lensing and Redshift Space Distortions," *Mon. Not. Roy. Astron. Soc.* **429** (2013) 2249, arXiv:1212.3339 [astro-ph.CO].

[215] A. A. Starobinsky, "Disappearing cosmological constant in f(R) gravity," *JETP Lett.* **86** (2007) 157–163, arXiv:0706.2041 [astro-ph].

[216] S. A. Appleby and R. A. Battye, "Do consistent $F(R)$ models mimic General Relativity plus Λ?," *Phys. Lett.* **B654** (2007) 7–12, arXiv:0705.3199 [astro-ph].

[217] S. Tsujikawa, "Observational signatures of $f(R)$ dark energy models that satisfy cosmological and local gravity constraints," *Phys. Rev.* **D77** (2008) 023507, arXiv:0709.1391 [astro-ph].

[218] S. Tsujikawa, R. Gannouji, B. Moraes, and D. Polarski, "The dispersion of growth of matter perturbations in f(R) gravity," *Phys. Rev.* **D80** (2009) 084044, arXiv:0908.2669 [astro-ph.CO].

[219] R. Gannouji, B. Moraes, and D. Polarski, "The growth of matter perturbations in f(R) models," *JCAP* **0902** (2009) 034, arXiv:0809.3374 [astro-ph].

[220] T. Narikawa and K. Yamamoto, "Characterising linear growth rate of cosmological density perturbations in f(R) model," *Phys. Rev.* **D81** (2010) 043528, arXiv:0912.1445 [astro-ph.CO].

[221] A. J. López-Revelles, "Growth of matter perturbations for realistic $F(R)$ models," *Phys. Rev.* **D87** no. 2, (2013) 024021, arXiv:1301.2120 [gr-qc].

[222] K. Bamba, A. Lopez-Revelles, R. Myrzakulov, S. D. Odintsov, and L. Sebastiani, "Cosmic history of viable exponential gravity: Equation of state oscillations and growth index from inflation to dark energy era," *Class. Quant. Grav.* **30** (2013) 015008, arXiv:1207.1009 [gr-qc].

[223] M. A. Resco and A. L. Maroto, "Testing for gravitational preferred directions with galaxy and lensing surveys," *JCAP* **02** (2020) 013, arXiv:1907.12285 [astro-ph.CO].

[224] D. B. Thomas, L. Whittaker, S. Camera, and M. L. Brown, "Estimating the weak-lensing rotation signal in radio cosmic shear surveys," *Mon. Not. Roy. Astron. Soc.* **470** no. 3, (2017) 3131–3148, arXiv:1612.01533 [astro-ph.CO].

[225] L. Amendola, S. Fogli, A. Guarnizo, M. Kunz, and A. Vollmer, "Model-independent constraints on the cosmological anisotropic stress," *Phys. Rev.* **D89** no. 6, (2014) 063538, arXiv:1311.4765 [astro-ph.CO].

[226] J. Lesgourgues, "The Cosmic Linear Anisotropy Solving System (CLASS) I: Overview," arXiv:1104.2932 [astro-ph.IM].

[227] S. Johnston and J. Wall, "Science with ASKAP - the Australian Square Kilometre Array Pathfinder," *Exper. Astron.* **22** (2008) 151, arXiv:0810.5187 [astro-ph].

[228] **SDSS** Collaboration, M. Tegmark *et al.*, "Cosmological Constraints from the SDSS Luminous Red Galaxies," *Phys. Rev.* **D74** (2006) 123507, arXiv:astro-ph/0608632 [astro-ph].

[229] V. Yankelevich and C. Porciani, "Cosmological information in the redshift-space bispectrum," *Mon. Not. Roy. Astron. Soc.* **483** no. 2, (2019) 2078–2099, arXiv:1807.07076 [astro-ph.CO].

[230] L. Santos, W. Zhao, E. G. Ferreira, and J. Quintin, "Constraining interacting dark energy with CMB and BAO future surveys," *Phys. Rev. D* **96** no. 10, (2017) 103529, arXiv:1707.06827 [astro-ph.CO].

[231] E. Majerotto *et al.*, "Probing deviations from General Relativity with the Euclid spectroscopic survey," *Mon. Not. Roy. Astron. Soc.* **424** (2012) 1392–1408, arXiv:1205.6215 [astro-ph.CO].

[232] D. Sapone, E. Majerotto, M. Kunz, and B. Garilli, "Can dark energy viscosity be detected with the Euclid survey?," *Phys. Rev. D* **88** (2013) 043503, arXiv:1305.1942 [astro-ph.CO].

[233] I. Tutusaus, B. Lamine, and A. Blanchard, "On the dark contents of the Universe: A Euclid survey approach," *Grav. Cosmol.* **117** (2016) 120, arXiv:1612.06745 [astro-ph.CO].

[234] **Euclid** Collaboration, A. Blanchard *et al.*, "Euclid preparation: VII. Forecast validation for Euclid cosmological probes," arXiv:1910.09273 [astro-ph.CO].

[235] M. A. Resco and A. L. Maroto, "The Fisher gAlaxy suRvey cOde (FARO)," arXiv:2007.05360 [astro-ph.CO].

[236] L. Amendola, M. Kunz, M. Motta, I. D. Saltas, and I. Sawicki, "Observables and unobservables in dark energy cosmologies," *Phys. Rev.* **D87** no. 2, (2013) 023501, arXiv:1210.0439 [astro-ph.CO].

[237] L. Pogosian, A. Silvestri, K. Koyama, and G.-B. Zhao, "How to optimally parametrize deviations from General Relativity in the evolution of cosmological perturbations?," *Phys. Rev. D* **81** (2010) 104023, arXiv:1002.2382 [astro-ph.CO].

[238] P. McDonald and U. Seljak, "How to measure redshift-space distortions without sample variance," *JCAP* **0910** (2009) 007, arXiv:0810.0323 [astro-ph].

[239] M. Aparicio Resco *et al.*, "J-PAS: forecasts on dark energy and modified gravity theories," *Mon. Not. Roy. Astron. Soc.* **493** no. 3, (2020) 3616–3631, arXiv:1910.02694 [astro-ph.CO].

[240] R. Boschetti, L. R. Abramo, and L. Amendola, "Fisher matrix for multiple tracers: all you can learn from large-scale structure without assuming a model," arXiv:2005.02465 [astro-ph.CO].

[241] **EUCLID** Collaboration, I. Tutusaus *et al.*, "Euclid: The importance of galaxy clustering and weak lensing cross-correlations within the photometric Euclid survey," arXiv:2005.00055 [astro-ph.CO].

[242] N. Mostek, A. L. Coil, M. C. Cooper, M. Davis, J. A. Newman, and B. Weiner, "The DEEP2 Galaxy Redshift Survey: Clustering Dependence on Galaxy Stellar Mass and Star Formation Rate at z 1," *Astrophys. J.* **767** (2013) 89, arXiv:1210.6694 [astro-ph.CO].

[243] N. P. Ross *et al.*, "Clustering of Low-Redshift (z <= 2.2) Quasars from the Sloan Digital Sky Survey," *Astrophys. J.* **697** (2009) 1634–1655, arXiv:0903.3230 [astro-ph.CO].

[244] Marín-Franch *et al.*, "JPCam: Development of a 1.2 Gpixel Camera for the J-PAS Survey," in *Highlights on Spanish Astrophysics IX*, S. Arribas, A. Alonso-Herrero, F. Figueras, C. Hernández-Monteagudo, A. Sánchez-Lavega, and S. Pérez-Hoyos, eds., pp. 670–675. Mar., 2017.

[245] N. Benitez *et al.*, "Measuring Baryon Acoustic Oscillations along the line of sight with photometric redshifs: the PAU survey," *Astrophys. J.* **691** (2009) 241–260, arXiv:0807.0535 [astro-ph].

[246] C. Padilla *et al.*, "The PAU Camera at the William Herschel Telescope," *SPIE Proc.* **9908** (2016) 99080Z.

[247] A. Benitez-Llambay, J. F. Navarro, M. G. Abadi, S. Gottloeber, G. Yepes, Y. Hoffman, and M. Steinmetz, "Dwarf Galaxies and the Cosmic Web," *Astrophys. J.* **763** (2013) L41, arXiv:1211.0536 [astro-ph.CO].

[248] S. Bonoli *et al.*, "The miniJPAS survey: a preview of the Universe in 56 colours," arXiv:2007.01910 [astro-ph.CO].

[249] P. Baqui *et al.*, "The miniJPAS survey: star-galaxy classification using machine learning," arXiv:2007.07622 [astro-ph.IM].

[250] A. A. Costa *et al.*, "J-PAS: forecasts on interacting dark energy from baryon acoustic oscillations and redshift-space distortions," *Mon. Not. Roy. Astron. Soc.* **488** no. 1, (2019) 78–88, arXiv:1901.02540 [astro-ph.CO].